From rocks to wastes: Tracing the fate of chromium in mining-impacted lateritic environments

Dissertation

to obtain the academic degree of

Doktor der Naturwissenschaften (Dr. rer. nat.)

submitted to the Department of Earth Sciences

of Freie Universität Berlin

by

Ruth Esther G. Delina

Berlin, 2024

First Reviewer (Erstgutachterin):

Prof. Dr. Liane G. Benning
Department of Earth Sciences, Freie Universität Berlin, Berlin, Germany
Interface Geochemistry Section, GFZ German Research Centre for Geosciences, Potsdam, Germany

Second reviewer (Zweitgutachter):

Prof. Dr. Sarah A. Gleeson
Department of Earth Sciences, Freie Universität Berlin, Berlin, Germany
Inorganic and Isotope Geochemistry Section, GFZ German Research Centre for Geosciences, Potsdam, Germany

Doctoral Committee (Promotionsausschuss):

Prof. Dr. Friedhelm von Blanckenburg (Vorsitz)
Department of Earth Sciences, Freie Universität Berlin, Berlin, Germany

Prof. Dr. Timm John (Stellv. Vorsitz)
Department of Earth Sciences, Freie Universität Berlin, Berlin, Germany

Prof. Dr. Liane G. Benning
Department of Earth Sciences, Freie Universität Berlin, Berlin, Germany
Interface Geochemistry Section, GFZ German Research Centre for Geosciences, Potsdam, Germany

Prof. Dr. Sarah A. Gleeson
Department of Earth Sciences, Freie Universität Berlin, Berlin, Germany
Inorganic and Isotope Geochemistry Section, GFZ German Research Centre for Geosciences, Potsdam, Germany

Dr. Pablo Forjanes
Interface Geochemistry Section, GFZ German Research Centre for Geosciences, Potsdam, Germany

Day of defense (Tag der Disputation):

3rd of December 2024

Erklärung der Eigenständigkeit

Ich erkläre hiermit, dass ich die vorliegende Arbeit selbständig verfasst und keine anderen als die angegebenen Quellen und Hilfsmittel benutzt habe. Ich bestätige, dass die eingereichte elektronische Fassung der Dissertation der schriftlichen Fassung entspricht und dass diese Dissertation nicht in einem früheren Promotionsverfahren eingereicht wurde.

Berlin, September 2024

_____

Ruth Esther G. Delina

Declaration

The presented thesis is a cumulative collection of peer-reviewed scientific papers, including those that have been published, have been submitted for publication, or are in advanced stages of preparation for submission. The candidate confirms that the work submitted is her own and that proper credit has been given throughout the thesis when referencing the work of others. The specific contributions of the candidate and other authors to each chapter are detailed below:

Chapter 3 reproduces a manuscript published in *Environmental Science & Technology*.

Delina, R.E.G.; Perez, J.P.H.; Stammeier, J.A.; Bazarkina, E.F.; Benning, L.G. (2024). Partitioning and Mobility of Chromium in Iron-Rich Laterites from an Optimized Sequential Extraction Procedure. *Environmental Science & Technology,* 58, 6391-6401.
DOI: https://doi.org/10.1021/acs.est.3c10774

REGD conceived and designed the study with the help of JPHP and LGB. REGD performed the synthesis and preparation of mineral standards, optimization and validation of the Cr sequential extraction procedure (SEP), mineralogical and geochemical characterization, and synchrotron-based Cr K-edge HERFD XAS. JPHP provided training on mineral synthesis and trace metal analysis using ICP-OES. JAS performed the chemical analysis of the laterite samples. EFB and JPHP helped in the collection of HERFD-XAS. REGD processed the data, interpreted the results, and prepared the manuscript with contributions from all authors.

Chapter 4 reproduces a manuscript in the advanced stages of preparation for submission in *Geochimica et Cosmochimica Acta.*

Delina, R.E.G.; Perez, J.P.H.; Bazarkina, E.F.; Prieur, D.; Kvashnina, K.O.; Scheinost, A.C.; Mathon, O.; Stammeier, J.A.; Rabang, D.C.V.; Arcilla, C.A.; Benning, L.G. Coupling of iron and manganese controls chromium speciation in laterites developed from ultramafic rocks.

REGD conceived and designed the study with the help of JPHP and LGB. REGD was responsible for part of the funding acquisition for the fieldwork as well as for the collection of the laterite samples. She performed all mineralogical and geochemical characterizations, as well as the synchrotron-based HERFD and TFY Cr, Fe, and Mn K-edge XAS analyses, and the synthesis and preparation of mineral standards. DCVR and CAA helped REGD and JPHP

obtain the core samples from the mining area. The analytical work done in this study was done with the help of the following people: JAS for the chemical analysis of the laterite samples; JPHP, EFB, and KOK for the HERFD XAS; and JPHP, DP, AS, and OM for the TFY XAS. REGD processed the data, interpreted the results, and prepared the manuscript with contributions from all authors.

Chapter 5 reproduces a manuscript in revision with *Environmental Science & Technology*.

Delina, R.E.G.; Perez, J.P.H.; Roddatis, V.V.; Stammeier, J.A.; Prieur, D.; Scheinost, A.C.; Tan, M.M.; Garcia, J.J.L.; Arcilla, C.A.; Benning, L.G. Immobilization of chromium by iron oxides in nickel-cobalt laterite mine tailings.

REGD conceived and designed the study with the help of JPHP and LGB. REGD organized the fieldwork, collected the mine tailings, performed the material characterization, synchrotron-based Cr K-edge XAS, and sequential extraction. The fieldwork and analytical work done in this study were done with the help of the following people: JPHP for the collection of the samples; VVR for the TEM images; JAS for chemical analysis of the mine tailings; MMT, JJLG, and CAA for the UV-Vis and IC analysis; and JPHP, DP, and ACS for the XAS. REGD processed the data, interpreted the results, and prepared the manuscript with contributions from all authors.

In addition to scientific papers included in this dissertation, the candidate also wrote and contributed to the following manuscripts:

Corkett, A.J.; Okhrymenko, M.; Roddatis, V.; Lebedev, O.; Leusen, J.V.; **Delina, R.E.G.**; Perez, J.P.H.; Benning, L.G.; Dronskowskia, R. The mixed transition-metal cyanamide $MnCr_2(NCN)_4$. *Under review in Inorganic Chemistry.*

REGD contributed to the collection, processing, and interpretation of the Mn and Cr K-edge XANES data.

Perez, J.P.H.; Tobler, D.J.; **Delina, R.E.G.**; Mathon, O.; Guilbaud, R.; Chi Fru, E.; Benning, L.G. Simulating iron mineral formation in Early Earth oceans and its impact on phosphorus bioavailability. *In the final stages of preparation for submission.*

REGD contributed to the mineral precipitation experiments and the collection of Fe K-edge XAS data.

Acknowledgements

Throughout my journey as a doctoral student, I experienced the support of many people and organizations, without whom this work would not have been possible. First of all, I would like to express my heartfelt gratitude to my supervisor Prof. Dr. Liane G. Benning for her guidance and mentorship for the past four years. Your encouragement, especially at times when I doubt myself, has not only boosted my confidence but has also empowered me to push beyond my limits. I owe much of my growth as a researcher to your invaluable support and all the opportunities you helped open.

I am also deeply grateful to my co-supervisor, Dr. Jeffrey Paulo H. Perez, for helping me navigate this academic journey—from the initial conceptualization of my doctoral thesis to the sleepless synchrotron analyses of my samples and throughout the final stages of this study. Thank you for introducing me to the colorful world of mineral synthesis and synchrotron analyses and for your patience with me as a newbie in atomic-scale investigations. I will certainly miss the adrenaline of these experiments and our long discussions around the clock. Finally, thank you for your encouragement that makes each obstacle feel surmountable. I could not have envisioned better guidance from a scientific mentor and friend.

None of this research would have been possible without the generous support of the following organizations. I would like to extend my sincere thanks to the DAAD German Academic Exchange Service for funding my doctoral research (grant no. 91769931), giving me the wonderful opportunity to conduct my thesis in the best institutions in Germany and around the world. I also acknowledge the European Synchrotron Radiation Facility for the XAS beamtime allocation; the British Geological Survey (BGS) International National Capability programme 'Geoscience to tackle Global Environmental Challenges' (NERC NE/X006255/1) for funding my research visit to perform experiments in the hydrothermal laboratories of BGS; the International Association of GeoChemistry for funding geochemical analyses conducted during this study; TravelingGeologist and DAAD for travel grants that supported my fieldwork in the Philippines; and the Deutsche Mineralogische Gesellschaft and European Mineralogical Union for the travel grants to present in conferences.

The fieldwork and analytical work conducted in this research were carried out with the help of my scientific collaborators, to whom I am grateful. Dainty Rabang, Mark Tan, Jhonard John Garcia, Narod Eco, and Prof. Dr. Carlo Arcilla of UP NIGS-EMS are thanked for their assistance throughout the fieldwork; RTNMC and CBNC for access to field sites and for their help during sample collection; Dr. Jessica Stammeier, Sabine Tonn, and the ElMiE-Lab for their help with ICP-OES analyses; HELGES Laboratories for access to their clean labs and

ICP-OES; Dr. Olivier Mathon of ESRF BM23 and Dr. Elena Bazarkina, Dr. Damien Prieur, Dr. Kristina Kvashnina, and especially Dr. Andreas Scheinost of ESRF BM20 for their support with XAS analysis; Dr. Roberts Blukis for training me how to do Rietveld refinements; and Dr. Vladimir Roddatis, Dr. Marcin Syczewski and Anja Schreiber of the GFZ PISA Facility for their expert guidance on electron microscopy; Dr. Alicja Lacinska, Keith Bateman, Finlay Banks, Dr. Matthew Vosper of BGS, and Dr. Karmina Aquino and Dr. Americus, Perez of PNRI for their invaluable contributions to the hydrothermal experiments and on-going projects. Your contributions and willingness to collaborate enriched the depth and breadth of my work.

Special thanks go to my lovely colleagues in the Interface Geochemistry research group at GFZ for making this journey more meaningful. Sandy Hermman, for your invaluable help in all administrative and bureaucratic related matters. Thank you Kuya Marc Paje for making it easy and comfortable to work in our laboratories, I will miss our volleyball conversations over lunch. Mamata Ghimire for all your help in the lab, Caitlyn Berryman for our shared sleepless XAS beamtime trips, and Chiara Bahl for helping me with my German translations. To the best co-PhDs I could ever ask for, thank you for all the shared experiences that I will forever cherish. Thank you roomies Elisa Peter, Karim Altona, Qi Dai, Maria Vlachodimitropoulou for the songs and conversations that kept me sane in the office. Zhengzheng, for being my constant conference buddy, I will surely miss our trips and late-night practices. Finally, my mineral girls, Alice Paskin and Rebecca Volkmann, I am deeply grateful for the friendship and our bonding over milktea among many other wonderful memories.

To my Filipino friends in Germany and around the world, my former flatmates, CCF and JIBFI Family, knowing I always have a family wherever I go, fills my heart with gratitude and joy. Your encouragement and prayers cheered me on.

I would not be where I am today if it were not for the unconditional love, care, and encouragement I have always received from my family. To my parents, Tatay Robert and Mami Ruby, Kuya JP, Ate Mila, Tita Pinky, and to Kevin's family, even though distance separates us, your unwavering support and prayers give me strength each day. I look forward to spending more time with you.

To my beloved husband, Kevin, you have been my rock throughout this journey. Thank you for being my greatest cheerleader, being there through every high and low, and especially when I needed you most. For packing my lunch and the long walks that kept my stomach and heart full while writing this thesis. I could not have achieved this without you by my side. *Mahal na mahal kita!*

Above all, I want to thank God for providing me with the strength, wisdom, and endurance to pursue this journey. To God, my refuge and ever-present help, be the glory!

Abstract

Chromium (Cr) levels surpassing regulatory limits remain a pressing environmental challenge worldwide, especially in natural waters associated with nickel (Ni) laterite ore deposits developed from ultramafic rocks. While Cr persists in the environment as Cr(III), an essential micronutrient for human nutrition, public concern lies with Cr(VI), the more mobile, toxic, and carcinogenic form of Cr. It is, therefore, crucial to quantify the speciation and mobility of Cr in Ni laterites and associated mine tailings and waters to predict possible pathways for its release in surrounding environments. However, the incomplete understanding of the interaction between Cr and prevalent iron (Fe) (oxyhydr)oxides in Ni laterites renders such quantification challenging. Although Fe (oxyhydr)oxides, as well as redox-active manganese (Mn) oxides, have been known to control the mobility of Cr in the environment, mechanistic evidence of their role in the release and sequestration of Cr during weathering of ultramafic rocks into laterites remains lacking. In addition, the mining and processing of worldwide Ni laterite ore deposits are expected to increase exponentially because of the global energy transition. Therefore, it is not only important to elucidate the fate of Cr during lateritization, but also to quantify its ultimate fate after mining and processing of the Ni laterite ores. To bridge these knowledge gaps, I conducted a holistic study combining field observations and detailed experimental evaluations based on a suite of highly complementary laboratory- and synchrotron-based analytical approaches, ultimately tracing the fate of Cr from source to sink.

Through laboratory mineral synthesis and dissolution experiments, I optimized a Cr sequential extraction procedure (SEP) that allows the quantitative assessment of the partitioning and, thus, the potential mobility of Cr in iron-rich laterites. I validated the new method using complementary mineralogical, geochemical, and synchrotron-based X-ray absorption spectroscopy (XAS) methods, which showed that my new SEP more efficiently and accurately quantifies the partitioning of Cr in natural Ni laterite samples compared to existing SEPs. With the optimized SEP, easily mobilizable Cr fractions, most especially adsorbed Cr(VI) oxyanions, could be better quantified compared to existing methods, improving our ability to evaluate the potential environmental impacts of Cr. Moreover, my new SEP more adequately leaches important Cr host phases like Fe (oxyhydr)oxides by considering the properties of different Cr species and the ability of Cr to stabilize crystal structures.

To trace the evolution of Cr from the weathering of ultramafic rocks to the formation of Ni laterites, I investigated the changes in Cr speciation along several Ni laterite profiles from the Philippines. By combining high energy resolution fluorescence detection (HERFD) and total fluorescence yield (TFY) Cr, Fe, and Mn K-edge XAS, I documented that Cr(III) released from

the weathering of ultramafic minerals (e.g., olivine, chromite) is redistributed to the saprolite zone by structural incorporation or adsorption onto secondary phyllosilicates such as serpentine and smectite. I also captured the Cr sequestration mechanism by secondary Fe (oxyhydr)oxides – starting from the polymerization of Cr(III) with Fe(III) to form poorly crystalline precursors to their crystallization, and their subsequent transformation to Cr(III)-substituted Fe (oxyhydr)oxides (e.g., goethite, hematite) in the overlying limonite zone. There, the redox dynamics between Cr(III) and Mn(IV/III) (oxyhydr)oxides also oxidized up to 13% of the total Cr into the toxic Cr(VI), resulting in detectable Cr(VI) concentrations ranging from 128 to 2,713 mg kg^{-1}, which is up to 80 times higher than the average Cr composition of the upper crust. My data documents that Cr(VI) could be adsorbed by Fe (oxyhydr)oxides as mononuclear edge-sharing (^2E) and monodentate mononuclear (^1V) inner-sphere surface complexes or leached downstream due to its high mobility, explaining the elevated Cr(VI) concentrations waterbodies associated with Ni laterites. By comparing Ni laterite profiles from different localities, my work also highlighted the role of environmental factors in mobilizing Cr, especially in tropical areas where the rate of weathering is enhanced.

Finally, I followed the fate of Cr after mining and high pressure acid leaching (HPAL) of Ni and Co from the laterite ores, revealing how and in what form Cr ends up in the mine tailings. Specifically, I employed nano-scale characterization using scanning transmission electron microscopy (STEM) and synchrotron-based XAS integrated with the optimized Cr SEP to investigate Cr in the liquid and solid phases of mine tailings collected from active and rehabilitated impoundments. I unraveled that Cr is undetectable in the liquid phase because it became immobilized in the form of Cr(III) in the structure of recalcitrant minerals. Secondary hematite that precipitates early in the HPAL process serves as the main Cr trap by structurally incorporating up to 61% of the total Cr. Meanwhile, the remaining Cr is primarily hosted in chromite residues from the source laterite ores. These results emphasized the crucial role of Fe (oxyhydr)oxides in the sequestration of Cr in highly stable sinks, preventing potential remobilization in the natural environment.

Overall, my doctoral work delivered new and significant insights into the release and sequestration of Cr in Ni laterite areas affected by geogenic (e.g., weathering) and anthropogenic (e.g., processing) activities. This data now allows us to better predict and monitor Cr pathways, contributing far-reaching implications for the environmental management and sustainable development of these important mineral resources.

Zusammenfassung

Chrom (Cr) überschreitet weltweit immer häufiger die gesetzlichen Grenzwerte und stellt damit ein drängendes Umweltproblem dar, insbesondere für Gewässer die mit Nickel (Ni)-Laterit-Erzlagerstätten in Verbindung stehen. Während Cr in der Umwelt in Form von Cr(III) als essentieller Mikronährstoff vorkommt, richtet sich die öffentliche Besorgnis vor allem auf Cr(VI), eine mobile, toxische und krebserregenden Form von Cr. Es ist daher essentiell, die Speziation und Mobilität von Cr in Ni-Lateriten, den zugehörigen Abraumhalden und Gewässern zu quantifizieren, um eine mögliche Kontamination der Umwelt vorherzusagen. Das unvollständige Verständnis der Wechselwirkung zwischen Cr und den in Ni-Lateriten vorherrschenden Fe-(oxyhydr)-oxiden macht eine solche Quantifizierung jedoch schwierig. Obwohl bekannt ist, dass Fe-(oxyhydr)-oxide sowie redoxaktive Mn-oxide die Mobilität von Cr in der Umwelt beeinflussen, sind die Mechanismen bei der Freisetzung und Sequestrierung von Cr während der Verwitterung von ultramafischem Gestein zu Lateriten unbekannt. Angesichts der erwarteten exponentiellen Zunahme des Abbaus und der Verarbeitung von Ni-Lateriterzvorkommen aufgrund der globalen ist es nicht nur wichtig, den Verbleib von Cr während der Lateritisierung zu klären, sondern auch den Verbleib nach dem Abbau und der Verarbeitung der Erze zu quantifizieren. Um diese Wissenslücken zu schließen, habe ich eine umfassende Studie durchgeführt, die Beobachtungen aus dem Feld mit Laborexperimenten kombiniert. Dabei wurde eine Reihe von Analyseverfahren, inkl. Synchrotron angewendet, die letztlich den Verbleib von Cr von der Quelle bis zur Senke nach verfolgen.

Anhang von Mineralsynthese- und Auflösungsexperimenten habe ich einen sequentiellen Extraktionsprozess (SEP) für Cr optimiert, der die Verteilung von Cr quantitativ bestimmt und damit auch die potenzielle Mobilität von Cr in eisenreichen Lateriten. Ich habe die neue Methode mithilfe ergänzender mineralogischer, geochemischer und Synchrotron-basierten röntgenabsorptionsspektroskopischer (XAS) Methoden validiert, und so gezeigt, dass mein neuer SEP die Verteilung von Cr in natürlichen Ni-Lateritproben im Vergleich zu bestehenden SEPs effizienter und genauer quantifiziert. Mit dem optimierten SEP konnten leicht mobilisierbare Cr-Fraktionen, insbesondere adsorbierte Cr(VI)-Oxyanionen, im Vergleich zu bestehenden Methoden besser quantifiziert werden, was unsere Möglichkeiten zur Bewertung der potenziellen Umweltauswirkungen von Cr deutlich verbessert. Darüber hinaus kann mein optimierter SEP wichtige Cr-Mineralphasen wie Fe-(oxyhydr)-oxide besser lösen, indem es die Eigenschaften verschiedener Cr-Spezies und die Fähigkeit von Cr zur Stabilisierung von Kristallstrukturen berücksichtigt.

Um die Entwicklung von Cr von der Verwitterung ultramafischer Gesteine bis zur Bildung von Ni-Lateriten zu verfolgen, habe ich die Veränderungen der Cr-Speziation entlang mehrerer Ni-Laterit-Profile auf den Philippinen untersucht. Durch die Kombination von High Energy Resolution Fluorescence Detection (HERFD) und Total Fluorescence Yield (TFY) Cr, Fe und Mn K-Edge XAS

habe ich gezeigt, dass Cr(III), das bei der Verwitterung ultramafischer Minerale (z. B. Olivin, Chromit) freigesetzt wird, durch strukturelle Inkorporation oder Adsorption an sekundäre Schichtsilikate wie Serpentin und Smektit in die Saprolitzone umverteilt wird. Ich habe auch den Mechanismus der Cr-Sequestrierung durch sekundäre Fe-(oxyhydr)-oxide erfasst - ausgehend von der Polymerisation von Cr(III) mit Fe(III) zur Bildung wenig kristalliner Vorstufen bis hin zu ihrer Kristallisation und ihrer anschließenden Umwandlung in Cr(III)-substituierte Fe-(oxyhydr)-oxide (z. B. Goethit, Hämatit) in der darüber liegenden Limonitzone. Dort werden durch Redoxreaktion zwischen Cr(III)- und Mn(IV/III)-(oxyhydr)oxiden werden bis zu 13 % des gesamten Cr in das giftige Cr(VI) oxidiert, was zu nachweisbaren Cr(VI)-Konzentrationen von 128 bis 2.713 mg kg^{-1} führt, bis zu 80-mal höher als die durchschnittliche Cr-Zusammensetzung der oberen Kruste. Meine Daten belegen, dass Cr(VI) von Fe-(oxyhydr)-oxiden in Form von mononuklearen kantenverknüpft (^2E) und monodentaten mononuklearen (^1V) Oberflächenkomplexen adsorbiert oder aufgrund seiner hohen Mobilität flussabwärts ausgewaschen werden kann, was die erhöhten Cr(VI)-Konzentrationen in Wasserkörpern in Verbindung mit Ni-Lateriten erklärt. Durch den Vergleich von Ni-Laterit-Profilen aus verschiedenen Orten hat meine Arbeit auch die Rolle von Umweltfaktoren bei der Mobilisierung von Cr hervorgehoben, insbesondere in tropischen Gebieten, in denen die Verwitterungsrate erhöht ist.

Abschließend habe ich das Schicksal von Cr nach dem Abbau und saurer Hochdrucklaugung (HPAL) von Ni und Co aus den Laterit Erzen verfolgt, um herauszufinden, wie und in welcher Form Cr in die Abraumhalden gelangt. Insbesondere habe ich die Charakterisierung im Nanomaßstab mit Hilfe der Rastertransmissionselektronenmikroskopie (STEM) und der Synchrotron-basierten XAS in Verbindung mit dem optimierten Cr-SEP eingesetzt, um Cr in den flüssigen und festen Phasen von Abraumhalden zu untersuchen, die aus aktiven und sanierten Lagerstätten stammen. Ich kann zeigen, dass Cr in der flüssigen Phase nicht nachweisbar ist, weil es in Form von Cr(III) in der Struktur von resistenten Mineralen gebunden ist. Sekundärer Hämatit fällt früh im HPAL-Prozess aus und bindet bis zu 61 % des gesamten Cr strukturell und ist damit die größte Senke für Cr. Das verbleibende Cr ist in erster Linie in Chromit-Rückständen aus den Ausgangs-Lateriterzen enthalten. Diese Ergebnisse unterstreichen die entscheidende Rolle von Fe-(oxyhydr)-oxiden bei der Bindung von Cr in resistenten Senken, die eine mögliche Remobilisierung in der natürlichen Umgebung verhindern.

Insgesamt liefert diese Arbeit neue und wichtige Erkenntnisse über die Freisetzung und Sequestrierung von Cr in Ni-Lateritgebieten, die von geogenen (z. B. Verwitterung) und anthropogenen (z. B. Abbau) Aktivitäten betroffen sind. Anhand dieser Daten können wir die Mobilität von Cr besser vorhersagen und überwachen, was weitreichende Auswirkungen auf das Umweltmanagement und die nachhaltige Entwicklung dieser wichtigen Mineralressourcen hat.

Table of Contents

Chapter 1

Introduction

Chromium (Cr) is an important transition metal in many metallurgical (e.g., alloy manufacturing), refractory (e.g., stainless steel production), and chemical (e.g., leather tanning) industries (Kotaś & Stasicka, 2000). However, it is also among the priority metals of public health concern due to the toxicity of its hexavalent species, Cr(VI) (Tchounwou et al., 2012). Chromium persists in the environment as Cr(III) or Cr(VI). In contrast to Cr(III), a vital micronutrient (Anderson, 1997), Cr(VI) is a known carcinogen and exhibits greater mobility in nature (Kotaś & Stasicka, 2000). Cr(VI) occurs naturally in soils and waterbodies associated with the weathering of ultramafic rocks worldwide (e.g., Brazil, Greece, Italy, New Caledonia, Philippines, USA, etc.) (Chrysochoou et al., 2016) which have an average Cr concentration (2,980 mg kg^{-1}) (Alloway & Ayres, 1997), a value that is nearly 100 times more than Earth's upper crustal average (35 mg kg^{-1}) (Hans Wedepohl, 1995). This chemical weathering can lead to the formation of nickel (Ni) laterite ore deposits that are further enriched in Cr (≤ 70,000 mg kg^{-1}) (Chrysochoou et al., 2016; Ulrich et al., 2019) and that are the world's largest terrestrial resource of Ni (USGS, 2023) and also important sources for cobalt, rare earth elements (REEs) and platinum group elements (PGEs) (Aiglsperger et al., 2016). Mining and processing of Ni laterite ores may lead to adverse environmental impacts such as air and groundwater pollution, and thus, not well-understood human health issues (Marsh et al., 2013). Despite the risks posed by such elevated Cr concentrations in Ni laterites, the speciation of Cr, as well as the mechanisms that control its release and sequestration during laterite mining and processing, remain poorly understood, and this was the main topic of my doctoral thesis. I addressed these open questions by following the fate of the chromium from source to sink and evaluating its speciation and bonding in various geomaterials.

1.1. Fate of geogenic chromium in lateritic environments

The term "laterite" broadly describes a highly weathered material rich in iron (Fe) and aluminum (Al) (oxyhydr)oxides that covers about 33% of the continents (Tardy, 1997; Stoops & Marcelino, 2018). Nickel laterites are Fe (oxyhydr)oxide-rich deposits mostly found in tropical to subtropical regions and tectonically active plate collision zones (e.g., Indonesia, Philippines, New Caledonia) where ultramafic rocks from ophiolite complexes are subjected to

intense weathering (Elias, 2002). Upon weathering, less soluble components (e.g., Fe, Al, Cr) are residually enriched with the dissolution of primary silicates and leaching of more mobile cations (e.g., Si and Mg) resulting in the stratification of the laterite profile (Elias, 2002; Gleeson et al., 2003). Fe (oxyhydr)oxides (e.g., goethite, hematite) that progressively increase with the extent of weathering, have been cited as important hosts for Cr released from primary minerals such as Cr-bearing silicates (e.g., olivine and pyroxene) and, to a lesser extent, from Cr-bearing spinels (e.g., chromite) (Garnier et al., 2008; Fandeur et al., 2009a). These Fe phases were found to host the majority of Cr (up to 85% of the total Cr content) in laterites from New Caledonia and Brazil (Quantin et al., 2002; Garnier et al., 2006). However, there is still a lack of direct evidence of their role in the partitioning of different Cr species and the mechanisms involved in Cr sequestration and stabilization in Fe (oxyhydr)oxides with the formation of laterites.

During lateritization, Cr(III) could be oxidized to Cr(VI) which adsorbs onto mineral surfaces, or leaches into pore waters, and eventually into surrounding waterbodies. Investigations of lateritic soils from New Caledonia (Fandeur et al., 2009b) have shown the occurrence of Cr(VI) comprising ≤ 20% of the total Cr concentration and related its presence to the abundance of Mn(IV/III) (oxyhydr)oxides, which are considered as the primary oxidants of Cr(III) in rocks and soil systems (Eary & Rai, 1987). In the evaluation of the potential release of Cr(VI) in Ni mining areas, leaching experiments with laterites and mine sediments from the Philippines (Delina et al., 2020) and New Caledonia (Gunkel-Grillon et al., 2014) yielded Cr(VI) concentrations up to 358 mg kg^{-1}. The transport of Cr(VI) to waterways was confirmed by their mine surface waters having Cr(VI) levels (≤ 213 μg L^{-1} and ≤ 1620^{-1}, respectively) (Gunkel-Grillon et al., 2014; Delina et al., 2020) far exceeding the international drinking water standards for Cr(VI) (50–100 μg L^{-1}) (USEPA, 2006; WHO, 2017). While the weathering of ultramafic rocks to laterites forms a complex combination of components (e.g., Fe and Mn (oxyhydr)oxides) heavily involved in the cycling of Cr in the environment, little is known about their influence on the partitioning, mobilization, and redox behavior of Cr.

Although there are few studies that link the prevalence of aqueous Cr(VI) in lateritic environments to mined Ni laterite ores, there are far fewer studies investigating the speciation of Cr when the laterites are processed and transformed into mine waste or tailings. Nickel (±Co) extraction from laterite ores results in millions of tons of mine tailings containing non-targeted metals like Fe and Cr (Marsh et al., 2013). Hydrometallurgical processing of laterites have been predicted to oxidize dissolved Cr to Cr(VI) (Whittington & Muir, 2000) while laboratory Ni and Co extraction tests have suggested the association of Cr with prevalent secondary Fe precipitates (e.g., hematite) (Önal & Topkaya, 2014). Still, the actual speciation of Cr is unknown. With the consistent rise in demand for Ni and Co because of the metal-reliant global energy transition (IEA, 2021), we expect not only an increase in mining activities but also the

amount of mine wastes generated from metal extraction (Hudson-Edwards & Dold, 2015). Thus, deciphering the fate of Cr from the laterite profile to the mine tailings is crucial for a holistic evaluation of the potential mobilization of Cr in Ni laterite mining areas worldwide.

1.2. Scope of this work

Because of the global industrial and economic importance of Ni laterite deposits, most research has extensively studied the weathering of ultramafic rocks to Ni laterites, and the consequent mineralization of critical metals (e.g., Ni, Co). Despite the known association of toxic Cr(VI) with ultramafic and lateritic environments, there is a dearth of research elucidating the evolution of Cr upon lateritization that could provide direct evidence of the Cr-mineral associations up to molecular-scale level. Furthermore, based on current literature, the behavior and environmental impact of Cr in the waste products generated from mining and processing Ni laterites has not been studied so far.

Therefore, with this work, I aimed to unravel the fate and cycling of Cr from laterite weathering profiles to mine wastes and to assess how these affect the potential toxicity, mobility, and long-term behavior in regions affected by Ni laterite mining and processing. By expanding our fundamental knowledge about the occurrence of Cr in lateritic environments, I aim to contribute to a better and more effective water quality and management strategy in Ni laterite areas.

1.3. Research objectives

My main aim was centered on addressing the knowledge gap about Cr in Ni laterite areas and to provide an in-depth and quantitative understanding of the mechanisms for the release and/or sequestration of Cr species in Ni laterite areas from source to sink and during both geogenic (e.g., weathering) and anthropogenic (e.g., mining and metal extraction) processes. I further wanted to assess the implications of Cr mobility from one process to the other and to surrounding environments. The specific objectives of my thesis were the following:

1. To decipher the role of Fe (oxyhydr)oxides in the sequestration of Cr in laterites and mine tailings
2. To elucidate the geochemical controls on the fate and speciation of Cr from lateritization to mine tailings formation
3. To assess the potential mobility and long-term behavior of Cr in Ni laterite mining environments

1.4. Thesis overview

My thesis is divided into six chapters, starting with this introductory chapter. This is followed by a literature review (Chapter 2), three results chapters that constitute the main outputs from my work, and a final chapter that summarizes the findings and provides a future outlook. In brief:

Chapter 2 provides an overview of the current knowledge on Ni laterite deposits, Cr occurrence in lateritic environments, and analytical approaches for Cr characterization.

Chapter 3 documents the optimization of a Cr sequential extraction procedure for Fe (oxyhydr)oxide-rich materials, revealing the importance of a Cr-specific method in investigating the partitioning and mobility of Cr in Ni laterites. This work has been published in *Environmental Science & Technology* (Delina et al., 2024).

Chapter 4 reports new insights on the influence of Fe and Mn (oxyhydr)oxides on the redox and speciation of Cr and provides direct evidence of the changes in the local bonding environment of Cr during laterite formation using molecular-scale techniques. This work is at the stage of an advanced manuscript to be submitted to *Geochimica et Cosmochimica Acta*.

Chapter 5 presents the first detailed work on deciphering the fate of Cr in Ni laterite mine tailings, enabling the prediction of the stability and long-term behavior of Cr in the Ni laterite mining cycle; this study focuses on the effect of Fe (oxyhydr)oxides in limiting the environmental mobility of Cr. This work is under revision with *Environmental Science & Technology*.

Chapter 6 summarizes the key findings and conclusions drawn from this work and proposes directions for future research.

Furthermore, **Appendices A and B** present additional work in progress at the time of submission of the thesis. Finally, to complement this work, **Appendix C** lists my scientific contributions and synchrotron work throughout the course of my doctoral research, while **Appendix D** details the awards and grants received during this period.

Chapter 2

Literature Review

2.1. Chromium geochemistry and toxicity

Chromium (Cr) occurs in the environment in its two most stable oxidation states, Cr(III) and Cr(VI), which manifest contrasting toxicity, mobility, and bioavailability (**Figure 2.1**). Cr(III) is a vital micronutrient (at a tolerable daily intake of 300 µg kg^{-1}) (EU, 2011; EFSA, 2014) that is involved in the metabolism of glucose, fat, and protein and that can be found in many food supplements (Anderson, 1997). In rocks and soils, Cr(III) is found incorporated in Cr-bearing minerals (e.g., chromite) or as species that are surface precipitated or strongly adsorbed onto mineral surfaces and/or organic matter (Schroeder & Lee, 1975; Kotaś & Stasicka, 2000; McClain et al., 2017). In aqueous environments, the trivalent Cr is thermodynamically stable at low *E*h mainly as Cr^{3+}, $Cr(OH)^{2+}$, $Cr(OH)_3^0$, and $Cr(OH)_4^-$ (Rai et al., 1987).

Figure 2.1. Diagram showing the contrasting properties of Cr(III) and Cr(VI)**.** The green Cr(III) and yellow Cr(VI) solutions were prepared using $CrCl_3 \cdot 6H_2O$ and K_2CrO_4, respectively.

In contrast to Cr(III), Cr(VI) exerts toxic effects on the environment, and upon exposure even to low concentration, it is considered a mutagen, teratogen, and carcinogen. For example, dermal exposure to Cr(VI) species may induce skin allergies, dermatitis, dermal necrosis, and corrosion, while ingestion and inhalation of such compounds may result in organ (e.g., stomach, kidney, nasal septum) complications and promote stomach, bronchogenic, and nasal cancers (Katz & Salem, 1994; Kuo et al., 1997; Beaumont et al., 2008; Wilbur et al., 2012). Cr(VI) is much more soluble and mobile than Cr(III) because of its tendency to form anionic species. As

such, the Cr(VI) oxyanions, $HCrO_4^-$ and CrO_4^{2-}, are the most mobile forms of Cr and most stable Cr species at oxidizing conditions (Rai et al., 1987; Kotaś & Stasicka, 2000). Due to its high solubility, Cr(VI) containing minerals are rarely found in nature. Instead, Cr(VI) is commonly found as anionic species adsorbed onto positively charged mineral surfaces such as iron (Fe), manganese (Mn), aluminum (Al) (oxyhydr)oxides (Richard & Bourg, 1991; Kotaś & Stasicka, 2000).

Because of its adverse health effects and high mobility, Cr(VI) has been monitored in soils and waters worldwide (Guertin et al., 2016). The primary geogenic source of Cr in soils and rivers is the weathering of ultramafic rocks (McClain & Maher, 2016), as they contain the highest Cr concentrations (2,980 mg kg^{-1}) compared to all other rock types (Alloway & Ayres, 1997). Laterites developed from the weathering of ultramafic rocks are even more enriched in Cr (up to 70,000 mg kg^{-1}) along with critical metals (e.g., nickel (Ni), cobalt (Co)) (Ulrich et al., 2019) that are mined and processed from these so-called Ni (or Ni-Co) laterite deposits. Elevate Cr(VI) levels in natural waters associated with such deposits (Gunkel-Grillon et al., 2014; Delina et al., 2020) have been a pressing environmental challenge worldwide. Therefore, in this thesis, I focused on deciphering the fate of Cr in and around Ni laterite deposits and mine wastes. In this chapter, I provide a brief review of the current literature on Ni laterite deposits, about the various aspects related to the environmental geochemistry of Cr, its Cr occurrence in lateritic environments, and various analytical approaches for Cr characterization.

2.2. Chromium occurrence in laterites and surrounding environments

2.2.1. Laterites and Ni laterite deposits

The term “laterite” broadly refers to a highly weathered material composed of mineral assemblages predominantly consisting of Fe or Al (oxyhydr)oxides, which are residually accumulated or enriched through the leaching and transport of other components (Tardy, 1997; Stoops & Marcelino, 2018). According to this definition, laterite encompasses bauxites, ferricretes, Fe or Al duricrusts, mottled horizons, “cuirasses”, pisolites, and ferralitic soils, among others (Tardy, 1992). Chromium is a common constituent in different types of laterites. It has been a subject of paleo-redox studies in laterites developed from felsic rocks (e.g., tonalites) (Berger & Frei, 2014) and of environmental studies in ferralsols and Ni laterite deposits resulting from the weathering of ultramafic rocks (e.g., harzburgites, dunites) (Garnier et al., 2013; Gunkel-Grillon et al., 2014; Economou-Eliopoulos et al., 2016; Delina et al., 2020). Among them, Ni laterites have shown the highest and most concerning Cr(VI) contents and are, therefore, more important sources of Cr to natural waters and surrounding environments.

Nickel laterite deposits are products of prolonged and pervasive weathering of ultramafic rocks in tropical to subtropical regions (within a band latitude of ~22°) and, to a lesser extent,

in latitudes as high as 40° (**Figure 2.2**) (Elias, 2002; Golightly et al., 2010). Most are found in accretionary terrains such as island arcs (e.g., Indonesia, Philippines, New Caledonia) where upper mantle peridotites and associated lithologies were obducted, forming ophiolite complexes that are typically Cretaceous to Tertiary in age (Elias, 2002). About 15% of the Ni laterite resources are in older, stable cratonic platforms and are developed from komatiites and ultramafic units belonging to layered mafic complexes in Archean and Proterozoic greenstone belts (e.g., in Western Australia, Brazil, Urals in Russia) (Brand et al., 1998; Elias, 2002). These older deposits likely formed during Paleozoic time periods with tropical to subtropical climates (Gleeson et al., 2003).

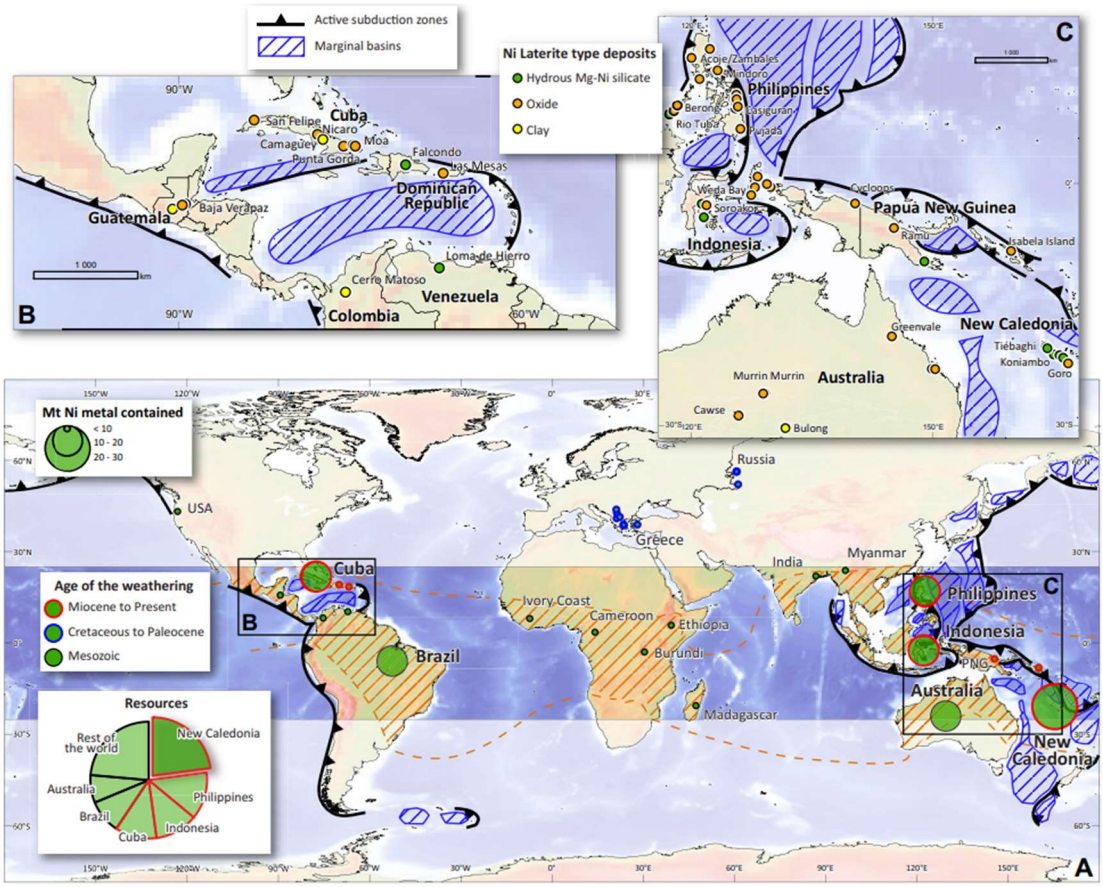

Figure 2.2. (A) Global distribution of Ni laterite deposits showing their ages and relative Ni contents. The intertropical zone, where most deposits are located, is highlighted with the blue band, with the world's main lateritic zones marked as orange dashed areas. Insets: (B) the Caribbean and (C) SW Asia–Oceania, showing currently known deposits and deposit types. Nickel laterite deposits are broadly classified into three types (colored solid circles) based on the dominant ore-bearing phases: hydrous Mg silicates (green), oxides (orange), and clays (yellow). Reproduced from Maurizot et al. (2019). Copyright © Geological Society of America.

Today, Ni laterite deposits account for 60% of the world's land-based Ni resources (USGS, 2023). In addition, these deposits are also important sources of Co as they account for 20-30% of the global Co supply (Wilburn, 2011; Butt & Cluzel, 2013), and recently, such deposits are

being sought for other valuable and critical metals (e.g., REEs, PGEs) (Aiglsperger et al., 2016; Teitler et al., 2019). Nickel laterite ores are typically mined through open-pit methods due to their large tonnage and shallow nature (Marsh et al., 2013). To extract Ni, the ores undergo either pyrometallurgical (e.g., ferronickel smelting, matte smelting) or hydrometallurgical (e.g., reductive roast/ammonia leaching, high temperature and pressure acid leaching) processing (Dalvi et al., 2004). This results in wastes that are, in most cases, managed through conventional tailings impoundments or in-pit disposal (Marsh et al., 2013). All these activities in ore processing, along with weathering in the large open-cast areas shaped by Ni mining, may lead to Cr release and adverse environmental impacts through various subsequent environmental reactions. For example, huge amounts of metal-rich dust may be transported into the atmosphere and pose air pollution problems (Pasquet et al., 2016; Tabios, 2018). Moreover, suspended particulate matter and leachates from exposed ores (e.g., in active mine areas, stockpiles) and mine wastes may be weathered and leached through rain and thus pollute surrounding water bodies and threaten drinking water supplies (Marsh et al., 2013; Tabios, 2018). With the expected increase in mining and processing of worldwide Ni laterite deposits due to the global energy transition (IEA, 2021), understanding the fate of Cr is crucial for the environmental management and sustainable development of Ni laterite regions.

2.2.2. Mineralogy and geochemistry of Cr along the Ni laterite profile

Intense chemical weathering of ultramafic rocks causes the breakdown of primary minerals (e.g., olivine, pyroxene), forming secondary silicates like serpentine. As weathering proceeds, the majority of Mg and Si are leached while less soluble elements (e.g., Fe, Al) are residually accumulated, resulting in Fe (oxyhydr)oxides (e.g., goethite, hematite) (Elias, 2002; Gleeson et al., 2003). These mineralogical and geochemical transformations form the stratified or layered weathering material known as the laterite profile.

A typical Ni laterite profile (**Figure 2.3**) is characterized by a bedrock made of partially to heavily serpentinized parent ultramafic rocks (e.g., dunite, harzburgite) overlain by regolith that manifests progressively advancing stages of the lateritization process (Elias, 2002). The lowermost horizon is a silicate-rich (e.g., serpentine, chlorite, talc) zone commonly referred to as *saprolite*. This can be divided into the *hard saprolite* or *saprock*, reflecting early stages of weathering through fractured bedrock of minimal alteration, and the *soft saprolite*, a more fractured zone where detached blocks of the parent rock are dispersed in a matrix of altered serpentinized material. Overlying the saprolite zone is a highly weathered Fe (oxyhydr)oxide-rich (e.g., goethite, hematite) horizon where the original rock fabric has been lost due to the intense weathering and mineral transformation reactions (Elias, 2002; Gleeson et al., 2003; Golightly et al., 2010). This unit is often referred to as oxisol, laterite, limonite, or oxide zone, among many others (Tardy, 1992; Elias, 2002; Golightly et al., 2010; Santoro et al., 2022). In

the case of Ni laterite deposits, the term "*limonite*" is most widely used, and this is the term I will use in this thesis. The limonite layer could be further divided into the *yellow limonite* and the overlying *red limonite*, which reflect the gradual transformation from the yellow- to orange-brown goethite to red-brown hematite as goethite dehydrolizes. Moreover, in cooler or drier regions or areas of low topographic relief where there is restricted circulation of water, smectite clays (e.g., nontronite) can form a *nontronite* or clay-rich zone between the saprolite and limonite layers (Golightly et al., 2010). Finally, at the surface, a Ni laterite profile may also have an indurated duricrust or ferricrete (Elias, 2002; Gleeson et al., 2003).

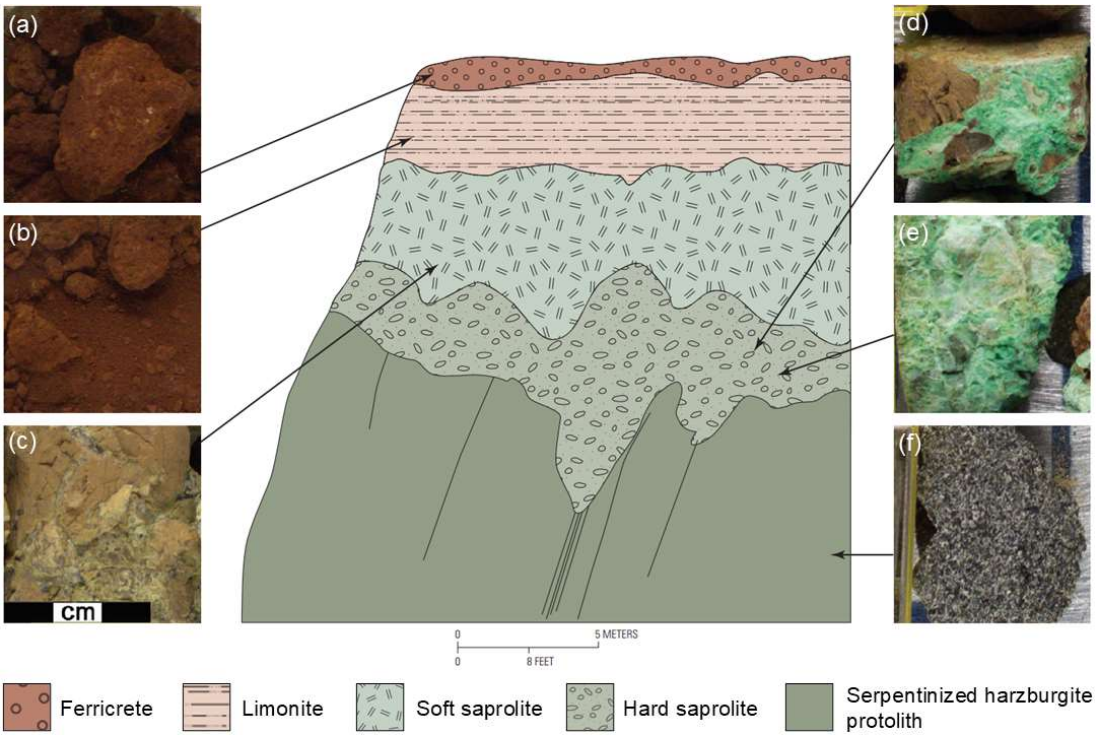

Figure 2.3. Schematic diagram of a Ni laterite profile from the Falcondo Deposit, Dominican Republic showing hand-specimen samples from each horizon: (a) ferricrete; (b) limonite; (c) soft saprolite; (d-e) hard saprolite with bright green garnierite (i.e. a mixture of Ni-rich phyllosilicates including e.g., serpentine, talc, smectite); and (f) serpentinized bedrock. Modified from Marsh et al. (2013), courtesy of the U.S. Geological Survey.

Chromium is found in Ni laterite profiles at a wide range of concentrations, influenced by diverse climatic and geological factors (e.g., topography, drainage, tectonics, protolith, structure, weathering intensity, and duration) (Elias, 2002). In **Table 2.1,** the Cr concentrations in the main horizons of several Ni laterite deposits around the world are listed. Among these, limonites from New Caledonia exhibited the highest Cr contents reaching up to ~70,000 mg kg^{-1} (Ulrich et al., 2019). Not surprisingly, when the weathering is most intense, Cr, together with Fe and Al, shows a very high relative enrichment in the upper units of a Ni laterite profile as a

result of residual accumulation, as exemplified in the profile from the Koniambo lateritic regolith in New Caledonia (**Figure 2.4**; Ulrich et al 2019).

Table 2.1. Chromium concentrations (mg kg^{-1}) in different horizons of Ni laterite deposits worldwide.

Deposit	Ferricrete	Limonite	Saprolite (± Clay)	Bedrock	References
Baro Alto, Brazil	-	1,090-6,290	620-5,640	-	Ratié et al. (2018)
Bavanat, Iran	9,175-29,600	931-30,900	1,559-2,187	804	Mongelli et al. (2019)
Cerro Matoso, Colombia	-	7,300-21,100	12,000-27,700	2,700-3,900	Gleeson et al. (2004)
Kolonadale, Indonesia	36,673	3,010-34,142	1,642-17,105	4,242	Fu et al. (2014)
Koniambo, New Caledonia	21,993	19,646-69,683	6,190-16,197	2,442	Ulrich et al. (2019)
Loma Caribe, Dominican Republic	3,260	3,260-21,781	2,205-4,170	2,596	Aiglsperger et al. (2016)
Punta Gorda, Cuba	16,438	14,589-28,288	2150-5670	2,669	Aiglsperger et al. (2016)
Rio Tuba, Philippines	-	17,789-28,462	5,268-14,095	1,192	Delina et al. (2020); Arcilla et al. (2019)
Semail, Oman	13,000-30,105	13,000-51,315	2,053-6,158	2,737	Al Khirbash and Semhi (2015)
Wingellina, W. Australia	6,637	616-28,257	7,184-18,816	2,668	Putzolu et al. (2019)
Yuanjiang, China	-	6,900-8,800	2,200-7,100	3,000	Fu et al. (2019)

The primary sources of Cr in ultramafic rocks are usually spinels such as chromite. Their weathering, along with the serpentinization of the host ultramafic rocks, leads to the enrichment of Cr (Becquer et al., 2003; Oze et al., 2004a; Garnier et al., 2013). In the weathering end member – the Ni laterites – as well as in their ultramafic protoliths, chromites contain up to 59 wt.% Cr (Marker et al., 1991; Garnier et al., 2008; Fandeur et al., 2009a; Ulrich et al., 2019). While chromites are usually minor mineral components in ultramafic rocks and serpentinites (< 5 vol.%), their presence accounts for a significant proportion of the total Cr (Marker et al., 1991; Robles-Camacho & Armienta, 2000; Oze et al., 2004a; Ulrich et al., 2019). Previous studies have shown that Cr concentrations in chromite tend to increase with the degree of weathering and are attributed to incongruent dissolution where the majority of Cr is retained compared to other elements (e.g., Mg and Al in Mg-Al chromites) (Oze et al., 2004a; Garnier

et al., 2008; Garnier et al., 2009). On the other hand, chromite grains from the Goro Ni laterite deposit in New Caledonia exhibited preferential leaching of Cr (Wells et al., 2022). Moreover, Cr-magnetite can also incorporate varying amounts of Cr (0.1–22 wt.%) (Oze et al., 2004a; Garnier et al., 2009; Eliopoulos et al., 2012) and are commonly present as individual grains or as rims surrounding chromite (Garnier et al., 2009; Morrison et al., 2015). Cr-magnetite rims can form from the incongruent dissolution of primary chromite or through secondary overgrowth following the partial dissolution of Fe-bearing silicate minerals (Garnier et al., 2009; Morrison et al., 2015).

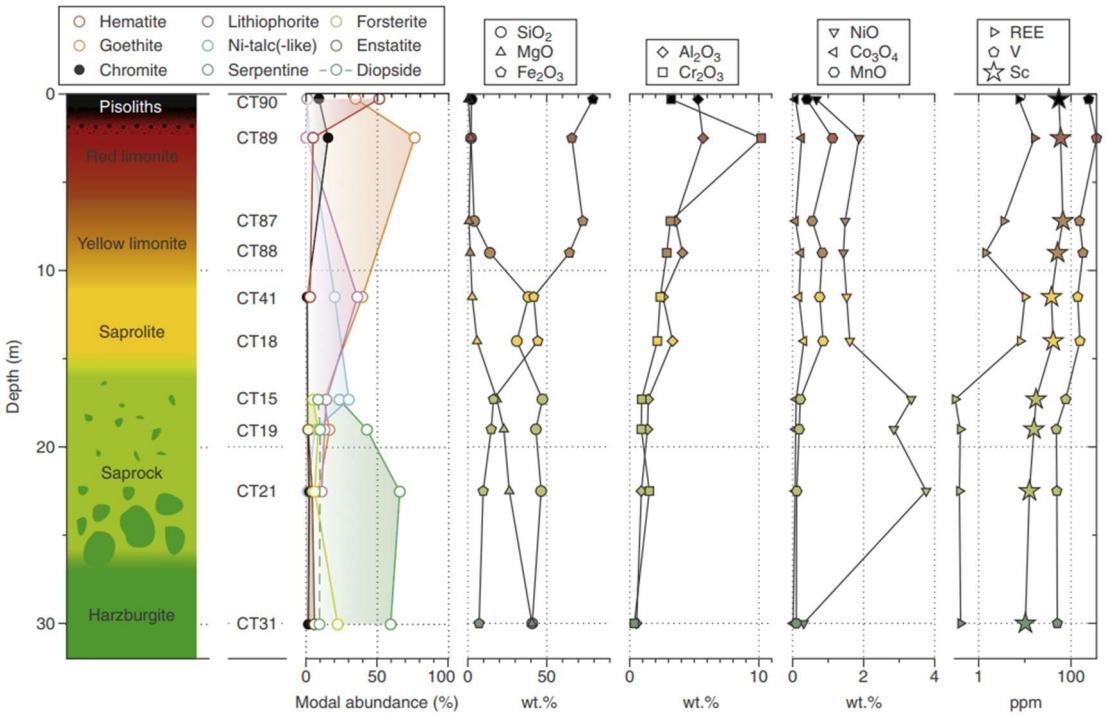

Figure 2.4. Mineralogical and geochemical trends along the Koniambo lateritic regolith in New Caledonia. Symbols for major oxides are colored based on the laterite horizons. REE, V, and Sc contents are shown on a logarithmic scale. Reproduced from Ulrich et al. (2019) with permission from Elsevier.

Silicates can also host appreciable amounts of Cr, especially in the bedrock and saprolite zones of a laterite profile (e.g., **Figure 2.4**). Although silicates contain far lower Cr contents than Cr-bearing spinels, their relative abundance and greater susceptibility to weathering make them important accessible Cr sources (Oze et al., 2004a). The primary silicates in the ultramafic protoliths are most often ferromagnesian silicates, olivine (e.g., forsterite) and pyroxenes (e.g., enstatite, diopside), that are typically poor in Cr (< 1 wt.%) (Gleeson et al., 2004; Eliopoulos et al., 2012; Fu et al., 2014; Ulrich et al., 2019; Tupaz et al., 2020). Secondary serpentine minerals such as lizardite contain up to 1.5 wt.% Cr (Gleeson et al., 2004; Fu et al., 2014; Villanova-de-Benavent et al., 2014; Ulrich et al., 2019; Tupaz et al., 2020) and are among the most significant

Cr sources in the serpentinized bedrock and saprolite zone due to their high abundance (up to 90 vol.%) (Gleeson et al., 2004; Fu et al., 2014; Teitler et al., 2019; Ulrich et al., 2019). Smectite clays, formed from the alteration of olivine, pyroxene, and serpentine, are also present in the saprolite zone and can form clay-rich layers, with the clays containing up to 12 wt.% Cr (Gaudin et al., 2005; Garnier et al., 2009; Kadır et al., 2015; Helvacı et al., 2018). Finally, other more minor silicates containing Cr include chlorite (≤ 2 wt.%) (Gleeson et al., 2004; Al-Khirbash, 2015), talc (0.05-0.84 wt.%) (Fu et al., 2019; Ulrich et al., 2019), sepiolite-falcondoite (< 0.1 wt.%) (Tupaz et al., 2020), garnierite (up to an average of 0.57 wt.%) (Wells et al., 2009; Fu et al., 2014; Villanova-de-Benavent et al., 2014; Tupaz et al., 2020), and kaolinite (average of 1 wt.%) (Kadır et al., 2015).

Finally, in the limonite zone, due to charge and size similarities (octahedral radii: Cr^{3+} = 0.615 Å, Fe^{3+} = 0.645 Å), Cr(III) can isomorphically substitute into the octahedral site of the dominant Fe(III)-bearing phases (Oze et al., 2004b; Chrysochoou et al., 2016). Analyses of goethite and hematite particles from laterites have shown up to 5 mol.% Cr-substitutions in these Fe (oxyhydr)oxides (Fandeur et al., 2009a; Garnier et al., 2009; Landers, 2010), while laboratory studies reported a maximum substitution of up to 10 mol.% (Cornell & Schwertmann, 2003). Sequential chemical extractions have further shown that Fe (oxyhydr)oxides are important hosts for Cr in the highly weathered laterite horizons. For example, in southern New Caledonia and Niquelandia, Brazil, crystalline Fe (oxyhydr)oxides (e.g., goethite, hematite) were found to host significant fractions of Cr, comprising 30-40% and 50-85% of the total Cr content, respectively (Quantin et al., 2002; Garnier et al., 2006), while poorly crystalline Fe (oxyhydr)oxides (e.g., ferrihydrite), account for up to 1.5% (Quantin et al., 2002; Garnier et al., 2006).

2.2.3. Chromium in soil solutions, surface- and groundwaters

Ultramafic source rocks and their weathering products have contributed to significantly elevated levels of Cr(VI) in natural waters, far exceeding the global average Cr concentration of freshwater (≤ 6 µg L^{-1}) (Alloway & Ayres, 1997) and international drinking water standards for Cr(VI) (50–100 µg L^{-1}) (USEPA, 2006; WHO, 2017). In particular, up to 73 µg L^{-1} of total Cr (Cr_{Tot} = Cr(III)+Cr(VI)) and Cr(VI) concentrations have been detected in waterbodies associated with ultramafic rocks and serpentinites worldwide (e.g., Mexico, Italy, US, Greece) (Robles-Camacho & Armienta, 2000; Fantoni et al., 2002; Margiotta et al., 2012; Kazakis et al., 2015; McClain & Maher, 2016; Kazakis et al., 2017). Important to note is the fact that in most of these areas, Cr(III) was below the detection limit, and Cr_{Tot} mainly occurred as Cr(VI) (Fantoni et al., 2002; Margiotta et al., 2012). Extreme outliers (≤ 2410 µg L^{-1}) of Cr_{Tot} and Cr(VI) concentrations were found in Ni laterite catchments (**Table 2.2.**). Groundwater Cr(VI) levels range from below detection limit in the Cerro Matoso mine in Colombia (Gleeson et al.,

2004) to up to 360 µg L^{-1} in central Evia, Greece characterized by widespread Ni laterite deposits (Economou-Eliopoulos et al., 2017). Monitoring of groundwater wells in central Evia showed small variations in Cr(VI) levels between dry and wet seasons but significantly higher concentrations at shallower wells characterized by phreatic (unconfined) and oxic conditions (Economou-Eliopoulos et al., 2017). Seasonal variations are more pronounced in surface mine water Cr(VI) levels. In the Poro mine waters in New Caledonia (**Figure 2.5**), Cr(VI) was found to decrease with increasing rainfall rates due to dilution. The opposite was observed in the waters reaching the downstream village due to the rain-induced remobilization of Cr from suspended materials supplied by mining sediments (Gunkel-Grillon et al., 2014). Similarly, coastal marine waters and surface waters near Ni laterite mining areas in Surigao, Philippines, have shown higher mean Cr_{Tot} concentrations during the wet season (300 µg L^{-1}) compared to the dry season (60 µg L^{-1}) (Apodaca et al., 2018). In my MSc work, I quantified seasonal variations in riverine Cr(VI) fluxes in a Ni laterite mine in Palawan, Philippines, and estimated comparable values (≤ 50 kg km^{-2} yr^{-1}) (Delina et al., 2020) with that of other ultramafic areas (0.04 to 48 kg km^{-2} yr^{-1}) (McClain & Maher, 2016). I could also show that during extreme stormflow conditions, these fluxes could increase by up to three orders of magnitude (Delina et al., 2020), creating a potential real issue for downstream village water supplies.

Table 2.2. Total Cr (Cr_{Tot}) and Cr(VI) concentrations in surface- and groundwaters associated with Ni laterite deposits. *bdl* – below detection limit

Location	Setting	Concentration (µg L^{-1}) Cr_{Tot}	Concentration (µg L^{-1}) Cr(VI)	Reference
Cerro Matoso S.A., Colombia	Mine waters (spring, trench)	*bdl* – 230	-	(Gleeson et al., 2004)
	River and groundwater	*bdl*	-	
Poro Mine, New Caledonia	Mine waters	50 – 2,410	180 – 1,620	(Gunkel-Grillon et al., 2014)
	Downstream village waters		20-340	
Central Evia Basin, Greece	Groundwater	*bdl* – 360	*bdl* – 360	(Economou-Eliopoulos et al., 2017)
Hinadkaban Bay, Surigao Provinces, Philippines	Coastal water	60-300 (mean)	-	(Apodaca et al., 2018)
Rio Tuba Deposit, Palawan, Philippines	Upstream	5.3	*bdl*	(Delina et al., 2020)
	Mine waters	8.8 – 163	*bdl* – 143	
Baro Alto Mine, Brazil	Mine waters (stream, pond)	13 – 757	-	(Bolaños-Benítez et al., 2021)
	Groundwater	0.16 – 2.39	-	

Figure 2.5. Mining area in Poro, New Caledonia showing the sites (A, B, D - mining catchment; river - E; river mouth - F) where high concentrations of Cr(VI) were measured, and images of the river before and after rainfall. Reproduced from Gunkel-Grillon et al. (2014) with permission from Springer Nature.

As part of the research that attempted to evaluate the potential of Cr(VI) release from Ni laterites, several studies have performed pore water analyses as well as laterite leaching experiments. For example, soil solutions collected *in situ* from ferralsols in New Caledonia usually contained below 70 µg L^{-1} Cr(VI), except when the pore waters were collected from phosphate-fertilized soils. In these soils, the values could reach up to 700 µg L^{-1} because of an exchange of Cr(VI) (as CrO_4^{2-} and $HCrO_4^-$) with the soil phosphate (Becquer et al., 2003). Much higher Cr(VI) contents (up to 1,300 µg L^{-1}) have been reported from Ni laterite leachates from deposits in Central Greece (Economou-Eliopoulos et al., 2016). In the final example, I use data from my own work in the Ni laterites from the Philippines ((Delina et al., 2020), where I reported water-extractable Cr(VI) with concentrations of ≤ 102 mg kg^{-1}, values that were close to those leached from Ni mine sediments in New Caledonia (≤ 358 mg kg^{-1}) (Gunkel-Grillon et al., 2014). From this data, I quantified how much Cr(VI) can migrate downward a laterite profile during water infiltration and estimated this to vary between 62 and 3446 t km^{-2} yr^{-1}. Such Cr(VI) infiltration fluxes are significantly higher than the above-mentioned riverine Cr(VI) fluxes in the mining area, reflecting natural attenuation processes along water flow paths. It is noteworthy that this is not happening in all cases, as for example, in serpentine soils (i.e., generic term for any soil derived from ultramafic rocks) from the California Coast Range (McClain et al., 2017) that have been reported with much lower Cr(VI) infiltration fluxes (0.01 to 3.9 kg km^{-2} yr^{-1}) due to lower Cr(VI) concentrations and slower infiltration rates as I also described in Delina et al. (2020).

2.2.4. Chromium cycle in lateritic environments

To understand the ultimate fate of Cr, it is necessary to quantify the changes in Cr speciation and mobility from the source - the ultramafic rocks and the Ni laterites - to all surrounding environments. The processes that affect these changes depend on processes linked to mineral dissolution and or reprecipitation, changes in oxidation-reduction in the solids and solutions, as well as interactions with existing and *de nuovo* formed solids via adsorption-desorption or structural incorporation (**Figure 2.6**). The dissolution of Cr(III)-bearing minerals is the primary source of soluble Cr since Cr(VI) minerals have very high solubility and are hardly present in the environment (Richard & Bourg, 1991). The relative susceptibility to weathering and dissolution of Cr(III)-bearing minerals in the ultramafic source rocks and laterite profiles are as follows: olivine < pyroxene < serpentine < chlorite < talc < Fe (oxyhydr)oxides (e.g., goethite, hematite) + spinels (e.g., chromite, magnetite) (Chrysochoou et al., 2016). Oze et al. (2004a), in their study of ultramafic rocks and serpentine soils, described silicates as the most accessible Cr sources. They inferred that due to their abundance and relative stabilities, they would dominate the Cr delivery, while chromite, which hosts most of Cr in the host rocks, would be less likely to contribute to the pool of bioavailable Cr due to its high resistance to weathering. In contrast, laterites examined by Garnier et al. (2008) and Wells et al. (2022) revealed dissolution features in chromite grains that indicate slow alteration during pedogenesis; these findings suggest that chromites can nevertheless also act as significant but more diffuse sources of Cr.

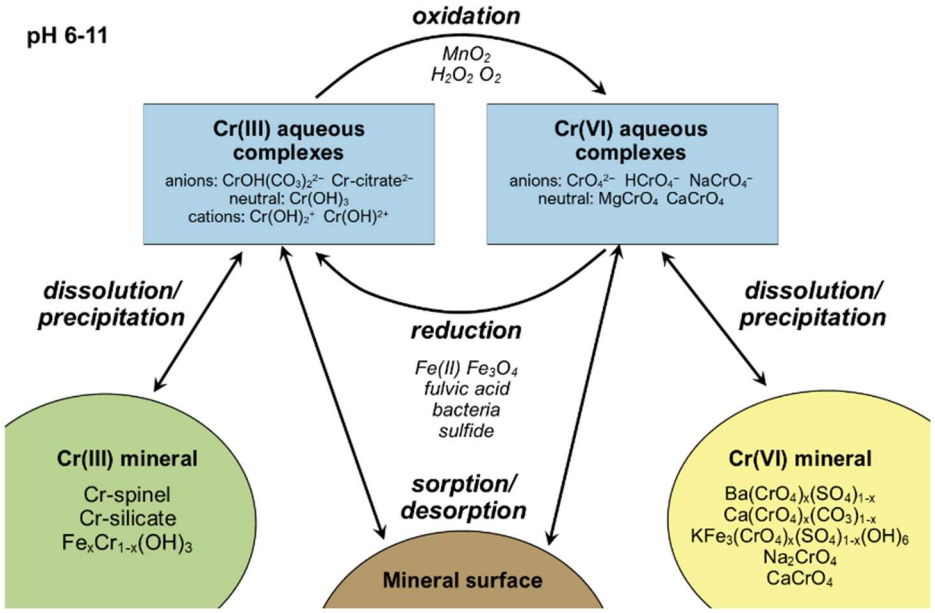

Figure 2.6. Conceptual model of the Cr cycle in natural waters at pH 6-11 modified from McClain and Maher (2016) and with permission from Elsevier.

Only a few oxidants in the environment are capable of transforming Cr(III) to Cr(VI) due to the high redox potential of the Cr(VI)/Cr(III) couple (Richard & Bourg, 1991). Among these, Mn oxides are considered the prime and speediest oxidants of Cr(III) in rocks and soil systems (Eary & Rai, 1987; Fandeur et al., 2009b). Mixed high-valence Mn(III/IV) oxides such as asbolane, lithiophorite, and birnessite are some of the most common Mn phases in Ni laterites (Domènech et al., 2022). Typically present as finely disseminated minerals or coatings on rock and soil grains (Garnier et al., 2013; Domènech et al., 2022), these minerals facilitate Cr(III) oxidation via electron transfer once Cr(III) is adsorbed onto the Mn oxide surface (Manceau & Charlet, 1992). Several lateritic regoliths have shown a strong spatial relationship between Mn(IV/III) oxides and Cr(VI) (Fandeur et al., 2009b; Garnier et al., 2013). It has also been reported that deposits containing larger amounts of Mn oxides can lead to larger Cr remobilization – as in the case of 650x higher concentrations of Cr(VI) in Ni laterite deposits in central Greece (Economou-Eliopoulos et al., 2016). Furthermore, Cr(III) can also be oxidized by dissolved oxygen (DO) or by reaction with hydrogen peroxide (H_2O_2). Although dissolved oxygen is considered a viable oxidant of Cr(III), the oxidation rate at atmospheric conditions is very slow compared to faster coincident reactions (sorption or precipitation) that involve Cr(III) (Schroeder & Lee, 1975). On the other hand, H_2O_2 is a metastable phase produced during serpentinization (Oze et al., 2016).

At the other end of the redox spectrum, Cr(VI) can be reduced by dissolved sulfides originating from decomposition of organic matter, bacterial sulfate reduction, or industrial wastes (Schroeder & Lee, 1975; Richard & Bourg, 1991). It can also be reduced by ferrous ions released from the weathering of Fe(II)-containing minerals or by the biologically driven reductive dissolution of Fe(III)-bearing minerals (Rai et al., 1987; Richard & Bourg, 1991). Organic matter in the form of amino, fulvic, or humic acids are also possible reductants of Cr(VI). For example, Garnier et al. (2013) suggested that slightly higher organic matter in surface horizons of ferralsols could account for at least part of the Cr(VI) reduction by promoting reductive dissolution of Fe(III) (oxyhydr)oxides. Similarly, Hausladen and Fendorf (2017) showed that organic carbon-rich environments (e.g., surface soil horizons) can generate more Fe(II), which can drive Cr(VI) reduction.

Hexavalent Cr may also be attenuated by adsorption. This process is a surface complexation reaction between chromate ions and solid phases that have either exposed inorganic hydroxyl groups like Al-, Mn-, Fe (oxyhydr)oxides or, to a lesser extent, clay minerals (Rai et al., 1989; Richard & Bourg, 1991). The reaction is pH-dependent, and Cr(VI) adsorption increases when pH is lowered due to the protonation of surface hydroxyl sites and the anionic nature of dissolved Cr(VI) (Rai et al., 1989). Fandeur et al. (2009b) related the discrepancy of Cr(VI) fractions measured through X-ray absorption near edge structure (XANES) and 0.1 M $(NH)_4H_2PO_4$ extraction to re-adsorption of chromate ions onto goethite and inferred that this

was promoted by the low pH conditions (pH 5) of the reacting solution. Indeed, chromate sorption, in particular to Fe (oxyhydr)oxides, is favored at pH less than 5 (Oze et al. (2004b). This is also relevant in laterites, as demonstrated through my work (Delina et al. (2020) and by Gunkel-Grillon et al. (2014). Both these studies demonstrated the important role of pH in Cr(VI) desorption in Ni laterites. In Delina et al. (2020), I documented higher water-extractable Cr(VI) contents in the silicate-rich saprolites compared to those in the Fe (oxyhydr)oxide-dominated limonites. This difference was ascribed to, among others, the increased adsorption of Cr(VI) to phases in the more acidic limonite horizon. Similarly, Gunkel-Grillon et al. (2014) noted an increase in water-soluble Cr(VI) with pH after batch leaching experiments. Furthermore, several studies have shown that Cr(VI) adsorption is influenced by dissolved organic carbon and the presence of competing anions, such as phosphate, as discussed in the previous section.

Overall, the above-presented studies all show that the weathering of ultramafic rocks to form Ni laterites provides a relatively rare combination of components (e.g., Mn and Fe (oxyhydr)oxides) that can all play various crucial roles in the cycling of Cr. However, little is still known about the extent and contribution of mineral phases or changing redox conditions to the speciation and concentration of Cr in these deposits.

2.3. Mine wastes as compartments of Cr

Once Cr is weathered from the ultramafic rocks to the Ni laterites via natural weathering processes, the story does not end. The next step is mining and processing the material to extract the valuable metals (e.g., Ni, Co) and the consequent production of vast amounts of mine wastes or tailings. The tailings are also interesting sites of geochemical and mineralogical reactions, but these are understudied features in the context of Cr fate in Ni laterite mining areas. Mine tailings containing non-target metals (e.g., Fe, Cr) are often managed through in-pit disposal or conventional impoundments (e.g., tailings dams). Such storage raises concerns as a possible source of groundwater contamination through leaching and, in the worst cases, through liquefaction and dam failure (Marsh et al., 2013).

The characteristics of Ni laterite mine tailings are largely dependent on the employed metallurgical processing method, which in turn depends on the dominant ore phase or laterite horizon to be processed (Dalvi et al., 2004; Kaya & Topkaya, 2011). Energy-extensive pyrometallurgical methods such as the ferro-nickel production route or matte smelting are utilized to recover Ni from the Mg silicate-rich saprolite unit of the laterite deposit. On the other hand, hydrometallurgical methods such as the Caron ammonia leach process and high pressure acid leaching are more suited for Ni and Co extraction from the limonite and clay-rich (e.g., nontronite) zones (Dalvi et al., 2004). Smelting of Ni laterite ores often generates slag

comprised mainly of Fe and Mg oxides and silica, while slurries from acid leaching primarily contain Fe precipitates and sulfates (Marsh et al., 2013).

High pressure acid leaching or HPAL (**Figure 2.7a**) is the primary method used in treating Fe (oxyhydr)oxide-rich laterites (e.g., in Cuba, Australia, Philippines, New Caledonia, Papua New Guinea, and Turkey) (Whittington & Muir, 2000; Keller & Anderson, 2018). HPAL is preferred over other hydrometallurgical techniques since it consumes less energy and offers higher Ni and Co recoveries (Dalvi et al., 2004; Gultom & Sianipar, 2020). This process extracts Ni and Co using sulfuric acid (H_2SO_4) at high temperature (230-270°C) and pressure (3.3-5.5 MPa) conditions (Ucyildiz & Girgin, 2017). Under these conditions, the predominant Fe (oxyhydr)oxides (e.g., goethite) and other minerals (e.g., asbolane, smectite, and serpentine) are dissolved, while more resistant phases such as chromite, maghemite, talc, kaolinite, and quartz are left in the residue (Kaya & Topkaya, 2011; Önal & Topkaya, 2014). Ferric ions from goethite dissolution rapidly hydrolyze and precipitate as hematite or basic ferric sulfate. The formation of hematite is favored at higher leaching temperatures and longer leaching times, whereas the precipitation of ferric sulfate is promoted at low pH conditions (Whittington & Muir, 2000; Önal & Topkaya, 2014; Ucyildiz & Girgin, 2017). Leached Al may also precipitate as Al sulfates (e.g., alunite), which could later be transformed into jarosite via Al-Fe substitution. Other sulfates, such as gypsum and anhydrite, have also been found in Ni laterite tailings (Marsh et al., 2013; Ucyildiz & Girgin, 2017), most often due to the neutralization processes that are undertaken prior to tailings discharge. Additionally, amorphous silica formed from the re-precipitation of dissolved silica is frequently observed in these materials (Önal & Topkaya, 2014).

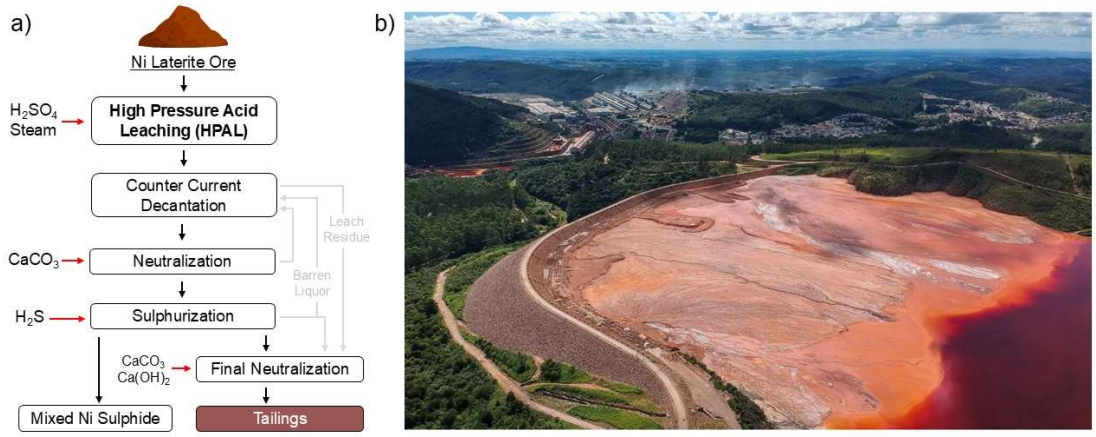

Figure 2.7. (a) Simplified flow diagram for HPAL (modified from Keller and Anderson (2018)) and (b) an example of a tailings dam in Alumínio, Brazil, containing red mud, a mine waste comparable with HPAL tailings (reproduced from Borra (2024) with permission from Springer Nature).

Nevertheless, HPAL extractions have demonstrated that only up to 25% of the total Cr could be leached from Ni laterite ores (Buarzaiga et al., 2003; Önal & Topkaya, 2014; Ucyildiz & Girgin, 2017). Under these oxidizing HPAL conditions, the leached Cr has been suggested to occur as Cr(VI), either as CrO_4^{2-} or $Cr_2O_7^{2-}$ (Sobol, 1969; Whittington & Muir, 2000; Buarzaiga et al., 2003). Previous studies of HPAL residues from Indonesia, New Caledonia, and Western Australia (Whittington et al., 2003; Ang et al., 2017; Gultom & Sianipar, 2020) reported to still contain Cr concentrations ranging from 0.5 to 1.3 wt.%. SEM-EDX analysis of HPAL test residues from Turkey has suggested an association of Cr with prevalent secondary Fe precipitates (e.g., hematite) (Önal & Topkaya, 2014). However, the actual speciation of Cr in the tailings remains unknown. Interestingly, there are many more studies about Cr in processing residues from aluminum ores/bauxite deposits, also known as "red mud" (**Figure 2.7b**). Red mud, like hematite-rich Ni laterite mine tailings, owes its typical red color to hematite and contains lower yet still significant concentrations of Cr (Economou-Eliopoulos et al., 2016). For example, a study on red mud ocean dumping zones in South Korea reported the potential long-term risk posed by mobile fractions of Cr (Kim et al., 2023), while leaching experiments performed on red mud from Greece yielded unexpectedly high Cr(VI) concentrations (2100 µg L^{-1}) (Economou-Eliopoulos et al., 2016), yet its fate is unknown. In contrast, Cr was found to occur as Cr(III) substituted into hematite in the red mud samples from the unfortunate Ajka spill site in Hungary, a finding that positively limits its potential mobility in the environment following the spill (Mayes et al., 2011; Burke et al., 2012). The potential risks from Cr in comparable mine wastes make the determination of Cr speciation and mobility in Ni laterite mine tailings an obvious need for managing, rehabilitating, or storing these wastes long-term. Whether these mine tailings are actively rehabilitated, stored in containment facilities, or abandoned, knowing the fate of Cr will help mitigate potential impacts on surrounding ecosystems and communities.

2.4. Tools in evaluating Cr mobility in Ni laterites

Evaluating the environmental impact of metals requires knowledge of not only their total concentration but also their partitioning or solid-phase association, which dictate their potential mobility, bioavailability, and toxicity (Benitez & Dubois, 1999; Gleyzes et al., 2002; Bacon & Davidson, 2008). Quantitative assessment of the partitioning of metals in soils or sediments has been done through complementary high-resolution analyses such as scanning and transmission electron microscopy (STEM), laser ablation inductively coupled plasma mass spectrometry (LA-ICP-MS), and synchrotron-based techniques (e.g., X-ray radiation fluorescence or SXRF, X-ray absorption spectroscopy or XAS) (Isaure et al., 2002; Bang & Hesterberg, 2004; Manceau et al., 2004; D'Amore et al., 2005; Bacon & Davidson, 2008; Xu et al., 2017). However, although such techniques deliver reliable results, they are limited by their

accessibility, and most often, they also present difficulties with data analysis due to the heterogeneous nature of the samples (Foster et al., 1998; Keon et al., 2001; Bacon & Davidson, 2008; Adamo et al., 2018), especially for ore grade materials (e.g., co-occurrence of various transition metals). For example, synchrotron-based XAS of Cr in heterogeneous materials like laterites could be complicated by several factors, including the relatively low concentration of Cr in a complex matrix of the natural samples, the background fluorescence from high concentrations of Fe, and the close K-edge energy positions of Cr and co-occurring transition metals (e.g., Mn). Moreover, such technique requires a wide range of comparable model compounds, which are still lacking for Cr, unlike for other metals (e.g., Mn) (Manceau et al., 2012; Zahoransky et al., 2023). In addition, such techniques may not be accessible or practical for mining companies to employ, and thus, alternative, simpler, and lower costs (in terms of personnel and time) have to be developed to target Cr and its fate.

In most cases, the metal partitioning is evaluated through sequential extraction procedures (SEPs) that are sufficiently sensitive and 'simple' to use for routine analyses (Keon et al., 2001). Sequential chemical extraction methods are widely used for the investigation of metal fractionation in soils and sediments. It is based on the application of a series of increasingly aggressive reagents (**Figure 2.8**) that (1) selectively dissolve different components where the metals could be partitioned and (2) is intended to simulate the different environmental conditions that could release these metals (Gleyzes et al., 2002). Earlier extracted metals are generally the most weakly bound to solid components and, therefore, manifest greater potential mobility than fractions solubilized later in the process (Bacon & Davidson, 2008). However, SEPs are widely criticized because of poor selectivity of reagents, redistribution of metals during extraction, incomplete dissolution, or potential lack of quality control (Gleyzes et al., 2002; Bacon & Davidson, 2008; Hass & Fine, 2010; Rodgers et al., 2015). In addition, and particularly for Cr, no optimized SEP has been developed and tested for Cr and Ni laterites. Operational aspects (e.g., sample preparation and storage, solid-to-solution ratios, extraction time and temperature, reagent concentrations, shaking speed, etc.) can also lead to inconsistent results among SEPs (Filgueiras et al., 2002). Despite the drawbacks, sequential extraction remains widely accepted and has been extensively applied to the characterization of pollution sources, assessment of metal mobility and bioavailability, and investigation of metal transport mechanisms (Filgueiras et al., 2002).

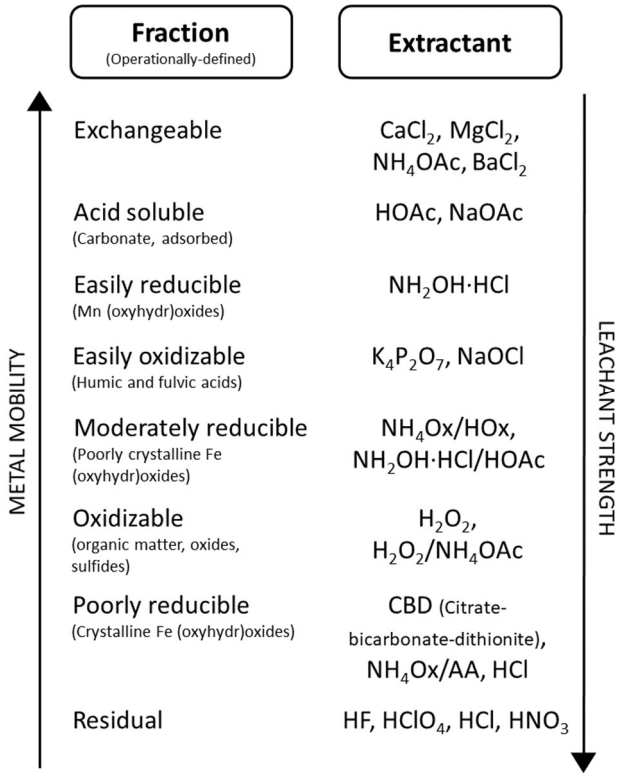

Figure 2.8. Common chemical reagents used in SEPs. Modified from Filgueiras et al., 2002 with permission from the Royal Society of Chemistry.

Sequential extraction has been extensively used to investigate the partitioning of Cr in soils and sediments developed from ultramafic rocks. However, as mentioned above, most have used non-laterite and non-Cr-specific methods. Since the classical work of Tessier et al. (1979), numerous researchers have developed SEPs for a variety of substrates, yet there have only been a few works tailored for tropical soils, including Fe-rich laterites (Ma & Uren, 1998; Silveira et al., 2006). While spinels and Fe (oxyhydr)oxides play an important role in the environmental cycling of Cr in laterites, most SEPs inefficiently dissolve these phases, resulting in the underestimation of metals partitioned in these minerals (Quantin et al., 2002; Garnier et al., 2006; Silveira et al., 2006; Delina et al., 2020) Studies on Cr partitioning in laterites by Quantin et al. (2002) and my own MSc work (Delina et al. (2020) have reported incomplete Fe (oxyhydr)oxide dissolution during the citrate-bicarbonate-dithionite (CBD) and hydroxylamine hydrochloride ($NH_2OH{\cdot}HCl$) steps in the sequential extractions. Furthermore, laboratory studies have also shown that Cr substitution for Fe can stabilize Fe (oxyhydr)oxides against dissolution in strong acids and reductants (e.g., dithionite), presenting an additional challenge in investigating the fractionation of Cr in these minerals (Schwertmann, 1991; Bousserrhine et al., 1999). Moreover, SEPs are commonly developed for cationic species and, thus, when applied to Cr, will likely underestimate the contribution of Cr(VI) oxyanions. Most SEPs, for example, use a pH 5 acetate buffer to extract adsorbed metals. However, Cr may be released as

chromate, which has been reported to adsorb onto Fe (oxyhydr)oxides at this acidic pH (Oze et al., 2004b; Fandeur et al., 2009b). Clearly, there is a need to evaluate the current sequential extraction schemes applied to Fe-rich tropical soils and optimize a procedure for the fractionation of Cr in Ni laterites to provide a better understanding of its potential environmental impacts.

Overall, the above review identifies gaps in knowledge mostly related to the speciation and mobility of Cr in potential Cr sources and compartments in Ni laterite mining environments, factors controlling its environmental cycling and ultimate fate from source to sink, and the lack of optimized, more practical techniques for quantifying the partitioning, and thus the potential mobility of Cr.

Chapter 3

Partitioning and mobility of chromium in laterites from an optimized sequential extraction procedure

This chapter is adapted from:

Delina, R.E.G.; Perez, J.P.H.; Stammeier, J.A.; Bazarkina, E.F.; Benning, L.G. (2024). Partitioning and Mobility of Chromium in Iron-Rich Laterites from an Optimized Sequential Extraction Procedure. *Environmental Science & Technology,* 58, 6391-6401.

Available at: https://doi.org/10.1021/acs.est.3c10774

Abstract

Chromium (Cr) leached from iron (Fe) (oxyhydr)oxide-rich tropical laterites can substantially impact downstream groundwater, ecosystems, and human health. However, its partitioning into mineral hosts, its binding, oxidation state, and potential release are poorly defined. This is in part due to the current lack of well-designed and validated Cr-specific sequential extraction procedures (SEPs) for laterites. To fill this gap, we have (i) first optimized a Cr SEP for Fe (oxyhydr)oxide-rich laterites using synthetic and natural Cr-bearing minerals and laterite references, (ii) used a complementary suite of techniques and critically evaluated existing non-laterite and non-Cr-optimized SEPs, compared to our optimized SEP, and (iii) confirmed the efficiency of our new SEP through analyses of laterites from the Philippines. Our results show that other SEPs inadequately leach Cr host phases and underestimate the Cr fractions. Our SEP recovered up to seven times higher Cr contents because it (a) more efficiently dissolves metal-substituted Fe phases, (b) quantitatively extracts adsorbed Cr, and (c) prevents overestimation of organic Cr in laterites. With this new SEP, we can estimate the mineral-specific Cr fractionation in Fe-rich tropical soils more quantitatively and thus improve our knowledge of the potential environmental impacts of Cr from lateritic areas.

3.1. Introduction

Laterite broadly refers to the iron or aluminum (oxyhydr)oxide-rich weathering mantle covering about 33% of the continents (Tardy, 1997; Stoops & Marcelino, 2018). Laterites developed from tropical weathering of ultramafic rocks (e.g., peridotites, dunites) predominantly consist of Fe (oxyhydr)oxides in the form of goethite (FeOOH) and hematite (Fe_2O_3), and are often enriched with critical metals such as nickel (Ni), cobalt (Co), and scandium (Sc) mainly incorporated into the minerals (Elias, 2002; Butt & Cluzel, 2013; Aiglsperger et al., 2016). Such metal deposits are known as nickel laterites, and they are the world's main source of Ni, accounting for ~60% of the global production (Butt & Cluzel, 2013; USGS, 2023).

Nickel laterites also contain elevated concentrations of chromium (up to ~70,000 mg kg^{-1}) (Chrysochoou et al., 2016; Ulrich et al., 2019) that are multiple orders of magnitude higher than upper crustal averages (35 mg kg^{-1}) (Hans Wedepohl, 1995). Chromium commonly occurs as Cr(III) and Cr(VI), with the latter being a highly mobile, toxic and carcinogenic pollutant (Katz & Salem, 1994; WHO, 2003; Guertin et al., 2016). The majority of Cr in Ni laterites is present as Cr(III) and preferentially substitutes into octahedral sites of Fe (oxyhydr)oxides (e.g., goethite, hematite), silicates and spinels (Oze et al., 2004a; Chrysochoou et al., 2016), while Cr(VI) predominantly exists as oxyanions (i.e., $HCrO_4^-$, CrO_4^{2-}) adsorbed onto these same minerals (Richard & Bourg, 1991; Kotaś & Stasicka, 2000) or dissolved in pore waters or soil solutions (Becquer et al., 2003). Since Ni laterites are exploited through large opencast surface mining, Cr(VI) leaches into surface- and groundwaters where it can reach concentrations (up to 1,600 μg L^{-1}) (Gunkel-Grillon et al., 2014; Economou-Eliopoulos et al., 2016; Delina et al., 2020), far exceeding international drinking water standards (50–100 μg L^{-1}) (USEPA, 2006; WHO, 2017). Elevated levels of Cr(VI) in these water resources can lead to, so far, not well understood health issues for the local population (Chrysochoou et al., 2016). Thus, it is important to quantify the partitioning and possible transport mechanisms of Cr species in laterite host phases, and evaluate how these Cr-mineral phase specific associations dictate the potential mobility, bioavailability and toxicity of Cr during geogenic (e.g., weathering) and anthropogenic (e.g., mining) processes.

The partitioning of elements in soils and sediments is traditionally evaluated through sequential extraction procedures (SEPs) which are based on a series of increasingly aggressive reagents that categorize the leached elements into chemical or mineralogical fractions (Gleyzes et al., 2002; Silveira et al., 2006). However, SEPs are criticized for poor selectivity of extraction reagents, redistribution of metals and incomplete dissolution (Gleyzes et al., 2002; Bacon & Davidson, 2008; Hass & Fine, 2010; Rodgers et al., 2015). For instance, in the case of Cr, most SEPs cannot completely dissolve common host phases such as chromite and Fe

(oxyhydr)oxides (Becquer et al., 2006; Delina et al., 2020). Chromites are highly recalcitrant to dissolution with most conventional digestion methods (Quantin et al., 2002; Rodgers et al., 2015; Delina et al., 2020), while the dissolution of Fe (oxyhydr)oxide is known to be affected by metal substitution. For example, substitution of Cr and aluminum (Al) for Fe in goethite has been shown to strongly inhibit its dissolution in strong acids and reductants (Schwertmann, 1991; Silveira et al., 2006); yet the effect of metal substitution is often overlooked when developing SEPs. In addition, SEPs are commonly optimized for cationic species (Gleyzes et al., 2002), and thus when applied to Cr, they likely underestimate the distribution of Cr(VI) oxyanions. More importantly, no SEP has been critically assessed for its suitability for Cr partitioning in tropical laterites which possess such a unique Fe mineral assemblage. Existing SEPs applied for Cr fractionation in tropical soils rich in Fe and Mn (oxyhydr)oxides (Quantin et al., 2002; Garnier et al., 2006; Tashakor et al., 2014; Delina et al., 2020) were originally developed for other metals and/or sample matrices. These include the modified Geological Survey of Canada (mGSC) procedure, which was initially developed to partition Cd in temperate soils (Benitez & Dubois, 1999), but has been tested to be also suitable for tropical soils (Doelsch et al., 2008). The SEP used in Quantin et al. (2002) was adapted from well-cited procedures including Tessier et al. (1979) which were intended for extracting metals such as Si, Ca, Cd, Fe from river sediments and temperate to subtropical soils (Tessier et al., 1979; Shuman, 1985; Leleyter & Probst, 1999). Finally, the SEP by Silveira et al. (2006) was designed for tropical soils and optimized for Zn, Cu, Fe and Mn but not Cr. Because these SEPs are neither optimized for Fe-rich laterites nor for Cr species, there is a need to optimize a Cr sequential extraction procedure, and thus provide a more quantitative evaluation of the fate and potential impacts that Cr can have in such lateritic environments.

To address this gap, we have characterized the partitioning of Cr in various tropical Ni laterite profiles using a new sequential extraction procedure for Fe (oxyhydr)oxide-rich laterites. We optimized different extractants using Cr- and Fe-bearing phases commonly present in Ni laterites and certified laterite references, and validated our new SEP using Ni laterites from different localities in the Philippines. We also compared and contrasted our results with the three aforementioned SEPs (Benitez & Dubois, 1999; Quantin et al., 2002; Silveira et al., 2006) and document the far more efficient and targeted nature of our new SEP.

3.2. Materials and methods

3.2.1. Natural laterites

The partitioning of Cr was examined in previously well-characterized Ni laterites from three major Ni mining districts in the Philippines (Palawan, Zambales, Surigao) (Arcilla et al., 2019; Delina et al., 2020). Palawan samples described in Delina et al. (2020) were obtained from a

6.8-m thick Ni laterite profile consisting of an upper Fe (oxyhydr)oxide (i.e., goethite and hematite) dominated limonite zone and a lower silicate-rich (i.e., serpentine and smectite) saprolite layer separated by a thin transition zone. From bottom to top, the profile is characterized by a dramatic increase in Cr and Fe contents (from 0.5 to 2.9 wt.% Cr and 9 to 54 wt.% Fe) (Delina et al., 2020). Samples from the limonite, transition, and saprolite zones (hereafter referred to as PAL-1, PAL-2, and PAL-3, respectively), representative of different Cr and Fe concentrations, were used to evaluate the efficiency of our new SEP. Furthermore, the robustness of our SEP was tested on five high Cr (1.1-1.7 wt.%) and Fe (38-55 wt.%) limonite samples from Zambales (ZAM-1 to ZAM-3) and Surigao (SUR-1 to SUR-2). These primarily contain goethite (>89%) with minor spinel (2.4-11%). Characterization of these samples are discussed in the Supporting Information (**Section 3.4.1**).

3.2.2. Synthesis and preparation of mineral standards

Various synthetic and natural mineral references (**Table S3.1**) representing the composition of Fe (oxyhydr)oxide-rich laterites (Elias, 2002; Fandeur et al., 2009a; Delina et al., 2020) were prepared to optimize the SEP. Pure and metal (Me)-substituted (Me = Al and Cr) ferrihydrite, goethite (α-FeOOH), and hematite (α-Fe_2O_3) and pure magnetite ($Fe(II)Fe(III)_2O_4$) were synthesized using standard procedures adapted from Schwertmann and Cornell (2000). In addition to Cr, Al-substituted Fe minerals were also prepared, since pedogenic Fe (oxyhydr)oxides often structurally incorporate Al (Schwertmann, 1991). Cr(VI)-adsorbed Fe (oxyhydr)oxides were also prepared. Details of the preparation and characterization of these synthetic minerals and natural samples (e.g., chromite) can be found in **Section 3.4.1**.

3.2.3. Testing and optimization based on the mineral references

Single extractions (detailed in **Section 3.4.1**) were carried out to assess the dissolution efficiency and selectivity of different reagents. Selection of extractants were based on extensive reviews of SEPs (Filgueiras et al., 2002; Gleyzes et al., 2002; Hass & Fine, 2010) and procedures applied to Fe (oxyhydr)oxides and Fe-rich soils and sediments (Raiswell et al., 1994; Poulton & Canfield, 2005; Silveira et al., 2006; Voelz et al., 2019). Operating conditions (e.g., temperature, duration, solid-to-liquid ratio) and concentrations were varied and tested to find the best possible extractant (**Table 3.1; Table S3.3**).

To partition adsorbed Cr(VI) oxyanions, we applied an alkaline (pH 8) 0.01 M $NH_4H_2PO_4$ treatment for 16 h (Tokunaga et al., 1991; Drahota et al., 2014) (see **Section 3.4.1** for detailed information) on Cr(VI)-adsorbed Fe (oxyhydr)oxides. We evaluated the selectivity of typically used extractants for the prior exchangeable fraction step (i.e., 0.1-1 M $Ca(NO_3)_2$ and 1 M $MgCl_2$ for 2 h) (Hass & Fine, 2010) with respect to the Cr(VI)-adsorbed phases. We also examined the effect of the following treatments on Cr- and Fe-bearing minerals: 1 M NaOAc buffer (pH 4.5)

for 5 h (carbonate-bound fraction) (Leleyter & Probst, 1999; Poulton & Canfield, 2005), ~5% NaOCl (pH 8.5) at boiling temperature for 30 min (organic fraction) (Shuman, 1983; La Force & Fendorf, 2000), and 0.1 M NH_2OH-HCl in 0.01 M HNO_3 for 10 min (Mn phase-bound fraction) (Denys et al., 2021). Furthermore, we assessed the effectiveness of different concentrations of HCl in dissolving Fe (oxyhydr)oxides of different crystallinities. We tested dilute (0.5 and 1 M) HCl (Raiswell et al., 1994; Claff et al., 2010) for the poorly crystalline fraction and 6 M HCl (Silveira et al., 2006; Porsch & Kappler, 2011) extractions at different temperatures (50, 75°C) and reaction times (≤48 h) for the crystalline fraction.

3.2.4. Sequential extractions

Based on the single extractions, we optimized a new SEP and tested it on mixtures of mineral references (**Table S3.5**) and Ni laterite certified reference materials (CRMs) (OREAS 182 and 190). The optimized SEP was applied to the Ni laterites and compared to the three SEPs previously used for Cr partitioning in laterites and related tropical soils: the mGSC procedure (Benitez & Dubois, 1999) (SEP 1), the SEPs used in Quantin et al. (2002) (SEP 2) and in Silveira et al. (2006) (SEP 3) (outlined in **Table S3.2**). All SEPs were performed in duplicate on the Palawan Ni laterite samples except for SEP 1, which was previously applied to the same samples in Delina et al. (2020).

In each SEP step, reagents were mixed with powdered samples in acid-cleaned centrifuge tubes and reacted in temperature-controlled orbital shakers at 150-250 rpm. Liquid phases were separated from the residue by centrifugation at 10,052*g* for 10 min. Between each extraction, residues were washed with Milli-Q water (~18.2 MΩ·cm) and freeze-dried before for the next extraction step. Analysis of supernatants were identical to that of the single extractions (**Section 3.4.1**). Relative standard deviations (RSDs) of Cr were <5% for ~80% of samples. RSD >10% was observed in extracts with Cr concentrations near the quantification limit.

The residues of the sequential extraction are chemically resistant minerals such as chromite (see **Figure 3.4**) that are highly prone to incomplete dissolution by conventional digestion methods (Hass & Fine, 2010; Rodgers et al., 2015; Delina et al., 2020). In our work, acid digestion post Na_2O_2 fusion (Bokhari & Meisel, 2017) (see **Section 3.4.1**) did not lead to full dissolution, and dark colored chromite grains persisted. We accounted for the Cr associated with this residual fraction as the difference of the total concentration and the sum of all extracted non-residual fractions and we mainly discuss and compare steps that target the latter.

To characterize the residual fraction and understand how different SEPs extract Cr, we analyzed the mineralogy and local bonding environment of Cr in selected SEP residues after the crystalline Fe phase-bound step using X-ray diffraction (XRD), scanning electron microscopy (SEM), and high-energy resolution fluorescence detection X-ray absorption spectroscopy (HERFD-XAS) fully described in the Supporting Information.

3.3. Results and discussion

3.3.1. Metal-substitution in natural Fe (oxyhydr)oxides

X-ray diffraction and infrared (IR) spectroscopy patterns of Fe (oxyhydr)oxide-dominated samples from each Ni laterite district (**Figure 3.1**) showed consistent patterns with the synthetic goethites (**Figure S3.1-S3.2**). PAL-1, containing nearly equal amounts of goethite (48%) and hematite (43%), exhibited combined patterns of the Fe phases. Diffraction peaks of the natural samples showed remarkable shifts to higher angles or Q (=2π/d) values compared with pure goethite ($\Delta Q_{(110)} \leq 0.012$) and hematite ($\Delta Q_{(110)} = 0.003$) (**Figure 3.1b-c**) suggesting metal substitution. This is supported by the similar shifts displayed by substituted goethites ($\Delta Q_{(110)} \leq 0.009$) and hematites ($\Delta Q_{(110)} \leq 0.015$), indicating a decrease in unit cell volume due to the smaller octahedral radii of Al(III) (0.530 Å, 18% smaller) and Cr(III) (0.615 Å, 5% smaller) compared to Fe(III) (0.645 Å). Consistent with previous studies (Trolard et al., 1995; Bousserrhine et al., 1999; Hua et al., 2018; Li et al., 2019), Al-substituted phases showed larger shifts due to the significantly smaller atomic radius of Al. The effect of substitution was also observed in the IR spectra (**Figure 3.1e-f**) where the separation of the OH bending modes of synthetic goethites at ~790 to 890 cm^{-1} increase from 95 cm^{-1} to 103 cm^{-1} and the Fe-O band of synthetic hematites at ~520 cm shift to higher wavenumbers.

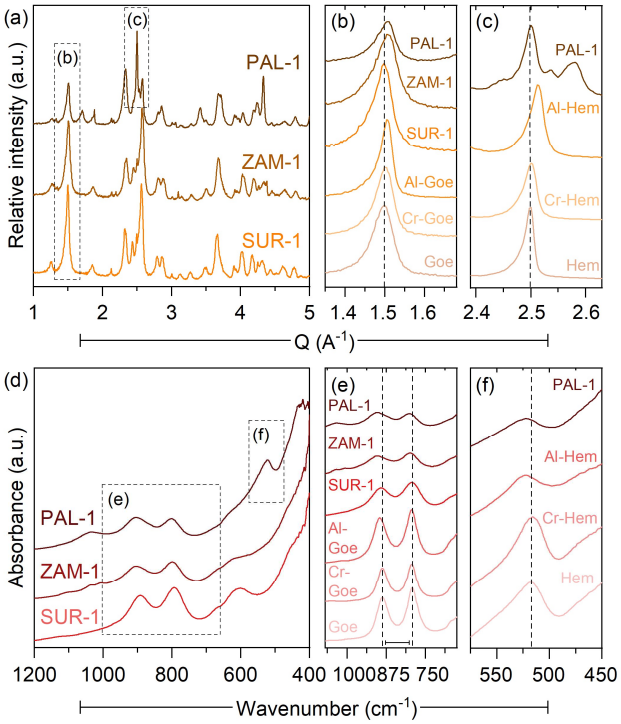

Figure 3.1. XRD patterns and IR spectra of the Fe (oxyhydr)oxide-rich laterites compared with pure and metal-substituted Fe phases. (a) XRD patterns with highlighted (110) diffraction peaks of (b) goethite (Goe) and (c) hematite (Hem). (d) IR spectra of the samples with highlighted (e) OH bonds of goethite and (f) Fe-O bond of hematite. Dashed vertical lines highlight peak shifts relative to pure phases due to metal substitution.

Among the natural goethites, PAL-1 showed the largest diffraction peak shift and IR band separation which are slightly higher than that of the Al-goethite. This may suggest a higher extent of substitution of many different cations, bigger differences in atomic radii of substituting metals, or crystal disorder (Trolard et al., 1995; Bousserrhine et al., 1999; Kaur et al., 2009; Ekstrom et al., 2010; Li et al., 2019). Aside from Al and Cr, Fe (oxyhyr)oxides in laterites have been found to be important hosts for Ni, Co, and Mn (Trolard et al., 1995; Dublet et al., 2017; Ugwu & Sherman, 2019).

3.3.2. Cr and Fe extractability from mineral standards

Given that Cr in laterites could occur as adsorbed species or structurally incorporated in predominant Fe (oxyhydr)oxides and metal-substitution could affect the crystal structure, and thus, the solubility and dissolution rate of these Fe phases (Ugwu & Sherman, 2019), we tested the efficiency and selectivity of different extraction steps with a range of Cr and Fe minerals (**Table 3.1, S3.3**).

Easily mobilizable fractions. Our data show that the 0.01 M $NH_4H_2PO_4$ treatment effectively desorbed more than 70% of Cr from the Cr(VI)-adsorbed Fe (oxyhydr)oxides, with negligible Fe dissolution. A disadvantage of phosphate treatment is that residual adsorbed phosphate can retard Fe dissolution (Cornell & Schwertmann, 2003; Claff et al., 2010) by surface passivation and decreasing the reactivity of the Fe (oxyhydr)oxides (Biber et al., 1994; Majzlan, 2011; Kraal et al., 2019). This was evident in the incomplete recovery of Fe from goethite and natural magnetite when the 6 M HCl extraction was preceded by phosphate treatment (**Table S3.4**). It is therefore necessary to perform a rinsing step after the phosphate extraction. While Ruttenberg (1992) recommended $MgCl_2$ wash for phosphorus extractions, we decided to use ultrapure water to minimize dissolved salts in the extract, and avoid possible interferences during measurements. A minimum of 3 successive water rinses were found sufficient to displace most of the phosphate (**Figure S3.4**).

$Ca(NO_3)_2$ and $MgCl_2$ extractions for the exchangeable fraction, usually applied at the beginning of SEPs, indiscriminately extracted up to 20% of Cr from the Cr(VI)-adsorbed Fe (oxyhydr)oxides (**Figure S3.5**). To avoid substantial underestimation of adsorbed Cr, the most dilute $Ca(NO_3)_2$ (0.1 M) treatment that extracted only 1-7% of Cr was chosen for the exchangeable fraction. Overall, these experiments imply that previous SEPs without a phosphate step and using only nitrate or chloride salts underestimated the easily mobilizable Cr fraction (exchangeable and adsorbed).

Table 3.1. Dissolution efficiencies of single extractions on selected mineral standards and sequential extractions on mixtures and Cr and Fe partitioning in laterite CRMs. FHY – ferrihydrite, Goe – goethite, Hem – hematite, Ox – (oxyhydr)oxides

Extractant	Ferrihydrite	Goethite	Hematite	Magnetite (synthetic)	Magnetite (natural)	Chromite
	Poorly cryst. Fe Ox	Crystalline Fe Ox				Residual
	Fe dissolution efficiency (%)					
0.1 M $Ca(NO_3)_2$	*bdl*	*bdl*	*bdl*	*bdl*	*bdl*	*bdl*
0.01 M $NH_4H_2PO_4$	0.02 (8E-4)	*bdl*	*bdl*	*bdl*	*bdl*	*bdl*
1 M NaOAc	1.40 (0.06)	*bdl*	*bdl*	*bdl*	0.15 (6E-3)	*bdl*
0.1 M NH2OH-HCl	0.27 (6E-3)	*bdl*	0.06 (1E-3)	0.11 (2E-3)	*bdl*	*bdl*
5% NaOCl (1:20, 2x)	0.004 (1E-4)	*bdl*	*bdl*	*bdl*	*bdl*	*bdl*
1 M HCl, 8 h	99.2 (2.3)	0.51 (0.02)	15.4 (0.5)	9.52 (0.32)	0.14 (3E-3)	*bdl*
6 M HCl, 75°C, 24 h	ND	104 (3)	105 (4)	99.0 (3.5)	97.6 (2.6)	*bdl*

Extractant	Cr(VI)-ads FHY	Cr(VI)-ads Goe	Cr(VI)-ads Hem	Cr-FHY	Cr-Goe	Cr-Hem	Chromite
	Adsorbed			Poorly cryst. Fe Ox	Crystalline Fe Ox		Residual
	Cr dissolution efficiency (%)						
0.1 M $Ca(NO_3)_2$	1.20 (0.06)	6.12 (0.31)	7.04 (0.36)	ND	ND	ND	ND
0.01 M $NH_4H_2PO_4$	76.8 (3.9)	81.3 (4.2)	75.9 (3.9)	ND	ND	ND	ND
5% NaOCl (1:5)	ND	ND	ND	4.07 (0.09)	49.2 (1.4)	4.76 (0.08)	0.15 (6E-4)
5% NaOCl (1:20, 2x)	ND	ND	ND	26.0 (1.4)	60.5 (1.7)	15.9 (0.4)	0.12 (1E-3)
0.5 M HCl, 4 h	ND	ND	ND	80.6 (2.1)	ND	ND	ND
1 M HCl, 4 h	ND	ND	ND	96.4 (2.5)	ND	ND	ND
1 M HCl, 8 h	ND	ND	ND	98.4 (2.5)	11.6 (0.6)	2.14 (0.07)	*bdl*
6 M HCl, 50°C, 48 h	ND	ND	ND	ND	52.8 (2.2)	98.6 (5.6)	*bdl*
6 M HCl, 75°C, 24 h	ND	ND	ND	ND	94.7 (5.7)	102 (6)	*bdl*

Extractant	Mixture 1	Mixture 2	Mixture 3	OREAS 182		OREAS 190	
	Cr dissolution efficiency (%)			*Cr ext. (%)*	*Fe ext. (%)*	*Cr ext. (%)*	*Fe ext. (%)*
Step 1: 0.1 M $Ca(NO_3)_2$				0.36 (0.01)	*bdl*	0.04 (1E-3)	*bdl*
Step 2: 0.01 M $NH_4H_2PO_4$	51.2 (0.1)			0.47 (0.01)	0.45 (0.01)	0.12 (3E-3)	0.26 (6E-3)
Step 3: 1 M NaOAc				0.01 (2E-4)	0.40 (0.01)	0.56 (0.02)	0.37 (8E-3)
Step 4: 0.1 M NH2OH-HCl				0.03 (1E-3)	0.23 (5E-3)	0.03 (1E-3)	0.18 (4E-3)
Step 5: 1 M HCl, 8 h		102 (2)	89.9 (1.9)	1.01 (0.03)	5.05 (0.11)	0.80 (0.02)	3.94 (0.08)
Step 6: 6 M HCl, 75°C, 24h	92.0 (1.9)	89.1 (1.9)	108 (2)	11.0 (0.3)	82.7 (1.8)	14.8 (0.4)	75.5 (1.6)
Step 7: 5% NaOCl (1:20, 2x)*				1.26 (0.04)	*bdl*	0.43 (0.01)	*bdl*
Residual	106	109	101				

Note: Dissolution efficiency or metal extracted (ext.) (%) = (wt.% extracted ⁄ wt.% total) x 100. (#) – analytical uncertainty (<5% relative) based on multiple measurements ($n \geq 5$) of QC solutions. Mixture compositions are further detailed in **Table S3.5**. For mineral mixtures, the residual fraction dissolution efficiency was represented by the (wt.% total Cr - ∑wt.% non-residual) ⁄ wt.% Cr in chromite. *bdl* – below detection limit; ND – no data

*The NaOCl step (Step 7) was applied after the 6 M HCl treatment (Step 6) to prevent the indiscriminate oxidation of Cr from Fe (oxyhydr)oxides.

Non-Fe phase-bound fractions. Acetate, hypochlorite and hydroxylamine-HCl extractions partitioned very little amounts of Fe (<1%) from the reference phases (**Table 3.1**). However, NaOCl leached a significant amount of Cr from all Cr-substituted Fe (oxyhydr)oxides. Among extractants used for organic matter (e.g., NaOCl, H_2O_2, $Na_4P_2O_7$), NaOCl was reported to exhibit greater efficiency and minimal attack of amorphous Fe (oxyhydr)oxides and clays in soils (Gleyzes et al., 2002; Mikutta et al., 2005; Hass & Fine, 2010). However, our results clearly showed that NaOCl treatment leads to substantial Cr release, irrespective of the S:L ratio used. The typical 1:5 ratio (Silveira et al., 2006) extracted 4-49% of the Cr incorporated in the Fe (oxyhydr)oxides; meanwhile, the 1:20 ratio performed once and twice (Shuman, 1983; La Force & Fendorf, 2000) released 12-56% and 16-60%, respectively. Extracts showed faint to strong yellow hues, suggesting the presence of chromate, and hence the possible oxidation of Cr(III) to Cr(VI). This aligns with prior work on the oxidative dissolution of Cr(III) hydroxide with NaOCl (Lee & Hering, 2005; Lindsay et al., 2012). Earlier SEPs of other metals also reported the indiscriminate oxidation of redox-sensitive elements by NaOCl. Gruebel et al. (1988) and Wright et al. (2003) revealed that adsorbed and incorporated Se species in selenides were oxidized to Se (VI), leading to substantial overestimation of the organic pool. Similarly, La Force and Fendorf (2000) showed that Fe(II) from mine wastes were oxidized by NaOCl, resulting in inaccurate partitioning of Fe. Therefore, to avoid the indiscriminate oxidation of Cr, we applied the NaOCl treatment after the Fe (oxyhydr)oxide dissolution.

Poorly crystalline Fe phase-bound fraction. Among tests using 0.5 and 1 M concentrations and a duration of 4 to 8 h (**Table 3.1, S3.3**), the 8-h 1 M HCl extraction was found to be most effective for poorly crystalline Fe (oxyhydr)oxides. All ferrihydrites were dissolved with >97% total Fe recovery, with Cr-substituted ferrihydrite showing the least recovery. To test the selectivity of 1 M HCl, we applied it to crystalline phases. It extracted up to 15% of total Fe in pure synthetic phases, comparable with earlier works showing dissolution of up to 33% of Fe from synthetic hematite and 9% from magnetite (Raiswell et al., 1994; Claff et al., 2010). It should be noted that pure minerals, such as these, rarely occur in nature, and thus, selectivity of reagents is better evaluated with respect to metal-substituted and natural phases. The substantially low Fe, Cr, and Al dissolution efficiencies (below detection to 12%) (**Table 3.1, S3.3**) from metal-substituted and natural Fe (oxyhydr)oxides validates the selectivity of the 1 M HCl treatment.

Crystalline Fe phase-bound fraction. We optimized a 6 M HCl extraction that has been used for the sequential extraction of crystalline Fe oxides and/or sheet silicates (Porsch & Kappler, 2011; Muehe et al., 2013; Patzner et al., 2020; Kraal et al., 2022). Extractions at 50°C after decreasing the S:L ratio (1:40 to 1:100) and increasing the duration (24 to 48 h) compared to previous SEPs (Silveira et al., 2006) did not completely dissolve the Fe (oxyhydr)oxides, especially Cr-goethite. Full dissolution was only achieved after further increasing the

temperature to 75°C. Time series experiments (**Figure 3.2**) revealed that all crystalline Fe (oxyhydr)oxides, except for Cr-goethite, were effectively dissolved within 2 hrs. Cr-goethite was only fully dissolved after 24 h while chromite was unaffected even after 48 h. In comparison to prior dissolution of goethites using 6 M HCl at 25°C (Schwertmann, 1991), the optimized 6 M HCl treatment reduced the time to fully dissolve Al-substituted goethite from ~220 h to 2 h and increased the dissolution extent of Cr-goethite from <50% after 350 h to >98% after only 24 h.

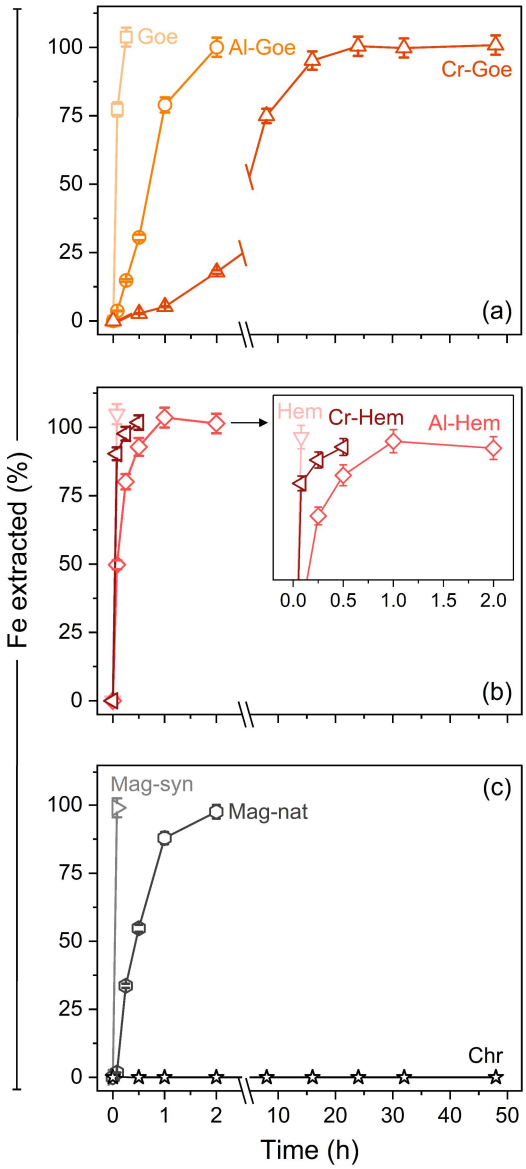

Figure 3.2. Dissolution time-curves of reference Fe minerals: (a) goethites (Goe), (b) hematites (Hem), and (c) spinels (Mag – Magnetite, Chr – chromite) in 6 M HCl at 75°C. Error bars indicate analytical uncertainty (<5% relative) based on multiple measurements (n = 8) of QC solutions.

Faster rates of dissolution were observed from pure minerals compared to their metal-substituted and natural counterparts. These findings are consistent with previous works on synthetic Fe (oxyhydr)oxides dissolved in HCl (Lim-Nunez & Gilkes, 1985; Schwertmann, 1991; Alvarez et al., 2007) where they attributed the slower dissolution rates of Cr- and Al-substituted Fe phases to the higher bond strength of the Me-OH/O bonds (e.g., Al(III)-O = 29.3 kJ mol^{-1}; Cr(III)-O = 24.5 kJ mol^{-1}) relative to Fe-OH/O (e.g., Fe(III)-O = 23.7 kJ mol^{-1}) (Weast, 1988). Moreover, very low rates of H_2O exchange of Cr^{3+} has been suggested to explain the higher resistance of Cr-substituted goethite (Burgess, 1988). In addition to metal-substitution, larger particle sizes and surface areas could explain the slower dissolution rates of natural samples.

We also tested the potential of the selected 24 h hot 6 M HCl treatment in extracting Fe from sheet silicates that could co-occur with the Fe (oxyhydr)oxides in the Ni laterites (Elias et al., 1981; Marsh et al., 2013). Significant amounts of Fe (65-70%) were extracted from nontronite and serpentine. We compared these with the boiling 12 M HCl treatment previously used to extract sheet silicate Fe (Poulton & Canfield, 2005), and document that the optimized 6 M HCl released 2.5 times higher Fe, most likely due to the higher S:L ratio and longer extraction duration. Overall, this demonstrates the ability of the 6 M HCl treatment to dissolve highly crystalline Fe-bearing phases such as metal-substituted (oxyhydr)oxides and sheet silicates without affecting the residual fraction hosted in chromite.

3.3.3. Enhanced efficiency of the optimized SEP

The resulting extraction scheme in **Figure 3.3** was validated with mineral mixtures and nickel laterite CRMs (**Table 3.1**). Chromium recoveries from mixtures were mostly >89%, matching the results of the single extractions. Only the phosphate step targeting the smallest fraction of Cr showed a lower recovery. Moreover, sequential extraction of the CRMs showed well-targeted crystalline Fe phases (**Figure S3.6**).

Easily mobilizable to non-Fe phase-bound fractions. Applying the optimized scheme and three existing SEPs (Benitez & Dubois, 1999; Quantin et al., 2002; Silveira et al., 2006) (**Figure 3.4a-c**) to the PAL laterites yielded very small amounts (<0.1% of total Cr) of exchangeable Cr. Our additional phosphate step leached up to 1% of the total Cr but with a notable Fe extraction (up to 2.6%) (**Figure S3.7**) in the transition and saprolite samples. During this step, we observed colloidal formation likely induced by the interaction of negatively charged phosphate ions and negatively charged surfaces of smectites identified through XRD (**Figure S3.10**). Some colloids might have passed through the filters resulting to the detected Fe. Another possible explanation is dissolution of Fe minerals previously reported during phosphate extractions of arsenic, although the mechanism of dissolution remains unclear (Eiche et al., 2010; Drahota et al., 2014). In the case of the smectite-free limonite samples from

Palawan and from Zambales and Surigao (**Figure S3.9**) where up to 7% of total Cr was recovered in the phosphate step, no such Fe extraction was observed. Thus, care should be taken when interpreting phosphate extracted metals from samples containing clays.

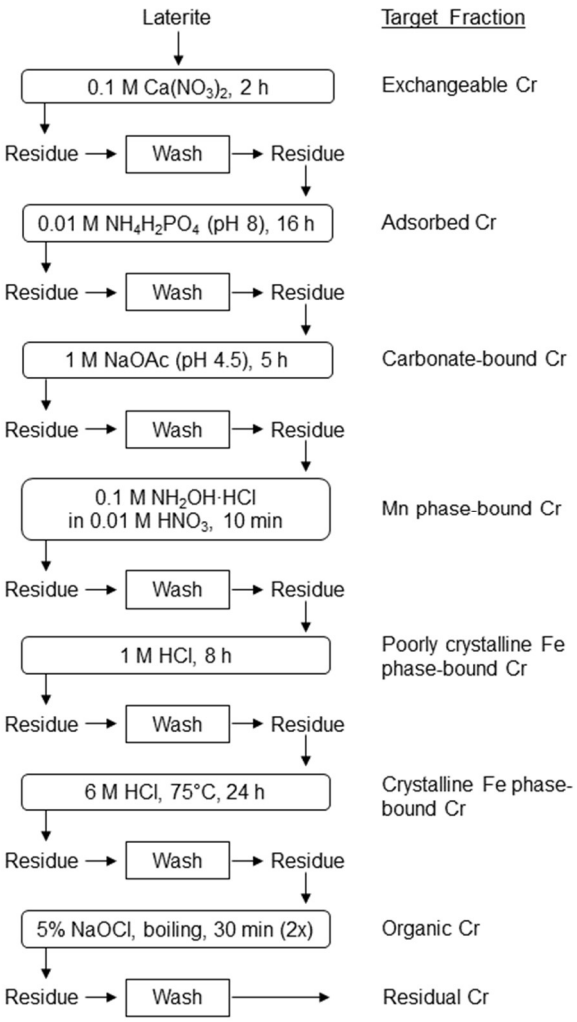

Figure 3.3. Optimized sequential extraction procedure for Cr in Fe-rich laterites. A solid-to-liquid ratio of 1:100 is applied for all except for organic Cr where 1:20 was employed. Residual Cr is the difference between the total concentration and the sum of the preceding extractable fractions.

In terms of organic Cr, the optimized SEP extracted comparable concentrations with SEP 2 which also used an oxidant (H_2O_2) after the crystalline Fe phase step, but generally lower amounts than SEP 3 where NaOCl was applied before Fe (oxyhydr)oxide dissolution. SEP 1 extracted the most (≤6.6%) due to the ligand promoted dissolution of Cr-bearing, poorly crystalline Fe (oxyhydr)oxides by $Na_4P_2O_7$ (Shuman, 1982; Kaiser & Zech, 1996; Kaiser et al., 2012). This is supported by the anomalously high organic bound Fe (≤14%) (**Figure S3.7**) that correlates with the increasing trend of poorly crystalline Fe (oxyhydr)oxides down the laterite profile (Delina et al., 2020). All other SEPs only extracted <1% of total Fe in this step.

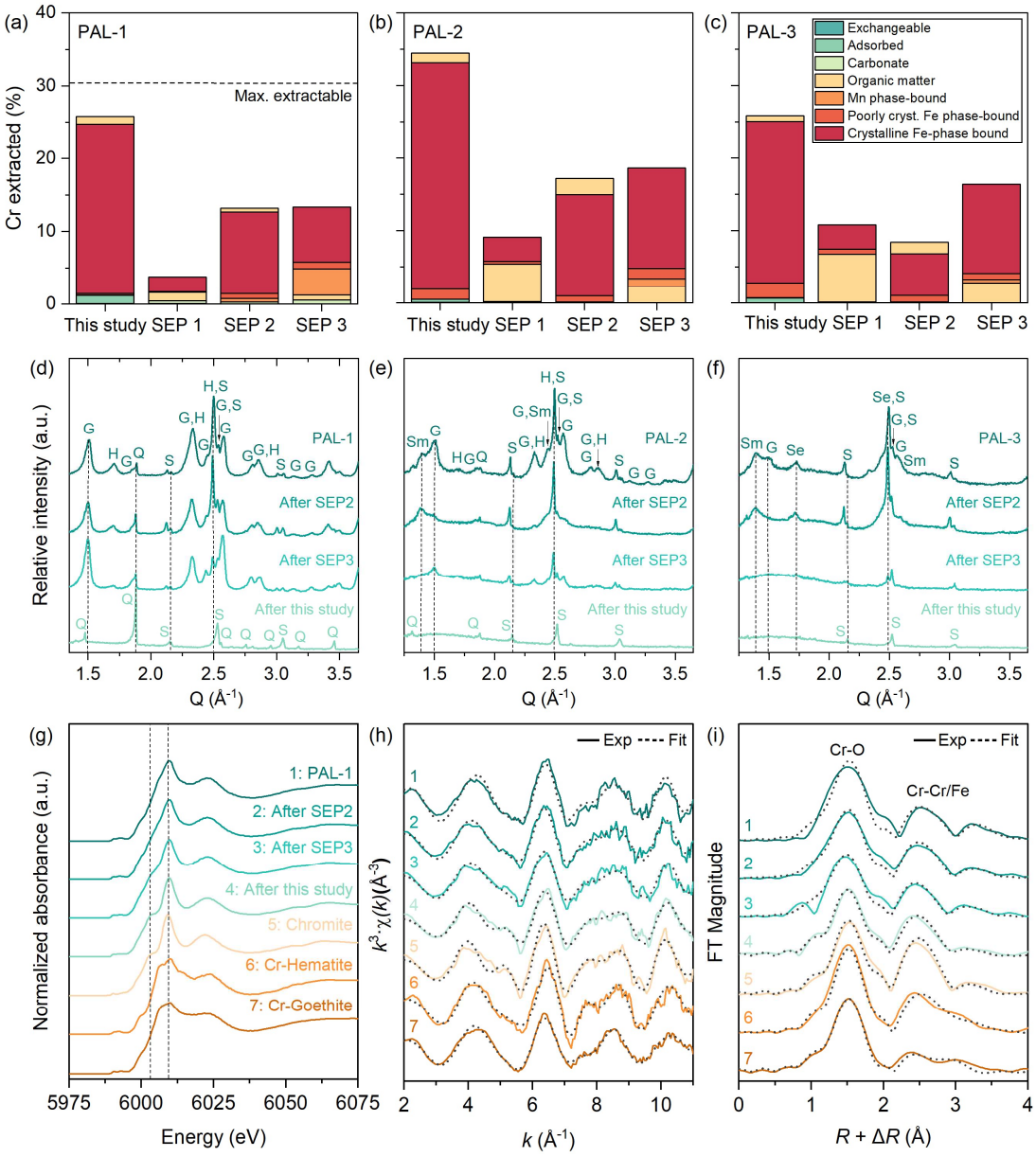

Figure 3.4. (a-c) Comparison of Cr partitioning (% of total concentration) and (d-f) residual fraction mineralogy of the Palawan Ni laterites (PAL-1 – limonite, PAL-2 – transition zone, PAL-3 – saprolite) based on the optimized method (This study) and existing sequential extraction procedures (SEP 1 to 3). The dashed line in (a) represent the maximum extractable Cr further discussed in **Section 3.4.1**. (g) Cr K-edge HERFD-XANES, (h) k^3-weighted EXAFS spectra and the corresponding (i) Fourier transforms (FT) of PAL-1 and its SEP residues and reference minerals. Vertical dashed lines in (g) denote energies discussed in the text. Dotted lines superimposed on the solid lines in (h) and (i) denote shell-by-shell fits of the EXAFS data, respectively. Fit parameters are given in **Table S3.6**. G – goethite, H – hematite, S – spinel, Sm – smectite, Se – serpentine, Q - quartz.

The optimized SEP and SEP 2 leached <1% of Cr using hydroxylamine-HCl, which targets the Mn phase-bound fraction. Conversely, SEP 3 extracted up to four times more Cr despite using the same reducing reagent. Unlike in the two SEPs, the hydroxylamine-HCl treatment of

SEP 3 is preceded by NaOCl. As previously discussed, NaOCl can oxidize mineral bound Cr(III) to Cr(VI), promoting adsorption onto Mn (oxyhydr)oxides which are known adsorbents of Cr(VI) species (Islam et al., 2020). This indicates that for Cr, applying an oxidant like NaOCl before the mineral dissolution step will not only overestimate organic Cr but also succeeding fraction(s) as a result of the carryover of oxidized Cr.

Fe phase-bound to residual fractions. Our SEP demonstrated the highest recoveries for Cr and Fe bound to Fe minerals. The 1 M HCl step dissolved increasing Cr (0.3-2%) and Fe (1-6%) fractions from PAL-1 to PAL-3, agreeing well with the increasing amount of poorly crystalline Fe (oxyhydr)oxides (Delina et al., 2020). SEP 1 showed the poorest recoveries for both poorly crystalline (<1% Cr, <1.5% Fe) and (<3.5% Cr, <12% Fe) crystalline fractions. Inefficient extraction by hydroxylamine-HCl (Delina et al., 2020) and the non-selective $Na_4P_2O_7$ step may account for these low recoveries. As discussed earlier, the latter can also retard the dissolution of Fe (oxyhydr)oxides.

Complete dissolution of Fe (oxyhydr)oxides by our optimized 6 M HCl step yielded up to 11-fold increase in crystalline Fe phase-bound Cr and Fe relative to existing SEPs. Residues after this step (**Figure 3.4d-f**) reveal the absence of Fe (oxyhydr)oxides, showing only chromite and quartz signals in XRD and SEM (**Figure S3.11**). In the limonite residue where chromite is predominant, we have estimated the maximum extractable Cr (**Section 3.4.1.**) and showed that our SEP yields the highest extraction efficiency, closest to the maximum value (**Figure 3.4a**) and showing ~85% recovery. In contrast, residues from the two most efficient existing SEPs (2 and 3) show the incomplete dissolution of goethite and hematite, especially in the limonite sample. While our 6 M HCl step recovered 78% of total Fe from PAL-1, both the widely used citrate-bicarbonate-dithionite (CBD) and 6 M HCl steps of SEP 2 and 3, respectively, only recovered half.

Chromium K-edge XAS of the PAL-1 residues unveil how the different SEPs affect the dissolution of Cr. The Cr K-edge HERFD-XANES spectrum of the initial sample show features common to chromite, Cr-hematite, and Cr-goethite while our SEP's residue displays features (dotted lines in **Figure 3.4g**) analogous only to chromite. Chromium EXAFS fitting of PAL-1 (**Figure 3.4h-i, Table S3.6**) revealed structural incorporation in chromite and Fe (oxyhydr)oxides and resulted in 7.5 neighboring oxygen (O) atoms at 2.00 Å, 4.8 Me_1 at 3.05 Å, 6.0 Me_2 at 3.27 Å, and 7.7 Me_3 at 3.48 Å, where "Me" cations corresponds to Cr and Fe. These cations have close atomic numbers and contribute similarly to the EXAFS signal (Dublet et al., 2012), and therefore cannot be distinguished from each other. The Cr-O distance is consistent with octahedral coordination of Cr(III) in chromite and Fe (oxyhydr)oxides but has a slightly higher coordination number (CN) that could be explained by the relatively high value of the correlated Debye-Waller factor (σ^2) and uncertainty (20-25%) of EXAFS CNs (Penner-Hahn, 2005). The 3.05 Å Cr-Me_1 distance is similar but slightly longer than the second shell

Cr-Cr/Fe distances of chromite and Cr-Fe (oxyhydr)oxides (2.97-2.98 Å). Rather, it is analogous to the average of the second shell distances and the Cr-Fe_{E2} distance of Cr-goethite (3.11 Å). Such strongly overlapping FT peaks often occur in natural heterogenous samples and complicate the EXAFS fitting (Foster et al., 1998). Similarly, the Cr-Me_2 distance is likely the average of the 3.11 Å and the distances of corner-shared Cr-Fe atoms of Cr-goethite and Cr-hematite (3.41-3.44 Å), resulting in a single peak at 3.27 Å. These corner-shared distances of Fe (oxyhydr)oxides and of chromite (Cr-Fe_c = 3.52 Å) could account for the fourth shell of PAL-1 at 3.48 Å. Only the outermost shell of Cr-hematite (~3.7 Å) could not be fitted in PAL-1. This may be due to the heterogeneity of Cr location as observed in previous EXAFS fitting (Marshall et al., 2014) where the outer shells of hematite were removed from the fit of a sample containing both hematite and goethite.

The PAL-1 residues after SEP 2 and 3 were similarly fitted with four shells while the residue after our SEP was best fit with only three shells. Cr-Me_1 distances considerably differ and exhibit a decreasing trend from the initial value: SEP 2 (3.02 Å) > SEP 3 (2.99 Å) > optimized SEP (2.96 Å). This indicates decreasing (down to non-existent) contributions from the Cr-Fe_{E2} shell of Cr-goethite and signifies the dissolution of Cr-bearing Fe (oxyhydr)oxides from the previous extraction steps. The Cr-Me_2 shells of SEP 2 (3.23 Å) and SEP 3 (3.20 Å) residues also show a similar trend while our SEP's residue lack this atomic correlation. Instead, our SEP's residue has a second shell distance of 3.49 Å and an overall fit matching the local bonding environment of Cr in chromite (Peterson et al., 1997; Galivarapu et al., 2016) only (**Table S3.6**). Such findings emphasize 1) the importance of laterite Fe (oxyhydr)oxides as hosts for Cr and 2) previous SEPs only partially dissolve these minerals and underestimate their contributions.

Even in samples with smaller amounts of Fe minerals (PAL-2 and PAL-3), SEP 2 and 3 exhibited limited dissolution of these phases (**Figure 3.4e-f**). On the other hand, our SEP completely dissolved these Fe phases leaving chromite, quartz, and traces of amorphous silicate showing a broad XRD peak at 1.57 Å. SEM-EDS confirms the presence of these Cr-free silicate phases (**Figure S3.11b-c**). With the optimization of Fe phase-bound extraction steps, our SEP significantly raised the recovery of extractable Cr, providing the best estimate of Cr in the Ni laterites. Additionally, it significantly increased the recovery of other equally important metals such as Mn and Ni (**Figure S3.8**).

Further tests on Zambales and Surigao limonites (**Figure S3.9**) revealed that our SEP yielded consistent high total recoveries for extractable and non-residual Cr (38-48%) and Fe (82-89%). In these samples, we highlight the importance of including the phosphate step and optimizing the crystalline Fe phase-bound step, especially because these steps extract the dominant pools for Cr. Adsorbed Cr comprised a maximum of 7% of the total Cr while the crystalline Fe phase-bound fraction comprise the largest non-residual pool for Cr (29-44%) and Fe (82-89%).

3.3.4. Environmental implications

Existing SEPs applied to tropical soils fail to adequately partition Cr from Fe-rich laterites because they do not consider the different species of Cr and its ability to stabilize the crystal structure of Fe (oxyhydr)oxides. By robust calibration with appropriate mineral standards, we optimized and validated a sequential extraction procedure (**Figure 3.3**), that is reproducible, efficient and selective for Cr in such Fe-rich materials. Identifying the binding sites of Cr is crucial for assessing its bioavailability, potential mobility and transport mechanisms from laterites all the way to drinking and groundwaters. Our newly optimized SEP offers an important tool for monitoring and predicting pathways for Cr release that could ensue due to changes in environmental conditions (e.g., pH, redox etc.). Our results also point to possible best practices for managing Cr-rich laterites, where the mobilization of Cr through weathering and mining may be linked to downstream containment and remediation efforts.

Exchangeable Cr targeted by $Ca(NO_3)_2$ represents easily mobilizable Cr in the presence of elevated salt inputs such as in the event of saltwater intrusion (Keon et al., 2001) or irrigation (Pickering, 1986). Adsorbed Cr could be liberated by phosphorus sources such as agricultural drainage (Keon et al., 2001). In a study by Becquer et al. (2003), increased Cr concentrations in soil solutions was correlated to the desorption of Cr(VI) by phosphorus fertilizer inputs. Thus, accounting for adsorbed Cr is vital especially in areas affected by agriculture and rehabilitation in the case of mining areas.

Chromium incorporated in Mn- and Fe-phases are more conservative pools and were only leached by reductive dissolution (NH_2OH-HCl) and protonation (HCl). Thus, potential Cr release may occur under reducing (e.g., by bacterial activity) (Pickering, 1986) and acidic conditions (e.g., by organic acids). For example, common organic acids such as oxalate and citrate has been found to solubilize Cr-bearing goethite (Sun et al., 2023). Reducing and acidic conditions are also used in hydrometallurgical processing of laterites (e.g., reductive bioleaching (Johnson et al., 2021), high pressure acid leaching (Whittington & Muir, 2000)). In such cases, Mn and predominant Fe (oxyhydr)oxides are dissolved to solubilize associated Ni and Co and knowledge of the extractable Cr from these phases is crucial in monitoring downstream processes and developing strategies for the immobilization of the leached Cr. Moreover, we demonstrated that interaction with strong oxidants like NaOCl could potentially release Cr from Cr-bearing Fe (oxyhydr)oxides. NaOCl is extensively used in water treatment and has been found to oxidize Cr(III) to Cr(VI) during chlorination of drinking water (Lindsay et al., 2012). Our results warrant further research to assess the occurrence of Cr during drinking water treatment in lateritic areas. Furthermore, we were able to distinguish the extractable fractions from the residual chromite-bound Cr which represent the weathering resistant and most stable pool for Cr.

Using our optimized SEP, we demonstrated through the example of Philippine Ni laterites, that these Fe-rich materials are significant sources of easily mobilizable and toxic Cr(VI) comprising up to 7% of total Cr. These fractions correspond to 30-1192 mg kg^{-1} Cr(VI) and are comparable to Cr(VI) detected in laterites from New Caledonia (≤358 mg kg^{-1}) (Gunkel-Grillon et al., 2014) and Brazil (≤1,014 mg kg^{-1}) (Garnier et al., 2006). We also highlight the predominant association and structural incorporation of Cr as Cr(III) in Fe (oxyhydr)oxides, suggesting potential release of Cr during hydrometallurgical processing of laterites. The quantification of these important Cr reservoirs is crucial in ensuring the meticulous and sustainable management of laterite mining and processing regions.

3.4. Supporting information

3.4.1. Experimental and analytical methods

Characterization of Ni laterites

All samples were crushed and sieved to <63 μm prior to analyses. The mineralogy of the Ni laterite samples was confirmed through X-ray diffraction (XRD). Powdered samples were loaded inside 0.5-mm ID capillaries, and then analyzed in Debye-Scherrer geometry using a STOE STADI P diffractometer (Ag Kα radiation; λ = 0.5594 Å) equipped with a curved Ge (111) monochromator and two DECTRIS MYTHEN2 R detectors. XRD patterns were recorded over a *Q*-range of 0 to 13.42 $Å^{-1}$, with each sample measurement taking 2 h. Quantitative mineralogical analysis was performed through Rietveld refinement using the GSAS-II software (Toby & Von Dreele, 2013). Infrared (IR) spectroscopy of selected samples was also performed using a ThermoFisher Nicolet iS5 FTIR spectrometer with an iD7 diamond attenuated total reflectance accessory. The IR spectra were collected in the 4000-400 cm^{-1} range after coadding 64 scans collected at a resolution of 4 cm^{-1}. Element concentrations of the Zambales and Surigao Ni laterites were determined by inductively coupled plasma optical emission spectrometry (ICP-OES) using an Agilent 5110 spectrometer, following total digestion after standard Na_2O_2 fusion (Bokhari & Meisel, 2017). In brief, 0.1 g finely ground sample was fused with 0.6 g Na_2O_2 in a vitreous carbon crucible at 480°C. The sinter cake was dissolved in ultrapure water. Undissolved residues were separated by centrifugation, dissolved in HCl and added to the supernatant. Concentrations were determined using standard addition. Blanks were determined on a procedural blank and included in the calibration. The precision of the methodology was determined on CRM OREAS 182, 185 and 190.

Synthesis and preparation of mineral standards

Metal-substituted Fe (oxyhydr)oxides were synthesized at mole fractions [X = Me/(Fe+Me), where Me = Al or Cr] up to 0.20, based on known compositions of Fe (oxyhydr)oxides in Fe-rich soils (Becquer et al., 2001; Fandeur et al., 2009a).

Ferrihydrite. Metal-substituted 2-line ferrihydrites were prepared by dropwise addition (2.9 mL min^{-1}) of 1 M NaOH to 150 mL of mixed solution of 0.17 M $Fe(NO_3)_3 \cdot 9H_2O$ and either 0.03 M $Al(NO_3)_3 \cdot 9H_2O$ or $Cr(NO_3)_3 \cdot 9H_2O$ until pH 7 was reached (Schwertmann & Cornell, 2000). The initial pH of the mixed solutions are very acidic (pH 1.5).

Goethite. Al-goethite was made by quickly adding 100 mL of 0.2 M $Fe(NO_3)_3 \cdot 9H_2O$ to a mixture of 120 mL of 0.06 M aluminate solution and 165 mL of 1 M NaOH. The aluminate solution was prepared by adding 500 mL of 0.1 M $Al(NO_3)_3 \cdot 9H_2O$ and 300 mL of 1 M NaOH. The resulting suspension was aged at 70°C for 14 days (Schwertmann & Cornell, 2000). Cr-goethite was synthesized similar to Al-goethite but with a longer aging time (120 days) and an alkaline Cr solution made by mixing 600 mL of 0.1 M $Cr(NO_3)_3$ solution with 360 mL of 1 M

NaOH. It was prepared by adding 45 mL of 0.2 M $Fe(NO_3)_3 \cdot 9H_2O$ to a mixed solution of 135 mL of the alkaline Cr solution and 64 mL of 1 M NaOH (Schwertmann & Cornell, 2000). Adsorbed ions and amorphous phases were removed from the Cr-goethite precipitates by a 2 h treatment with 3 M H_2SO_4 at 50°C and at a solid:liquid (S:L) ratio of 1:100. The washed precipitate was dried at 50°C for 24 h (Bousserrhine et al., 1999).

Hematite. Al-substituted hematite was prepared by combining 160 mL of 0.1 M $Fe(NO_3)_3 \cdot 9H_2O$ and 40 mL of 0.1 M $Al(NO_3)_3 \cdot 9H_2O$ and adjusting the pH of the mixture (initial: pH 1.8) to 7 by dropwise addition of 1 M NaOH. The precipitate was washed three times and resuspended with Milli-Q water (~18.2 MΩ·cm) at pH 7 adjusted with NaOH. The suspension was stored at 80°C for 65 days (Schwertmann & Cornell, 2000). Cr-hematite was formed by vigorously mixing 3.43 g of $Fe(NO_3)_3 \cdot 9H_2O$ and 0.6 g of $Cr(NO_3)_3 \cdot 9H_2O$ into a 0.01 M HNO_3 solution pre-heated at 98°C (Liu et al., 2019). The slurry was stored for 25 days at 98°C and washed with 0.25 M HCl (1:100) for 2 h to remove adsorbed ions and amorphous materials. The Cr-hematite precipitates were washed with Milli-Q water until a pH >5 was reached and then oven dried at 70°C (Frierdich et al., 2011).

Cr(VI)-adsorbed Fe (oxyhydr)oxides. Cr(VI)-adsorbed ferrihydrite, goethite, and hematite were prepared by reacting 500 mg of the minerals with 100 mg L^{-1} Cr(VI) solution (pH 7) in a 100 mL headspace vial shaken for 24 h at 150 rpm.

All other syntheses were performed in perfluoroalkoxy (PFA) reactors with a magnetic stirrer. After each experiment, the samples were transferred to polypropylene (PP) bottles or centrifuge tubes and washed with Milli-Q water to remove remaining electrolytes through four to eight cycles of centrifugation (10,052*g*, 10 min) until the total dissolved solids (TDS) of the supernatant is constantly low (~5 mg L^{-1}). Unless stated otherwise, all synthetic minerals except for ferrihydrite were dried in a vacuum desiccator. Poorly crystalline minerals such as ferrihydrite were freeze-dried to prevent possible transformation to crystalline Fe (oxyhydr)oxides like goethite and hematite.

The purity of the phases was examined through XRD and IR spectroscopy described above. The reference minerals were also observed under a FEI Quanta 3D FEG scanning electron microscope (SEM) coupled with an energy dispersive spectroscopy (EDS) system. Prior to analysis, the samples were mounted onto a double-sided carbon tape attached to SEM stubs and carbon-coated using a Leica EM ACE600 sputter coater. SEM images were collected at high vacuum mode, 20 kV and 60 pA using a Everhart Thornley secondary electron detector. Elemental composition of the minerals was determined using ICP-OES (Varian 720-ES) after aqua regia digestion. Note that not all added metals were incorporated in the Fe (oxyhydr)oxides during their formation as shown in the differences in intended and final mol. % substitution (**Table S3.1**).

Natural minerals. Magnetite from the mineral collection of the Institute of Applied Geosciences of Karlsruhe Institute of Technology, and chromite sample from the UG2 chromitite layer of the Bushveld Igneous Complex of South Africa were used in this study. Fe sheet-silicates such as nontronite (NAu-2) was procured from the Source Clays Repository of The Clay Minerals Society. The clay sample was fractioned to <2µm through a series of centrifugation adapted from Jackson (1969) and washed with dilute HCl (0.25 M) for 2 h and rinsed seven times with Milli-Q water to remove potential impurities. The serpentine used in this study was obtained from the Berliner Mineralien Zentrum. Mineralogical and geochemical characterization of the samples were conducted using XRD and X-ray fluorescence (XRF), respectively. Fused beads were analyzed with a Malvern Panalytical AXIOS XRF. Reproducibility was determined on three certified reference materials (CRMs) and is within the analytical precision, which is better than 2% for main elements and better than 10% for trace elements.

Figure S3.1, **S3.2**, and **S3.3** show the XRD, IR, and SEM results, respectively, while **Table S3.1** summarizes the details and composition of all the mineral standards used in this study.

Justification for the addition of the phosphate step

Most sequential extraction procedures used to study Cr partitioning in laterites have been originally designed for cationic metal species. However, Cr can exist as oxyanions of Cr(VI) (e.g., $HCrO_4^-$, CrO_4^{2-}), which under the common pH of Fe (oxyhydr)oxide-rich laterites (close to pH 5) (Myagkiy et al., 2017), will be primarily controlled by adsorption/desorption reactions (Rai et al., 1989). Phosphate extractions at pH 5 to 8 (Bartlett, 1991; Keon et al., 2001; Wright et al., 2003; Larios et al., 2012) have been used for single extraction of Cr(VI) (Bartlett, 1991; Fandeur et al., 2009b; Gunkel-Grillon et al., 2014) to desorb Cr(VI) oxyanions by competitive adsorption (Bartlett & Kimble, 1976; Gleyzes et al., 2002; Hass & Fine, 2010). Previous works have shown maximum sorption of chromate onto Fe (oxyhydr)oxides at pH close to 5 (Oze et al., 2004b), leading to chromate re-adsorption when phosphate extraction was done at pH 5 (Fandeur et al., 2009b). X-ray absorption near edge structure (XANES) measurements by Fandeur et al. (2009b) revealed that only 50% of Cr(VI) from a lateritic regolith was recovered using a phosphate solution at pH 5. Hence, we employed an alkaline (pH 8) 0.01 M $NH_4H_2PO_4$ treatment for 16 h (Tokunaga et al., 1991; Drahota et al., 2014). At this pH, adsorption of Cr(VI) onto Fe (oxyhydr)oxides was found to be minimum (Oze et al., 2004b). Additionally, comparative studies on phosphate extractions applied at pH 7 and 8 revealed a higher desorption capacity from the higher pH solution (Wright et al., 2003). Furthermore, phosphate extractions have been employed at concentrations ranging from 0.01 to 0.1 M (Barlett & James, 1996; Wright et al., 2003; Drahota et al., 2014). Here, we used a lower concentration wherein minimum Fe (oxyhydr)oxide alteration is expected and extraction equilibrium has been

achieved at 16 h, as reported in a previous study (Drahota et al., 2014). The addition of the phosphate step can distinguish the easily mobilizable Cr(VI) from the exchangeable Cr which represents weakly-sorbed cations (e.g., Cr(III)) that can be released from mineral surfaces (e.g., clays) through ion-exchange processes.

Single extractions

Extractions were performed at solid-to-liquid (S:L) ratios from 1:5 to 1:100 using a temperature-controlled orbital shaker (250 rpm) or manual shaking when in a boiling water bath. For example, 50 mg of the reference minerals, equivalent to 50% of a single phase in a 100 mg sample was mixed with 2 to 10 mL of the extractants. The resulting solutions were centrifuged at 10,052*g* for 10 min and filtered using 0.2-µm polyvinylidene fluoride (PVDF) syringe filters. For time-sensitive (e.g., 5 min) extractions, vacuum filtration using 0.2-µm polycarbonate membrane filters were directly conducted after extraction. All, except for the HCl extracts, were acidified with HCl (Aristar® VWR) and all samples were stored at 4°C prior to analysis. Elemental concentrations of the solutions were determined via ICP-OES (Varian 720-ES) following the method described by Perez et al. (2019) and detailed below.

Inductively coupled optical emission spectrometry (ICP-OES)

Samples analyzed using the Varian 720-ES ICP-OES system were prepared by gravimetric dilution using 0.3 M HNO_3 containing 1 mg g^{-1} Cs acting as an ionization buffer and an internal standard. Indium (1.33 µg g^{-1}) was used as an internal standard for the sequential extraction supernatants while Sc (1 µg g^{-1}) was used for the aqua regia digested samples and single extraction supernatants. Calibration standards were prepared using multi-element and single element standards (e.g., Merck Certipur®, Sigma Aldrich, etc.) mixed with 1 mg g^{-1} Cs, 0.3 M HNO_3, and appropriate amounts of HCl for sample matrix matching. For each analysis, Ar, Cs, and In or Sc were monitored for instrument stability and drift. Instrumental statistical LoD (3SD above background) or limits of quantification (LoQ = 10SD) were quantified using ≥5 repeat analysis of the sample diluent (0.3 M HNO_3 + 1 mg g^{-1} Cs + 1.33 µg g^{-1} In or 1 µg g^{-1} Sc). Analytical uncertainties of analyte concentrations were determined by ≥5 repeat analysis of a QC solution.

High-energy resolution fluorescence detected X-ray absorption spectroscopy (HERFD-XAS)

Cr K-edge X-ray absorption near edge structure (XANES) and extended X-ray absorption fine structure (EXAFS) spectra were collected on the bending magnet ROBL BM20 beamline of the European Synchrotron Radiation Facility (Grenoble, France) (Scheinost et al., 2021). The storage ring was operated at 6 GeV with a ~200 mA current in 7/8+1 filling mode. The energy of the incoming beam was selected using a double Si(111) crystal monochromator with higher harmonics suppressed by two Si mirrors operating in the total reflection mode while the beam size was 50 × 2000 µm^2. Energy calibration was done using a Cr metal foil, setting the

maximum of the first derivative of the main edge to 5989 eV. Samples and reference compounds were pressed in pellets, placed vertically, rotated 45° to the incident beam and analyzed under ambient conditions. Pressed pellets (7-mm diameter) were prepared by loading ~20 mg of the powder sample in a Specac® mini-pellet press and sealing with a Kapton® polyimide tape. Depending on their stability, the samples were diluted with up to 5 mg of boron nitride (BN), resulting in a mixture of ~20 mg.

Due to the relatively low concentration of Cr, background fluorescence from Fe, and complex matrix of natural samples, the spectra were recorded in HERFD mode. The details about HERFD measurements and advantages for the environmental sciences were discussed previously (Proux et al., 2017). In this study, a Johann-type X-ray emission spectrometer (XES) in a vertical Rowland geometry available at BM20 (Kvashnina & Scheinost, 2016) was equipped with spherically bent crystal analyzers with a 1 m bending radius, and a silicon drift X-ray detector (©Ketek). For our measurements, five Ge(211) crystal analyzers were aligned at the maximum of the Cr $K\alpha_1$ emission line (5414.9 eV) using (422) reflection and the 82.5° Bragg angle. To optimize the XES, the maximum of the corresponding non-resonant emission line of the Cr metal foil was selected. A helium-filled bag was placed to fill the optical path sample-crystal analyzers-detector to minimize the absorption of the fluorescence signal by air. A total experimental energy resolution of ~1.2 eV was estimated using the width of the elastic scatter peak at 5415 eV.

All HERFD-XAS spectra were normalized to the intensity of the incident beam measured using a Canberra photodiode and Kapton foil placed at the incident beam optical path before the sample. Depending on data quality, an average of 3 scans were performed on each sample, with an acquisition time of ~35 min/scan. Spectra were aligned, averaged, and background-subtracted using the ATHENA (Ravel & Newville, 2005) and SIXpack (Webb, 2005) software.

Shell-by-shell fits (**Table S3.6**) were performed from 1.2 to 3.8 Å R+ΔR-space in SIXpack (Webb, 2005) using the algorithms derived from IFEFFIT (Newville, 2001). The fitted Fourier transforms were filtered from the k^3-weighted EXAFS data by a Kaiser-Bessel window. Theoretical phase and amplitude functions for single and multiple scattering paths (Cr-O, Cr-O-O, Cr-Cr, Cr-Fe) were calculated using FEFF6 (Rehr et al., 1992) from the crystal structure of chromite (Lenaz et al., 2009). Similar to previous work (Thomas et al., 2018), the passive electron reduction parameter, S_0^2, was constrained to a value of 0.7. The reference minerals (chromite, Cr-hematite, Cr-goethite) were chosen based on the dominant mineralogy of the limonite sample. The best fits of their EXAFS spectra were obtained by defining shells of neighboring atoms and then iterating the coordination numbers (CN), distances (R), and the mean squared atomic displacement parameter or Debye-Waller factors (σ^2). To reduce the number of degrees of freedom and fit-derived standard errors from highly correlated parameters

(e.g., CN and σ^2), the CN of the references were fixed according to theoretical values. This fitting technique was used by previous studies (Singh et al., 2002b; Toner et al., 2009; Marshall et al., 2014; Bots et al., 2016) and results showed consistent local bonding environment of structurally incorporated elements in chromite (Peterson et al., 1997; Galivarapu et al., 2016), hematite (Marshall et al., 2014; Bots et al., 2016), and goethite (Singh et al., 2002b). Only the outer Cr-Fe shell of chromite was best fitted with a lower CN (i.e. 4) than literature value (i.e. 6) (Galivarapu et al., 2016) probably due to multiple metal-substitution (e.g., Mg, Mn) in the natural specimen. Fitting of the limonite and SEP residues were performed based on their mineralogical data and single scattering paths of the references. Because of the heterogeneity of the samples, the coordination numbers were not constrained. Instead, the σ^2 was set to the value reported for the corresponding reference mineral scattering path to avoid high fit-derived standard errors in these fitting parameters. Fit quality was evaluated based on the R-factor: $R = \sum_i(data_i - fit_i)^2/\sum_i(data_i)^2$, where a value of <0.05 signifies a reasonable fit (Kelly et al., 2008).

Estimation of maximum extractable Cr in limonite

To account for metal-substitution and natural heterogeneity of chromites, we determined the concentration of Cr in the residues through SEM-EDS. We collected single EDS spectrum from representative (i.e. size, morphology) chromite grains (n=15). The statistics of the composition of the grains in the limonite sample, PAL-1, are as follows:

	Concentration (wt.%)						
	Al	Cr	Fe	Mg	Mn	Si	Ti
Minimum	2.2	18.1	5.3	1.0	0.2	0.1	0.0
Maximum	10.5	48.6	16.3	5.4	1.6	15.5	0.8
Median	5.4	27.0	9.1	3.4	0.4	0.4	0.1
Average	5.3	30.0	10.5	3.5	0.6	1.8	0.2

The amount of maximum extractable Cr in the residue (i.e. chromite) was calculated as follows:

$$Maximum\ extractable\ Cr = \left(1 - \frac{C_{SEM}\ x\ Wt_{Res}}{C_{Tot}\ x\ W_{Tot}}\right)\ x\ 100$$

where,
C_{SEM} = median Cr concentration measured using SEM-EDS
Wt_{Res} = weight of residue
C_{Tot} = total Cr concentration of sample
Wt_{Tot} = total weight of sample

It is noteworthy that this quantification approach can only be applied to the limonite samples where the residue is mainly composed of chromite.

3.4.2. Supplementary tables

Table S3.1. Chemical composition of metal-substituted Fe (oxyhydr)oxides. Initial mol % substitution [Al or Cr/(Fe + Al or Cr)] was calculated from the synthesis procedure while the concentration and final mol % substitution were determined through ICP-OES.

Mineral references	Concentration (wt.%)			Initial mol % subs.	Final mol % subs.	Synthesis method
	Al	Cr	Fe			
Synthetic (pure)						
Ferrihydrite	-	-	56.6 (1.2)			(Schwertmann & Cornell, 2000)
Goethite	-	-	62.5 (2.0)			
Hematite	-	-	61.9 (2.0)			(Börsig et al., 2017)
Magnetite	-	-	69.1 (2.2)			(Schwertmann & Cornell, 2000)
Synthetic (substituted)						
Al-Ferrihydrite	4.0 (0.04)	-	51.1 (1.1)	15	14.0 (0.3)	(Schwertmann & Cornell, 2000)
Al-Goethite	2.2 (0.09)	-	55.8 (1.8)	27*	7.6 (0.4)	
Al-Hematite	6.0 (0.06)	-	54.5 (1.2)	20	18.5 (0.4)	
Cr-Ferrihydrite	-	7.9 (0.17)	47.7 (1.0)	15	15.0 (0.5)	(Bousserrhine et al., 1999; Schwertmann & Cornell, 2000)
Cr-Goethite	-	7.3 (0.21)	50.1 (1.6)	27*	13.5 (0.6)	
Cr-Hematite	-	0.63 (0.01)	67.3 (1.4)	15	1.0 (0.03)	(Frierdich et al., 2011; Liu et al., 2019)
Synthetic (adsorbed)						
Cr(VI)-ads. Ferrihydrite	-	1.3 (0.02)	54.0 (0.7)			
Cr(VI)-ads. Goethite	-	0.31 (0.01)	59.5 (0.8)			
Cr(VI)-ads. Hematite	-	0.32 (0.01)	65.1 (0.8)			
Natural						Source
Magnetite	0.09 (0.001)	-	58.5 (1.3)			Institute of Applied Geosciences of Karlsruhe Institute of Technology
Chromite	14.4	33.0	18.4			UG2 chromitite layer, Bushveld Igneous Complex
Nontronite	5.5	0.01	20.9			The Clay Minerals Society
Serpentine	0.7	0.06	1.3			Berliner Mineralien Zentrum

*reported Al/Cr for Fe substitution is <12 mol.% (Schwertmann & Cornell, 2000)
(#) – analytical uncertainty (<5% relative) based on multiple measurements ($n \geq 5$) of QC solutions.

Table S3.2. Reagents and operating conditions of existing SEPs applied to extractable, non-residual fractions. Each SEP is applied to 1 g of sample.

Step	Target Fraction*	Extractant	Conditions
SEP 1 *(Benitez & Dubois, 1999)***			
1	Exchangeable	30 mL 0.1 M $NaNO_3$	1.5 h, 25 °C
2	Carbonate	30 mL 1 M NaOAc (pH 5)	1.5 h, 25 °C
3	Organic matter	30 mL 0.1 M $Na_4P_2O_7$	1.5 h, 25 °C
4	Poorly crystalline Fe (oxyhydr)oxides	30 mL 0.25 M $NH_2OH \cdot HCl$ in 0.05 M HCl	1.5 h, 60 °C
5	Crystalline Fe (oxyhydr)oxides	30 mL 1 M $NH_2OH \cdot HCl$ in 25% CH_3COOH	1.5 h, 90 °C
SEP 2 *(Quantin et al., 2002)*			
1	Exchangeable	10 mL 0.1 M KCl	2 h, 20°C
2	Carbonate	10 mL NaOAc (pH 5)	5 h, 20°C
3	Mn (oxyhydr)oxides	10 mL 0.1 M $NH_2OH \cdot HCl$ (pH 2)	30 min, 20 °C
4	Poorly crystalline Fe (oxyhydr)oxides	10 mL 0.2 M $(NH_4)_2C_2O_4 \cdot H_2O$ + 0.2 M $H_2C_2O_4$ (pH 3)	4 h, 20 °C, dark
5	Crystalline Fe (oxyhydr)oxides	50 mL CB: $Na_3C_6H_5O_7$, $2H_2O$ (78.4 g/L) + $NaHCO_3$ (9.82 g/L); 1 g $Na_2S_2O_4$ (pH 7)	15 min in CB, 30 min after + $Na_2S_2O_4$; 80 °C
6	Organic matter	1) 3 mL 0.2 M HNO_3 - 8 mL 35% H_2O_2 2) 5 mL 3.2 M NH_4OAc (20% v/v HNO_3)	1) 5 h, 85 °C 2) 30 min, 85 °C
SEP 3 *(Silveira et al., 2006)*			
1	Exchangeable	15 mL 0.1 M $CaCl_2$	2 h, room temp
2	Adsorbed	30 mL 1 M NaOAc (pH 5)	5 h, room temp
3	Organic matter	5 mL NaOCl (pH 8.5)	30 min, 90-95 °C
4	Mn (oxyhydr)oxides	30 mL 0.05 M $NH_2OH \cdot HCl$ (pH 2)	30 min, room temp
5	Poorly crystalline Fe (oxyhydr)oxides	30 mL 0.2 M $(NH_4)_2C_2O_4 \cdot H_2O$ + 0.2 M $H_2C_2O_4$ (pH 3)	2 h, dark
6	Crystalline Fe (oxyhydr)oxides	40 mL 6 M HCl	24 h, room temp

*For clarity, names of target fractions were made consistent based on the nature of extractants. Please refer to respective sources for original terminologies.
**Each step except is repeated twice

Table S3.3. Fe and Al dissolution efficiencies of tested single extractions on Cr- and Al-bearing references. ads – adsorbed, FHY – ferrihydrite, Goe – goethite, Hem – hematite, Ox – (oxyhydr)oxides.

Extractant	Cr(VI)-ads FHY	Cr(VI)-ads Goe	Cr(VI)-ads Hem	Cr-FHY	Cr-Goe	Cr-Hem	Chromite
	Adsorbed Cr			Poorly cryst. Fe Ox	Crystalline Fe Ox		Residual
	Fe dissolution efficiency (%)						
0.1 M $Ca(NO_3)_2$	*bdl*	*bdl*	*bdl*	ND	ND	ND	ND
0.01 M $NH_4H_2PO_4$	*bdl*	*bdl*	*bdl*	ND	ND	ND	ND
5% NaOCl (1:5)	ND	ND	ND	*bdl*	*bdl*	*bdl*	*bdl*
5% NaOCl (1:20, 2x)	ND	ND	ND	*bdl*	*bdl*	*bdl*	*bdl*
0.5 M HCl, 4 h	ND	ND	ND	79.8 (1.9)	ND	ND	ND
1 M HCl, 4 h	ND	ND	ND	95.4 (2.2)	ND	ND	ND
1 M HCl, 8 h	ND	ND	ND	97.6 (2.3)	0.22 (0.01)	2.06 (0.05)	*bdl*
6 M HCl, 50°C, 48 h	ND	ND	ND	ND	51.8 (1.9)	98.0 (3.5)	*bdl*
6 M HCl, 75°C, 24 h	ND	ND	ND	ND	100 (4)	102 (4)	*bdl*

Extractant	Al-FHY	Al-Goe	Al-Hem	Al-FHY	Al-Goe	Al-Hem
	Poorly cryst. Fe Ox	Crystalline Fe Ox		Poorly cryst. Fe Ox	Crystalline Fe Ox	
	Fe dissolution efficiency (%)			*Al dissolution efficiency (%)*		
0.5 M HCl, 4 h	95.8 (2.2)	ND	ND	97.1 (1.2)	ND	ND
1 M HCl, 4 h	98.8 (2.3)	ND	ND	100 (1)	ND	ND
1 M HCl, 8 h	99.3 (2.3)	0.05 (2E-3)	5.61 (0.15)	99.5 (1.3)	0.57 (0.02)	9.13 (0.15)
6 M HCl, 50°C, 48 h	ND	103 (4)	103 (4)	ND	104 (5)	103 (5)
6 M HCl, 75°C, 24 h	ND	100 (4)	101 (4)	ND	100 (4)	100 (4)
5% NaOCl (1:5)	*bdl*	*bdl*	*bdl*	*bdl*	*bdl*	*bdl*
5% NaOCl (1:20, 2x)	*bdl*	*bdl*	*bdl*	*bdl*	*bdl*	*bdl*

Dissolution efficiency = (wt.% extracted ⁄ wt.% total) x 100
(#) – analytical uncertainty (<5% relative) based on multiple measurements ($n \geq 5$) of QC solutions
bdl – below detection limit; ND – no data

Table S3.4. A comparison of Fe extracted (%) after HCl extraction without and with prior PO_4 treatment. For the comparison, extractions were performed at the same duration. syn – synthetic, nat – natural.

Reference mineral	HCl extraction	HCl extraction after PO_4 treatment
Ferrihydrite	99 (2)	96 (3)
Goethite	104 (4)	69 (2)
Hematite	105 (5)	102 (4)
Magnetite (syn)	99 (4)	99 (1)
Magnetite (nat)	98 (4)	87 (2)
Chromite	*bdl*	*bdl*

(#) – analytical uncertainty (<5% relative) based on multiple measurements ($n \geq 5$) of QC solutions
bdl – below detection limit

Table S3.5. Chromium recovery from mixture of mineral standards after applying selected SEP steps.

Extractant	Mixture composition	Actual individual mineral wt.% Cr	Expected fraction wt.% Cr	Measured fraction wt.% Cr*
	Mixture 1			
Step 1: 0.1 M $Ca(NO_3)_2$				0.003
Step 2: 0.01 M $NH_4H_2PO_4$	Cr(VI)-ads Goe	0.02	0.03	0.02
	Cr(VI)-ads Hem	0.02		
Step 5: 1 M HCl, 8 h				0.06
Step 6: 6 M HCl, 75C, 24h	Cr-Goe	2.90	3.15	2.90
	Cr-Hem	0.25		
Residual	Chromite	3.34	3.34	3.54
	Mixture 2			
Step 1: 0.1 M $Ca(NO_3)_2$				
Step 2: 0.01 M $NH_4H_2PO_4$				
Step 5: 1 M HCl, 8 h	Cr-FHY	0.80	0.80	0.82
Step 6: 6 M HCl, 75C, 24h	Cr-Goe	2.89	2.93	2.61
	Cr-Hem	0.03		
Residual	Chromite	3.31	3.31	3.61
	Silica glass**			
	Mixture 3			
Step 1: 0.1 M $Ca(NO_3)_2$				
Step 2: 0.01 M $NH_4H_2PO_4$				
Step 5: 1 M HCl, 8 h	Cr-FHY	1.20	1.20	1.08
Step 6: 6 M HCl, 75C, 24h	Cr-Goe	0.74	0.74	0.80
Residual	Chromite	4.92	4.92	4.98
	Silica glass			

*Residual wt.% was represented by the (wt.% total Cr - ∑wt.% non-residual) ⁄ wt.% Cr in chromite
**Silica glass spheres (high purity, Sigma-Aldrich) was added to Mixture 2 and 3 to mimic lower Fe containing samples

Table S3.6. Cr K-edge EXAFS fitting results summarizing the local coordination environment around a central Cr atom for the limonite sample (PAL-1) and residues (after SEP 2, SEP 3 and the optimized SEP in this study), and reference minerals.

Sample	Path	CN	R (Å)	σ^2 (Å^2)	ΔE_0 (eV)	*R*
PAL-1	Cr-O	7.5 (1.6)	2.00 (1)	0.006 (2)	-1.2 ± 2.4	0.0432
	Cr-Cr	4.8 (1.7)	3.05 (2)	*0.006*		
	Cr-Fe	6.0 (3.4)	3.27 (3)	*0.006*		
	Cr-Fe	7.7 (3.8)	3.48 (3)	*0.01*		
After SEP 2	Cr-O	6.7 (1.3)	1.99 (1)	0.005 (2)	-4.3 ± 2.2	0.0222
	Cr-Cr	4.6 (1.3)	3.02 (2)	*0.006*		
	Cr-Fe	3.6 (2.3)	3.23 (3)	*0.006*		
	Cr-Fe	4.7 (2.9)	3.46 (4)	*0.01*		
After SEP 3	Cr-O	6.7 (1.3)	1.98 (1)	0.006 (2)	-6.5 ± 2.4	0.0214
	Cr-Cr	4.4 (1.2)	2.99 (2)	*0.006*		
	Cr-Fe	3.3 (2.1)	3.20 (2)	*0.006*		
	Cr-Fe	4.4 (2.6)	3.43 (3)	*0.01*		
After this study	Cr-O	5.1 (0.8)	1.98 (08)	0.003 (1)	-7.0 ± 1.7	0.0201
	Cr-Cr	3.6 (1.2)	2.96 (1)	0.006 (2)		
	Cr-Fe	2.8 (1.4)	3.49 (4)	*0.01*		
Chromite	Cr-O	5.6 (1.3)	1.99 (1)	0.003 (2)	-6.2 ± 2.3	0.0497
	Cr-Cr_E	*6*	2.98 (2)	0.007 (1)		
	Cr-Fe_C	*4*	3.52 (5)	0.01 (05)		
Cr-Hematite	Cr-O	*6*	1.98 (1)	0.003 (1)	-3.3 ± 2.3	0.0280
	Cr-Fe_{F+E}	*4*	2.97 (2)	0.008 (1)		
	Cr-Fe_{C1}	*3*	3.44 (6)	0.01 (06)		
	Cr-Fe_{C2}	*6*	3.74 (8)	0.02 (1)		
Cr-Goethite	Cr-O	*6*	1.98 (09)	0.005 (05)	-3.6 ± 1.7	0.0204
	Cr-Fe_{E1}	*2*	2.97 (2)	0.006 (4)		
	Cr-Fe_{E2}	*2*	3.11 (3)	*0.006*		
	Cr-Fe_C	*4*	3.41 (6)	0.02 (1)		

Note: CN - coordination number, R - interatomic distance, σ^2 - mean-squared atomic displacement, ΔE_0 - change in threshold energy, and *R* - "goodness of fit" factor. Subscripts refer to: E – edge-shared, F – face-shared, C – corner-shared. Numbers in parenthesis are fit-determined standard errors on the last decimal place except when the error has the same significant figures as the fitted value. Constrained parameters appear in italics.

3.4.3. Supplementary figures

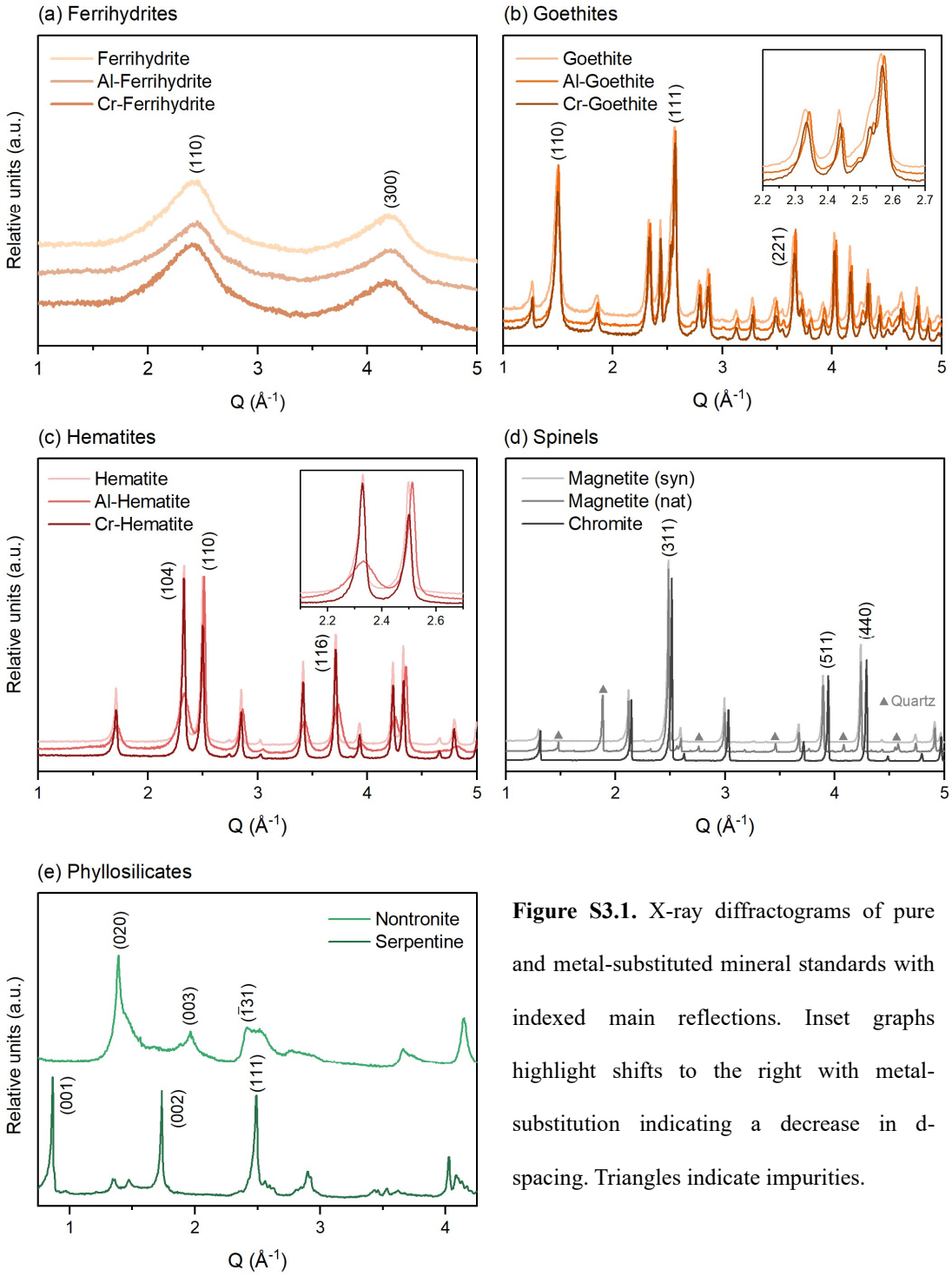

Figure S3.1. X-ray diffractograms of pure and metal-substituted mineral standards with indexed main reflections. Inset graphs highlight shifts to the right with metal-substitution indicating a decrease in d-spacing. Triangles indicate impurities.

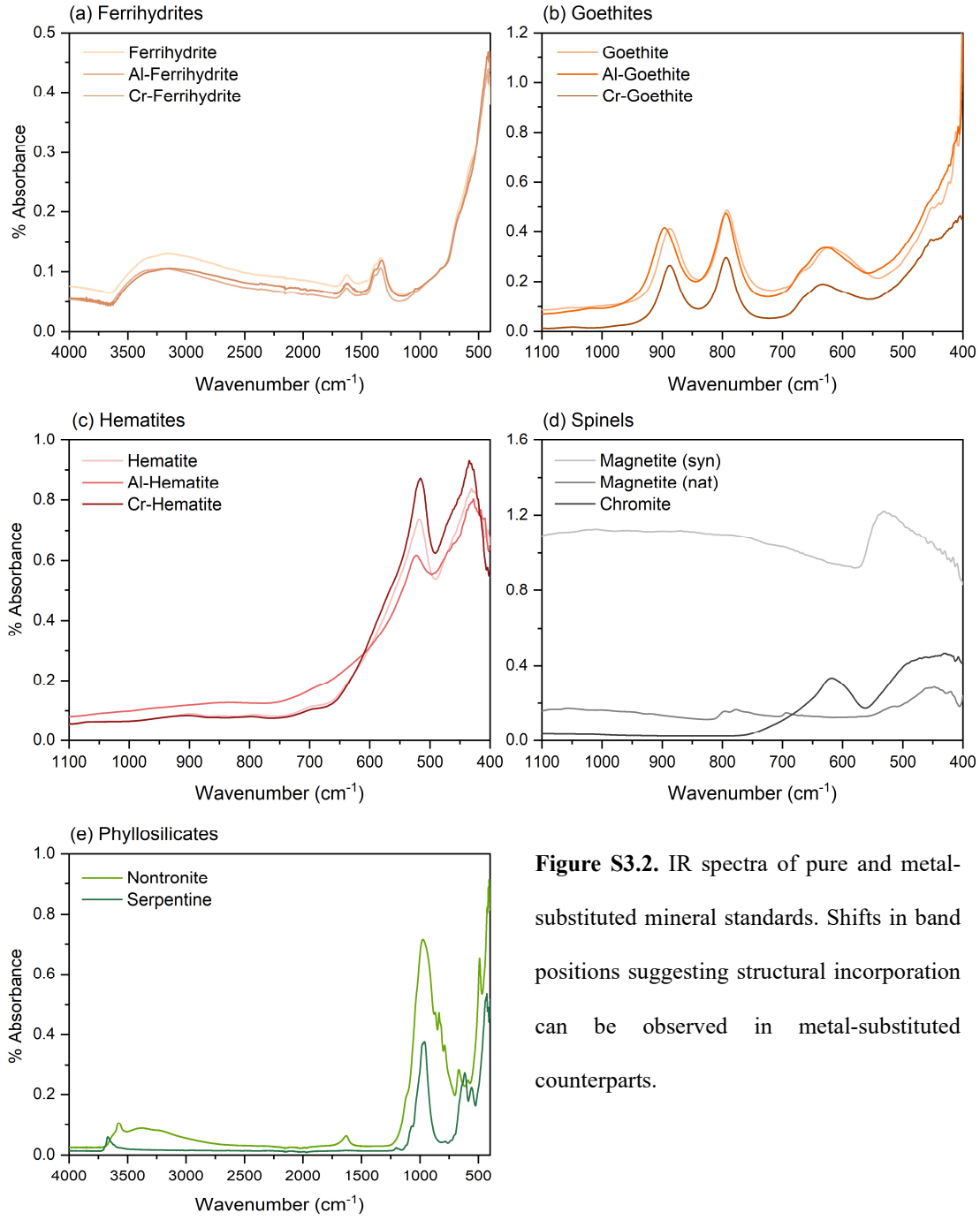

Figure S3.2. IR spectra of pure and metal-substituted mineral standards. Shifts in band positions suggesting structural incorporation can be observed in metal-substituted counterparts.

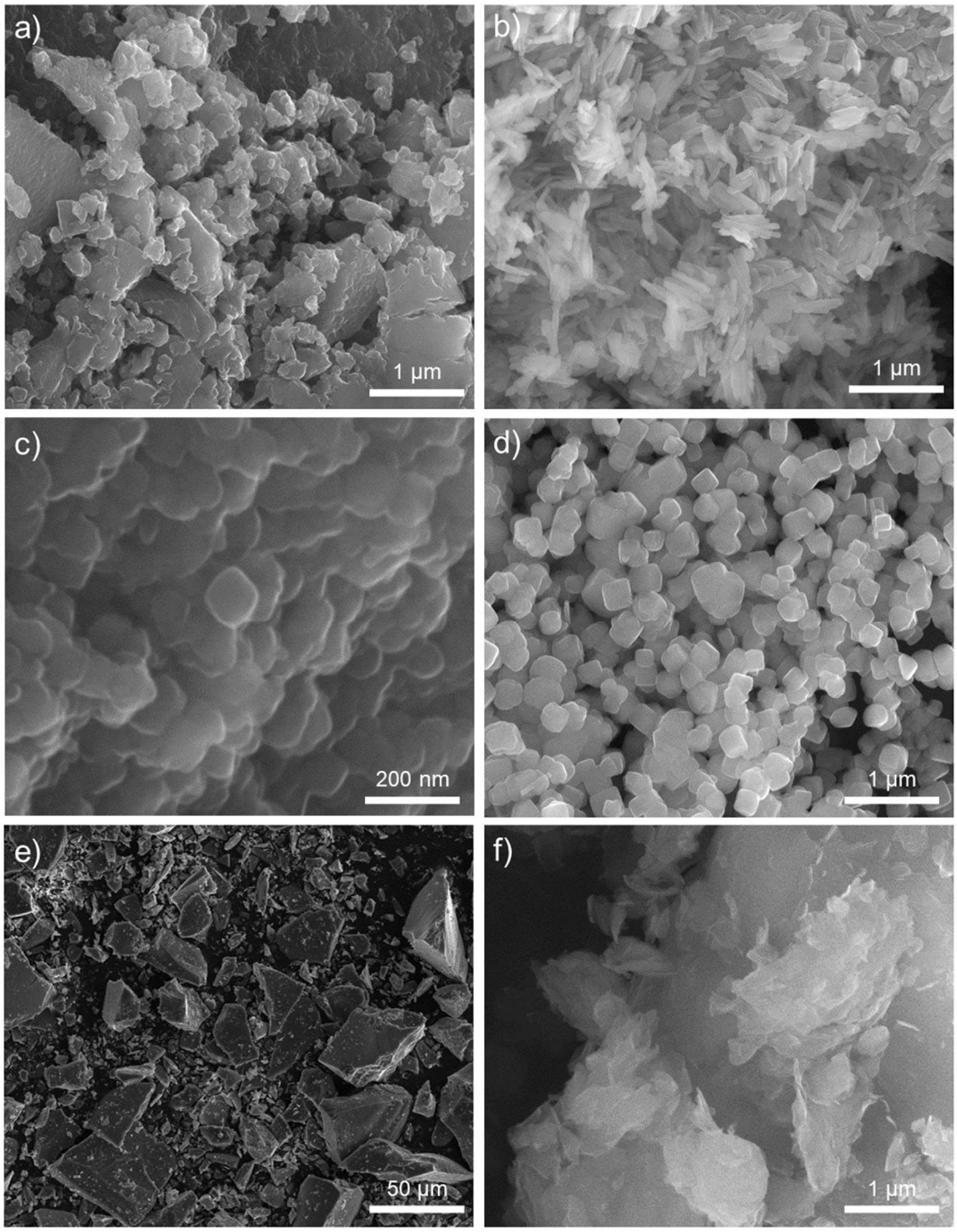

Figure S3.3. SEM images of representative samples: (a) ferrihydrite, (b) acicular goethite, (c) rhombus-like shaped hematite, (d) cubic magnetite, (e) chromite grains, and (f) nontronite clay.

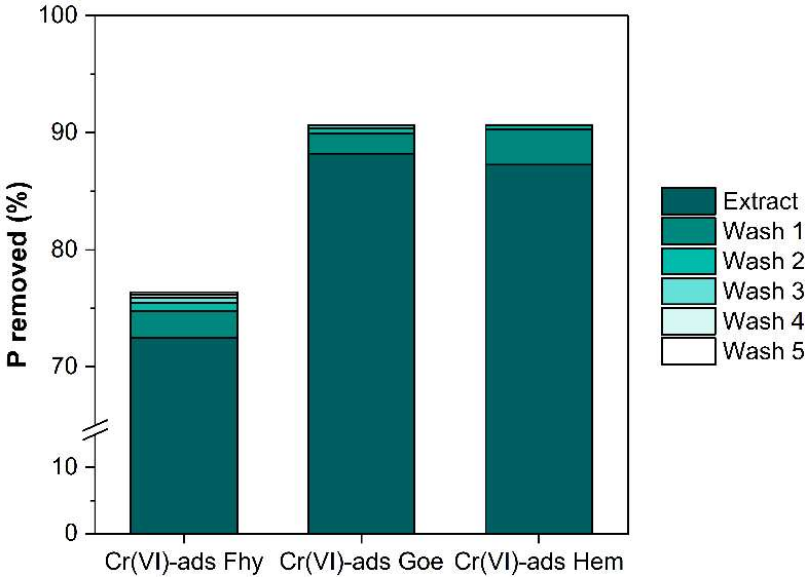

Figure S3.4. Phosphorus removed from Cr(VI)-adsorbed minerals after serial H_2O washing. Fhy – Ferrihydrite, Goe – Goethite, Hem – Hematite.

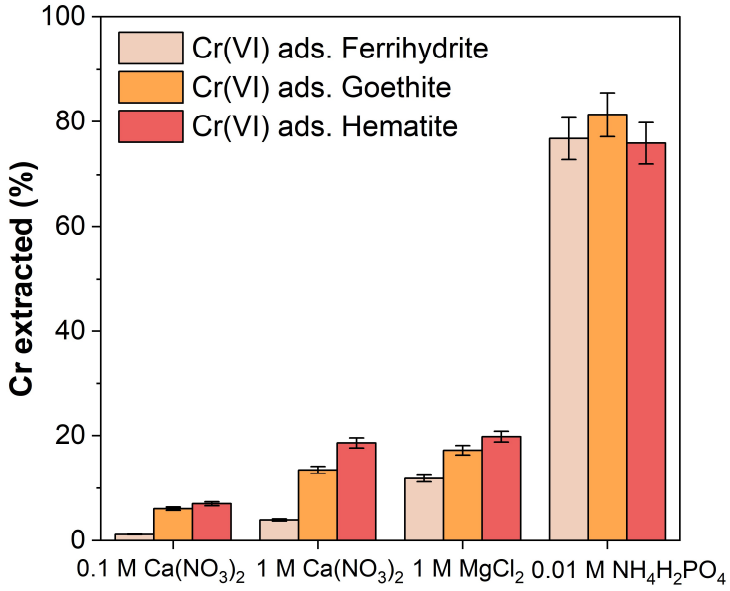

Figure S3.5. Chromium extracted from Cr(VI)-adsorbed Fe (oxyhydr)oxides using different reagents. Error bars indicate analytical uncertainty (<5% relative) based on multiple measurements (n = 5) of QC solutions.

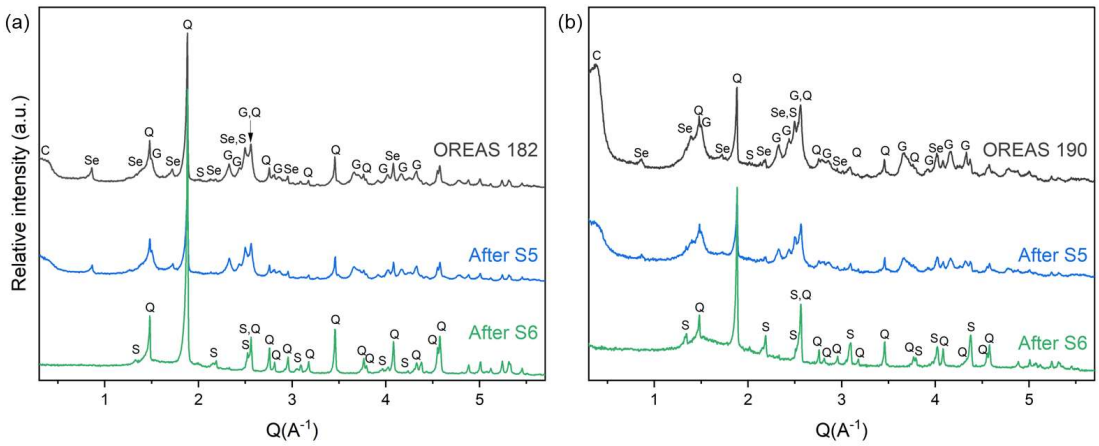

Figure S3.6. Comparison of the residues of the laterite CRMs (a) OREAS 182 and (b) OREAS 190 after Step 5 (poorly crystalline Fe phase-bound) and Step 6 (crystalline Fe phase-bound) of the optimized SEP showing the complete dissolution of goethite (G), serpentine (Se), and clays (C) leaving quartz (Q) and spinels (S) after Step 6.

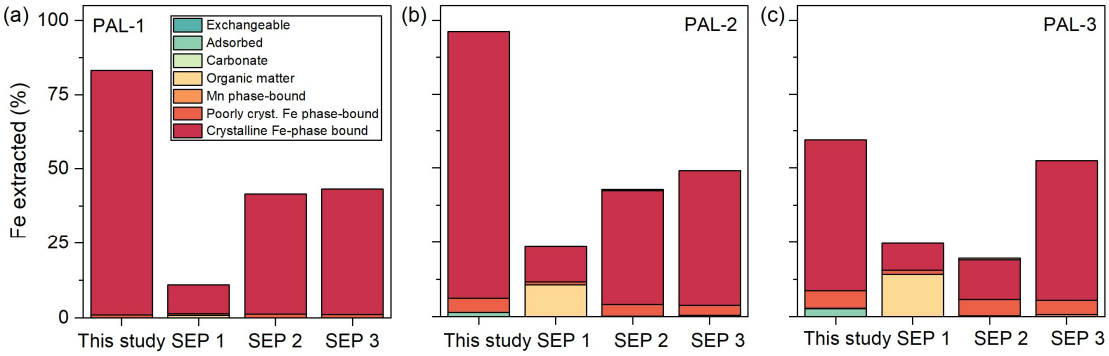

Figure S3.7. Distribution of Fe (% of total concentration) among the different fractions of the Palawan Ni laterites (PAL-1 – limonite, PAL-2 – transition zone, PAL-3 – saprolite) based on the optimized method (This study) and existing sequential extraction procedures (SEP 1 to 3). The remaining proportion of Cr are distributed in the residual fraction.

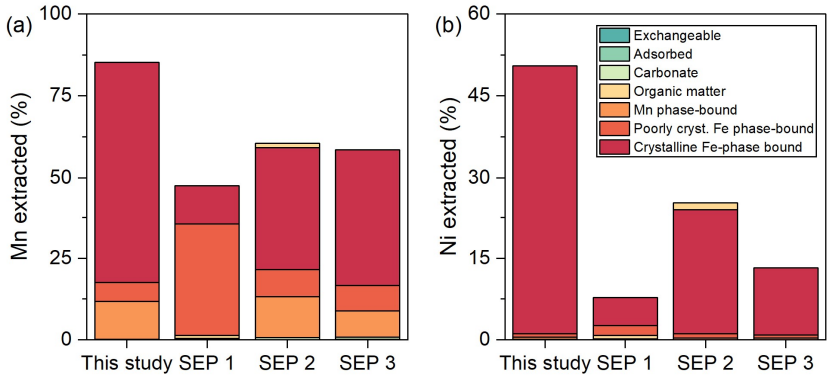

Figure S3.8. Distribution of extractable (a) manganese and (b) nickel in the Palawan limonite sample (PAL-1) based on the optimized SEP (This study) and existing SEPs.

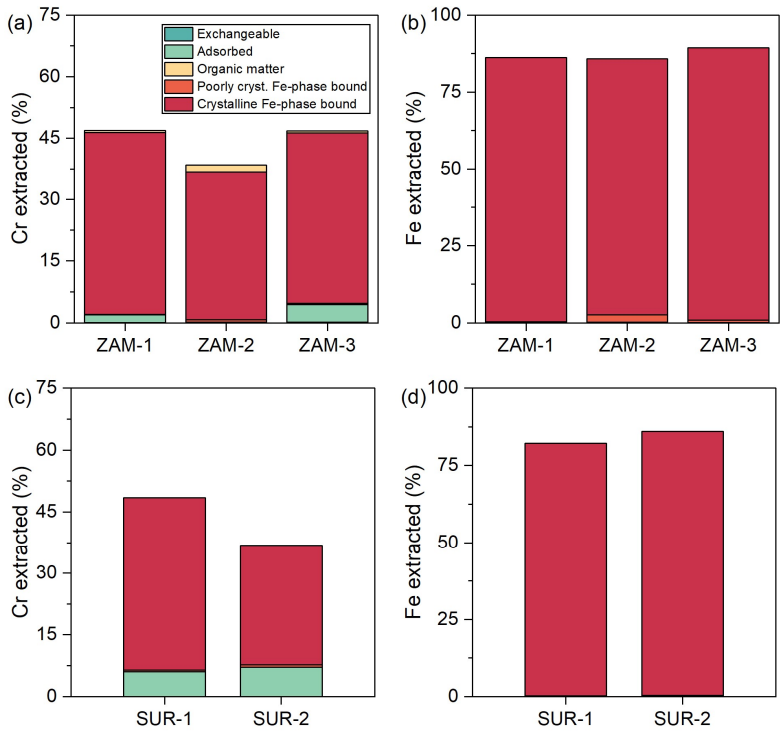

Figure S3.9. Distribution of Cr and Fe in the (a-b) Zambales (ZAM) and (c-d) Surigao (SUR) limonite samples according to the optimized SEP. The SEP was further simplified by not including the carbonate-bound and Mn-bound fractions, found to host negligible amounts of Cr.

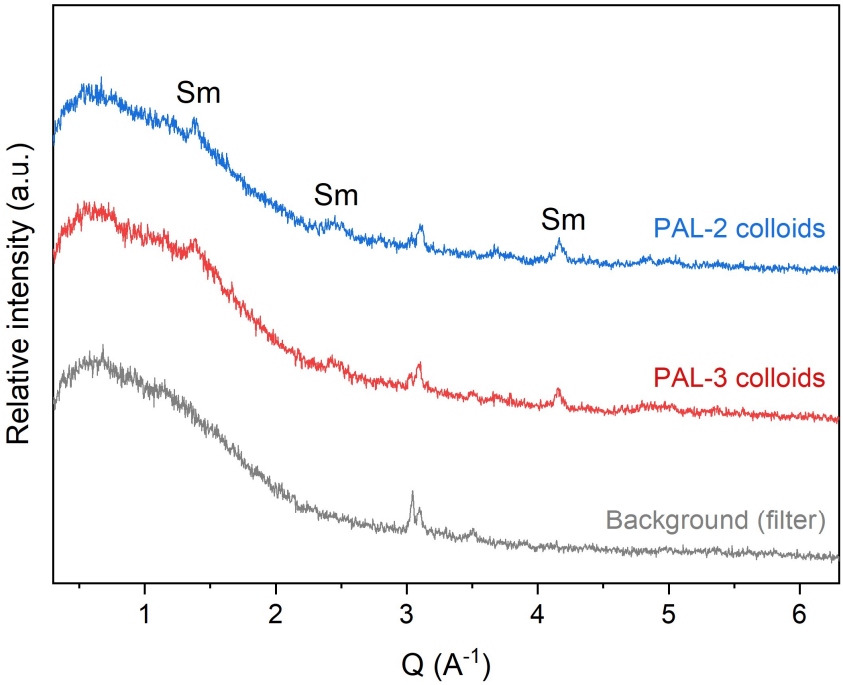

Figure S3.10. XRD patterns of colloids recovered from vacuum filtration of the phosphate extracted solutions. The thin films of colloids were analyzed with the filter (0.2-µm polycarbonate membrane). Compared with the background signal from the filter, the colloids from PAL-2 and PAL-3 showed diffraction peaks from smectite (Sm).

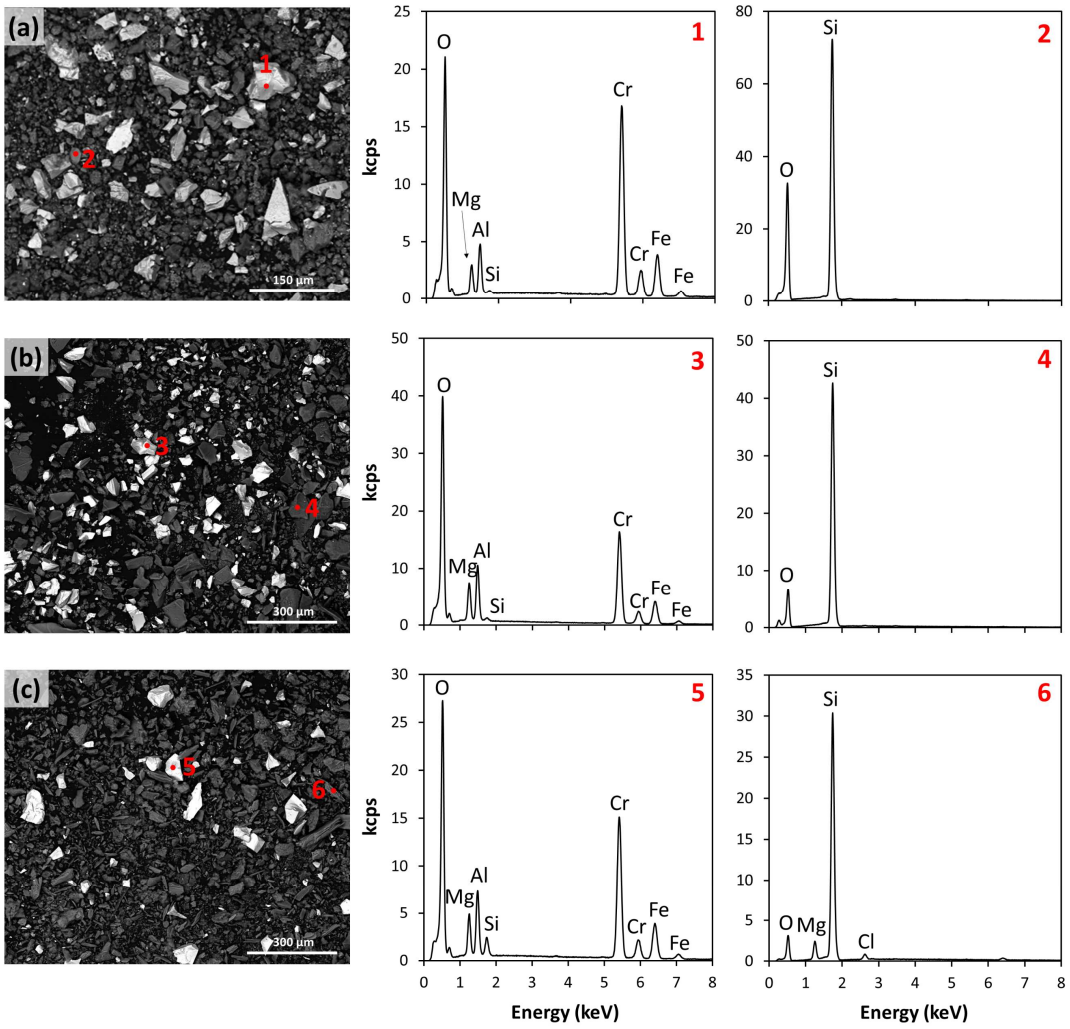

Figure S3.11. SEM-EDS analyses of chromites and silicate phases of (a) PAL-1, (b) PAL-2, and (c) PAL-3 residues after applying the optimized sequential extraction.

Chapter 4

Vertical distribution and speciation of chromium in laterite profiles developed from ultramafic rocks

This chapter is adapted from:

Delina, R.E.G.; Perez, J.P.H.; Bazarkina, E.F.; Prieur, D.; Kvashnina, K.O.; Scheinost, A.C.; Mathon, O.; Stammeier, J.A.; Rabang, D.C.V.; Arcilla, C.A.; Benning, L.G. Coupling of iron and manganese controls chromium speciation in laterites developed from ultramafic rocks. *In the final stages of preparation for submission.*

Abstract

Nickel laterite regoliths developed from the tropical weathering of ultramafic rocks are important sources of critical metals (e.g., Ni, Co, REEs) as well as potentially toxic metals like chromium. Elevated Cr concentrations in natural waters associated with such deposits continue to pose a significant environmental challenge. However, the mechanisms and geochemical factors controlling the fate of Cr in the Ni laterite sources remain unclear but are critically needed for the fundamental understanding of Cr cycling in the environment. In this study, we investigated the vertical changes in the distribution and speciation of Cr along mined and unmined Ni laterite profiles in different localities in the Philippines. By combining high energy resolution fluorescence detection (HERFD) X-ray absorption spectroscopy (XAS) at the Cr and Mn K-edge with classical XAS at the Cr and Fe K-edge and mineralogical and geochemical characterization, we have documented the evolution of Cr with Fe and Mn during laterite formation. Upon weathering, Cr(III) initially repartitions from primary ultramafic minerals to secondary phyllosilicate hosts (e.g., serpentine), followed by association with poorly crystalline Fe precursors that ultimately evolve to structural incorporation into more crystalline phases (e.g., goethite, hematite). We also found that at advanced stages of weathering, Mn(IV/III) oxidizes up to ≤13% of total Cr into its toxic hexavalent form, and then Fe (oxyhydr)oxides sequester a fraction of Cr(VI) through the inner sphere adsorption complexes. These findings underscore the crucial yet contrasting roles of Fe and Mn in controlling the environmental mobility of Cr in lateritic environments, particularly in tropical regions where the weathering rate is accelerated.

4.1. Introduction

Deep weathering of ultramafic rocks under humid climate conditions forms Fe (oxyhydr)oxide-rich laterites that could be exceptionally enriched in critical metals (e.g., Ni, Co, REEs) (Elias, 2002; Butt & Cluzel, 2013; Aiglsperger et al., 2016). Such deposits, known as Ni (±Co) laterites, host the world's largest terrestrial resource of Ni (Butt & Cluzel, 2013; USGS, 2023). Most are found in tropical to subtropical regions and tectonically active plate collision zones (e.g., Indonesia, Philippines, New Caledonia), where ultramafic rocks from ophiolite complexes undergo intense chemical weathering (Elias, 2002). Upon weathering, mobile cations (e.g., Mg and Si) are depleted while less soluble elements like Fe, Al, and Cr are enriched along the laterite weathering profile (Elias, 2002; Gleeson et al., 2003; Golightly et al., 2010). Chromium, for example, can reach concentrations as high as 70,000 mg kg^{-1} (Chrysochoou et al., 2016; Ulrich et al., 2019) compared to the average ultramafic rock composition of 2,980 mg kg^{-1} Cr (Alloway & Ayres, 1997). In ultramafic regions and Ni laterite mining areas, Cr is of environmental concern due to the high mobility, toxicity, and carcinogenic hazard of its hexavalent species. Significant Cr(VI) concentrations up to two magnitudes higher than international drinking water standards (50–100 µg L^{-1}) (USEPA, 2006; WHO, 2017) have already been measured in surface- and groundwaters interacting with Ni laterite deposits all over the world (e.g., Colombia, Greece, New Caledonia, Philippines) (Gleeson et al., 2004; Gunkel-Grillon et al., 2014; Economou-Eliopoulos et al., 2016; Delina et al., 2020). Therefore, the knowledge of Cr redox behavior in laterite profiles is crucial to understanding Cr(VI) genesis and the potential impacts of its release in Ni laterite mining areas.

In primary ultramafic minerals (e.g., silicates, chromite), Cr would exist as Cr(III) (Oze et al., 2004b; Garnier et al., 2008; Garnier et al., 2013), which when compared to Cr(VI), has lower solubility, much lower toxicity, and is considered as an essential nutrient for metabolism (Rai et al., 1989; Anderson, 1997; Shanker & Venkateswarlu, 2011). However, the weathering of ultramafic rocks not only leaches Cr but also forms Mn(IV/III) (oxyhydr)oxides considered as the primary and fastest oxidants of Cr(III) in natural settings (Eary & Rai, 1987; Fandeur et al., 2009b). While laboratory studies have demonstrated the oxidation of Cr(III) to Cr(VI) by Mn(III/IV) (oxyhydr)oxides (Kim et al., 2002; Hausladen & Fendorf, 2017; Pan et al., 2017), there are only a few evidences for this redox dynamics in lateritic regoliths (Fandeur et al., 2009b; Garnier et al., 2013). Chromium has also been found to be strongly associated with Fe in laterites. Several studies have reported that the weathering process repartitions leached Cr to Fe (oxyhydr)oxides (Becquer et al., 2003; Garnier et al., 2006; Fandeur et al., 2009b; Delina et al., 2020) via isomorphic substitution of Cr(III) for Fe(III) and adsorption of different species of Cr at surface sites (Schwertmann & Latham, 1986; Oze et al., 2004a; Fandeur et al., 2009a; Fandeur et al., 2009b). Still, direct mechanistic evidence of the role of Fe (oxyhydr)oxides in

the speciation and sequestration of Cr upon weathering of ultramafic rocks into laterites remains lacking.

In this study, we combined high energy resolution fluorescence detection (HERFD) and classical X-ray absorption spectroscopy (XAS) to investigate the role of Fe and Mn in Cr redox and speciation along a representative laterite profile in the Philippines. Together with mineralogical and geochemical data, our results reveal the contrasting roles of Fe and Mn in the release and sequestration of Cr. Further analyses of Cr redox in other mined and unmined laterite profiles in the Philippines emphasize the importance of in-depth understanding of such mechanisms in evaluating the potential environmental impacts of Cr weathering in tropical ultramafic environments.

4.2. Materials and methods

4.2.1. Sample location

We studied five Ni laterite profiles developed on serpentinized ultramafic rocks along major ophiolite belts traversing Palawan, Zambales, and Surigao del Norte (**Figure 4.1**). Ni laterites from Bataraza, Palawan (PAL, PAL-G05, PAL-U12 profiles) were derived from serpentinized peridotites (e.g., harzburgite, dunite) (De los Santos, 1959; MGB, 2010). The PAL samples, previously characterized in Delina et al. (2020), were collected from an actively mined site, while PAL-G05 and PAL-U12 samples were obtained from drill cores collected by a mining company in currently undisturbed and unmined areas. The mined Ni laterites samples from Sta. Cruz, Zambales (ZAM) were formed from an ultramafic massif made up of lherzolite and harzburgite (Zhou et al., 2000; Aquino et al., 2022), while the last set of samples (SUR) resulted from the weathering of harzburgites in Claver, Surigao del Norte (MGB, 2010; Arcilla et al., 2019). The latter two profiles have been previously investigated in Arcilla et al. (2019), but only focused on general geochemical trends. In addition to differences in parent material and location, the profiles are subjected to different local climate types based on the distribution of rainfall (PAGASA, 2011). Bataraza, Palawan experiences a short dry season (~3 months) with no pronounced maximum rain period, while Sta Cruz, Zambales has an equally distributed dry and wet season. Meanwhile, Claver, Surigao del Norte experiences wet season throughout the year (PAGASA, 2011) and the highest average annual rainfall among the three localities (PAGASA, 2024).

Along each profile, representative samples of the different weathering horizons (Fe (oxyhydr)oxide-dominated limonite, transition zone, silicate-rich saprolite, bedrock) were collected at intervals of ≤3 m.

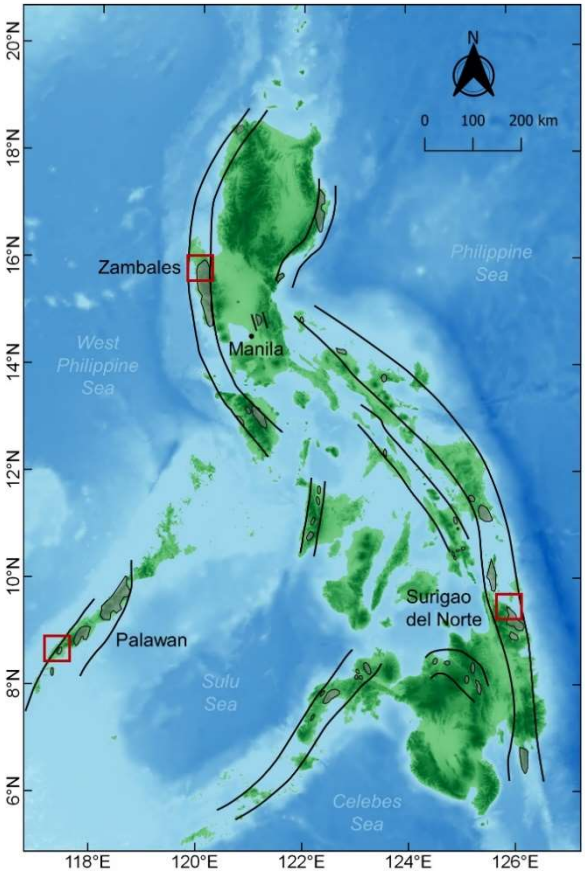

Figure 4.1. Distribution of major ophiolite belts (black parallel lines) and ophiolite/ophiolitic rocks (shaded gray areas) in the Philippines (modified from Andal et al. (2005)) highlighting the location of the Ni laterites in red boxes.

4.2.2. Chemical and mineralogical analyses

For this study, the samples were ground to powder (<63 µm particle size). The mineralogical composition of the Ni laterites was determined with a STOE STADI P diffractometer equipped with a curved Ge (111) monochromator and two DECTRIS MYTHEN2 R detectors. XRD patterns were collected out to 70° 2θ using Ag Kα radiation (λ = 0.5594 Å) to minimize background fluorescence by Fe. Bulk elemental concentrations were determined at the ElMiE labs at the GeoForschungsZentrum, Potsdam. The samples were quantified by Na_2O_2 sintering (Bokhari & Meisel, 2017) and subsequent dissolution in HCl, then analyzed by inductively coupled plasma optical emission spectrometry (ICP-OES) using a 5110 spectrometer (Agilent, Santa Clara, USA). This method was assessed using nickel laterite certified reference materials (OREAS 182, 185, and 190) and was within analytical uncertainty.

4.2.3. X-ray absorption spectroscopy (XAS) data collection

Classical or total fluorescence yield (TFY) Cr-K edge XAS was performed at the Rossendorf beamline (ROBL-II) BM20 of the European Synchrotron Radiation Facility (ESRF) Grenoble, France (Scheinost et al., 2021). The energy of the X-ray beam was tuned with a Si(111) double-

crystal monochromator, and the maximum of the first derivative of a Cr foil was used to calibrate the beam at 5,989 eV. To determine the Cr oxidation state of the samples, Cr K-edge X-ray absorption near edge structure (XANES) spectra were collected in fluorescence mode using an energy-dispersive 18-element Ge detector (Mirion) equipped with a Falcon-X read-out spectrometer (XIA) using energy steps of 0.5 eV. The measurements were performed in a closed-cycle He cryostat (~15K) to minimize beam damage that could alter the speciation of Cr. Samples were homogenized with cellulose in ratios calculated using the XAFSmass software (Klementiev et al., 2016) and prepared as pressed pellets (13-mm diameter).

Cr K-edge extended X-ray absorption fine structure (EXAFS) was measured to determine the local bonding environment around Cr. Given the low concentration of Cr in a complex matrix of the natural samples, the background fluorescence from high concentrations of Fe, and the close K-edge energy positions of Cr and Mn, the spectra were recorded in high-energy resolution fluorescence detection (HERFD) mode (Proux et al., 2017). Here, we used a Johann-type X-ray emission spectrometer in a vertical Rowland geometry equipped with spherically bent crystal analyzers with a 1 m bending radius, and a silicon drift X-ray detector (Ketek) available at BM20. Five Ge(211) crystal analyzers were aligned at the maximum of the Cr $K\alpha_1$ emission line (5,414.9 eV) using (422) reflection and the 82.5° Bragg angle. The EXAFS spectra were collected out to a wave vector value of 11.5 $Å^{-1}$.

Mn K-edge XANES were also collected in HERFD mode, between 6,530-6,660 eV. For HERFD measurements at Mn K-edge (6,539 eV), four Ge(111) crystal analyzers were aligned at the maximum of Mn $K\alpha_1$ emission line (5,900.3 eV) using (333) reflection and the 74.8° Bragg angle. The X-ray emission spectrometer was optimized by selecting the maximum of the corresponding non-resonant emission line of Cr or Mn metal foil. The optical path between the sample, the crystal analyzers, and the detector was contained inside a He-filled bag to minimize the strong absorption of the fluorescence signal by air. A total experimental energy resolution of ~1.2 eV (Cr) and ~1.3 eV (Mn) was estimated using the width of the elastic scatter peak (at 5,900 eV for Mn and 5,415 eV for Cr). The HERFD experiments were conducted under ambient conditions; eventual beam-induced redox reactions could be excluded by averaging fast individual scans and by monitoring an (unchanging) intensity over time (see **Figure S4.1**). All samples were prepared as pressed pellets (7-mm diameter) as pure material or mixed with boron nitride (BN) (up to 25% of the total sample mass), depending on the pellet stability.

Fe K-edge XAS measurements were carried out at BM23 of the ESRF (Mathon et al., 2015). EXAFS spectra were recorded at 15 K in both transmission and fluorescence mode out to a wave vector value of 12.8 $Å^{-1}$. The energy of the X-ray beam was selected with a double-crystal fixed-exit Si(111) monochromator and the fluorescence data were collected using a Vortex silicon drift detector (Hitachi). The incident beam energy was calibrated by measuring an Fe

foil and setting the position of the maximum of the first derivative to 7,112 eV. For the measurements, samples were prepared in a similar manner with the pressed pellets (13-mm) used for Cr XANES.

In all XAS measurements, 2 to 6 scans were collected for each sample depending on data quality. The resulting spectra were aligned, averaged, and background-subtracted using the Athena (Ravel & Newville, 2005) and SIXpack (Webb, 2005) software.

4.2.4. XAS data processing

Cr and Mn K-edge XANES spectra were analyzed with linear combination fitting (LCF) using the Athena (Ravel & Newville, 2005) software and model compounds (described below) as fitting components. In the case of Cr, the pre-edge region (5,986-5,997 eV) providing information about the redox state of Cr, was first extracted from the normalized XANES spectra by baseline subtraction with the XANES dactyloscope software (Klementiev, 2006)

To estimate the contributions of Cr and Fe hosts in each sample, we applied LCF to k^3-weighted EXAFS spectra from k range of 2–10.5 $Å^{-1}$ (Cr) and 2–12 $Å^{-1}$ (Fe) using SIXpack (Webb, 2005). The accuracy of such method has been reported to lie between ±25 and ±5% for each component based on the overall quality of the spectra (Manceau et al., 2000a; Fandeur et al., 2009a). On the basis of the maximum deviation of the sum of all components (see **Table S4.2, S4.3**) from unity, we estimated an accuracy of ±7% and ±5% for the Fe and Cr K-edge EXAFS, respectively. Thus, components that contribute below these were not considered during the LCF procedure.

We obtained Fourier transforms of the k^3-weighted EXAFS spectra of the Cr model compounds after weighting by a Kaiser-Bessel window and performed shell-by-shell fitting in R space range = 1.2 to 3.8 Å using the algorithms derived from IFEFFIT (Newville, 2001). Theoretical EXAFS paths were calculated using FEFF6 (Rehr et al., 1992) based on the crystal structure of chromite (Lenaz et al., 2009) and crocoite (Quareni & De Pieri, 1965). The quality of all fits was evaluated based on the R-factor: $R = \sum_i(data_i - fit_i)^2/\sum_i(data_i)^2$, where a value of <0.05 signifies a reasonable fit (Kelly et al., 2008).

4.2.5. Model compounds for XAS analyses

For our XAS analyses, we prepared a wide range of model compounds from natural to synthetic Cr-, Mn-, and Fe-bearing (oxyhydr)oxides, spinels, and silicates based on the mineralogy of the studied Ni laterite samples. While we have previously confirmed the occurrence of Mn oxides in the Ni laterites through sequential extractions (Delina et al., 2024), these minerals could not be easily distinguished by our XRD analysis because of their minor abundance. Thus, we refer to known occurrences of Mn oxides in other Ni laterites (Domènech et al., 2022). Details on the mineralogy of the standards can be found in **Figure S4.2**. Provided hereafter are the details on the source or synthesis procedures for the mineral references.

Fe (oxyhydr)oxides

Synthetic ferrihydrite, goethite, and hematite, including Cr- and Mn-substituted counterparts prepared using the standard protocols adapted from Schwertmann et al. (2000), were used in this study. We utilized pure and Cr-bearing Fe (oxyhydr)oxides that were previously synthesized and characterized in Delina et al. (2024) and Delina et al. (under review). Mn-substituted ferrihydrite was prepared by slowly adding 1 M NaOH to 150 mL of 0.17 M $Fe(NO_3)_3 \cdot 9H_2O$ and 0.03 M $MnCl_2 \cdot 4H_2O$ mixed solution. After pH 7 had been reached, the precipitate was separated by centrifugation then washed eight times using Milli-Q water (~18.2 MΩ·cm) and freeze-dried. Mn-goethite was made by adding 175 mL of 0.5 M NaOH to a mixture of 45 mL 0.13 M $Fe(NO_3)_3 \cdot 9H_2O$ and 5 mL 0.13 M $MnCl_2 \cdot 4H_2O$. After centrifugation, the precipitate was resuspended in 250 mL 0.3 M NaOH and aged at 60°C for 15 days. To synthesize Mn-hematite, 3.4 g of $Fe(NO_3)_3 \cdot 9H_2O$ and 0.2 g of $MnCl_2 \cdot 4H_2O$ were vigorously mixed into 250 mL 0.01 M HNO_3 pre-heated at 98°C and stored for 15 days at the same temperature (Liu et al., 2019). The Mn-goethite and Mn-hematite precipitates were washed three times with Milli-Q water and freeze-dried.

Mn oxides

Natural Mn oxides, including asbolane, cryptomelane, pyrolusite, and hausmannite, were obtained from the geoscientific collection of the Federal Institute for Geosciences and Natural Resources (BGR) in Berlin, Germany. Research grade Mn_2O_3 was procured commercially from Sigma–Aldrich Co., and birnessite was synthesized as described by Min and Kim (2020). To obtain birnessite, a 100 mL solution containing 3% H_2O_2 and 0.6 M NaOH was added to 50 mL of 0.3 M $MnCl_2$. The mixed solutions were stirred for an hour and aged at room temperature for 24 h.

Silicates, spinels and others

For Fe XAS analysis, we analyzed an iron-rich smectite (i.e., nontronite) (NAu-2) procured from the Source Clays Repository of The Clay Minerals Society and prepared as detailed in Delina et al. (2024). In the case of Cr and Mn XAS, we used a Cr- and Mn-bearing nontronite resulting from the alteration of mafic rocks from Southern Parana Basin, Brazil. We also used natural antigorite and lizardite, two common types of serpentine (i.e., antigorite and lizardite) found in Ni laterites, previously described in Scicchitano et al. (2018) and Siebecker et al. (2017), respectively. Magnetite acquired from the mineral collection of the Institute of Applied Geosciences of Karlsruhe Institute of Technology and a chromite sample from the UG2 chromitite layer of the Bushveld Igneous Complex of South Africa were utilized in this study. For Mn speciation, rhodochrosite was acquired from Kremner Pigments.

4.3. Results

4.3.1. Geochemical trends along the laterite profiles

Based on mineralogy (**Figure 4.2**) and geochemistry (**Table S4.1**), the laterite profiles can be divided into two (profile ZAM and SUR) to three (profile PAL, PAL-G05, and PAL-U12) horizons that may include the bedrock, saprolite, transition zone, and limonite units. The horizons show a dramatic upward increase in Fe concentrations from 7.1-11.9 wt.% Fe_2O_3 in the bottommost bedrock or saprolite to up to 9 times higher concentrations (66-76 wt.% Fe_2O_3) in the most weathered limonite sample of the profiles. From the bedrock to the limonite unit, both Fe_2O_3 and Al_2O_3 were enriched while more soluble oxides (e.g., MgO and SiO_2) were depleted. Therefore, these oxides have been used in chemical weathering indices such as the Ultramafic Index of Alteration (UMIA) and the Index of Lateritization (IOL) plotted in **Figure 4.3** and calculated as follows:

$$UMIA = 100 \times ((Al_2O_3 + Fe_2O_3)/(SiO_2 + MgO + Al_2O_3 + Fe_2O_3) \quad (1)$$

$$IOL = 100 \times ((Al_2O_3 + Fe_2O_3)/(SiO_2 + Al_2O_3 + Fe2O_3)) \quad (2)$$

The UMIA combined with the AF-S-M ternary plot (**Figure 4.3a**) depicts the general weathering trend of the Ni laterites from the ultramafic bedrock. The bedrock and most saprolite samples have low UMIA values (3-17) and plotted near the base of the diagram, confirming that they represent original compositions with little to no weathering. As weathering progresses, an intermediate UMIA value, such as in the transition zone (i.e., value of 34), caused by the progressive mobilization of MgO and SiO_2 through the weathering of Mg-bearing silicates (e.g., olivine, serpentine), and the relative enrichment of Fe_2O_3 and Al_2O_3. In contrast, the highly weathered limonite samples had high UMIA values (>50) and plotted near the apex of Al_2O_3 + Fe_2O_3. The IOL, visualized through an S-A-F ternary diagram (**Figure 4.3b**), classifies the different stages of advanced chemical weathering and shows that most limonite samples were strongly laterized, but the SUR samples had the highest degree of weathering.

The sharp geochemical changes along the profiles were accompanied by a progressive mineralogical transition from a silicate-rich bedrock or saprolite unit to a Fe (oxyhydr)oxide-dominated limonite layer (**Figure 4.2**). The bedrock samples identified at 22 m and 19 m in the PAL-G05 and PAL-U12 profiles, respectively, mainly consisted of primary (e.g., olivine, enstatite) or secondary (e.g., serpentine) silicates. Serpentine minerals dominated all saprolite units, with occurrences of smectite in the PAL and PAL-U12 profiles. Strong XRD peaks from quartz were also found in the saprolite samples of PAL-U12, indicating the presence of local silica veins that have been reported in laterite regoliths (Elias, 2002). At advanced stages of weathering, Fe (oxyhydr)oxides replaced the phyllosilicates, with the transition zone (3.8 m)

from the PAL profile capturing a mixture of these two mineral groups. Goethite was the main Fe phase in all limonite units, occurring with hematite in the PAL and PAL-U12 samples. From the bedrock to the limonite zone, spinels (e.g., chromite) have been consistently detected, suggesting their high resistance to alteration.

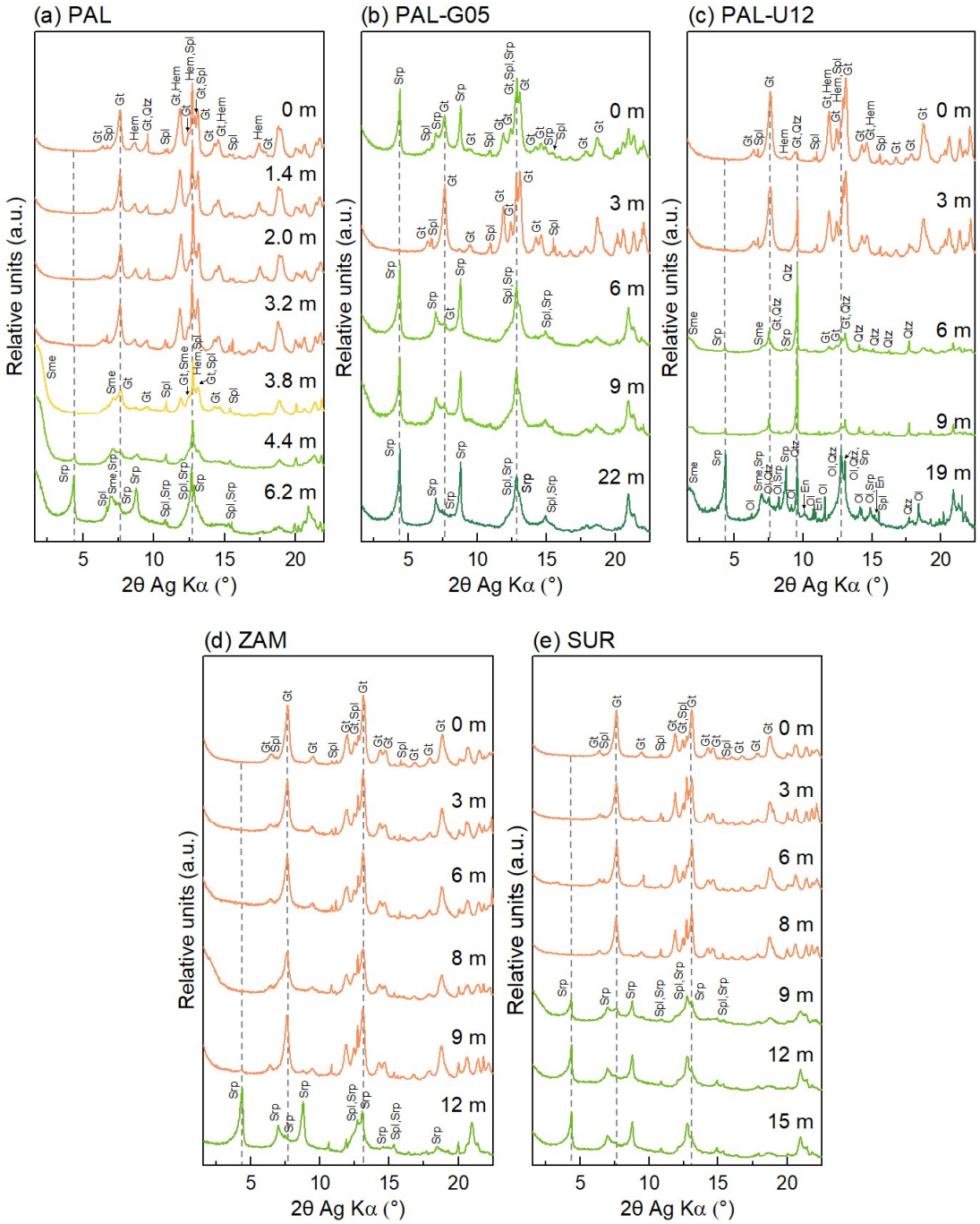

Figure 4.2. Powder X-ray diffraction patterns of samples taken at different depths (m) along the Ni laterite profiles. The color of the patterns refers to the laterite horizon: limonite (orange), transition zone (yellow), saprolite (light green), bedrock (dark green). Minerals identified include goethite (Gt), hematite (Hem), spinel (Spl), quartz (Qtz), smectite (Sme), serpentine (Srp), enstatite (En), olivine (ol).

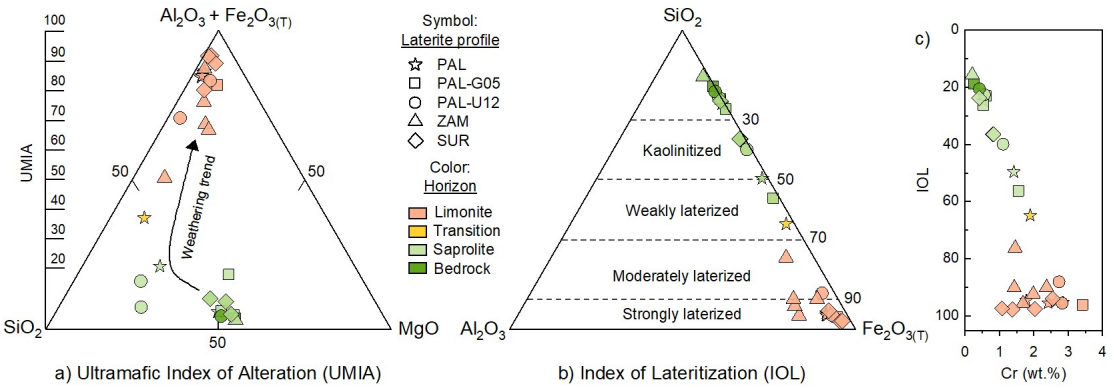

Figure 4.3. (a) Molar ternary plot of Al_2O_3+Fe_2O_3-SiO_2-MgO (AF-S-M) showing the weathering trend from the bedrock to limonite samples according to the ultramafic index of alteration (UMIA). (b) Mass ternary plot of SiO_2-Al_2O_3-Fe_2O_3 (S-A-F) depicting the different stages of chemical weathering based on the index of lateritization (IOL). (c) Plot showing the relationship of IOL and bulk Cr concentrations.

Chromium concentrations (0.2-3.4 wt.%) also showed vertical changes consistent with the division of horizons. The IOL vs. Cr diagram (**Figure 4.3c**) revealed two main clusters: (1) one that includes the bedrock, saprolite, and transition zone samples and has a steep positive correlation; and (2) another that includes only limonite samples, which exhibit a positive, yet narrow correlation. Unraveling the IOL vs. Cr into the individual parameters shows that Fe is the major cause for the observed positive correlation of the saprolite and bedrock samples with an $R^2 = 0.95$ (green samples and trendline in **Figure 4.4**) with a less pronounced correlation of Cr vs. Si ($R^2 = 0.23$) and Cr vs. Al ($R^2 = 0.58$, not shown here). For the limonite samples however, there is no overall correlation with either of these parameters. Instead, the limonite correlates as a response to depth, revealing a slight decrease in Cr concentrations toward the surface while Fe concentration increases. This suggests changes in processes controlling the fate of Cr during advanced stages of weathering. Moreover, it shows that Cr concentrations in the limonite zone are independent of the initial Cr concentration of the source rock.

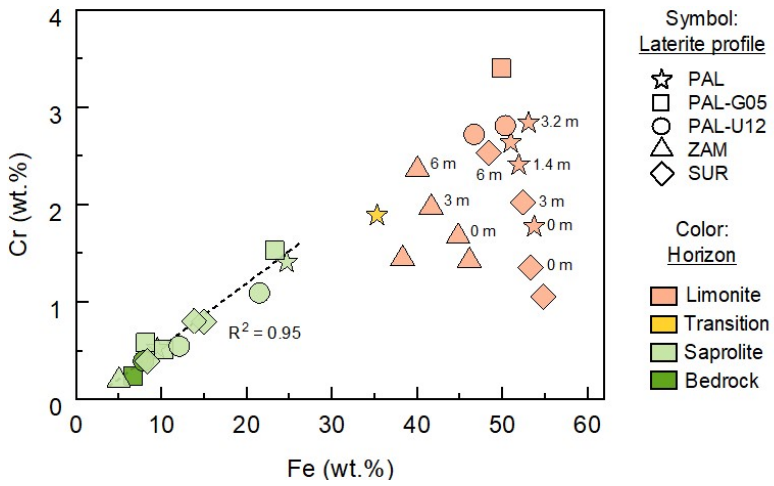

Figure 4.4. Plot of Cr concentrations (wt.%) as a function of Fe (wt.%) along the Ni laterite profiles. Two distinct clusters are observed, with one group including the bedrock and saprolite samples showing a clear linear trend that is represented by a trendline.

4.3.2. Evolution of Fe phases in the PAL profile

Fe K-edge analysis of representative limonite, transition zone, and saprolite samples from the PAL profile provided a better understanding of the mineral transformations during laterite formation. The pre-edge region of the XANES spectra (**Figure 4.5a**) displayed an absorption feature centered around 7,114 eV which is characteristic of Fe(III) (Wilke et al., 2001), suggesting the major occurrence of this Fe species. In contrast with EXAFS (**Figure 4.5b**), no pronounced differences can be observed from the XANES spectra of the laterite samples. Thus, we made use of the more contrasted features found in the k^3-weighted EXAFS spectra and model compounds (**Figure S4.3**) based on the mineralogy of the samples to quantify the mineral speciation of Fe (**Figure 4.5c, Table S4.2**). LCF analysis of the saprolite sample at 4.4 m showed that Fe is strongly associated with phyllosilicates in the form of smectite (54% of total Fe), relative to Fe spinels (i.e., magnetite; 10%) and the Fe (oxyhydr)oxides (36%). Along with goethite, we detected nearly equal proportions of ferrihydrite, a poorly crystalline Fe hydroxide often difficult to quantify with conventional methods (e.g., XRD, electron microscopy) due to its short-range order (Houben & Kaufhold, 2011; Sun et al., 2018). With the increase of these Fe (oxyhydr)oxides and appearance of hematite in the transition zone (3.8 m), we observed a decrease in smectite and disappearance of spinel. With further weathering, phyllosilicates were, as expected, replaced by the Fe (oxyhydr)oxides. The more crystalline Fe phases, goethite, and hematite, dominated at the expense of ferrihydrite and appeared as the dominant Fe pools on the limonite sample.

4.3.3. Vertical changes in speciation and local bonding environment of Cr

Cr speciation in the PAL profile

The Cr K-edge XANES spectra of the laterite samples (**Figure 4.5d**) exhibited a similar shape, with an observable narrowing of the white line on the bottommost samples, implying a vertical change in Cr speciation along laterite depth. LCF analysis of the EXAFS spectra (**Figure 4.5e-f, Table S4.3**) of the least weathered saprolite (6.2 m) indicated that Cr is mainly hosted by primary Cr-spinel or chromite (63%), followed by serpentine (37%). Cr-serpentine disappears along the profile, and the proportion of Cr hosted in chromite decreases as Cr is repartitioned into smectite and Fe (oxyhydr)oxides. This shift in Cr speciation is consistent with our XRD data (**Figure 4.2a**), showing the disappearance of serpentine relative to the smectite, goethite, and hematite. Cr-bearing smectite accounts for 7% and 26% of the total Cr content in the upper saprolite (4.4 m) and transition zone (3.8 m) samples, respectively. In the limonite zone (0-3.2 m), i.e., in the most weathered zone, Cr hosted in Fe (oxyhydr)oxides dominate. At the first occurrence of Fe (oxyhydr)oxides in the saprolite zone (4.4 m), goethite already incorporated a significant portion (42%) of total Cr. Along with Cr-goethite, we detected the association of Cr with ferrihydrite (10%) and hematite (8%) in the transition zone (3.8 m). Cr-

ferrihydrite disappeared after the transition zone, while Cr-hematite (8 to 42%) consistently increased until near the surface (2.0 m). Together, goethite and hematite hosted the major fraction of Cr (78-97%) in the highly weathered limonite zone. Their proportions decreased on the surface where Cr hosted in chromite (27%) was higher compared to the underlying limonite samples (8-12%).

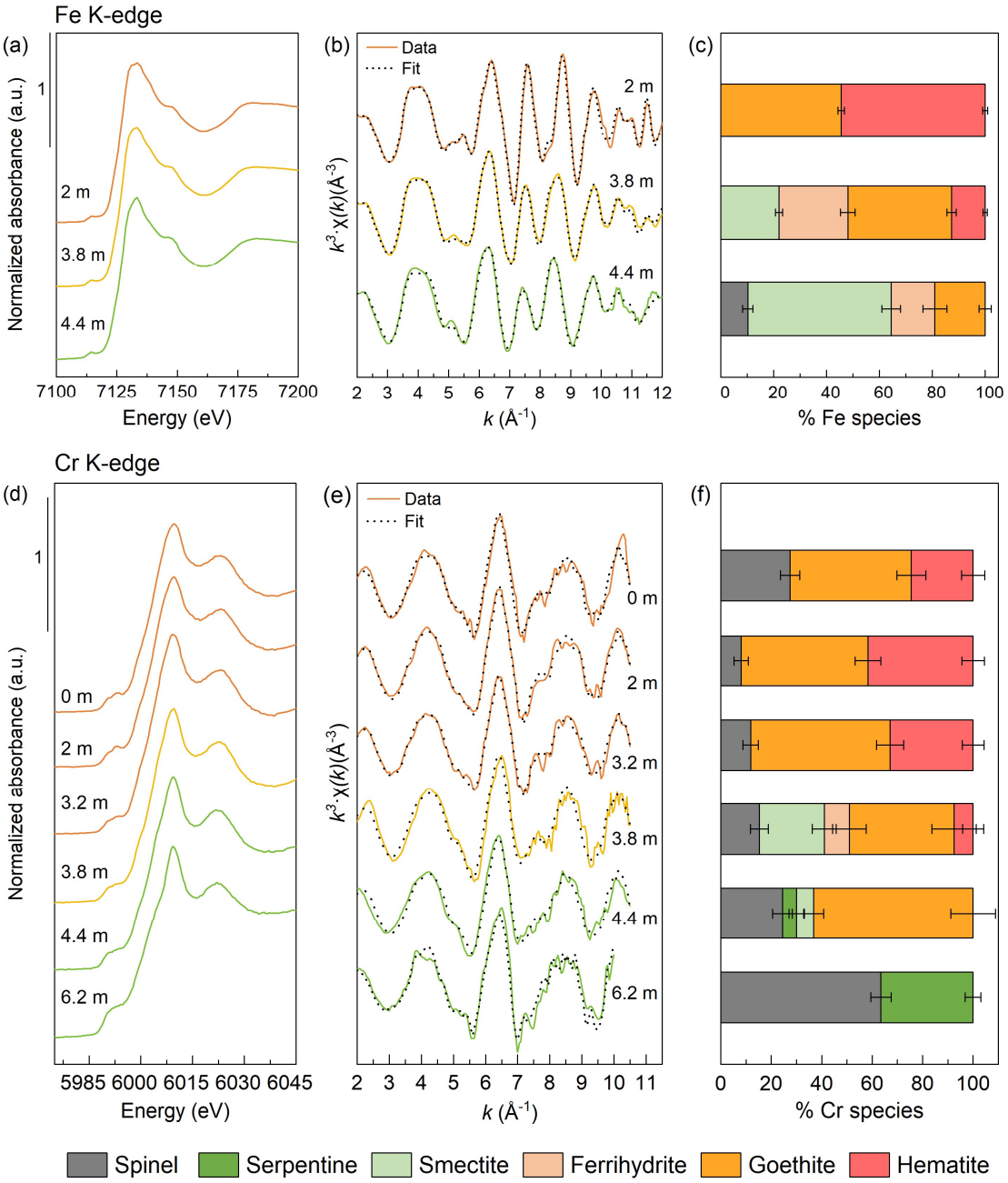

Figure 4.5. (a-b) Fe and (d-e) Cr K-edge XANES and EXAFS spectra of representative PAL samples showing the vertical evolution of Fe phases and Cr partitioning along the laterite profile. (c) The speciation of Fe and (f) Cr was determined by LCF analysis of the EXAFS spectra where the colored solid lines (orange – limonite; yellow – transition zone; light green – saprolite) and black dotted lines correspond to the experimental data and LCF fits, respectively.

Crystal chemistry of Cr in the model compounds

We analyzed the local bonding environment of Cr in the model compounds (**Figure 4.6, Table 4.1**) to gain an in-depth understanding of the changes in Cr speciation along the studied laterite profile. Shell-by-shell fitting of the natural chromite sample yielded second-neighbor atoms of Cr at 2.98 ± 0.01 Å and Fe at 3.49 ± 0.02 Å, respectively, consistent with the edge- and corner-sharing Cr(III)O_6 octahedra of the cubic spinel structure of chromite (Peterson et al., 1997; Galivarapu et al., 2016). The lower number of neighboring Cr (N = 3) and Fe (N = 1) atoms around the central Cr atom compared to the literature value of 6 (Galivarapu et al., 2016) could be explained by the multiple metal-substitution (e.g., Mg, Mn) in the natural sample. It is also important to consider that EXAFS-derived coordination numbers have a high uncertainty (20-25%) (Penner-Hahn, 2005).

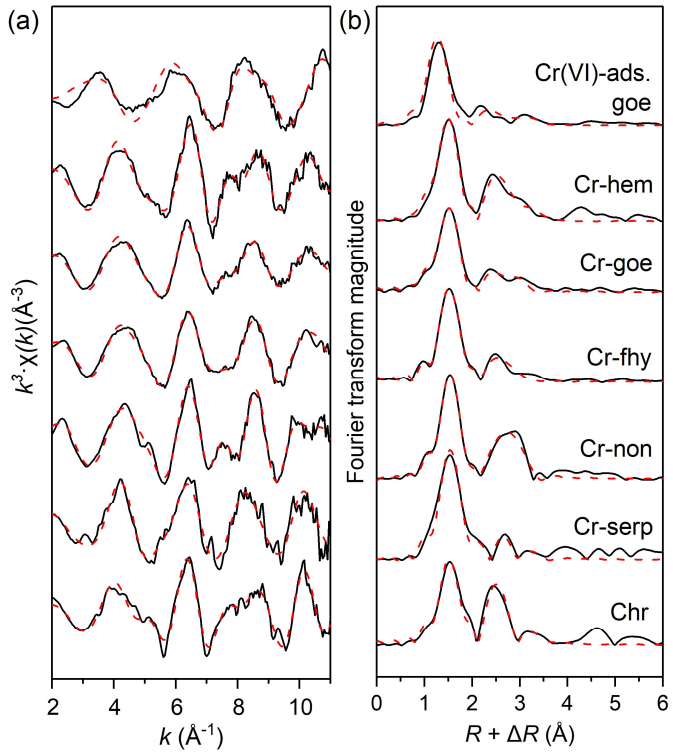

Figure 4.6. (a) Cr K-edge EXAFS and (b) Fourier-transformed EXAFS spectra of Cr mineral references used in the LCF analysis of the experimental EXAFS data of the laterite samples. The black solid lines and red dashed lines correspond to the experimental data and shell-by-shell fits, respectively. Cr(VI)-ads. goe – synthetic Cr(VI)-adsorbed goethite; Cr-hem – synthetic Cr-substituted hematite; Cr-goe – synthetic Cr-substituted goethite; Cr-fhy – synthetic Cr-bearing ferrihydrite; Cr-non – natural Cr-bearing smectite (i.e. nontronite); Cr-serp – natural Cr-bearing serpentine; Chr – natural chromite.

For Cr-serpentine, the distances for atomic pairs of Cr-Mg at 3.20 ± 0.04 Å and Cr-Si at 3.73 ± 0.05 Å suggest the incorporation of Cr(III) in the octahedral sheet of antigorite (Dódony et al., 2002). These distances are higher compared to the Mg (3.00-3.08 Å) and Si (3.28-3.42 Å) neighbors of previously studied metals (e.g., Ni, Mn, Co) in serpentines that are of the lizardite-

type (Dublet et al., 2012; Noël et al., 2015; Dublet et al., 2017). EXAFS fitting of the Cr-bearing smectite shows Cr-O (1.99 ± 0.01 Å) and Cr-Cr (3.07 ± 0.01 Å) distances resembling edge-sharing Cr(III)O_6 octahedra in the γ-CrOOH structure, and a Cr-Si path at 3.64 ± 0.03 Å that is consistent with Cr sorption on silicate minerals (e.g., clays, amorphous silica) (Corker et al., 1991; Fendorf et al., 1994; Peterson et al., 1997). Rather than structural incorporation, these results suggest that Cr associated with our natural smectite sample is adsorbed onto the silica sheet or present within the interlayer space as a Cr hydroxide phase.

Table 4.1. Summary of shell-by-shell fitting results for Cr model compounds.[a]

Sample	Path	*CN*	*R* (Å)	σ^2 (Å^2)	ΔE_0 (eV)	*R*-factor
Chromite	Cr-O	5.2 (0.8)	1.99 (1)	0.002 (1)	-5.9 ± 1.6	0.018
	Cr-Cr	3.4 (0.8)	2.98 (1)	0.003 (1)		
	Cr-Fe	1.3 (0.5)	3.49 (2)	$\sigma^2_{Cr\text{-}Cr}$		
Cr-serpentine	Cr-O	6.7 (0.9)	2.01 (1)	0.002 (1)	-3.1 ± 1.7	0.015
	Cr-Mg	3.1 (2.3)	3.20 (4)	0.008 (7)		
	Cr-Si	3.0 (2.5)	3.73 (5)	$\sigma^2_{Cr\text{-}Mg}$		
Cr-smectite	Cr-O	6.1 (0.7)	1.99 (1)	0.003 (1)	-0.7 ± 1.4	0.019
	Cr-Cr	3.5 (1.3)	3.07 (1)	0.004 (3)		
	Cr-Si	2.5 (1.3)	3.64 (3)	$\sigma^2_{Cr\text{-}Cr}$		
Cr-ferrihydrite[b]	Cr-O	5.1 (0.6)	1.98 (1)	0.002 (1)	-1.0 ± 1.4	0.014
	Cr-Fe	2.8 (1.4)	3.05 (2)	0.009 (4)		
Cr-goethite	Cr-O	6.7 (1.1)	1.98 (01)	0.005 (1)	-3.9 ± 2.0	0.020
	Cr-Fe1	2[a]	2.97 (3)	0.006 (5)		
	Cr-Fe2	$CN_{Cr\text{-}Fe1}$	3.11 (4)	$\sigma^2_{Cr\text{-}Fe1}$		
	Cr-Fe3	2*$CN_{Cr\text{-}Fe1}$	3.41 (7)	0.02 (1)		
Cr-hematite	Cr-O	8.1 (1.2)	1.98 (1)	0.005 (1)	-4.5 ± 1.9	0.015
	Cr-Fe1	4[a]	2.96 (2)	0.008 (1)		
	Cr-Fe2	3[a]	3.43 (4)	0.009 (4)		
	Cr-Fe3	6[a]	3.73 (6)	0.02 (1)		
Cr(VI)-ads. Goethite[b,c]	Cr-O	3.8 (0.6)	1.59 (2)	0.001	-17.6 ± 7.3	0.068
	Cr-O-O	12	1.82($R_{Cr\text{-}O}$)	$\sigma^2_{Cr\text{-}O}$		
	Cr-Fe1 (^2E)	0.9 (0.4)	2.83 (4)	0.003		
	Cr-Fe2 (^1V)	0.8 (0.6)	3.56 (6)	0.003		

[a]CN, coordination number; R, interatomic distance; σ^2, mean-squared atomic displacement; ΔE_0, change in threshold energy; and *R*, "goodness of fit" factor. The passive electron reduction factor (S_0^2) was fixed at 0.7. Numbers in parenthesis are fit-determined standard errors, whereas constrained parameters are without parenthesis. The multiple scattering Cr-O-O path was constrained geometrically to the single scattering Cr-O path ($R_{Cr\text{-}O\text{-}O}$ = 1.82 x $R_{Cr\text{-}O}$). All fits were carried out from 1.2 to 3.8 Å in *R*+Δ*R* space.
[b]F-test done for the Cr-Fe paths are summarized in Table S4.5.
[c]all model compounds were analyzed in HERFD mode under ambient conditions except for Cr(VI)-ads. Goethite. The Cr(VI) reference was measured in classical XAS at 15K to prevent possible reduction of Cr(VI) due to beam damage.

The Cr K-edge EXAFS spectrum of the poorly crystalline Cr-ferrihydrite was best fit with five O neighbors at 1.98 ± 0.01 Å and three second-neighbor Fe atoms at 3.05 ± 0.02 Å. Compared with previous EXAFS fitting of pure ferrihydrite that yielded up to 3 Fe-Fe shells (i.e., edge- and corner-shared FeO_6 octahedra) (Manceau & Drits, 1993; Papassiopi et al., 2014), our F-test for EXAFS results (**Table S4.5**) confirmed that only one Cr-Fe shell corresponding to the edge-sharing octahedra was enough to explain our EXAFS data and additional Cr-Fe shells did not significantly improve the fit of the model. It also contrasts with the results of previous analyses of Cr-Fe hydroxides aged longer (i.e., 3-7 days) (Charlet & Manceau, 1992; Hansel et al., 2003). Instead, it is in agreement with the EXAFS fit of similarly prepared "fresh" Cr-Fe hydroxides in Papassiopi et al. (2014) EXAFS-derived distances of Cr-goethite resulted in two edge-sharing (Cr-Fe)O_6 octahedra at 2.97 ± 0.03 Å and 3.11 ± 0.04 Å, and a corner-shared (Cr-Fe)O_6 octahedra at 3.41 ± 0.07 Å, consistent with Cr(III) substituting for Fe(III) in the goethite structure (Singh et al., 2002a). The EXAFS fit for Cr-hematite matched well with previous EXAFS analysis of cation-substituted (e.g., Al, Mn, Ni) hematites and indicates Cr(III) incorporation in the hematite structure (Singh et al., 2000; Marshall et al., 2014; Bots et al., 2016; Li et al., 2016). The first second-neighbor Fe distance (2.96 ± 0.02 Å) corresponds to face- and edge-sharing (Cr-Fe)O_6 octahedra, while the outer Fe atoms at 3.43 ± 0.04 Å and 3.73 ± 0.06 Å represent the corner-sharing (Cr-Fe)O_6 octahedra.

Additionally, we deduced that the local bonding environment of a Cr(VI)-adsorbed Fe (oxyhydr)oxide corresponded to chromate tetrahedra ($R_{Cr\text{-}O}$ = 1.59 ± 0.02) adsorbed as inner-sphere complexes with mononuclear edge-sharing (^2E) and monodentate mononuclear (^1V) geometries. Adding bidentate binuclear (^2C) geometries to the fit led to a better goodness of fit (*R*-factor) value but did not statistically improve the fit (**Table S4.5**). Therefore, we argue that Cr(VI) adsorbed to goethite is mainly dominated by ^2E and ^1V complexes, and if bidentate binuclear complexes are present, they are of minor quantity (< 5%). Similar observations of the surface structures of Cr(VI) on Fe (oxyhydr)oxides (e.g., goethite, hematite) have been reported in several laboratory studies (Fendorf et al., 1997; Johnston & Chrysochoou, 2014; Li et al., 2022; Li et al., 2023). Despite the minor abundance of Cr(VI) in the PAL profile (discussed further in **Section 4.3.4**) which precluded its detection in the EXAFS analysis, previous studies have suggested the adsorption of Cr(VI) onto Fe (oxyhydr)oxides in laterite regoliths (Fandeur et al., 2009b; Garnier et al., 2013).

4.3.4. Redox behavior of Cr along laterite profiles

To determine the oxidation state of Cr, we took advantage of the significant difference between the pre-edge features of Cr(III) and Cr(VI). The Cr(III)-bearing ferrihydrite standard showed two weak pre-edge peaks at 5,990 and 5,993 eV, characteristic of spin-forbidden transitions in octahedral Cr(III). In contrast, the Cr(VI)-bearing ferrihydrite standard exhibited

a strong pre-edge peak at 5,993 eV, characteristic of tetrahedral Cr(VI) (Peterson et al., 1997). However, compared to Cr(III)-ferrihydrite, both Cr-goethite and Cr-hematite both show a higher second pre-edge peak at 5,993 eV (**Figure S4.4**). This phenomenon has also been noted in previous studies (Fandeur et al., 2009b; Delina et al., under review), but does not indicate the presence of Cr(VI). Rather, it could be attributed to the structural distortion as Cr(III) substitutes for Fe(III) in the Fe (oxyhydr)oxide structure. Thus, in addition to the Cr(III)- and Cr(VI) ferrihydrite, we also add Cr-goethite and Cr-hematite in the LCF analysis.

Cr redox behavior in the PAL profile

The XANES spectra of the PAL samples displayed two pre-edge peaks at 5,990 eV and 5,993 eV, with the latter peak gradually increasing in intensity from the least weathered saprolite (6.2 m) to the limonite sample at 1.4 m (**Figure 4.7a**). Quantifying the proportion of Cr redox species through LCF analysis (**Figure 4.7c**) revealed that Cr dominantly occurs as Cr(III) and that Cr(VI) only occurs in the limonite samples at 1.4 m and 2.0 m where total Cr is relatively enriched (up to 5 times higher) compared to the underlying samples. At 1.4 m and 2.0 m, Cr(VI) comprises 2% of the total Cr concentration, corresponding to 496 and 549 mg kg^{-1}, respectively. These amounts are within the range of Cr(VI) concentrations found in limonite samples from Goiás State, Brazil (up to 1,014 mg kg^{-1}) (Garnier et al., 2006; Raous et al., 2013), and in laterite mining sediments from Poro, New Caledonia (64 to 577 mg kg^{-1}) (Gunkel-Grillon et al., 2014).

Cr redox behavior in other laterite profiles

More intense Cr(VI) peaks at 5,993 eV were found in the limonite samples of the unmined laterite profiles in Palawan (**Figure 4.8a,c**). At the 3 m samples of PAL-G05 and PAL-U12, Cr(VI) comprise 7.7% and 6.4% of total Cr (**Figure 4.8b,d**), respectively, which correspond to up to five times greater concentrations (2635 and 1760 mg kg^{-1}) than those observed in the mined PAL profile. Similar to the mined PAL profile, no Cr(VI) was found in the bedrock, saprolite, and surface limonite sample of the unmined profiles. We also measured significant occurrences of Cr(VI) in limonite samples of mined profiles in Zambales (**Figure 4.8e-f**) and Surigao (**Figure 4.8g-h**). Upper limonite samples from 0 to 6 m of the ZAM profile contained 3.1-5.4% or 610-1,278 mg kg^{-1} Cr(VI). Among all profiles, we detected the highest proportions (up to 13%) of Cr(VI) in the Surigao laterites. Cr(VI) concentrations increase upward within the limonite zone from 128 mg kg^{-1} to 2,713 mg kg^{-1} until it reaches the surface, where the amount decreases by half to 1422 mg kg^{-1}. Overall, we detected Cr(VI) in samples where total Cr and/or Mn concentrations were higher.

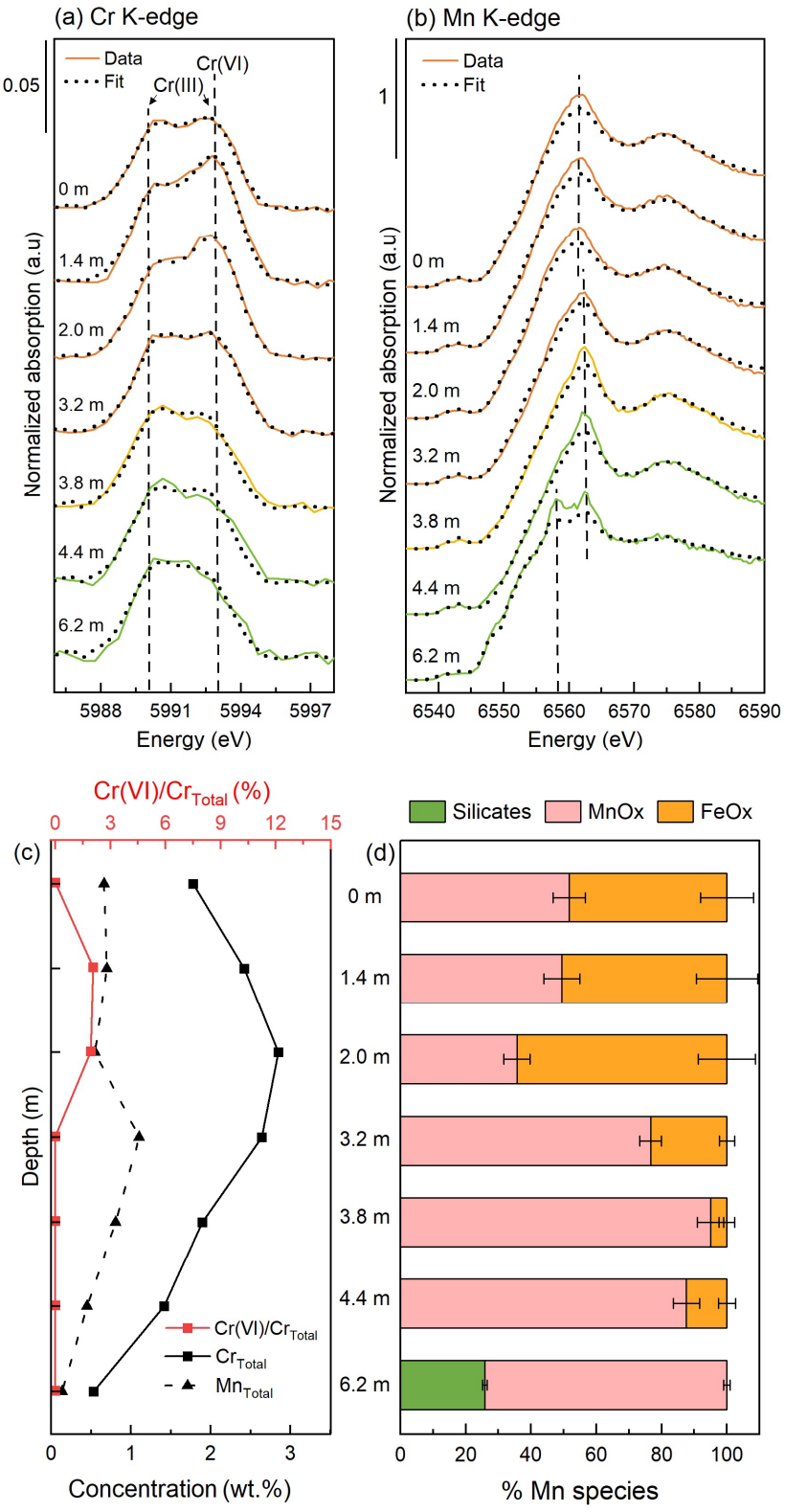

Figure 4.7. (a) Cr K-edge pre-edge region and (b) Mn K-edge XANES spectra of PAL laterites and their (c) LCF-derived Cr(VI) fraction with total Cr and Mn concentrations and (d) Mn speciation, respectively. Colored solid lines (orange – limonite; yellow – transition zone; light green – saprolite) in (a) and (b) and the black dotted lines correspond to the experimental data and LCF fits, respectively. The blacked dashed lines in (a) outline the position of the two weak Cr(III) peaks at 5990 and 5993 eV and the strong absorption peak of Cr(VI) at 5993. Meanwhile, the blacked dashed lines in (b) highlight the maximum absorption peaks of the Mn K-edge XANES experimental data.

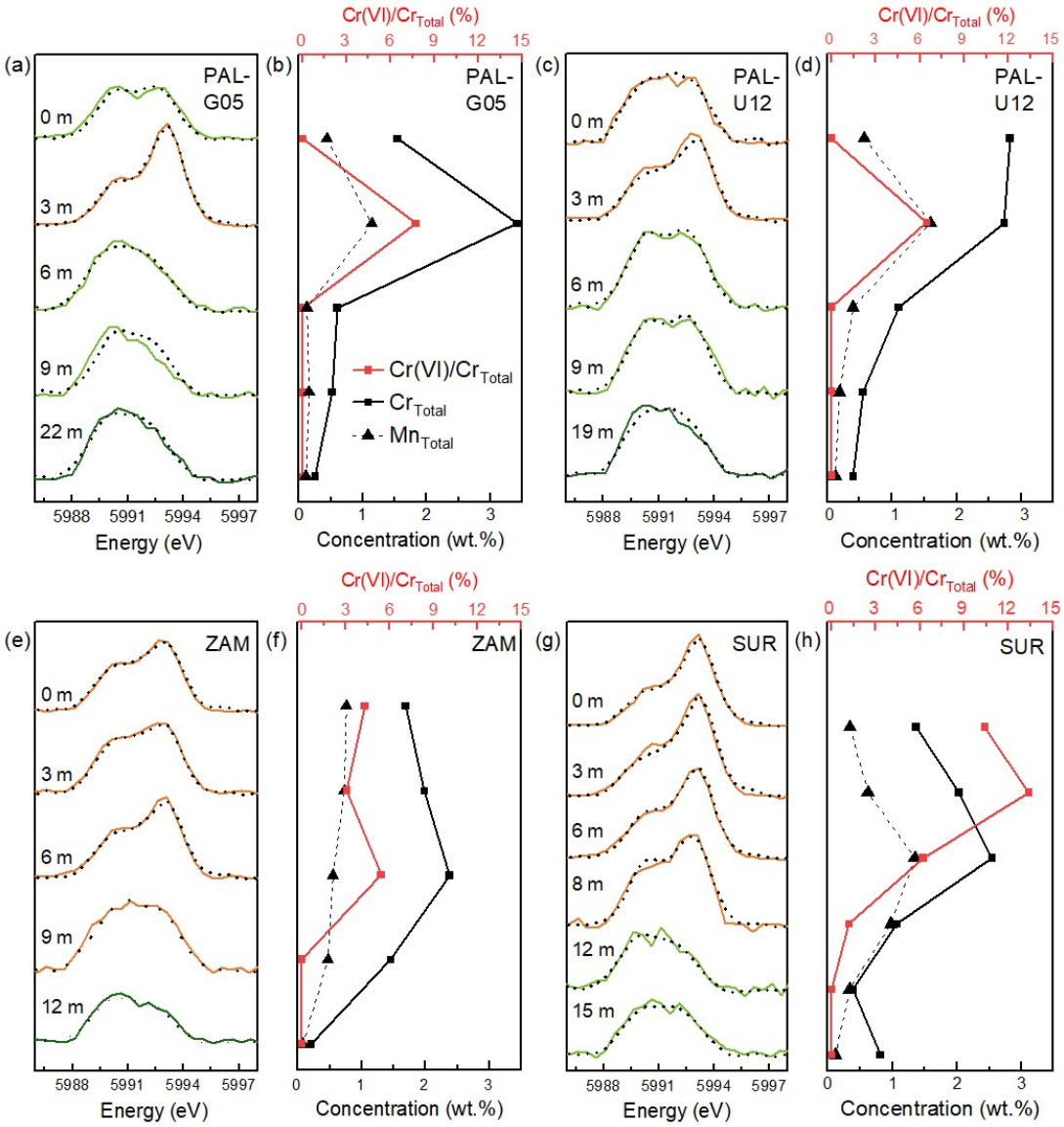

Figure 4.8. Cr K-edge (a, c, e, g) pre-edge regions and (b, d, f, h) corresponding Cr(VI) fractions and total Cr and Mn concentrations of the laterite profiles: PAL-G05, PAL-U12, ZAM, and SUR. The Cr(VI) fractions were determined by LCF analysis of the XANES spectra where the colored solid lines (orange – limonite; yellow – transition zone; light green – saprolite; dark green – bedrock) and black dotted lines correspond to the experimental data and LCF fits, respectively.

4.3.5. Mn speciation in the PAL profile

To elucidate the relationship between Cr and Mn during weathering, we investigated the redox and speciation of Mn in the PAL profile. Manganese-bearing minerals display higher absorption edge energies with increasing oxidation state (**Figure S4.5**). Mn-silicates, serpentine and olivine, display several shoulders and absorption maxima between 6,551 to 6,557 eV, indicating a mixed Mn(II) and Mn(III) content (Dublet et al., 2017). Mn-smectite has an absorption maximum at 6,553 eV close to that of Mn(II)-adsorbed clays in Zahoransky et al. (2023) and Mn(II)-bearing rhodochrosite. On the other hand, Mn-bearing Fe (oxyhydr)oxides

show higher maximum absorption peaks in the range of 6,557-6,561, similar to the Mn(III) standard, Mn_2O_3, and coherent with the substitution of Mn(III) for Fe(III) in the crystal structure of Fe (oxyhydr)oxides (Manceau et al., 2000b; Dublet et al., 2017). Common Mn oxides in Ni laterites (Domènech et al., 2022), asbolane, birnessite, and cryptomelane show white lines at higher energies, around 6,562-6,563 eV, a characteristic feature of mixed Mn(III) and Mn(IV) minerals (Zahoransky et al., 2023). Other Mn oxides, Mn(IV)-bearing pyrolusite and Mn(II)/(III)-bearing hausmannite, exhibit more features but have a maximum absorption peak around 6,560 eV.

Comparison of the Mn K-edge XANES spectra of the mined Palawan samples (**Figure 4.7b**) shows two shifts in absorption maxima along the laterite profile. The least weathered saprolite at 6.2 m displays a shoulder at 6,553 and two maxima at 6,558 and 6,562 eV, suggesting a mixed oxidation state from Mn(III) to Mn(IV). LCF analysis (**Figure 4.7d**) indicated that the lower oxidation states are accounted for by Mn-serpentine comprising 26% of the total Mn species, while the remainder is hosted by the higher redox Mn oxide, asbolane. The overlying saprolite to upper limonite samples (3.2 to 4.4 m) differ from the bottommost sample by having a single absorption maximum at 6,562 eV. This complete shift to a higher Mn oxidation state is explained by the disappearance of Mn-serpentine and the subsequent dominance of asbolane (77-95%) co-occurring with Mn-bearing Fe (oxyhydr)oxides (i.e., goethite and ferrihydrite). After further weathering, we observe a slight shift to a lower oxidation state in the limonite samples from 2.0 m to the surface, resulting from the increase in Mn-bearing Fe (oxyhydr)oxides at the expense of asbolane. In these samples, Mn-bearing Fe (oxyhydr)oxides host half to up to 64% of the total Mn pool.

4.4. Discussion

4.4.1. Weathering and evolution of Cr with Fe during laterite formation

The investigated laterites show that tropical weathering of ultramafic rocks lead to the dissolution of primary silicates (e.g., olivine, enstatite) (**Figure 4.2**) and thus leaching of Si and Mg cations, while Fe and Cr are enriched in the residuum (**Table S4.1**). These trends are reflected by the clear progression in weathering indices (i.e. UMIA and IOL) from bedrock to limonite (**Figure 4.3**) and the strong correlation of Fe and Cr contents (**Figure 4.4**).

Our XAS analysis (**Figure 4.5d-f**) revealed that in the early stages of weathering reflected in the saprolite unit, Cr occurs as Cr(III) mainly hosted in primary chromite. Serpentine minerals coexisting with chromite in the saprolite unit also hosted a fraction of Cr(III) likely mainly released from primary silicate minerals. Cr EXAFS fitting (**Table 4.1**) demonstrated that Cr(III) substituted for Mg(II) in the octahedral sheets of the phyllosilicate. Indeed, the difference in ionic radius of Cr(III) (0.615 Å) and Mg(II) (0.72 Å) is less than 15%, which

suggests that Cr(III) can substitute for Mg(II) during the formation of serpentine. Our findings are consistent with laboratory studies reporting Cr(III) substitution for Mg(II) in silicates (Tang et al., 2019) and the occurrence of natural Cr-bearing serpentines (Gleeson et al., 2004; Fandeur et al., 2009a; Villanova-de-Benavent et al., 2017).

Upon further weathering, Cr-bearing serpentine minerals get dissolved, and the more resistant chromite becomes a minor host for Cr as Cr(III) is repartitioned into Fe-bearing minerals that increase in abundance upward the laterite profile (**Figure 4.5f**). The fraction of Fe that interacts with Si and Al to form clays like smectite provided sorption sites for the leached Cr(III) (**Table 4.1**). Previous studies have found that maximum sorption of Cr(III) onto silicates occurs at pH 6-6.5 (Fendorf et al., 1994; Hao et al., 2022). This explains the higher fraction of Cr-adsorbed smectite observed in the transition zone which is known to have pH values closer to 6-6.5 relative to the underlying saprolite unit which would have a more alkaline pH (Myagkiy et al., 2017).

Cr(III) and Fe(III) have close octahedral radii (0.615 Å and 0.645 Å, respectively). Therefore, during the formation of Fe (oxyhydr)oxides at the expense of the phyllosilicates, the leached Cr(III) can isomorphically substitute for Fe(III) in the crystal structure. In this study, we elucidated the fate of Cr from the formation of poorly crystalline Fe (oxyhydr)oxides that serve as precursor to more thermodynamically stable crystalline phases, such as goethite and hematite (Elias, 2002; Cornell & Schwertmann, 2003; Cudennec & Lecerf, 2006; Myagkiy et al., 2017). At the Fe K-edge, there was a clear progression from poorly crystalline ferrihydrite to goethite to hematite upward the profile (**Figure 4.5c**). However, at the Cr K-edge, we only observed the presence of Cr-bearing ferrihydrite in the transition zone. This contrasts with previous sequential extraction studies of the same laterites (Delina et al., 2020) showing the association of Cr with poorly crystalline Fe (oxyhydr)oxides decreasing from the saprolite to the limonite zone. This could be explained by the "fresh" nature of our model compound versus the "aged" Cr-ferrihydrites likely present in the highly weathered laterites. When compared with Cr-ferrihydrites aged in suspension for a week, our sample synthesized without aging lack contributions from corner-sharing Cr-Fe bonds at ~3.4 Å (Charlet & Manceau, 1992; Hansel et al., 2003), and have edge-sharing Cr-Fe as the dominant linkage mechanism. According to Papassiopi et al. (2014), this phenomenon suggests that during the formation of ferrihydrite, Cr initially adsorbs or forms surface precipitates onto ferrihydrite and with aging becomes incorporated in the crystal structure. However, a recent study on phosphate interaction with ferrihydrite (Chen et al., 2024) attributed the lack of corner-sharing octahedra to the impediment of the Fe(III) polymerization by the foreign compound. Cations like Cr as well as silica has also been found to hinder the crystallization of ferrihydrite (Cornell et al., 1987; Giovanoli & Cornell, 1992; Cornell & Schwertmann, 2003), and dissolved silica from the active weathering of silicates in the transition zone (Dublet et al., 2015) could contribute to the presence of our

"fresh" Cr-ferrihydrite. Detecting "fresh" Cr-ferrihydrite in the studied laterites enabled us to capture the potential initial sequestration mechanism of Cr through attachment of Cr(III) during polymerization of Fe(III) forming the Fe (oxyhydr)oxide precursor.

Cycles of dissolution/reprecipitation and dehydration during lateritization have been known to transform ferrihydrite to goethite, and goethite to hematite, respectively (Elias, 2002; Cudennec & Lecerf, 2006; Myagkiy et al., 2017). Goethite and hematite, which host majority of Cr from the upper saprolite to the limonite zone, represent an important retention mechanism for Cr released from primary ultramafic minerals as well as secondary Cr-bearing phyllosilicates. These findings provide a direct evidence for previous studies of laterites reporting significant association of Cr (up to 85% of total concentration) Fe (oxyhydr)oxides (Quantin et al., 2002; Garnier et al., 2006). They are also consistent with synchrotron-based speciation of Cr in lateritic soils of New Caledonia showing 22-64% and 10-12% of total Cr hosted in goethite and hematite, respectively (Fandeur et al., 2009a; Garnier et al., 2013). More importantly, our Cr EXAFS point to the structural incorporation of Cr(III) in the goethite and hematite structure via Fe(III) substitution as the main mechanism that limits the mobility of Cr during weathering. Laboratory experiments have demonstrated Cr substitution in goethite for up to 14 mol.% (Singh et al., 2002a; Kaur et al., 2009; Delina et al., 2024) and up to 5 mol.% in hematite (Scullett-Dean et al., 2023; Delina et al., 2024). While the transformation goethite to hematite in laterite profiles have been reported to release cations like Ni (Elias, 2002), this has not been observed in Cr. Instead, Cr-hematite increases from the transition zone to the limonite sample at 2.0 m suggesting full incorporation of Cr into the structure of hematite.

As Fe (oxyhydr)oxides dominate and sequester Cr with weathering, Cr in chromite appears to be a minor molecular environment for Cr. However, the consistent association of Cr with chromite in all laterite units indicates it high stability against weathering. The higher proportion of Cr hosted in chromite on the surface of the studied laterite profile (**Figure 4.5f**) could be related to its higher stability compared to co-occuring Fe (oxyhydr)oxides during enhanced weathering and erosion on the surface. Alternatively, it could be explained by the contribution of allochthonous material on the surface.

4.4.2. Role of Mn and Fe in Cr redox behavior

Chromium is mainly present as Cr(III) in the laterite profiles and no Cr(III) was oxidized to detectable Cr(VI) concentrations until the latter stages of weathering where Cr and/or Mn are enriched (**Figures 4.7 and 4.8**). We documented through Mn XAS analysis of the PAL profile (**Figure 4.7d**) that Mn is oxidized from Mn(II,III)-bearing serpentine to the predominant Mn(IV,III) oxides followed by incorporation in Fe (oxyhydr)oxides as Mn(III). The co-occurrence of Cr(VI) with abundant Mn(IV/III) oxides and Mn(III)-substituted Fe (oxyhydr)oxides within the limonite unit strongly suggest the oxidative reaction between Cr(III)

and these minerals. Cr(VI) genesis upon interaction of Cr(III) with Mn(III,IV) oxides (e.g., birnessite, lithiophorite, pyrolusite) has already been reported in laboratory studies (Kim et al., 2002; Hausladen & Fendorf, 2017; Pan et al., 2017). In another experiment, Mn-goethite was also found to oxidize Cr(III), where the oxidation rate increased with Mn substitution (Wu et al., 2007). Oxidation happens via electron transfer after Cr(III) is adsorbed onto the Mn sites (Manceau & Charlet, 1992; Wu et al., 2007), and studies on natural Fe-rich soils in Niquelandia, Brazil and Grand Terre, New Caledonia have shown a strong spatial relationship between Cr(VI) and Mn- and Fe-oxides (Fandeur et al., 2009b; Garnier et al., 2013). In this study, the progressive transition of Mn speciation from Mn(IV/III) oxide to Mn(III)-substituted Fe(oxyhydr)oxides upward the profile could also provide additional evidence for the redox dynamics between Cr and Mn. Cr(III) oxidation by Mn(IV,III) oxides results in the reduction of the latter to Mn(II) (Eary & Rai, 1987; Manceau & Charlet, 1992; Hausladen & Fendorf, 2017) and Mn(III) (Chen et al., 2021) which are necessary precursors for the formation of Mn-bearing Fe (oxyhydr)oxides (Scheinost et al., 2001). Alternatively, the similar trend in Mn speciation observed in a lateritic regolith in Goro, New Caledonia were attributed to more favorable conditions, such as higher humidity and slightly higher pH, which promote Mn oxide precipitation and stabilization at deeper levels rather than shallower depths (Dublet et al., 2017).

Detectable Cr(VI) concentrations in the limonite zone of PAL and all other profiles could also be explained by the abundance of Fe (oxyhydr)oxides that provide sorption sites for Cr(VI) after oxidation. Our EXAFS fitting of Cr(VI)-adsorbed goethite (**Table 4.1**) provides direct evidence that Cr(VI) adsorbs as inner-sphere complexes onto Fe (oxyhydr)oxides. At the typical acidic conditions in the limonite zone (Myagkiy et al., 2017), anionic species of Cr(VI) (e.g., $HCrO_4^-$) would have a high affinity for metal hydroxides because of their higher pHpcz values (pH 6 to 9). Rai et al.[5] even showed that Fe (oxyhydr)oxides are the predominant adsorbents of Cr(VI) in acidic to neutral oxidized soils. Previous water extractions of the PAL laterites (Delina et al., 2020), also demonstrated that significantly lower Cr(VI) could be easily mobilized from the limonite zone ($\leq$ 2.3 mg kg^{-1}) compared to the saprolite to transition zones (up to 100 mg kg^{-1}) because of Cr(VI) adsorption onto Fe (oxyhydr)oxides. However, in comparison to Cr(III) that is dominantly incorporated in the minerals, adsorbed Cr(VI) is more labile and could be transported during weathering as shown in surface waters of Ni laterite mining areas (Gunkel-Grillon et al., 2014; Delina et al., 2020). This could account for the general decrease in total Cr concentrations towards the surface in most profiles (**Figures 4.7c and 4.8**) that led to the shift from the correlated to the dispersed Cr versus Fe clusters in **Figure 4.4**. More prevalent organic matter at the surface could also play a role by reductive dissolution of the Fe (oxyhydr)oxides and the mobilization of Cr (Garnier et al., 2013; Delina et al., 2020).

4.4.3. Implications for Cr mobility in ultramafic and lateritic environments

Determining the speciation and mobility of metals is necessary for evaluating their potential environmental risks and impacts. Through atomic-scale investigations, we unraveled the fate of Cr and the role of Fe and Mn in controlling its speciation and mobility during laterite formation from ultramafic rocks (**Figure 4.9**). Our results indicate that upon weathering of ultramafic rocks, Cr(III) is released from primary silicates and likely gradually from chromite, and repartitioned into initial Mg phyllosilicate weathering products (e.g., serpentine) in the saprolite zone by structural incorporation of Cr(III) into the Mg site. When present, other secondary phyllosilicates, in particular Fe-bearing smectite (e.g., nontronite), can trap Cr(III) via sorption onto its mineral surface.

Prolonged weathering leads to the dissolution of these phyllosilicates and the redistribution of Cr into the Fe (oxyhydr)oxides that proliferate in the overlying limonite horizon (Oze et al., 2004b; Chrysochoou et al., 2016). We have shown that Fe (oxyhydr)oxides sequester Cr initially by polymerization of Cr(III) with Fe(III) during the formation of poorly crystalline precursors (i.e. ferrihydrite). After weathering cycles, ferrihydrite crystallizes and transforms to goethite then hematite, where Cr(III) isomorphically substitutes for Fe(III) and incorporates into the crystal structure. This increase in crystallinity and stability of the Fe (oxyhydr)oxides decreases the mobility of Cr. Altogether, the significant scavenging of Cr(III) by phyllosilicates and comparatively more weathering resistant Fe (oxyhydr)oxides limits Cr leaching and mobility during laterite formation, as evidenced by the residual enrichment of Cr with weathering (**Figure 4.3c**). However, at the later stages of weathering, Cr becomes less correlated with the intensity of weathering (**Figure 4.3c**) as well as Fe (**Figure 4.4**), suggesting changes in Cr mobility. Here, oxidation-reduction reactions between Cr(III) released after dissolution-crystallization cycles and Mn oxides and Mn-substituted Fe (oxyhydr)oxides transform a fraction of Cr(III) to more mobile and toxic Cr(VI). Adsorption of Cr(VI) onto Fe(oxyhydr)oxides is favored in the acidic conditions of the limonite zone but with the higher mobility of Cr(VI), it is highly likely that a fraction of Cr(VI) could be leached downward the profile and/or downstream, accounting for the observable decrease in Cr towards the surface and the elevated Cr(VI) concentrations in waterbodies situated in Ni laterite areas (Gunkel-Grillon et al., 2014; Delina et al., 2020).

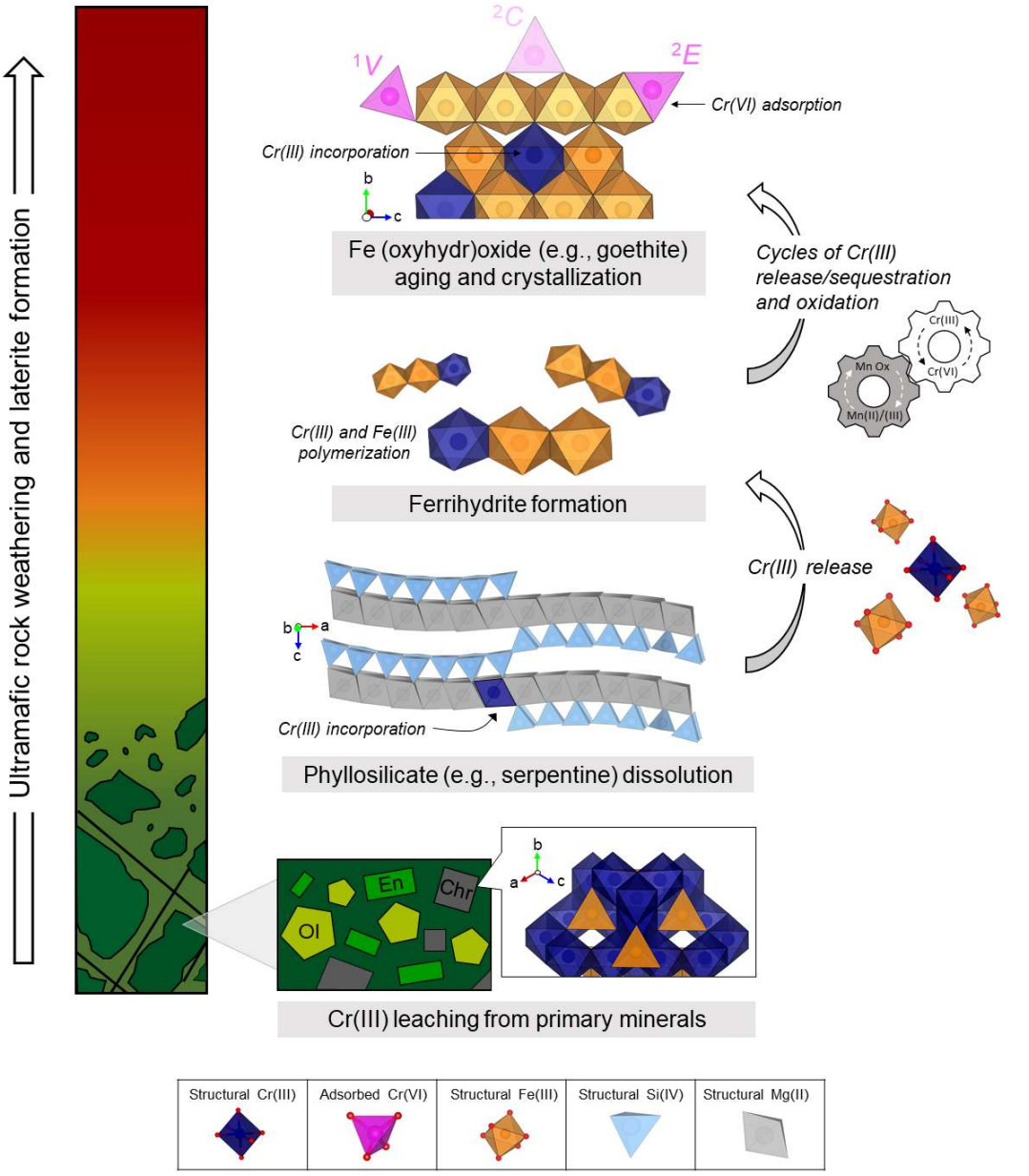

Figure 4.9. Schematic diagram explaining the fate and evolution of Cr upon tropical weathering of ultramafic rocks into a laterite profile. Cr(III) leached from primary minerals (e.g., Ol – olivine, En – enstatite, Chr – chromite) are initially sequestered by phyllosilicates by structural incorporation (e.g., serpentine) or, in the presence of smectite clays, adsorption. Dissolution of such phyllosilicates release Cr(III) which polymerizes with Fe(III) to form poorly crystalline ferrihydrite and becomes structurally incorporated with aging and crystallization of ferrihydrite to goethite hematite. At advanced stages of weathering, dissolution-crystallization cycles release a fraction of Cr(III) that is oxidized by Mn (oxyhydr)oxides (Mn Ox) to Cr(VI) that favorably adsorbs onto the Fe (oxyhydr)oxides. The redox dynamics between Cr and Mn reduces Mn Ox to Mn(II) and Mn(III), where the latter also incorporates into the crystal structure of Fe (oxyhydr)oxides. Note: The faded pink tetrahedra depicts a possible coordination geometry of Cr that was not detected in the fitting. ^{1}V - monodentate mononuclear geometry, ^{2}C - bidentate binuclear geometry, ^{2}E - mononuclear edge sharing geometry

Whether mined or unmined, all Ni laterite profiles in the Philippines contain Cr(VI) in concentrations up to two magnitudes higher than the average composition of the Earth's crust (35 mg kg^{-1} Cr) (Hans Wedepohl, 1995) but comparable to Cr(VI) contents of Ni laterite deposits worldwide (Garnier et al., 2006; Raous et al., 2013; Gunkel-Grillon et al., 2014). Among them, the SUR profile showed the highest fraction of Cr(VI) (**Figures 4.7 and 4.8**) and the most weathered limonite samples (**Figure 4.3a,b**). This could be due to the consistently wet climate and the high amount of rainfall experienced by the area. Intensive weathering and continuous exposure to rainfall can enhance the formation of soluble Cr(III) (Garnier et al., 2013) and oxidative conditions necessary for the transformation of Cr(III) to Cr(VI). The above highlights that the occurrence of elevated Cr(VI) contents in ultramafic and lateritic areas is not a direct consequence of anthropogenic activities (e.g., mining) but is a natural phenomenon driven by a combination of species heavily involved in Cr redox and speciation and promoted by environmental factors, especially in tropical areas where the rate of weathering is enhanced. Our present results emphasize that Mn and Fe exert contrasting forces on Cr, where Mn promotes its mobilization and association with Fe represents the main scavenging process for Cr during laterite formation. Further investigations on Cr immobilization by Fe (oxyhydr)oxides could help minimize the environmental release of Cr(VI), which is especially important in extensive exposures of Ni laterites, such as in mining sites and agricultural areas. Overall, this study not only advances our fundamental understanding of the geochemical behavior of Cr in Ni laterite regoliths but also offers crucial insights for the sustainable management of critical metal resources and the mitigation of potential environmental impacts associated with laterite mining activities.

4.5. Supporting information

4.5.1. Supporting figures

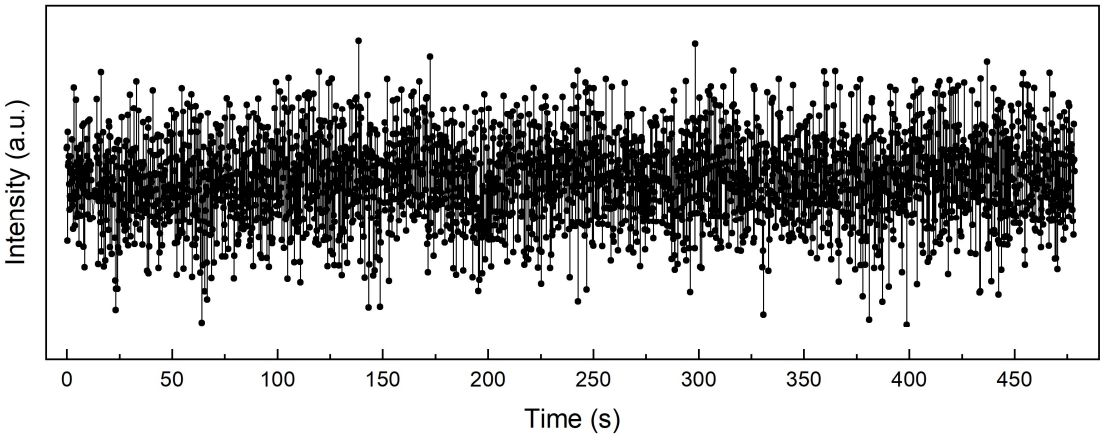

Figure S4.1. Example beam damage test at the Mn K-edge XAS for the PAL profile sample at 0 m. The test was performed by subjecting one sample spot to the X-ray beam at 6,552 eV and checking for changes in detected intensity through time. The homogenous distribution of intensities indicates no significant beam damage on the sample.

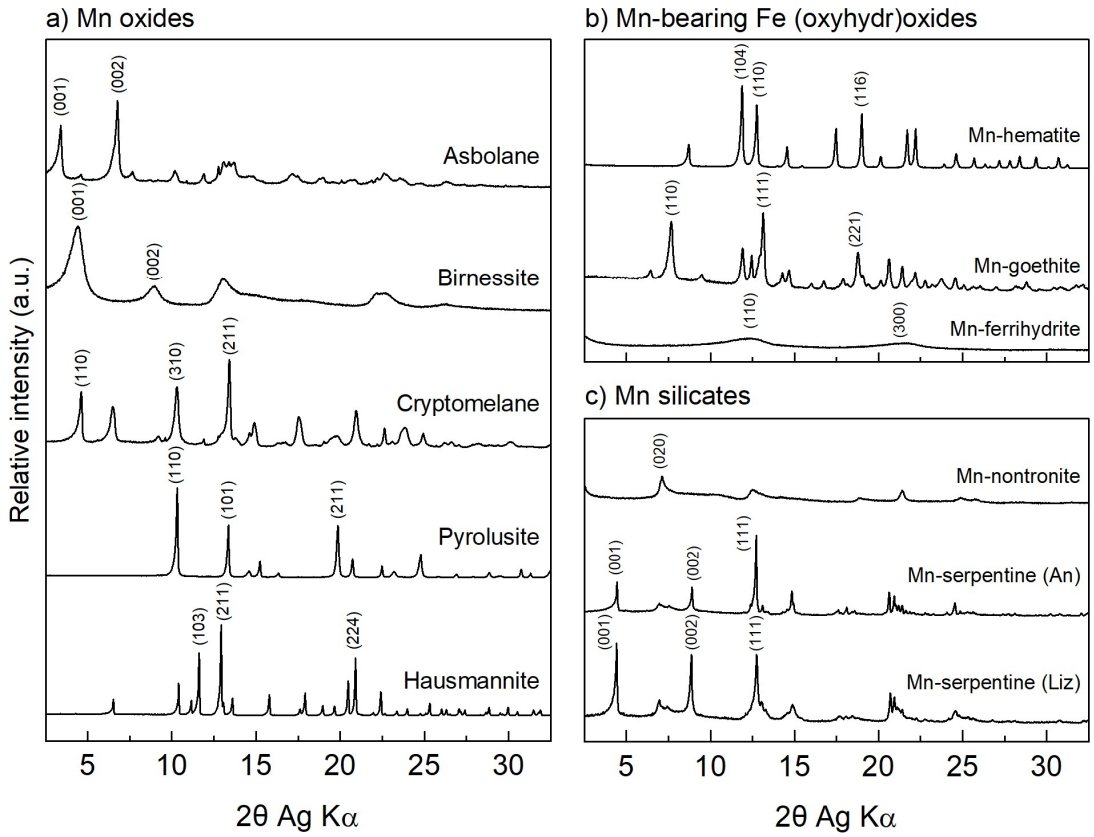

Figure S4.2. X-ray diffractograms of Mn model compounds: (a) Mn oxides, (b) Mn-bearing Fe (oxyhydr)oxides, and (c) Mn silicates. Only the main reflections are indexed, but no other phases were detected in each reference phase.

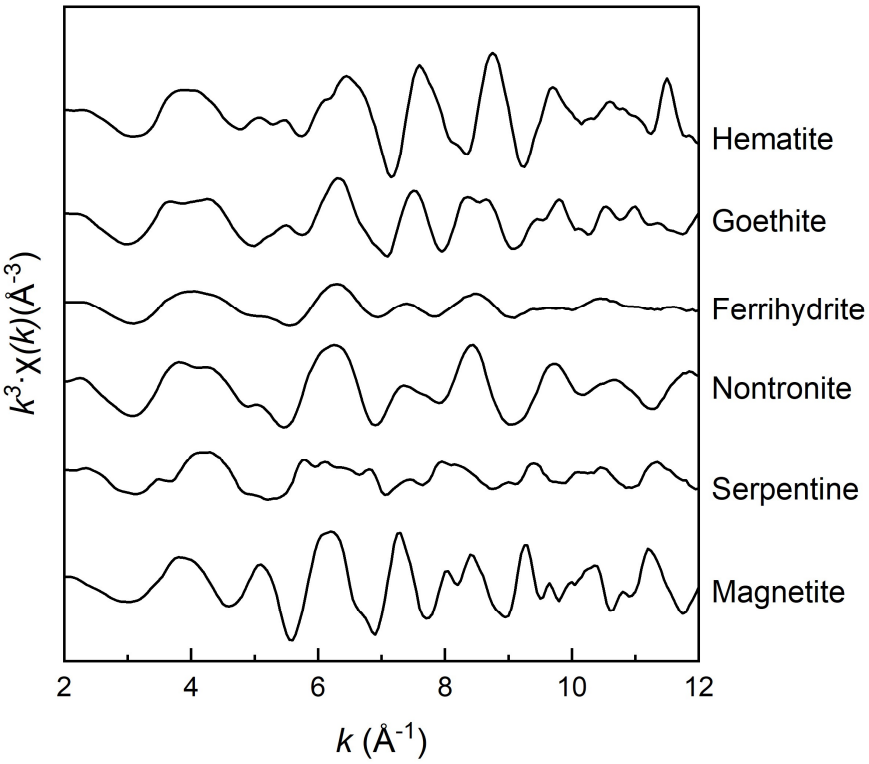

Figure S4.3. Fe K-edge EXAFS spectra of the model compounds used for LCF analysis of the laterite EXAFS spectra. The serpentine EXAFS spectrum is replotted from Noël et al. (2014).

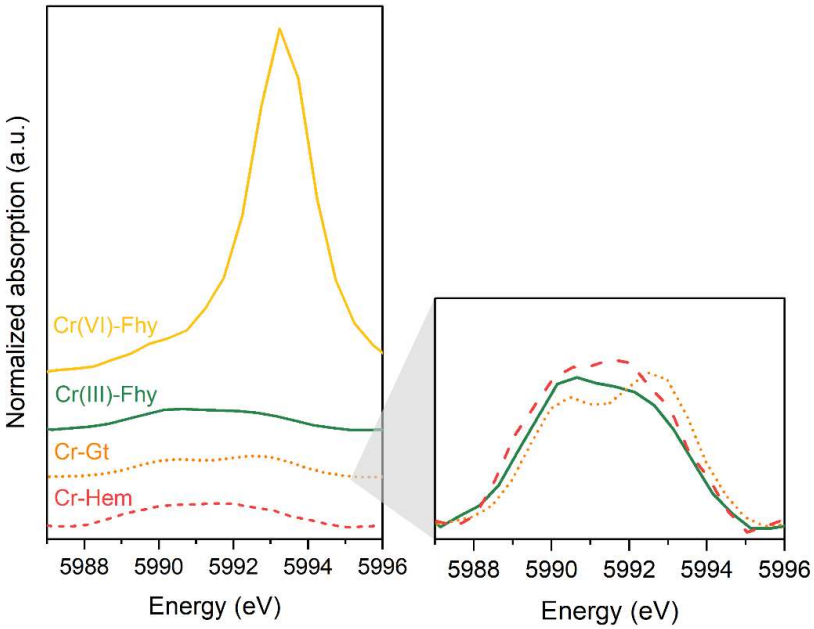

Figure S4.4. Cr K-edge XANES pre-edge of model compounds used to determine Cr redox in the laterite samples through LCF analysis. Fhy – ferrihydrite, Gt – goethite, Hem – hematite.

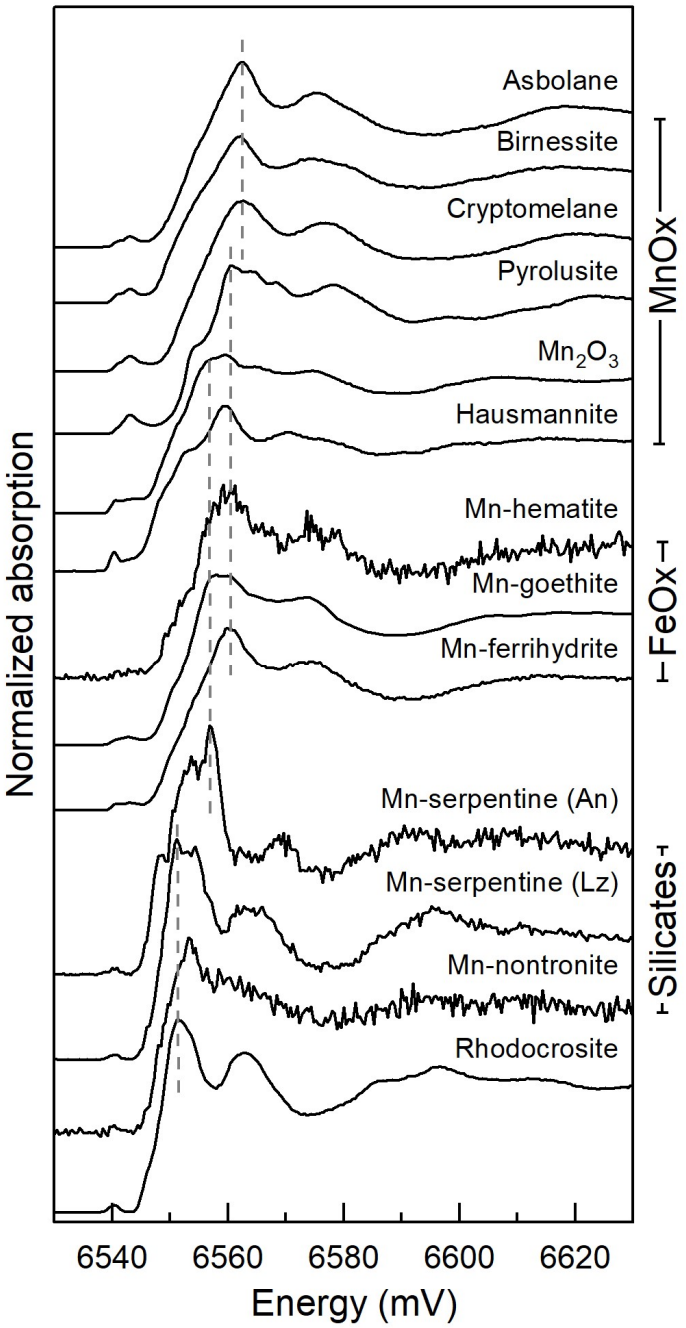

Figure S4.5. Mn K-edge XANES spectra of the model compounds used for LCF analysis of the laterite XANES spectra. Vertical dashed lines outline the maximum absorption peak of the XANES spectra. MnOx – Mn oxides; FeOx – Fe(oxyhydr)oxides; An – antigorite; Lz – lizardite

4.5.2. Supporting tables

Table S4.1. Chemical composition (wt. %) and weathering indices of the Ni laterite samples of each profile. Lim – limonite, TZ – transition zone, Sap – saprolite, Rock – bedrock.

Depth (m)	Horizon	Al_2O_3	CaO	Cr_2O_3	Fe_2O_3	MgO	SiO_2	MnO	TiO_2	NiO	CoO	UMIA[†]	IOL[*]
Palawan - PAL[**]													
0.0	Lim	4.88	0.01	2.60	76.8	0.72	4.87	0.86	0.12	2.01	0.12	84	94
1.4	Lim	4.95	0.01	3.53	74.2	0.71	3.87	0.90	0.13	1.76	0.13	86	95
2.0	Lim	5.14	0.00	4.16	75.9	0.70	4.16	0.71	0.15	1.70	0.09	86	95
3.2	Lim	3.78	0.01	3.86	72.9	0.67	4.29	1.42	0.09	3.02	0.22	85	95
3.8	TZ	1.98	0.03	2.77	50.4	3.61	28.5	1.04	*bdl*	4.14	0.13	37	65
4.4	Sap	1.24	0.02	2.06	35.3	10.1	37.3	0.59	0.01	3.49	0.09	21	49
6.2	Sap	0.52	0.01	0.77	13.5	28.6	43.0	0.18	*bdl*	2.05	0.03	6	25
Palawan - PAL-G05													
0.0	Sap	1.12	*bdl*	2.25	33.3	21.0	27.0	0.57	*bdl*	2.25	0.14	18	56
3.0	Lim	2.44	*bdl*	4.98	71.3	2.00	3.27	1.47	0.04	1.71	0.32	82	96
6.0	Sap	0.22	*bdl*	0.87	11.6	32.3	40.0	0.16	*bdl*	2.56	0.03	5	23
9.0	Sap	0.31	*bdl*	0.76	14.7	29.4	42.3	0.21	*bdl*	1.12	0.03	6	26
22	Rock	0.27	*bdl*	0.37	9.49	34.9	42.6	0.14	*bdl*	0.41	0.02	4	19
Palawan - PAL-U12													
0.0	Lim	3.35	*bdl*	4.12	71.9	1.38	3.77	0.74	0.05	1.23	0.06	83	95
3.2	Lim	2.87	*bdl*	3.99	66.7	0.88	9.72	2.05	0.02	1.12	0.15	71	88
6.0	Sap	0.98	0.14	1.61	30.6	9.70	48.0	0.52	*bdl*	1.44	0.19	16	40
9.0	Sap	0.54	0.08	0.81	17.2	14.4	61.7	0.24	*bdl*	1.02	0.08	8	22
19	Rock	0.44	0.18	0.59	11.3	31.7	45.8	0.16	*bdl*	0.46	0.02	5	20
Zambales - ZAM													
0.0	Lim	11.0	0.04	2.46	64.1	0.58	3.64	0.98	0.24	1.03	0.23	87	95
3.0	Lim	10.3	< 0.05	2.89	59.5	1.95	5.98	0.94	0.24	1.18	0.00	76	92
6.0	Lim	9.50	0.10	3.46	57.2	3.16	7.64	0.71	0.18	1.24	0.00	69	90
8.3	Lim	6.45	0.12	2.12	54.7	2.94	19.3	0.61	0.11	1.67	0.10	51	76
9.0	Lim	4.71	0.22	2.09	65.9	3.82	8.01	1.02	0.09	1.09	0.19	67	90
12	Sap	0.89	0.94	0.30	7.07	35.9	43.4	0.10	*bdl*	0.27	0.01	3	15
Surigao del Norte - SUR													
0.0	Lim	3.86	*bdl*	1.99	76.2	0.49	2.11	0.44	0.10	1.37	0.05	92	97
3.0	Lim	2.51	*bdl*	2.97	74.9	1.02	2.10	0.81	0.05	1.36	0.00	89	97
6.0	Lim	3.61	*bdl*	3.71	69.1	1.36	4.97	1.74	0.13	1.36	0.00	80	94
8.3	Lim	1.99	0.05	1.56	78.4	0.28	2.41	1.26	0.03	1.75	0.10	92	97
9.0	Sap	0.91	0.02	1.18	21.4	23.6	39.2	0.44	0.01	2.55	0.11	10	36
12	Sap	0.47	0.32	0.58	11.8	31.2	39.9	0.16	*bdl*	2.20	0.02	5	24
15	Sap	0.90	0.68	1.19	19.7	26.7	36.2	0.29	*bdl*	2.28	0.04	9	36

[†]Ultramafic index of alteration (UMIA) values are expressed in molar rations

[*]Index of lateritization (IOL) values are expressed in wt. %

[**]Data for PAL was adapted from Delina et al. (2020)

bdl – below detection limit

Table S4.2. LCF fit results and statistics of the Fe K-edge EXAFS spectra collected on selected samples from the PAL profile.

Sample		Magnetite	Serpentine†	Smectite	Ferrihydrite	Goethite	Hematite	Sum	*R*-factor
2 m	Weights*					0.453 (0.010)	0.542 (0.007)	0.996	0.009
	Bulk comp. (%)					45.5 ± 1.2	54.5 ± 1.0		
3.8 m	Weights			0.233 (0.012)	0.274 (0.027)	0.415 (0.013)	0.134 (0.007)	1.006	0.010
	Bulk comp. (%)			22.1 ± 1.4	26.0 ± 2.7	39.3 ± 1.8	12.7 ± 0.8		
4.4 m	Weights	0.095 (0.018)		0.504 (0.019)	0.153 (0.041)	0.176 (0.019)		0.929	0.020
	Bulk comp. (%)	10.2 ± 2.0		54.2 ± 3.5	16.5 ± 4.5	19.0 ± 2.2			

†Serpentine spectra from Noël et al. (2014)

*Values in parenthesis denote uncertainty values

Table S4.3. LCF fit results and statistics of the Cr K-edge EXAFS spectra of samples from the PAL profile.

Sample		Chromite	Serpentine(An)	Smectite	Ferrihydrite	Goethite	Hematite	Sum	*R*-factor
0 m	Weights*	0.277 (0.033)				0.483 (0.047)	0.246 (0.042)	1.007	0.037
	Bulk comp. (%)	27.5 ± 3.8				48.0 ± 4.7	24.5 ± 4.6		
2 m	Weights	0.085 (0.030)				0.528 (0.042)	0.438 (0.038)	1.051	0.026
	Bulk comp. (%)	8.1 ± 2.9				50.3 ± 5.1	41.7 ± 4.5		
3.2 m	Weights	0.113 (0.028)				0.527 (0.040)	0.313 (0.036)	0.953	0.031
	Bulk comp. (%)	11.8 ± 3.1				55.3 ± 5.4	32.8 ± 4.3		
3.8 m	Weights	0.153 (0.031)		0.258 (0.037)	0.099 (0.066)	0.415 (0.073)	0.076 (0.041)	1.000	0.037
	Bulk comp. (%)	15.3 ± 3.6		25.8 ± 4.7	9.9 ± 6.7	41.5 ± 8.8	7.6 ± 4.2		
4.4 m	Weights	0.245 (0.032)	0.056 (0.030)	0.068 (0.039)		0.634 (0.069)		1.003	0.057
	Bulk comp. (%)	24.4 ± 3.9	5.6 ± 3.0	6.8 ± 3.9		63.2 ± 8.9			
6.2 m	Weights	0.634 (0.031)	0.365 (0.027)					0.999	0.062
	Bulk comp. (%)	63.5 ± 4.1	36.5 ± 3.1						

*Values in parenthesis denote uncertainty values; An - antigorite

Table S4.4. LCF fit results and statistics of the Mn K-edge XANES spectra of samples from the PAL profile.

Sample	Weights						Bulk composition (%)		
	Serpentine(An)	Asbolane	Goethite	Ferrihydrite	Sum	*R*-factor	Silicate	MnOx	FeOx
0 m		0.522 (0.027)	0.113 (0.047)	0.375 (0.060)	1.01	0.006		51.7 ± 4.9	48.3 ± 8.1
1.4 m		0.500 (0.031)	0.125 (0.054)	0.387 (0.068)	1.01	0.009		49.4 ± 5.5	50.6 ± 9.4
2 m		0.357 (0.028)	0.266 (0.049)	0.378 (0.062)	1.00	0.007		35.7 ± 4.1	64.3 ± 8.8
3.2 m		0.764 (0.022)		0.233 (0.022)	1.00	0.005		76.6 ± 3.3	23.4 ± 2.3
3.8 m		0.953 (0.024)		0.050 (0.024)	1.00	0.006		95.0 ± 4.0	5.0 ± 2.4
4.4 m		0.878 (0.026)		0.124 (0.026)	1.00	0.007		87.6 ± 4.1	12.4 ± 2.6
6.2 m	0.260 (0.007)	0.746 (0.007)			1.01	0.010	25.9 ± 0.7	74.1 ± 1.0	

*Values in parenthesis denote uncertainty values; An - antigorite

Table S4.5. F-test results of additional scattering paths used in the Cr K-edge EXAFS fitting of selected samples.†

Fit	Path	CN	*R* (Å)	σ^2 (Å^2)	ΔE_0 (eV)	χ^2	χ_v^2	R-factor	N_{IDP}	N_{VARYS}	DF	Confidence level α (%)
Cr-ferrihydrite												
Cr-O only	Cr-O	5.6 (1.2)	1.98 (0.01)	0.003 (0.002)	-0.9 (3.0)	1751	167	0.0988	14.5	4	10.5	
Addition of Cr-Fe_1	Cr-O	5.1 (0.6)	1.98 (0.01)	0.002 (0.001)	-1.0 (1.4)	366	55	0.0144	13.7	7	6.7	99%
	Cr-Fe_1	2.8 (1.4)	3.05 (0.02)	0.009 (0.004)								
Addition of Cr-Fe_2	Cr-O	5.1 (0.6)	1.98 (0.01)	0.002 (0.001)	-0.9 (1.5)	301	64	0.0118	13.7	9	4.7	37%
	Cr-Fe_1	8.9 (7.6)	3.08 (0.03)	0.017 (0.008)								
	Cr-Fe_2	5.3 (4.4)	3.36 (0.05)	$\sigma^2_{Cr\text{-}Fe1}$								
Cr(VI)-adsorbed Goethite												
Cr-MS only	Cr-O	3.4 (0.5)	1.61 (0.02)	0.001	-9.7 (7.8)	582	57	0.1413	13.2	3	10.2	
	Cr-O-O	12	1.82($R_{Cr\text{-}O}$)	$\sigma^2_{Cr\text{-}O}$								
Addition of Cr-Fe1 (^2E)	Cr-O	3.9 (0.6)	1.59 (0.02)	0.001	-19.5 (7.1)	356	43	0.0867	13.2	6	7.2	71%
	Cr-O-O	12	1.82($R_{Cr\text{-}O}$)	$\sigma^2_{Cr\text{-}O}$								
	Cr-Fe1	1.0 (0.4)	2.82 (0.04)	0.003								
Addition of Cr-Fe2 (^1V)	Cr-O	3.8 (0.6)	1.59 (0.02)	0.001	-17.6 (7.3)	281	45	0.0681	13.2	7	6.2	76%
	Cr-O-O	12	1.82($R_{Cr\text{-}O}$)	$\sigma^2_{Cr\text{-}O}$								
	Cr-Fe1	0.9 (0.4)	2.83 (0.04)	0.003								
	Cr-Fe2	0.8 (0.6)	3.56 (0.06)	0.003								
Addition of Cr-Fe3 (^2C)	Cr-O	4.0 (0.6)	1.58 (0.02)	0.001	-21.2 (6.3)	199	47	0.0483	13.2	10	3.2	26%
	Cr-O-O	12	1.82($R_{Cr\text{-}O}$)	$\sigma^2_{Cr\text{-}O}$								
	Cr-Fe1	1.2 (0.4)	2.81 (0.03)	0.003								
	Cr-Fe2	1.7 (1.2)	3.34 (0.05)	0.003								
	Cr-Fe3	2.4 (1.4)	3.53 (0.04)	0.003								

†CN, coordination number; R, interatomic distance; σ^2, mean-squared atomic displacement; ΔE_0, change in threshold energy; χ^2, chi-square; χ_v^2, reduced chi-square; *R*, "goodness of fit" factor; N_{IDP}, number of independent points; N_{VARYS}, number of variables; DF, degrees of freedom; and Confidence level α, statistical validity that added scattering path improved the fit based on the F-test. The passive electron reduction factor (S_0^2) was fixed at 0.7. Numbers in parenthesis are fit-determined standard errors, whereas constrained parameters are without parenthesis. The multiple scattering Cr-O-O path was constrained geometrically to the single scattering Cr-O path ($R_{Cr\text{-}O\text{-}O}$ = 1.82 x $R_{Cr\text{-}O}$). All fits were carried out from 1.2 to 3.8 Å in *R*+Δ*R* space

Chapter 5

Revealing the fate and immobilization of chromium in nickel laterite mine tailings

This chapter is adapted from:

Delina, R.E.G.; Perez, J.P.H.; Roddatis, V.V.; Stammeier, J.A.; Prieur, D.; Scheinost, A.C.; Tan, M.M.; Garcia, J.J.L.; Arcilla, C.A.; Benning, L.G. Immobilization of chromium by iron oxides in nickel-cobalt laterite mine tailings. *In revision with Environmental Science & Technology.*

Abstract

Mine tailings generated from hydrometallurgical processing of nickel-cobalt laterite deposits contain high levels of chromium (Cr), with the hexavalent species being a toxic pollutant and carcinogen. However, the partitioning, speciation and local bonding environment of Cr in the mine tailings remain largely unknown, hindering our ability to predict its toxicity and long-term behavior. Coupling detailed mineralogical, spectroscopic and geochemical characterization with sequential extraction of tailings from active and rehabilitated dams, we show that Cr is present in its least toxic form, Cr(III), and largely immobilized by recalcitrant minerals. This immobilization also regulates dissolved Cr concentrations in the interacting waters to levels up to five times lower than the global regulatory limits (50 μg L^{-1}). Solid-phase Cr concentrations were ≤1.5 wt.% with 39-61% of Cr incorporated into hematite, and to a lesser extent, alunite, both of which formed early in the hydrometallurgical extraction process of mined laterite ores. The remaining Cr was present as recalcitrant chromite residues from the primary source laterite. We highlight that, although hydrometallurgical extractions liberate majority of Cr from laterite ores during processing, they also provide ideal chemical pathways for the formation of highly stable, crystalline hematite that successfully sequester Cr, while restricting is environmental mobility.

5.1. Introduction

Global transition to cleaner energy sources has raised the demand for critical metals (European Commission, 2023), exponentially also increasing the amount of wastes generated from their extraction (Hudson-Edwards & Dold, 2015). The extraction of nickel (Ni) and cobalt (Co), both vital energy transition metals, from very large-tonnage, low-grade laterite ore deposits results in millions of tons of tailings containing potentially toxic heavy metals (e.g., chromium) (Marsh et al., 2013; Aitken & Maluly Kemeid, 2016). Chromium (Cr) is a common constituent of Ni-Co laterite deposits, occurring as Cr(III) incorporated in minerals such as primary Cr-spinels (e.g., chromite) and laterite weathering phases like Fe (oxyhydr)oxides (e.g., goethite, hematite). Chromium may also be present as Cr(VI) oxyanions adsorbed onto these weathering mineral surfaces (Richard & Bourg, 1991; Kotaś & Stasicka, 2000). The presence and chemical nature of Cr in Ni-Co laterite ores is actively studied (Fandeur et al., 2009b; Gunkel-Grillon et al., 2014; Delina et al., 2020), but its fate during ore processing and later in the mine wastes or tailings remains largely unknown. Such knowledge is important because Cr at high concentrations is toxic. Although in its Cr(III) state, it is a vital micronutrient (Anderson, 1997), Cr(VI) is carcinogenic (Katz & Salem, 1994; WHO, 2003; Guertin et al., 2016). Hexavalent Cr is more mobile than Cr(III), and is often detected in Ni-Co laterite mine waters at concentrations sometimes exceeding international drinking water standards (i.e., World Health Organization (WHO) limit of 50 µg L^{-1}) (Gunkel-Grillon et al., 2014; Economou-Eliopoulos et al., 2016; Delina et al., 2020). However, the potential sources of Cr in lateritic environments, and the release or transformation pathways of Cr from ores to mine tailings need to be critically evaluated.

In most worldwide Ni-Co laterite processing plants (e.g., in New Caledonia, Australia, Philippines), high pressure acid leaching (HPAL) is the primary hydrometallurgical method used to concentrate Ni and Co from iron (Fe) (oxyhydr)oxide-rich or oxide-type Ni-Co laterite deposits (Whittington & Muir, 2000). Under high temperature (230-270°C) and pressure (3.3-5.5 MPa) conditions, sulfuric acid (H_2SO_4) is used to leach Ni and Co from the Fe (oxyhydr)oxides. This process is followed by the precipitation of secondary Fe (oxyhydr)oxides and sulfates (Whittington & Muir, 2000; Ucyildiz & Girgin, 2017). The resulting acid leach residue are neutralized by limestone ($CaCO_3$) or lime (CaO) addition (Whittington & Muir, 2000; Azimi & Papangelakis, 2010; Shibayama et al., 2016), forming calcium (Ca) sulfates as a by-product (Marsh et al., 2013). This neutralized slurry is discharged to a tailings dam or storage facility (Marsh et al., 2013; Shibayama et al., 2016). HPAL tests on laterite ores showed that up to 25% of the total Cr could be leached (Buarzaiga et al., 2003; Önal & Topkaya, 2014; Ucyildiz & Girgin, 2017). Under oxidizing HPAL conditions, dissolved Cr has been predicted to exist as Cr(VI), either as CrO_4^{2-} or $Cr_2O_7^{2-}$ (Sobol, 1969; Whittington & Muir, 2000;

Buarzaiga et al., 2003). However, there is no direct evidence yet for the dissolved and solid-phase speciation and mobility of Cr in the acid leach residues that end up downstream as tailings, although such quantitative information is crucial for an adequate evaluation of the toxicity and risks possibly posed by Cr-bearing tailings. To this date, the potential leaching of Cr from tailings to waterways in Ni-Co laterite mining areas has not been investigated.

To address this knowledge gap, we have carried out detailed mineralogical, spectroscopic and geochemical characterization of tailings from an active and a rehabilitated HPAL tailings dam in a mining district in the Philippines. We coupled these findings with targeted sequential extraction in order to determine the host minerals, the Cr speciation, as well as the fate and mobility of Cr in these environments. Our findings enable us to predict the long-term behavior of Cr in Ni-Co laterite mine tailings, and to assess its implications for tailings management and disposal.

5.2. Materials and methods

5.2.1. Sample collection and field-based measurements

HPAL tailings (solids and water samples) from an active tailings dam and a rehabilitated tailings dam decommissioned for more than 10 years were collected in Palawan, Philippines in May 2022. The solid samples can be divided into: (i) wet or waterlogged tailings (AW – active wet) and (ii) dry tailings (AD – active dry) from the active tailings dam, and (iii) rehabilitated (RH) tailings from the decommissioned tailings dam (**Figure S5.1**). Samples were collected by digging small pits and removing ~10 cm of surface cover. The field moist samples were freeze-dried and ground for subsequent analyses. Water samples were obtained from the waterlogged areas of the active tailings dam and from its outflow pond (**Figure S5.1**). We measured temperature, pH, redox potential (ORP), electrical conductivity (EC), and dissolved oxygen (DO) *in situ* using freshly calibrated HACH HQd and Hanna HI portable multi-parameter meters. Duplicate water samples were collected in low-density polypropylene bottles, that were filled to the brim, capped tightly and stored at ~4 °C. A batch of water samples was filtered through Nalgene™ Rapid-Flow™ filter units using 0.2 µm PES membranes. The filtrate was split into unacidified subsamples for Cr(VI) and anion measurements and acidified (0.3 M HNO_3) subsamples for cation analysis. The second batch was used for alkalinity measurements.

5.2.2. Aqueous phase analyses

Dissolved Cr(VI) concentrations (LoD = 10 µg L^{-1}) were determined within 24 h of sampling using a Shimadzu UV 1800 UV-Vis spectrophotometer and following the USEPA 7196A (USEPA, 1992) method. Total Cr (LoD = 14 µg L^{-1}) and major element concentrations in all water samples were measured by inductively coupled optical emission spectrometry (ICP-OES Varian 720-ES) (Delina et al., 2024). Dissolved anion concentrations were quantified by ion

chromatography (Metrohm AG - 883 Basic IC plus) and alkalinity was analyzed by titration following the USEPA 310.1 method (USEPA, 1978). Based on the water chemistry data, mineral saturation indices were calculated using the Geochemist's Workbench® (Bethke, 2022).

5.2.3. Mineralogical and geochemical characterization

The bulk chemical composition of the solids was quantified by ICP-OES (Agilent 5110) analysis following total digestion of solid aliquots that had been prepared by Na_2O_2 fusion, and data is reported as oxide (wt.%) following standard methods (Bokhari & Meisel, 2017). The analytical uncertainty of this approach was determined using OREAS certified reference materials (CRMs) 182, 185 and 190. The mineralogical composition of all samples was quantified from patterns recorded with a STOE STADI P X-ray diffractometer (XRD, Ag Kα radiation; λ = 0.5594 Å) equipped with a curved Ge (111) monochromator and two DECTRIS MYTHEN2 R detectors. XRD patterns were collected over a *Q*-range of 0 to 13.42 $Å^{-1}$, and data was processed by Rietveld refinement using the GSAS-II software (Toby & Von Dreele, 2013). The particle morphologies and elemental compositions of solids were examined using a FEI Quanta 3D FEG scanning electron microscope (SEM) coupled with an EDAX energy dispersive spectroscopy (EDS) system. SEM images of the carbon-coated (20 nm) samples were acquired at high vacuum mode, and at 20 keV and 4 nA using an Everhardt-Thornley secondary electron detector (ETD) and a backscattered electron detector (BSED). For selected samples, thin foils were prepared by Ar^+ ion milling using a Gatan PIPS II 695 setup and a focused ion beam milling (FIB) system using a FEI Helios G4 UC Dual Beam FIB-SEM instrument. On these FIB foils, high angle annular dark-field scanning transmission electron microscopy (HAADF-STEM) micrographs and energy dispersive X-ray (EDX) maps were acquired using a Thermo Fisher Scientific™ Themis Z (3.1) Scanning Transmission Electron Microscope operated at 300 kV and equipped with a Super-X EDX system, and a Gatan Continuum ER/1065 imaging filter.

5.2.4. Cr speciation and bonding environment

To evaluate the speciation and local bonding environment of Cr in the tailings, we employed synchrotron-based X-ray absorption spectroscopic (XAS) analyses of the solid fractions. Cr-K edge XAS was conducted in the Rossendorf beamline (ROBL-II) BM20 (Scheinost et al., 2021) of the European Synchrotron Radiation Facility (ESRF, Grenoble, France). XAS spectra were collected in fluorescence mode using an energy-dispersive 18-element Ge detector out to a wavevector value of 11.5 $Å^{-1}$. Energy calibration was done by measuring a Cr foil and setting the position of the first maximum of the first derivative to 5989 eV. The collected spectra were compared with Cr-bearing reference mineral standards (e.g., Cr(III)- and Cr(VI)-ferrihydrites, Cr-hematite, chromite; **Figure S5.2**). Pressed pellets (13-mm) of the samples and calibration standards diluted in cellulose were analyzed in a closed-cycle He cryostat (~15K) to minimize

beam damage that can potentially change the speciation of Cr and to eliminate the thermal component of the Debye-Waller term. Dilution factors for the pellet mixtures were calculated using XAFSmass (Klementiev & Chernikov, 2016). For each sample, two to four scans were collected to obtain a good signal-to-noise ratio. Spectra were aligned, averaged, and background-subtracted using the ATHENA (Ravel & Newville, 2005) and SIXpack (Webb, 2005) software. Details of the synthesis of Cr-hematite and the preparation of chromite can be found in Delina et al. (2024), while the synthesis of the Cr-ferrihydrite standards and further information on data analysis of the XAS spectra can be found in the Supporting Information (**Section 5.5.1**).

5.2.5. Cr sequential extraction

To evaluate the different chemical and mineral fractions that could influence the potential mobility and toxicity of Cr in the solid tailing samples, we employed a Cr sequential extraction procedure (SEP) that we developed, tested and validated previously for Fe-rich laterites, soils and sediments (Delina et al., 2024). To account for the presence of large proportions (up to 34%) of water-soluble minerals like gypsum in the solids we slightly modified our SEP and included an additional water-soluble extraction step. Thus, our 7-step SEP discriminated between S1: water-soluble, S2: exchangeable, S3: adsorbed, S4: carbonate, S5: poorly crystalline Fe (oxyhydr)oxide S6: crystalline Fe (oxyhydr)oxide, and S7: organic matter associated Cr fractions (**Table S5.1**) with the residual fraction associated with recalcitrant chromite.

5.3. Results

5.3.1. Solid-phase Cr geochemistry and mineralogy

Solid-phase Cr concentrations in the studied tailings ranged from 1.0 to 1.5 wt.% (**Table S5.2**), comparable to values reported for other HPAL residues (e.g., 0.9 wt.% in North Maluku, Indonesia (Gultom & Sianipar, 2020); 1.3 wt.% in South Province, New Caledonia (Ang et al., 2017); 0.5–1.2 wt.% in Bulong, Western Australia (Whittington et al., 2003)). The tailings contained high concentrations of Fe_2O_3 (41–53 wt.%) as well as SiO_2 (7.9–18 wt.%) and minor Al_2O_3 (2.7–4.0 wt.%) and MgO (1.5–3.4 wt.%). Significant concentrations of CaO (3.7–12 wt.%) from the neutralizing agents were also detected from the tailings. These compositions and, in particular, the high Fe contents were confirmed by our XRD analysis (**Figure 5.1**) that revealed high proportions of hematite (Fe_2O_3; 46–70%), gypsum ($CaSO_4{\cdot}2H_2O$; 14–34%), quartz (SiO_2; 12–13%) with minor (<10%) calcite ($CaCO_3$), alunite ($(K,Na)(Al,Fe)_3(SO_4)_2(OH)_6$), and chromite ($(Fe,Mg)Cr_2O_4$; <1%), with the latter chromite being clearly a relic mineral from the HPAL processing (Kaya & Topkaya, 2011). Among the tailings, the waterlogged sample is distinguished by its higher hematite content and the smallest amount of gypsum, likely attributed to the undersaturation of gypsum in the reacting waters (**Table S5.3**). For all other solids, we observed only minor differences in mineralogical compositions between the samples from the active and rehabilitated tailings.

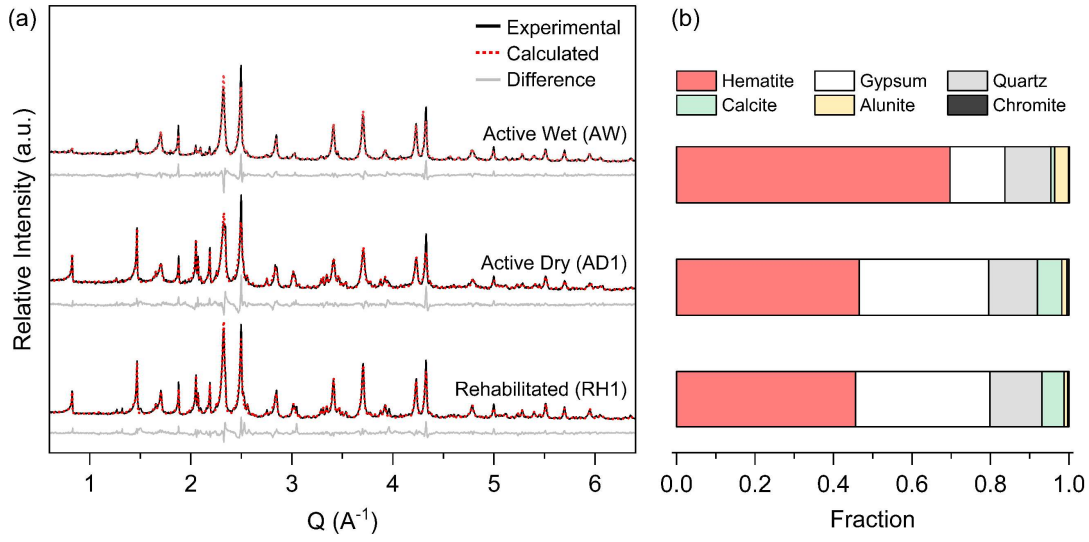

Figure 5.1. (a) XRD patterns and Rietveld refinements of representative samples from the active wet (AW), active dry (AD1) and rehabilitated (RH1) tailings; experimental data (solid black line); fitted data (dashed red line); and difference profiles (solid gray line). (b) Proportions of phase of AW, AD1 and R1 based on Rietveld refinements. The XRD patterns of all samples can be found in **Figure S5.3**.

When we imaged and spectrally analyzed the tailings (**Figure 5.2**), we only detected Cr associated with chromite, hematite, and alunite crystals. Chromite was the only discrete Cr-bearing mineral found, with Cr concentrations between 23 and 45 wt.% (SEM-EDS analyses; **Table S5.4**). SEM-EDS point analysis of hematite grains yielded Cr concentrations ranging from 0.5 to 1.3 wt.%, close to values measured from alunite crystals (0.3–1.1 wt.%).

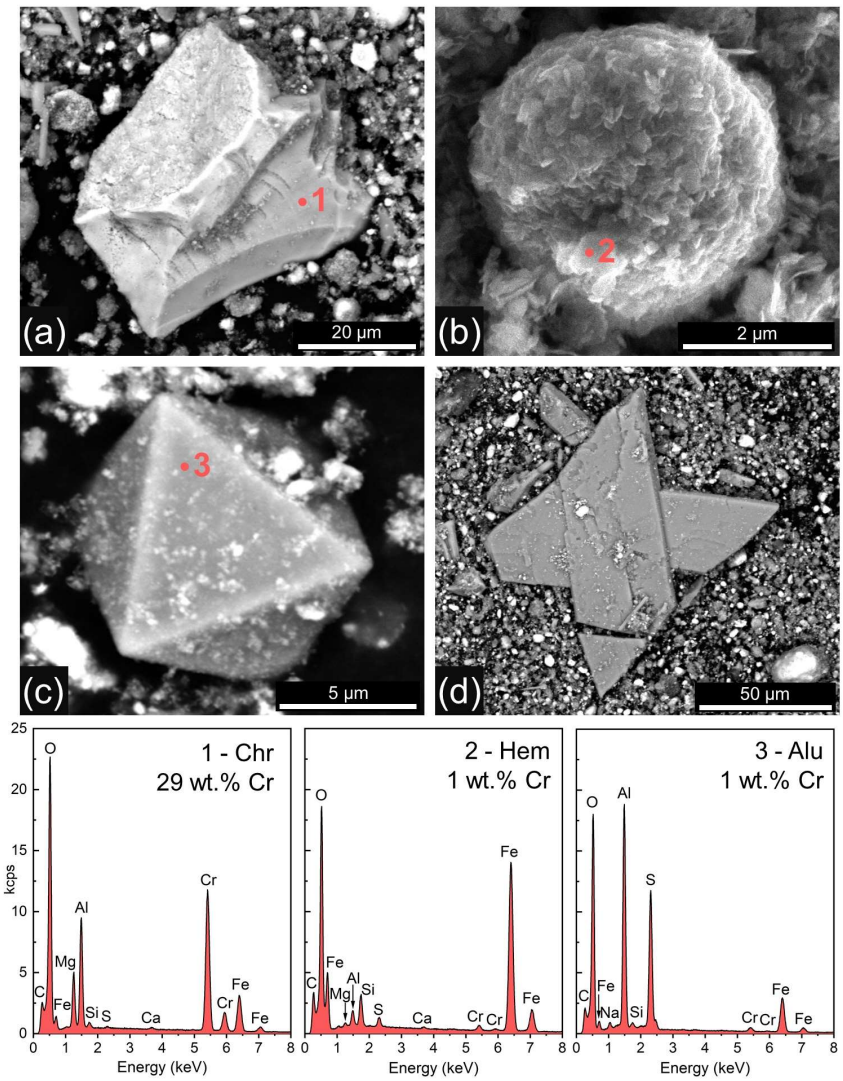

Figure 5.2. SEM images of selected minerals found in the tailings: (a) a relic chromite (Chr) grain with a pitted and fractured appearance indicative of past extractive processes (e.g., milling), (b) an aggregate of nano-sized platy hematite (Hem), (c) a pseudo-octahedral crystal of alunite (Alu), and (d) a relatively large twinned gypsum crystal. Below the images are the corresponding EDS spectra and Cr concentrations of the numbered points on the Cr-bearing minerals (a-c).

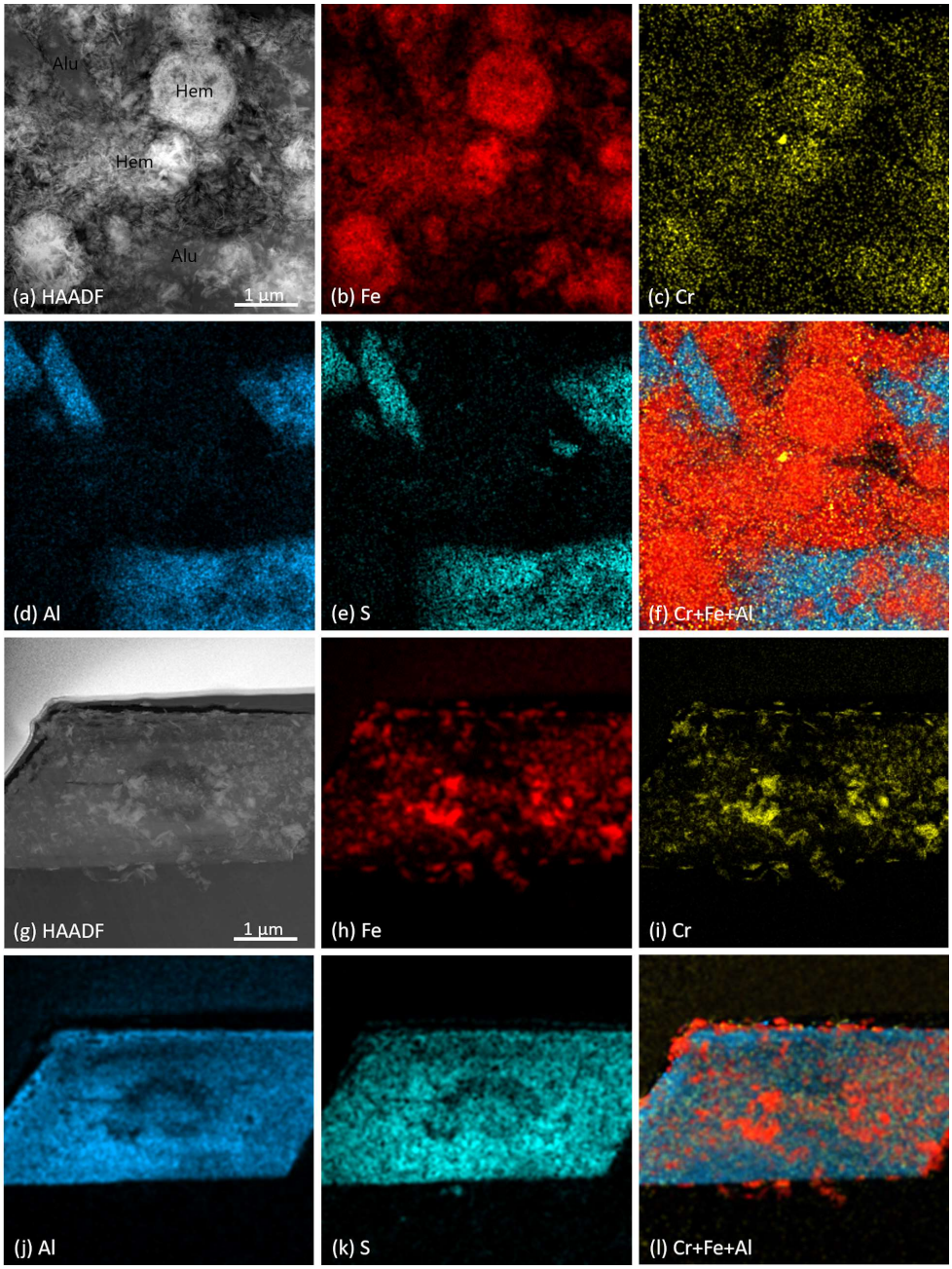

Figure 5.3. HAADF-STEM images of (a) hematite (Hem) aggregates and matrix with alunite (Alu) and a (g) FIB section of alunite, and their corresponding EDX elemental maps: (b,h) Fe (red); (c,i) Cr (yellow); (d,j) Al (blue); (e,k) S (magenta); and (f,l) combined Cr, Fe, and Al.

Elemental distribution maps acquired by TEM-EDX of tailings (**Figure 5.3a-e**) confirmed that Cr (yellow), was closely associated with the hematite aggregates and the Fe-rich matrix (red). There was also an overlap between Cr and the Al- and S-rich lath-shaped sections of alunite (blue and cyan, respectively), supporting the SEM-EDS observations. However, the combined EDX elemental maps of Cr, Fe and Al (**Figure 5.3f**) clearly indicate higher Cr intensities associated with hematite (i.e., Cr + Fe = orange), compared to alunite (i.e., blue only). Nevertheless, it remained unclear if alunite or hematite is the prime Cr host. Thus, we

analyzed FIB sections through an alunite crystal and could confirm in the EDX maps (**Figure 5.3g-l**) that indeed Cr displayed a stronger affinity to associated Fe oxides (orange hotspots in **Figure 5.3l**) compared to alunite.

5.3.2. Chromium XAS analysis

When analyzing Cr XAS patterns, there is a unique advantage in that the pre-edge features of Cr(III) and Cr(VI) are significantly different from each other (**Figure S5.4**). The X-ray absorption near edge structure (XANES) spectra of all tailings (**Figure 5.4, Figure S5.5**) displayed two weak pre-edge peaks at 5990 and 5993 eV, which are characteristic of spin-forbidden electron transitions in octahedrally coordinated Cr(III). The absence of the large and sharp pre-edge peak of tetrahedrally coordinated Cr(VI) at 5993 eV indicates that Cr predominantly exists as Cr(III) in the tailings, which is supported by the direct quantification through linear combination fitting (LCF) of the Cr XANES of the tailings (**Figure 5.4b**).

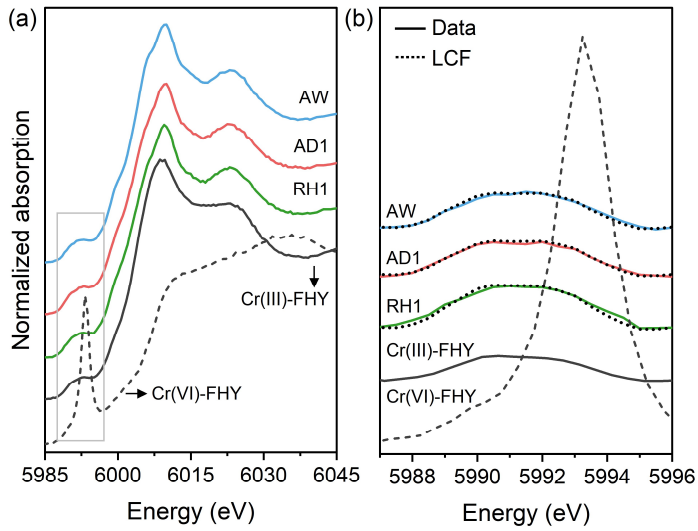

Figure 5.4. (a) Normalized Cr K-edge XANES spectra of the tailings, Cr(III)- and Cr(VI)-ferrihydrite (FHY) references, and the (b) baseline subtracted pre-edge of the enclosed features (gray solid box) in (a). Dotted line superimposed on the data in (b) denote linear combination fits (LCF) using Cr(III)-FHY, Cr(VI)-FHY, and Cr-hematite references (detailed in **Section 5.5.1.**).

The extended X-ray absorption fine structure (EXAFS) spectra of the tailings show similar coordination environments (**Figure 5.5a-b**). Shell-by-shell fitting of the EXAFS spectra (**Table S5.5**) further confirmed the speciation of Cr, showing octahedrally coordinated Cr(III) with two distinct Cr-O shells at distances of 1.97-1.98 Å (axial) and 2.44-2.45 Å (equatorial). The Cr-hematite standard was also best fit with two Cr-O shells, suggesting Jahn-Teller distortion of Cr(III), similar to previous observations in Mn(III)-substituted Fe (oxyhydr)oxides (Scheinost et al., 2001). In fitting the closest neighboring shells, we refer to both Cr and Fe as "Cr/Fe" as their unique contributions to the EXAFS signal could not be distinguished because of their close

atomic numbers. The best fit to the EXAFS data showed Cr-Cr/Fe shells at 2.94-2.95 Å, 3.43-3.46 Å, and 3.68-3.70 Å, matching the distances for the face-, edge-, and corner-shared octahedra of Cr-hematite and chromite (**Figure 5.5c-d**). Cr-hematite and chromite have very close first and second Cr-Cr/Fe distances and their contributions could be better distinguished through their coordination numbers. However, due to the high uncertainty of EXAFS-derived coordination numbers (20-25%) (Penner-Hahn, 2005), this proved to be difficult. As such, we combined the EXAFS fitting results with our mineral characterization data, and show that in the HPAL tailings, Cr was mainly structurally incorporated as Cr(III) in chromite and via substitution for octahedral Fe(III) in hematite.

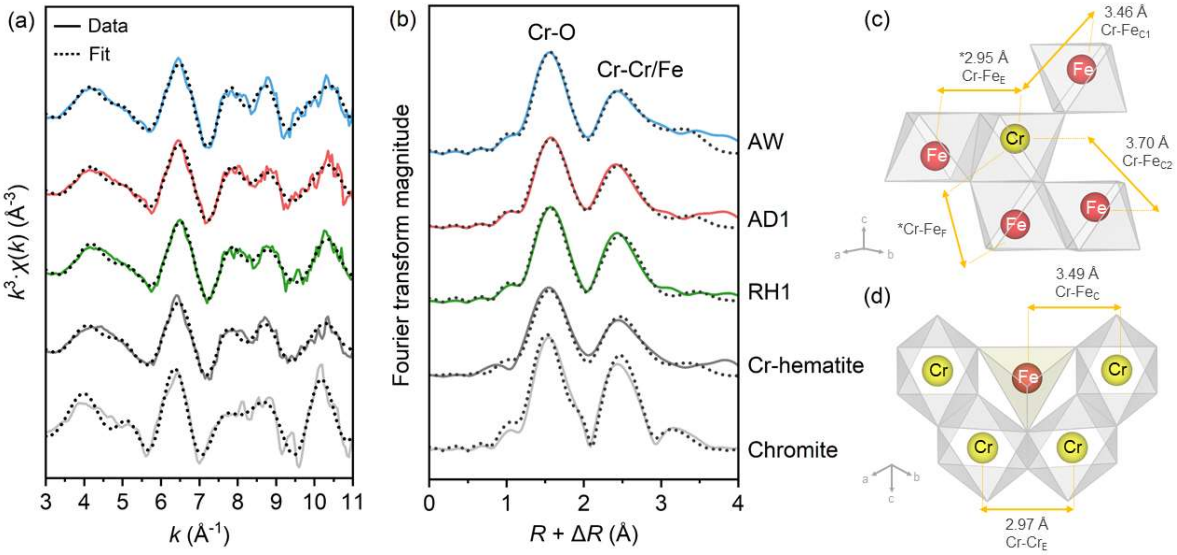

Figure 5.5. (a) Cr K-edge k^3-weighted EXAFS spectra and the corresponding (b) Fourier transforms (FT) of tailings samples and reference minerals, Cr-hematite and chromite. Dotted lines superimposed on the solid lines denote shell-by-shell fits of the EXAFS data. Structural models show the Cr coordination environment of (c) Cr-hematite and (d) chromite including the Cr-Cr/Fe distances based on the best fit given in **Table S5.5**.

5.3.3. Partitioning and mobility of Cr

Using sequential extraction, we gained a better understanding of the partitioning of solid-phase Cr in the different tailing samples. This allowed us to assess the potential mobility of Cr species to the surrounding environment. The first extraction step (S1, **Table S5.1**) estimates water-soluble Cr upon interaction of the solids with water. No Cr was mobilized during this step (**Figure 5.6a,b**), confirming the absence of Cr in gypsum, a water-soluble mineral primarily dissolved in S1. Our XRD results (**Figure 5.6c**) also confirmed the removal of gypsum in this step. These extraction and XRD results also corroborate the aqueous chemical results in the water samples collected from the active tailings dam and from its outflow pond

that were characterized by high calcium and sulfate contents (**Table S5.3**) but negligible Cr (<14 µg L^{-1}) and Cr(VI) (<10 µg L^{-1}) concentrations. The next two extraction steps: exchangeable Cr (S2) and adsorbed Cr (S3) were also negligible in all tailing samples. Typically, exchangeable Cr represents weakly-bound Cr that is susceptible to releases when changes in ionic strength occur, like for example during interaction with saline waters. On the other hand, adsorbed Cr represent Cr(VI) oxyanions likely to be desorbed from Fe (oxyhydr)oxides and other minerals in the presence of other competing aqueous ions (e.g., phosphate in agricultural drainage) (Delina et al., 2024). Our documented negligible amounts of Cr released through the extraction steps S1 to S3 demonstrate that the Cr that was present in the solid tailing samples is not easily mobilizable.

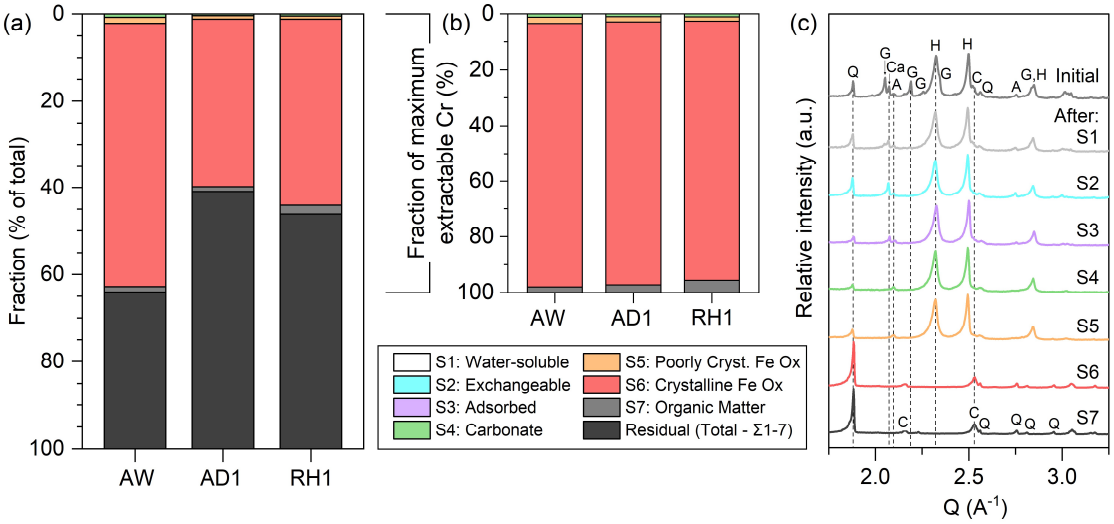

Figure 5.6. Sequential extraction data showing the distribution of Cr fractions with respect to the (a) total concentration and to the (b) maximum extractable or non-residual fractions (sum of S1 to S7). (c) XRD patterns of the residues of RH1 after each extraction step. See **Figure S5.8** for the XRD patterns of AW and AD1 residues. A – alunite, C – chromite, Ca – calcite, G – gypsum, H – hematite, Q - quartz

Upon further extraction steps, we show that minor proportions of the total Cr could be extracted from the carbonate (S4), poorly crystalline Fe (oxyhydr)oxide (S5), and organic matter (S7) fractions (**Figure 5.6a**). Below 1% of Cr was extracted by the acetate step (S4) that dissolves any carbonate remnants from the neutralization process (see also XRD patterns of residue in **Figure 5.6c**), and 0.7-1.4% were removed using 1 M HCl (S5) which dissolves poorly crystalline Fe (oxyhydr)oxides which are often difficult to quantify by XRD as they would appear only as a background in samples with many crystalline phases. Both these analyses were cross-confirmed by the minor (<0.5 wt.%) amount of Cr in the SEM-EDS analysis of the original limestones (**Figure S5.6**) used for neutralization, and by the low proportion of Fe (<1%) extracted in the poorly crystalline fraction (**Figure S5.7**). These two fractions are sensitive to changes in pH experienced during rainfall events or interaction with

organic acids (Pickering, 1986), among others. Furthermore, the organic matter associated Cr (S7) corresponding to the oxidizable fraction of Cr also comprised only between 1.1 and 2.0 wt.% of the tailings Cr content.

The largest pools for Cr was associated with the crystalline Fe (oxyhydr)oxide (S6) and the recalcitrant, residual fractions. These accounted for 39-61% and 37-60% of the total Cr concentration, respectively. Both hematite and alunite were dissolved during the 6 M HCl step (S6) (**Figure 5.6c**). To calculate the amount of Cr in each of these two mineral fractions, we combined our Rietveld analysis and SEM-EDS data of alunite (**Section 5.5.1**) and estimated that only 0.5-1.9% of the total Cr was associated with alunite while the majority was associated with hematite, supporting our TEM-EDX and XAS results (**Figure 5.3 and 5.5**). Comparing the various samples, the active wet sample (AW) exhibited the highest crystalline Fe (oxyhydr)oxide-bound Cr content (**Figure 5.6a**) matching its higher hematite proportion (**Figure 5.1**). The residual fraction was mainly chromite and this remained undissolved after sequential extraction (**Figure 5.6c**).

5.4. Discussion

5.4.1. Fate of Cr during tailings formation

The studied tailings were characterized by mineral compositions that were similar to HPAL residues of processed laterites from Turkey (Önal & Topkaya, 2014), Indonesia (Gultom & Sianipar, 2020), New Caledonia (Ang et al., 2017), and Western Australia (Whittington et al., 2003) with one big difference being the presence of the neutralization products (e.g., calcite, gypsum) in our samples (**Figure 5.1**). In the HPAL process, acid leaching mainly dissolves Fe (oxyhydr)oxides (e.g., goethite) and extracts Ni and Co together with Fe, Al, and Cr. At elevated HPAL temperatures (230-270°C), the leached Fe and Al undergo rapid hydrolysis, resulting in hematite and alunite precipitation (Whittington & Muir, 2000; Ang et al., 2017; Ucyildiz & Girgin, 2017). Our SEM and TEM analyses (**Figures 5.2 and 5.3**) support previous SEM studies of HPAL residues from Turkish laterites (Önal & Topkaya, 2014) that showed similar association between Cr and hematite and alunite. Our TEM EDX maps (**Figure 5.3**) help strengthen the suggestion that Cr coprecipitated during the formation of hematite and alunite during the HPAL process. Cr(III) is among the most common cations that readily substitutes for Fe(III) in the structure of Fe (oxyhydr)oxides (Cornell & Schwertmann, 2003; Caraballo et al., 2022), and our Cr K-edge XAS analysis (**Figure 5.5**) provides direct evidence for the above suggested structural incorporation of Cr(III) in hematite. Considering that the residual chromite-bound Cr was not leached during HPAL, our sequential extraction results (**Figure 5.6b**) reveal that more than 90% of the non-residual Cr was extracted in step S6, which documents that the hematite predominantly dissolved during this step was the main mineral that

sequestered the majority of Cr that was leached during the HPAL process. Our extraction data (**Figure 5.6**) combined with the XRD and TEM results (**Figures 5.1 and 5.3**) revealed that alunite, a minor component compared to hematite, also only sequestered minor amounts of Cr (≤2%). Previous studies have shown that Cr could substitute in alunite as Cr^{3+} for Al^{3+} or $Cr^{VI}O_4^{2-}$ for SO_4^{2-} (Sobol, 1969). Although some studies on HPAL products from Cuba have suggested that the acid leach liquors Cr(III) can oxidize to Cr(VI) (Sobol, 1969; Whittington & Muir, 2000), in our samples this could not be confirmed by our XAS analyses as no Cr(VI) was found in any of the HPAL tailings. The controlled oxidation-reduction potential in the HPAL autoclaves and the downstream processing of the acid leaching solutions involving sulfidization, or addition of H_2S gas as applied in the Palawan site, might limit and/or reduce the oxidation of the original Cr(III) to unwanted Cr(VI) (Whittington & Muir, 2000; Shibayama et al., 2016). The absence of Cr in the minerals resulting from the HPAL neutralization process (e.g., gypsum) or in the easily mobilizable fractions (e.g., adsorbed complexes) clearly support the fact that the coprecipitation of Cr with primarily hematite happens early in the HPAL process, and is thus, an effective means of sequestering Cr in poorly soluble iron-bearing phases.

5.4.2. Implications for long-term behavior of chromium

Chromium mobilization in Ni-Co laterite mining areas and its potential transfer to and toxicity in- ground- and drinking waters worldwide is of huge concern. While significant Cr remobilization is observed in laterite deposits, it is not clear whether the same phenomena occurs for HPAL tailings. For example, in the Philippines and New Caledonia where laterite mines are exposed to tropical climates, Cr(VI) contents in surface waters draining the mines (≤143 and ≤1620 μg L^{-1}, respectively) (Gunkel-Grillon et al., 2014; Delina et al., 2020) are significantly higher than regulatory limits (50 μg L^{-1}). Our work highlights that in tailings derived from HPAL treated Ni laterite ores, Cr is immobilized as Cr(III) incorporated in recalcitrant poorly soluble minerals, and that aqueous Cr and specifically hexavalent Cr is removed from the system. In addition to Cr in highly inert primary chromite grains that have not been efficiently removed by the HPAL treatment (**Figure 5.2a**), the majority of Cr liberated by the HPAL acid-leaching becomes locked in secondary hematite that is making up the tailings. Interestingly, unlike the goethite and hematite in the source Palawan laterites and in other laterites (e.g., New Caledonia), significant concentrations of Cr are present as adsorbed Cr(VI) species that are easily mobilizable, and that serve as major sources of Cr(VI) to the surrounding environment (Gunkel-Grillon et al., 2014; Delina et al., 2020).

Hematite, one of the thermodynamically most stable Fe (oxyhydr)oxides, is poorly soluble over a wide range of pH (2-14) (Langmuir, 1997; Cornell & Schwertmann, 2003; Jang et al., 2007). Moreover, the incorporation of Cr into Fe (oxyhydr)oxides like hematite has been found

to increase mineral stability and resistance to dissolution (Schwertmann, 1991; Delina et al., 2024) since Cr forms stronger bonds with oxygen (e.g., Cr(III)-O = 24.5 kJ mol^{-1}) compared to iron (e.g., Fe(III)-O = 23.7 kJ mol^{-1}) (Weast, 1988). The current lack of significant differences in speciation and partitioning of Cr between the active and rehabilitated tailings attest to the stability of Cr-hematite under various conditions (e.g., waterlogged vs. dry), and even after long-term storage (>10 years) and rehabilitation. Although Cr-hematite may be stable under the present surface conditions of the tailings, reducing conditions could induce hematite dissolution (Sulzberger et al., 1989; Cornell & Schwertmann, 2003) and remobilization of Cr. Thus, it is crucial to monitor the stability of hematite where anoxic conditions are expected (e.g., subsurface, deep-sea tailings disposal). It also important to monitor rehabilitated tailings as organic acids from root exudates and siderophores have been reported to induce proton- and ligand-promoted dissolution of hematite (Lin et al., 2018).

To the best of our knowledge, this is the first study to show the fate of Cr in high pressure acid-leached Ni-Co laterite tailings, improving our mechanistic understanding of Cr immobilization and other contaminants (e.g., Pb, V, Np, U) in other types of tailings (e.g., red mud) (Burke et al., 2012), and other natural and engineered settings where hematite is actively forming (Vu et al., 2013; Marshall et al., 2014; Bots et al., 2016; Scullett-Dean et al., 2023). Overall, the incorporation of Cr in resistant minerals like chromite and hematite combined with the very slow oxidation kinetics observed for Cr(III) in the environment (Whittleston et al., 2011), controls the long-term stability of Cr and inhibits its transformation to the more mobile and toxic Cr(VI).

5.5. Supporting information

5.5.1. Experimental and analytical methods

Synthesis of Cr-ferrihydrites

Following the method of Schwertmann and Cornell (2000), Cr(III)- and Cr(VI)-bearing ferrihydrites containing 1 wt.% Cr were synthesized by dropwise addition (2.9 mL min^{-1}) of 1 M NaOH to 150 mL of mixed solution of 195.6 mM $Fe(NO_3)_3 \cdot 9H_2O$ and 4.4 mM $Cr(NO_3)_3 \cdot 9H_2O$ or K_2CrO_4 until pH 7 is reached. The solids were separated by centrifugation (10,052*g*, 10 min), washed eight times using Milli-Q water (~18.2 MΩ·cm) to remove remaining electrolytes, and freeze-dried. **Figure S5.2** shows the diffractogram of the mineral standards used in this study confirming the purity of the Cr-ferrihydrites and other references.

Cr K-edge XANES data analysis

The redox state of Cr in the tailings samples was determined through linear combination fitting (LCF) of the pre-edge region (5986-5997 eV) extracted from the normalized XANES spectra by baseline subtraction using the XANES dactyloscope software (Klementiev, 2006). The LCF was performed using the ATHENA (Ravel & Newville, 2005) software and Cr(III)-ferrihydrite, Cr(VI)-ferrihydrite, and Cr-hematite as references. Tetrahedral Cr(VI) shows a strong absorption peak at 5993 eV while octahedral Cr(III) has two weak peaks at 5990 and 5993 eV (Peterson et al., 1997). Considering the significant partitioning of Cr in hematite based on the sequential extraction data, Cr-hematite was added as reference as it shows a relatively more intense pre-edge peak in the 5991-5993 eV range compared to Cr(III)-ferrihydrite (**Figure S5.4**). Such feature can be explained by the structural distortion of the octahedral environment of Cr(III) in hematite structure (Fandeur et al., 2009b). By adding Cr-hematite in the LCF, we avoid identifying peaks around 5993 eV as Cr(VI). This technique has also been applied by previous studies (Fandeur et al., 2009b).

Cr K-edge EXAFS fitting

EXAFS fitting was performed following the shell-by-shell approach described in Delina et al. (2024). In brief, Fourier transforms filtered from the k^3-weighted EXAFS data were fit over 1.2 to 3.8 Å R+ΔR-space in SIXpack (Webb, 2005) using the algorithms derived from IFEFFIT (Newville, 2001). The fitting was done by defining shells of neighboring atoms and then iterating the coordination numbers (CN), distances (R), and the mean squared atomic displacement parameter or Debye-Waller factors (σ^2) while the passive electron reduction parameter, S_0^2, was constrained to a value of 0.7. In this approach, the CN of the reference minerals (i.e. chromite, Cr-hematite) were fixed according to literature values to decrease the degrees of freedom and fit-derived standard errors from highly correlated parameters (e.g., CN and σ^2). The coordination environment of Cr in the references were used to constrain the σ^2

values in the tailings' spectra, allowing CN to adjust in the fit. The goodness of fit represented by the R-factor: $R = \sum_i(data_i - fit_i)^2/\sum_i(data_i)^2$ was used to assess the quality of the spectral fits. An R-factor below 0.05 signifies a reasonable fit (Kelly et al., 2008).

Estimation of mineral fraction using Rietveld and SEM-EDS data

To estimate the fraction of Cr (% of total concentration) associated with certain minerals, we use the following formula:

$$Cr\ fraction\ \% = \frac{Phase\ composition\ x\ C_{SEM}}{C_{Total}}\ x\ 100$$

where,

Phase composition = Rietveld calculated phase composition (%)

C_{SEM} = median Cr concentration of mineral measured using SEM-EDS

C_{Total} = total Cr concentration of tailings measured using ICP-OES (**Table S5.2**)

In the case of alunite that comprise 0.9-3.5% of the mineral composition of the tailings and is characterized by a median Cr concentration (n = 15) of 0.7 wt.% based on SEM-EDS analysis, the calculated Cr fraction in alunite is 0.5-1.9% of the total Cr.

5.5.2. Supplementary figures

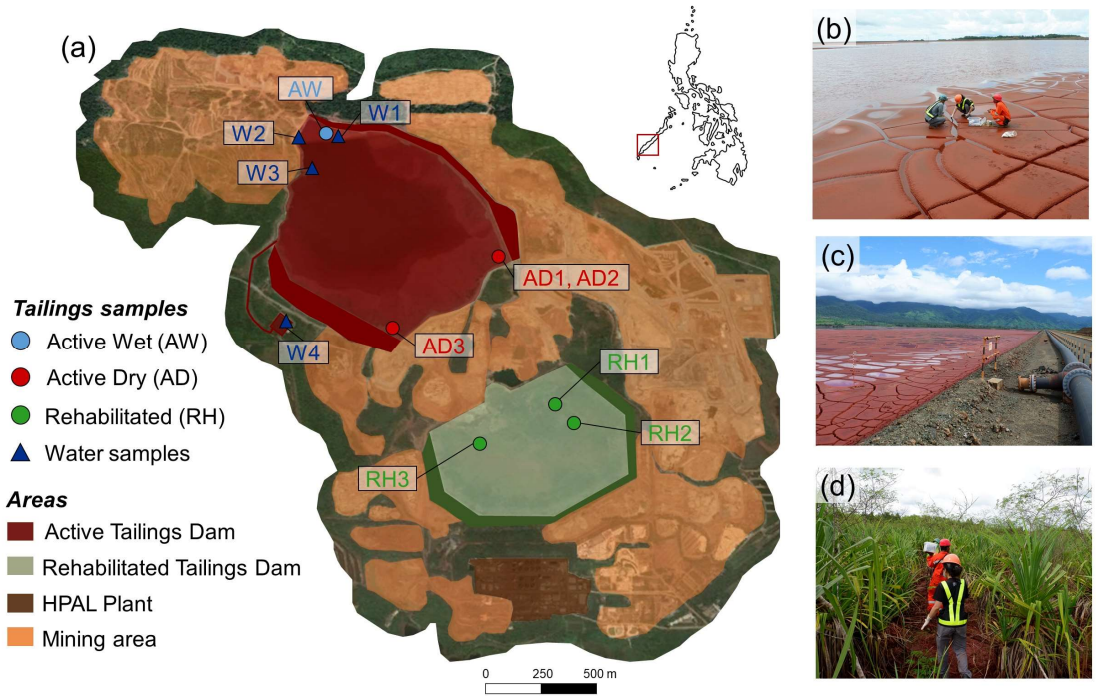

Figure S5.1. (a) Map of the study area showing the sampling sites, with photographs of the (b) waterlogged and (c) dry areas of the active tailings dam, and a (d) lush green revegetated area of the rehabilitated tailings dam. Average human height of 1.6 m (b,d) and meter rod (c) as scale.

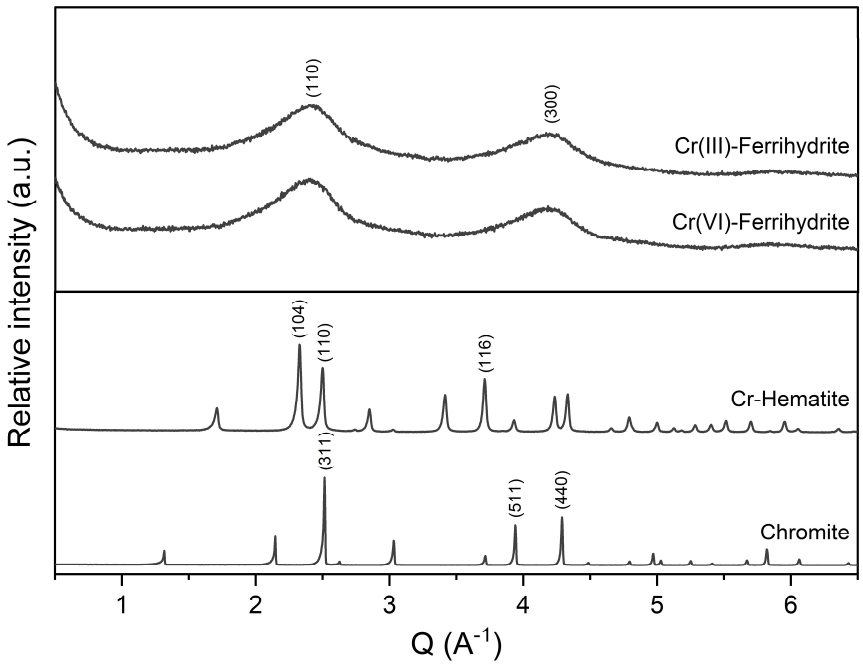

Figure S5.2. Powder X-ray diffractograms of mineral standards with indexed main reflections.

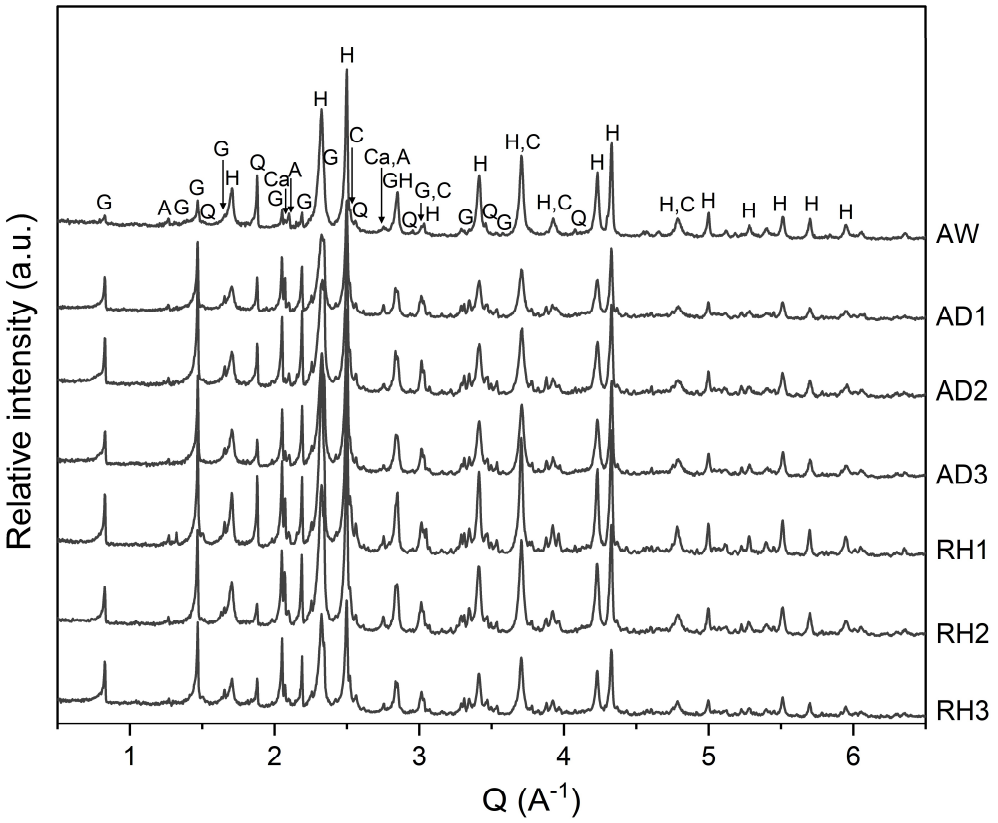

Figure S5.3. Powder X-ray diffraction patterns of the active wet (AW), active dry (AD) and rehabilitated (RH) tailings and their corresponding mineral composition: A – alunite, C – chromite, Ca – calcite, G – gypsum, H – hematite, Q – quartz

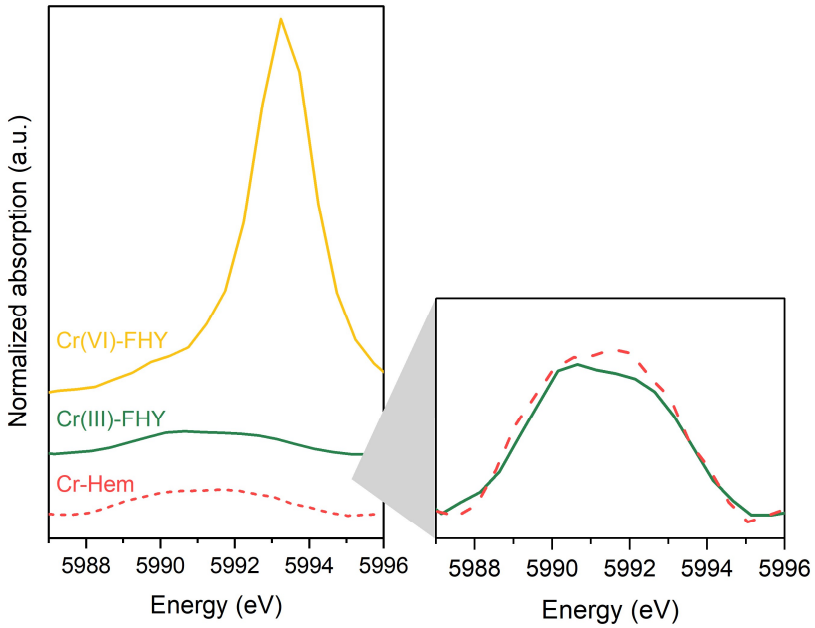

Figure S5.4. Comparison of the Cr K-edge XANES pre-edge collected from the Cr (III)- and Cr(VI)-ferrihydrites (FHY) and Cr(III)-hematite (Hem).

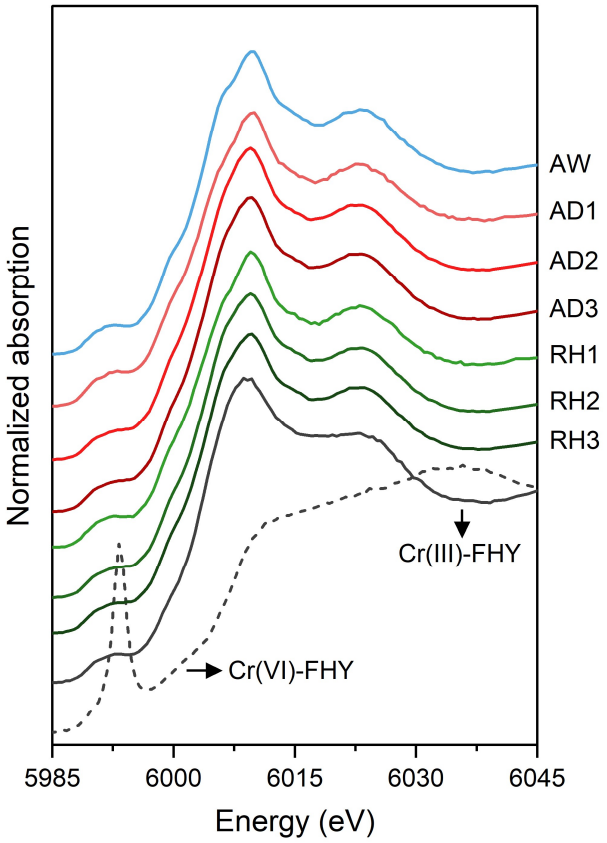

Figure S5.5. Normalized Cr K-edge XANES spectra of all tailings samples (AW – active wet, AD – active dry, RH – rehabilitated), and Cr(III)- and Cr(VI)-bearing ferrihydrites.

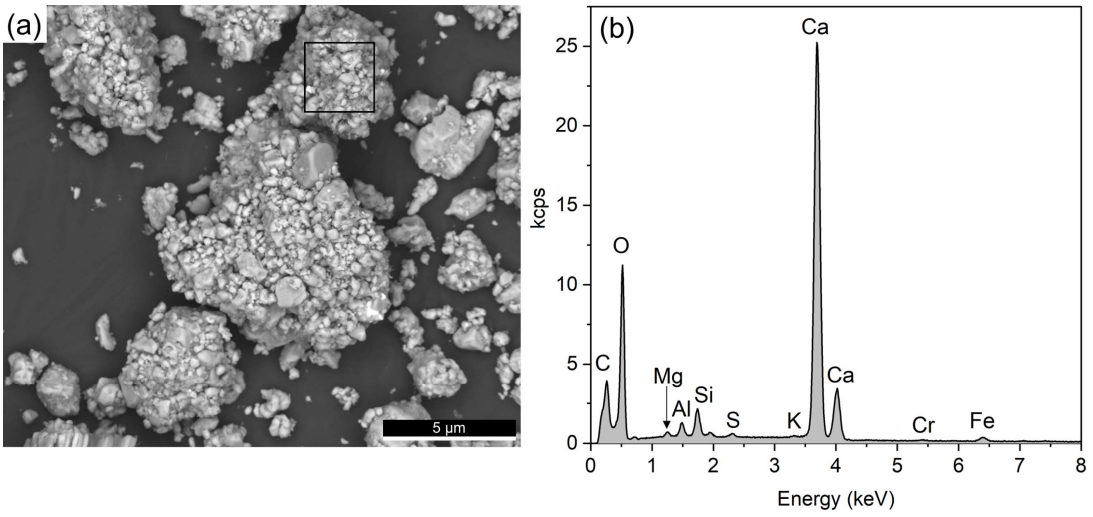

Figure S5.6. (a) SEM image of a limestone used for neutralization in the HPAL process and the (b) corresponding EDS spectrum of the boxed area in (a) showing a minor amount of Cr (<0.5 wt.%).

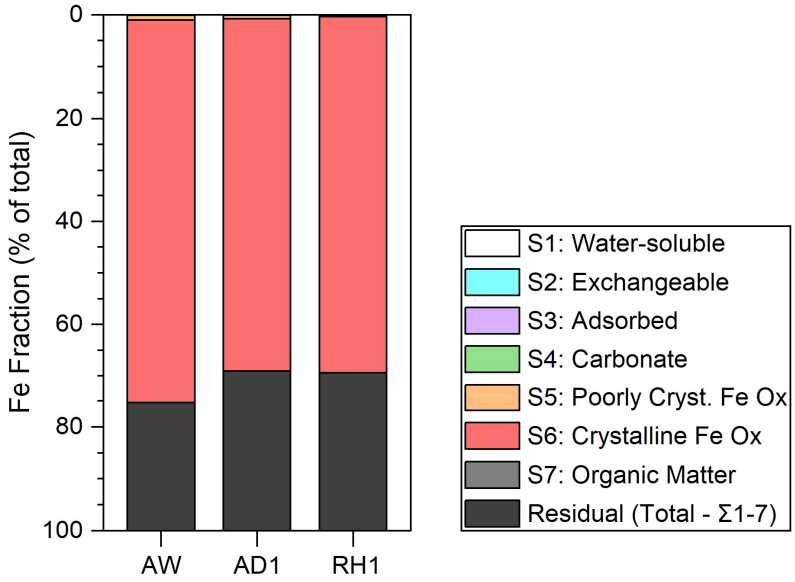

Figure S5.7. Fe partitioning in the representative samples from the active wet (AW), active dry (AD1), and rehabilitated (RH1) tailings. Ox – (oxyhydr)oxide

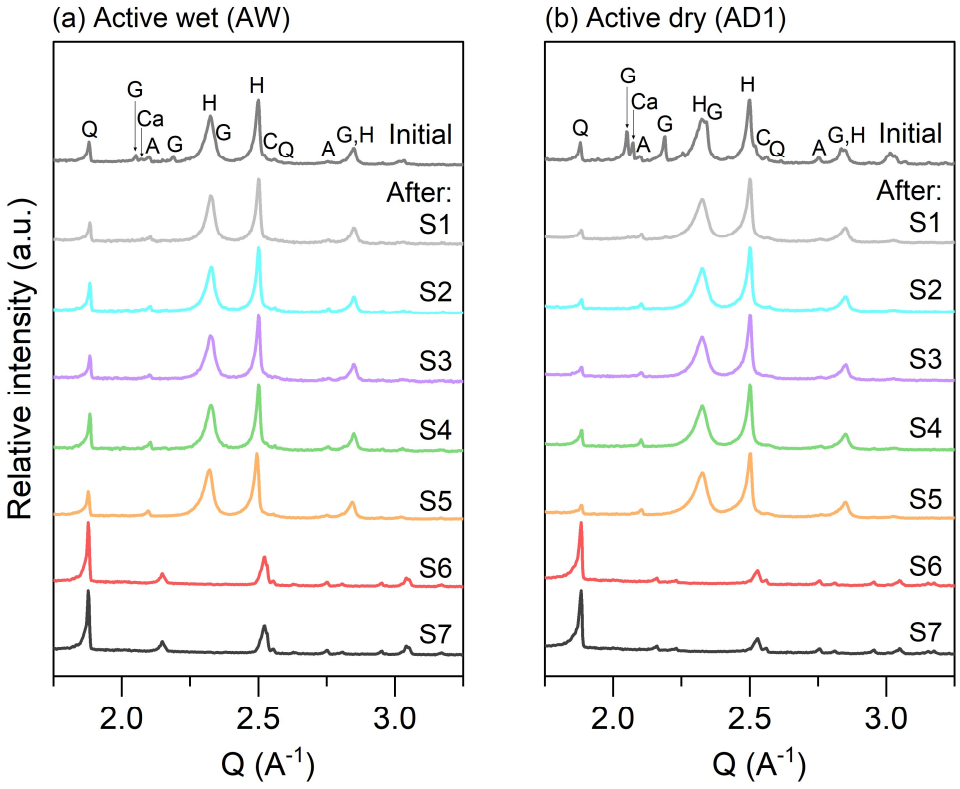

Figure S5.8. Powder XRD patterns of the residues of tailings samples (a) AW and (b) AD1 after each sequential extraction step. S1 – Water-soluble, S2 – Exchangeable, S3 – Adsorbed, S4 – Carbonate, S5 – Poorly crystalline Fe (oxyhydr)oxide, S6 – Crystalline Fe (oxyhydr)oxide, S7 – Organic matter

5.5.3. Supplementary tables

Table S5.1. Sequential extraction procedure adapted for the tailings. A solid-to-liquid ratio of 1:100 was applied for all except for organic Cr where 1:20 was employed.

Step	Target Fraction	Extractant	Conditions	References
S1	Water-soluble	Milli-Q water (~18.2 MΩ·cm)	1 h, 25 °C	Dold (2003)
S2	Exchangeable	1 M $MgCl_2$	1 h, 25 °C	Claff et al. (2010)
S3	Adsorbed	0.01 M $NH_4H_2PO_4$ (pH 8)	16 h, 25 °C	Delina et al. (2024)
S4	Carbonate	1 M NaOAc (pH 4.5)	5 h, 25 °C	Delina et al. (2024)
S5	Poorly crystalline Fe (oxyhydr)oxides	1 M HCl	8 h, 25 °C	Delina et al. (2024)
S6	Crystalline Fe (oxyhydr)oxides	6 M HCl	24 h, 75 °C	Delina et al. (2024)
S7	Organic matter	5% NaOCl (pH 8.5)	Boiling	Delina et al. (2024)

Note: For each extraction step, the extractant was added to the powdered sample in an acid-cleaned centrifuged tube, and mixed using a temperature-controlled orbital shaker at 250 rpm. Phase separation was done by centrifugation at 10,052*g* for 10 min. Each step was followed by an intermediate washing step with Milli-Q water (~18.2 MΩ·cm). The solid residue was freeze-dried while the extracts and washes were acidified with concentrated HCl (Aristar® VWR) and analyzed by ICP-OES.

Table S5.2. Major element composition of the tailings reported as oxide (wt.%) following standard methods (Bokhari & Meisel, 2017).

	Active Wet	Active Dry			Rehabilitated		
	AW	AD1	AD2	AD3	RH1	RH2	RH3
Al_2O_3	3.99	3.71	3.68	2.84	3.18	2.67	3.02
CaO	3.68	10.50	10.10	9.08	12.00	10.70	11.60
Cr_2O_3	1.88	2.07	2.17	1.74	1.8	1.5	1.5
Fe_2O_3	53.2	43.4	44.4	41.2	48.9	40.8	42.5
MgO	3.41	2.91	2.84	2.43	1.69	1.51	2.14
MnO	0.84	0.61	0.57	0.58	0.69	0.63	0.72
SiO_2	17.6	15.2	15.1	10.8	8.85	7.85	11.05
TiO_2	0.11	0.11	0.11	0.09	0.07	0.09	0.06

Table S5.3. Summary of the physicochemical characteristics and major ion composition of the water samples (see **Figure S5.1**) and the saturation indices of mineral phases calculated from the water chemistry. EC – electric conductivity, DO – dissolved oxygen

Sample	Active Dam		Outflow pond	
	W1	W2	W3	W4
Parameters				
Temperature (°C)	30.1	31.5	32.7	30.8
pH	7.8	7.8	8.0	7.5
Eh (mV)	366	372	390	397
EC (mS cm^{-1})	3.74	3.76	3.65	3.78
DO (mg L^{-1})	6.3	6.3	7.1	6.8
Major ions (mg L^{-1})				
Ca^{2+}	477	468	465	398
K^{+}	0.33	0.36	0.30	0.21
Mg^{2+}	237	225	221	176
Na^{+}	417	405	399	299
Cl^{-}	92.9	93.9	92.1	93.1
HCO_3^{-}	75.1	72.6	72.4	81.9
NO_3^{-}	*bdl*	693	*bdl*	*bdl*
SO_4^{2-}	1955	2409	1482	1968
Mineral saturation indices (SI)				
Anhydrite ($CaSO_4$)	-0.46	-0.40	-0.54	-0.49
Brucite ($Mg(OH)_2$)	-3.32	-3.38	-2.91	-4.06
Calcite ($CaCO_3$)	0.57	0.51	0.79	0.23
Dolomite ($CaMg(CO_3)_2$)	2.02	1.89	2.43	1.28
Epsomite ($MgSO_4 \cdot 7H_2O$)	-2.94	-2.90	-3.05	-3.03
Gypsum ($CaSO_4 \cdot 2H_2O$)	-0.28	-0.23	-0.37	-0.32
Halite (NaCl)	-6.13	-6.14	-6.14	-6.26
Magnesite ($MgCO_3$)	-0.18	-0.25	0.01	-0.58

bdl – below detection limit

Table S5.4. Elemental composition (in wt. %) from SEM-EDS point analysis of chromite, hematite, and alunite grains found in the tailings balanced to 100% with O.

Mineral types	Point	Chemical composition (wt.%)										
		C*	Na	Mg	Al	Si	S	Ca	Cr	Mn	Fe	O
Chromite	1	4.4	0.3	4.5	4.8	0.1	0.1	0.1	34.7	0.1	10.4	40.1
	2	*bdl*	*bdl*	2.9	4.5	0.2	*bdl*	*bdl*	43.1	*bdl*	16.1	33.0
	3	3.2	*bdl*	5.5	8.6	0.5	0.3	0.4	27.8	0.5	13.4	39.6
	4	1.0	*bdl*	2.4	5.1	0.1	*bdl*	*bdl*	38.9	0.7	15.8	34.3
	5	0.0	*bdl*	1.7	2.8	0.1	*bdl*	*bdl*	44.9	0.9	17.2	32.2
	6	8.3	*bdl*	4.4	4.3	0.8	0.3	0.1	22.8	0.4	12.3	46.2
	7	2.6	*bdl*	6.3	10.5	0.3	0.1	0.2	29.4	0.4	10.8	39.4
	8	0.2	0.1	5.7	4.6	0.4	0.1	0.1	41.0	*bdl*	13.9	33.9
	9	1.9	0.1	1.0	1.7	0.2	0.1	0.8	43.2	*bdl*	14.6	35.0
	10	1.5	*bdl*	0.8	1.9	0.2	*bdl*	0.5	41.9	*bdl*	17.9	34.2
	Min.	*bdl*	*bdl*	0.8	1.7	0.1	*bdl*	*bdl*	22.8	*bdl*	10.4	32.2
	Max.	8.3	0.3	6.3	10.5	0.8	0.3	0.8	44.9	0.9	17.9	46.2
	Median	1.9	0.1	3.7	4.6	0.2	0.1	0.2	40.0	0.5	14.3	34.7
	Ave.	**2.6**	**0.2**	**3.5**	**4.9**	**0.3**	**0.2**	**0.3**	**36.8**	**0.5**	**14.2**	**36.8**
Hematite	1	0.5	*bdl*	0.8	1.4	2.4	0.6	0.2	1.0	0.7	59.3	33.0
	2	0.2	*bdl*	0.8	1.4	2.4	1.0	0.4	1.0	0.6	59.4	32.8
	3	2.7	*bdl*	0.2	1.5	2.9	0.6	0.2	0.9	0.4	53.8	36.8
	4	0.5	*bdl*	0.2	1.0	1.5	0.6	0.2	1.0	0.7	61.9	32.3
	5	10.7	0.2	0.4	1.8	2.3	0.3	0.2	0.5	0.3	33.8	48.6
	6	*bdl*	*bdl*	2.9	2.7	4.7	1.2	1.7	1.0	0.9	50.3	34.5
	7	*bdl*	*bdl*	1.2	1.3	3.2	0.8	0.9	1.2	1.5	56.4	32.8
	8	4.4	0.7	1.6	2.1	3.1	0.4	0.3	0.9	0.6	46.3	39.6
	9	8.8	*bdl*	0.9	1.2	1.4	0.6	*bdl*	0.9	*bdl*	40.6	45.5
	10	3.7	*bdl*	0.4	0.8	1.4	0.7	*bdl*	1.3	*bdl*	54.5	37.4
	11	1.8	*bdl*	0.9	1.6	3.0	0.7	0.6	0.9	0.4	54.5	35.4
	12	8.2	*bdl*	3.5	2.5	3.7	0.8	0.2	0.5	0.5	33.7	46.5
	13	8.3	0.7	0.7	1.4	1.5	0.6	0.2	0.6	0.5	40.3	44.7
	14	5.7	*bdl*	0.1	0.7	1.5	0.5	0.4	0.7	0.5	49.2	40.3
	15	8.6	*bdl*	1.2	1.7	1.9	0.6	0.5	0.6	0.4	38.7	45.6
	Min.	*bdl*	*bdl*	0.1	0.7	1.4	0.3	*bdl*	0.5	*bdl*	33.7	32.3
	Max.	10.7	0.7	3.5	2.7	4.7	1.2	1.7	1.3	1.5	61.9	48.6
	Median	4.4	0.7	0.8	1.4	2.4	0.6	0.3	0.9	0.5	50.3	37.4
	Ave.	**4.9**	**0.5**	**1.1**	**1.5**	**2.5**	**0.7**	**0.5**	**0.9**	**0.6**	**48.8**	**39.1**
Alunite	1	13.6	*bdl*	0.7	11.8	0.6	6.8	*bdl*	0.3	5.5	*bdl*	60.6
	2	9.9	0.6	0.3	13.3	0.6	8.2	0.5	0.5	*bdl*	9.9	56.2
	3	*bdl*	0.2	*bdl*	19.4	0.4	14.5	0.3	0.8	0.1	16.8	47.2
	4	7.9	1.3	0.2	12.5	0.4	8.8	*bdl*	0.6	0.1	15.1	53.1
	5	14.5	*bdl*	0.7	10.4	0.7	6.1	*bdl*	0.3	*bdl*	6.1	61.1
	6	5.7	0.0	0.2	17.1	0.7	12.0	0.2	0.6	*bdl*	9.4	53.9
	7	4.1	0.6	0.7	15.7	1.2	10.5	0.3	0.8	0.1	15.7	50.1
	8	*bdl*	1.3	0.6	19.0	1.2	13.7	*bdl*	0.9	*bdl*	16.3	47.0
	9	6.8	1.0	0.5	14.3	0.8	10.7	*bdl*	0.8	*bdl*	11.5	53.7
	10	0.0	1.2	*bdl*	22.3	0.4	16.0	*bdl*	0.9	*bdl*	9.7	49.4
	11	9.2	0.1	0.5	13.0	1.2	7.8	0.1	0.5	*bdl*	12.4	55.2
	12	0.0	0.3	0.3	15.7	0.7	14.1	0.2	1.1	0.2	20.7	46.0
	13	0.0	0.7	*bdl*	19.7	0.3	15.7	0.1	0.7	*bdl*	13.6	48.0
	14	2.7	0.5	0.5	15.9	1.1	13.1	0.7	0.7	*bdl*	14.7	49.7
	15	15.6	0.2	0.3	9.8	0.4	5.1	0.2	0.3	*bdl*	6.6	61.6
	Min.	*bdl*	*bdl*	*bdl*	9.8	0.3	5.1	0.1	0.3	*bdl*	*bdl*	46.0
	Max.	15.6	1.3	0.7	22.3	1.2	16.0	0.7	1.1	5.5	20.7	61.6
	Median	6.8	0.6	0.5	15.7	0.7	10.7	0.2	0.7	0.1	13.0	53.1
	Ave.	**6.9**	**0.6**	**0.5**	**15.3**	**0.7**	**10.9**	**0.3**	**0.7**	**1.2**	**12.8**	**52.9**

*C values may be affected by C deposition in the SEM chamber during analyses but they were left in to account for the presence in some samples of a C signal from C-bearing minerals (e.g., calcite). *bdl* – below detection limit

Table S5.5. Cr K-edge EXAFS fitting results summarizing the local coordination environment around a central Cr atom for the reference minerals and the tailings.[a]

Sample	Atomic pair	CN	R (Å)	σ^2 (Å^2)	ΔE_0 (eV)	*R*-value
AW - Active (wet)	Cr-O_1	4.9 (0.5)	1.98 (0.02)	*0.001*	-4.6 (3.7)	0.017
	Cr-O_2	2.5 (0.9)	2.44 (0.04)	$\sigma_{Cr\text{-}O1}$		
	Cr-Cr/Fe_1[c]	3.8 (0.7)	2.95 (0.03)	*0.005*		
	Cr-Cr/Fe_2	5.2 (2.6)	3.43 (0.04)	*0.008*		
	Cr-Cr/Fe_3	8.4 (4.2)	3.69 (0.04)	*0.011*		
AD1 - Active (dry)	Cr-O_1	4.0 (0.5)	1.97 (0.02)	*0.001*	-4.6 (4.1)	0.020
	Cr-O_2	2.7 (0.8)	2.44 (0.04)	$\sigma_{Cr\text{-}O1}$		
	Cr-Cr/Fe_1	3.8 (0.6)	2.94 (0.03)	*0.005*		
	Cr-Cr/Fe_2	4.0 (2.6)	3.44 (0.05)	*0.008*		
	Cr-Cr/Fe_3	5.7 (4.4)	3.68 (0.05)	*0.011*		
RH1 - Rehabilitated	Cr-O_1	4.2 (0.4)	1.97 (0.01)	*0.001*	-3.2 (3.0)	0.015
	Cr-O_2	2.1 (0.6)	2.45 (0.03)	$\sigma_{Cr\text{-}O1}$		
	Cr-Cr/Fe_1	4.1 (0.5)	2.94 (0.02)	*0.005*		
	Cr-Cr/Fe_2	3.6 (2.1)	3.46 (0.04)	*0.008*		
	Cr-Cr/Fe_3	4.8 (3.6)	3.70 (0.05)	*0.011*		
Cr-hematite	Cr-O_1	*4*	1.97 (0.02)	0.001 (0.001)	-5.7 (4.2)	0.028
	Cr-O_2	*2*	2.43 (0.04)	*0.001*		
	Cr-Fe_{F+E}[b]	*4*	2.95 (0.03)	0.005 (0.001)		
	Cr-Fe_{C1}	*3*	3.46 (0.07)	0.008 (0.006)		
	Cr-Fe_{C2}	*6*	3.70 (0.06)	0.011 (0.006)		
Chromite	Cr-O	*6*	1.98 (0.01)	0.0009 (0.0006)	-7.1 (1.7)	0.039
	Cr-Cr_E	*6*	2.97 (0.01)	0.005 (0.001)		
	Cr-Fe_C	*4*	3.49 (0.03)	0.008 (0.003)		

[a] CN, coordination number; R, interatomic distance; σ^2, mean-squared atomic displacement; ΔE_0, change in threshold energy; and *R,* "goodness of fit" factor. Numbers in parenthesis are fit-determined standard errors. Constrained parameters appear in italics and without a parenthesis.

[b] F – face, E – edge, C – corner sharing

[c] Cr/Fe – pertains to Cr and Fe as their unique contributions to the EXAFS signal could not be distinguished due to their close atomic numbers

Chapter 6

Summary and Outlook

The research presented in this doctoral dissertation advances the fundamental understanding and holistic evaluation of Cr behavior from source to sink in lateritic environments affected by mining and processing operations. From field observations to atomic-scale investigations and using a suite of laboratory- and synchrotron-based experiments and analyses, I elucidated the binding of Cr to Fe (oxyhydr)oxides in laterites and mine tailings, I unraveled the drivers and mechanisms of Cr release and sequestration during lateritization and mine tailings formation, and I optimized a method to assess the potential mobility and environmental impact of Cr.

6.1. Chromium binding to Fe (oxyhydr)oxides in laterites and mine tailings

Iron(III) (oxyhydr)oxides (e.g., ferrihydrite, goethite, hematite) have been widely studied as excellent agents for the uptake of nutrients, trace elements, and contaminants. This is due to their high surface area and reactivity, low solubility, and high stability in nature (Cornell & Schwertmann, 2003). In lateritic environments where prevalent Fe(III) (oxyhydr)oxides co-occur with elevated concentrations of Cr, earlier sequential extraction studies (Quantin et al., 2002; Garnier et al., 2006) and Cr K-edge XAS (Fandeur et al., 2009a; Garnier et al., 2013) documented the significant association between Cr and Fe phases. However, what was clearly lacking at the beginning of my research, was direct structural and mechanistic evidence of Cr binding to Fe (oxyhydr)oxides in Ni laterites and mine tailings. This information is critical to ascertain their role in immobilizing Cr. To derive such information, I synthesized Cr-bearing Fe (oxyhydr)oxides via co-precipitation and adsorption (**Chapter 3**) and compared their local coordination environment with that of natural Ni laterite and mine tailings samples from the Philippines.

By comparing shifts in X-ray diffraction peaks and infrared spectroscopy (IR) bands between synthetic Cr-substituted Fe (oxyhydr)oxides and the Fe-rich limonite samples (Figure 3.1, Section 3.3.1), I derived qualitative evidence of metal-substitution for Fe(III) in natural goethite and hematite. However, the small difference in the octahedral radii between Fe(III) (0.645 Å) and Cr(III) (0.615 Å) compared with Fe(III) and other common pedogenic metals (e.g., Al(III) = 0.530 Å) and the presence of many other substituting cations (e.g., Ni, Co, Mn) made it difficult to pinpoint Cr substitution in these minerals. However, to address this, I have developed, tested, and validated a sequential extraction procedure (SEP) that specifically and

selectively targets Cr in Fe-rich laterites (see also Section 7.3). My results revealed that Cr can be structurally incorporated into or absorbed onto poorly crystalline and crystalline Fe (oxyhydr)oxides and that, using my SEP, these can be quantitatively differentiated. This work is published in *Environmental Science & Technology.*

In order to verify the binding mechanisms of Cr on laterite Fe (oxyhdr)oxides, I investigated its local bonding environment by applying a robust Cr K-edge EXAFS spectral fitting approach (**Chapter 4**). Contrary to previous EXAFS studies of aged, poorly crystalline ferrihydrite, that showed the substitution of Cr in all Fe sites (i.e., edge- and corner-sharing FeO_6 octahedra) (Charlet & Manceau, 1992; Hansel et al., 2003), my data revealed the presence of natural Cr-ferrihydrite resembling 'freshly' synthesized ferrihydrite, wherein Cr(III) polymerized with Fe(III) through edge-sharing octahedra only. Ferrihydrite is a typical precursor of crystalline goethite and hematite, and with these results, I was able to capture and describe the sequestration mechanism of Cr in Fe (oxyhydr)oxides. I showed that in the highly weathered limonites, Cr was mainly structurally incorporated as Cr(III) in goethite and hematite via substitution for Fe(III) in all its edge-sharing and corner-sharing octahedral sites. I also documented through EXAFS fitting that Cr(VI) adsorbed onto goethite as inner-sphere complexes with mononuclear edge-sharing (^2E) and monodentate mononuclear (^1V) geometries. These research results (**Chapter 4**) are in and advanced stage prior to submission to *Geochimica et Cosmochimica Acta.*

After I identified the binding mechanisms of Cr on natural laterite Fe (oxyhydr)oxides, I conducted preliminary experiments (detailed in **Appendix A**) to visualize these interactions at the atomic scale. Using (scanning) transmission electron microscopy (STEM), I gained first insights and was able to document the incorporation of Cr with a possible concentration gradient along the edges of goethite crystals. Oxidizing the Cr-bearing Fe (oxyhydr)oxides resulted in the leaching of Cr(VI) and its re-deposition and/or adsorption of Cr onto the surface of goethite, supporting my findings in **Chapter 4.** Although these findings need to be further developed and investigated, the preliminary results are relevant for understanding the nanoscale interactions that are often not discernable in the bulk analyses (e.g., XRD, EXAFS) like those presented in **Chapters 3 and 4.** Together with my findings in **Chapters 3 and 4**, these results uncovered the sequestration mechanisms of Fe (oxyhydr)oxides for Cr(III) as well as Cr(VI) during the lateritization of ultramafic rocks. However, I also demonstrated that they also serve as potential sources of oxidizable Cr, providing important insights for the monitoring of Ni laterite areas as well as other environments where potential oxidants like naturally occurring Mn phases or industrially used oxidizing agents (e.g., NaOCl for water treatment) occur.

Fe (oxyhydr)oxides, particularly hematite, also dominated the mine tailings resulting from the hydrometallurgical extraction of Ni and Co from the laterite ores. Both Fe and Cr were non-targeted metals that accumulated in these mine wastes, yet their interactions remained unknown

prior to this study. Investigating Cr in the mine tailings by combining spatially resolved electron microscopic and bulk Cr K-edge EXAFS and my own developed Cr SEP (**Chapter 3**) revealed that the majority of Cr became structurally incorporated into the secondary hematite. Hematite precipitates during the high pressure (sulfuric) acid leaching (HPAL) of the Fe (oxyhydr)oxide-rich Ni laterite ores, and through this process, Cr becomes immobilized in the mine tailings (**Chapter 5**; under review in *Environmental Science & Technology*). To further understand this process, I conducted initial laboratory-scale HPAL experiments, and my preliminary results confirmed the strong association between Cr and Fe during the dissolution of the laterite ore minerals and the re-precipitation of Fe as hematite (**Appendix B**). These results revealed that although the hydrometallurgical processing of Ni laterites initially dissolves and liberates Cr from these ores, it also creates optimal chemical pathways for the precipitation of highly stable, crystalline hematite, which effectively traps Cr.

Taken together, my results from Ni laterites to mine tailings demonstrated the important role of Fe (oxyhydr)oxides in sequestering Cr during geogenic (e.g., weathering) and anthropogenic (e.g., hydrometallurgical extraction) processes at play in lateritic environments. Elevated Cr levels in Ni laterite areas pose serious risks, including groundwater contamination, and by elucidating mechanisms through which Cr is immobilized, we can establish more effective strategies to mitigate its release and improve the safety of mining and processing practices. Moreover, new knowledge on the stability of these Cr-bearing Fe (oxyhydr)oxides, particularly within mine tailings, contributes to the development of circular economy strategies for managing these vast amounts of waste. Furthermore, deciphering the role of Fe (oxyhydr)oxides in Cr sequestration offers valuable perspectives on other natural and engineered settings where Cr and Fe would co-exist (e.g., red mud).

6.2. Tracing the fate and speciation of Cr from rocks to wastes

In a broader context, Fe (oxyhydr)oxides are secondary minerals representing an integral, albeit partial, element of the story. Understanding the occurrence of Cr in surface- and groundwaters of mining-impacted Ni laterite areas requires tracing its fate from the source ultramafic rocks to the Ni laterites and surrounding environments. This entails quantifying the changes in Cr speciation and the processes driving these transformations, such as mineral dissolution-reprecipitation, changes in oxidation-reduction, and interactions with both existing and newly formed solids via adsorption-desorption or structural incorporation. Chromium transformation from ultramafic rocks to Ni laterites via natural weathering processes is also just one part of the larger picture. Invariably, mining and processing of Ni laterite ores to extract valuable metals (e.g., Ni, Co) generates millions of tons of mine tailings which could serve as a vast sink for Cr. However, in the context of the fate of Cr in Ni laterite mining areas, mine tailings remain understudied.

Therefore, in my work, I followed the transformation pathways of Cr during the lateritization process from ultramafic rocks to limonites, by studying different unmined and mined Ni laterite profiles in the Philippines. Through complementary mineralogical and geochemical analysis, I could document an initial residual enrichment of Cr upon weathering of the host ultramafic rocks. However, in some cases, I also documented a remarkable decrease in Cr towards the surface (Figures 4.3-4.4, Section 4.3.1), implying significant changes in Cr speciation and mobility during the advanced stages of lateritization. By atomic-scale investigations of Cr and other key elements (i.e., Fe and Mn) in these profiles, I assessed the factors that influence the cycling of Cr during weathering using conventional and synchrotron HERFD-XAS techniques. I validated and cross-correlated these with an extensive set of mineral standards I prepared and synthesized in the laboratory (e.g., silicates, Fe (oxyhydr)oxides, Mn oxides). This way, I was able to determine the redistribution and redox transformations of Cr from the primary ultramafic phases to the secondary limonite minerals (see Figure 4.9, Section 4.4.3).

My detailed study in **Chapter 4** unraveled that when ultramafic rocks are weathered, Cr(III) is released from primary silicates and chromites and repartitioned into the dominant phyllosilicates in the saprolite zone. Chromium can be bound by structural incorporation such as in serpentine, or by adsorption in the case of smectite clays. As weathering proceeds, the dissolution of phyllosilicates releases Cr(III) once more, while the formation of secondary Fe (oxyhydr)oxides effectively sequesters it. One of the highlights of my work was the fact that I uncovered mechanistic evidence for the trapping of Cr by Fe (oxyhydr)oxides, initially by polymerization of Cr(III) with Fe(III) upon the formation of poorly crystalline Fe precursors (i.e., ferrihydrite). After weathering cycles, ferrihydrite crystallizes and transforms to goethite followed by hematite, in which Cr(III) isomorphically substitutes for Fe(III) and incorporates into the crystal structures.

Interestingly, advanced weathering of ultramafic rocks also produces Mn oxides, which are known as the primary oxidants of Cr in soils. This result in the unfavorable genesis of the far more toxic and mobile Cr(VI) species. Compared to the extensive laboratory studies demonstrating the Cr(III) to Cr(VI) oxidation by Mn(III/IV) (oxyhydr)oxides (Kim et al., 2002; Hausladen & Fendorf, 2017; Pan et al., 2017), my results provide one of the very few evidence for this same redox dynamics in natural lateritic regoliths. This could account for the leaching of Cr towards the surface of the laterite profile and the elevated Cr(VI) concentrations in waterbodies situated in Ni laterite areas (Gunkel-Grillon et al., 2014; Delina et al., 2020). Nevertheless, on a positive note, the acidic conditions in the limonite zone and the adsorptive properties of Fe (oxyhydr)oxides limit the mobility of Cr(VI) by promoting its adsorption; hence, the detectable Cr(VI) concentrations in the limonite zone. Overall, I emphasized in my work that the occurrence of Cr(VI) in ultramafic and lateritic areas is not a direct consequence of anthropogenic activities (e.g., mining) but is a natural phenomenon driven by an interplay of

species actively involved in Cr redox and speciation and promoted by environmental factors, particularly in tropical regions where the weathering rate is accelerated.

To shed light on what becomes of Cr after the hydrometallurgical extraction of Ni (±Co), I studied mine tailings resulting from HPAL or high pressure acid leaching of Fe (oxyhydr)oxide-rich laterite ores. I characterized solid and liquid mine wastes from an actively used tailings dam and a rehabilitated tailings dam decommissioned more than 10 years ago (Figure 5.7, Section 5.5.2) (**Chapter 5**). Compared with earlier studies which predicted the occurrence of dissolved Cr(VI) under oxidizing HPAL conditions (Sobol, 1969; Whittington & Muir, 2000; Buarzaiga et al., 2003), I found no Cr(VI) in the mine tailings. I documented that Cr was present solely as Cr(III) and that it was primarily immobilized in the hematite that formed in the HPAL process. I confirmed this with my preliminary laboratory-scale HPAL experiments (**Appendix B**) which showed that both Cr and Fe follow a similar fate from dissolution of the laterite Fe (oxyhydr)oxides to the precipitation of hematite in solid HPAL residue. This suggests isomorphic substitution of Cr(III) for Fe(III) during hematite formation, and this immobilization of Cr by hematite explains the absence of Cr in the later-formed minerals (e.g., gypsum) in the actual tailings, as well as in the interacting waters I documented in **Chapter 5**. I also highlighted that the lack of significant differences between the redox and speciation of active and rehabilitated tailings demonstrate the stability of Cr-hematite under various conditions (e.g., waterlogged *vs.* dry) and even after long-term storage (>10 years) and rehabilitation.

6.3. Potential mobility and long-term behavior of Cr in Ni laterite mining environments

One goal of my doctoral research was to develop a Cr-specific sequential extraction procedure or SEP to determine the partitioning of Cr in iron-rich laterites. I had this aim because specific associations between Cr and the various mineral phases dictate its bioavailability, potential mobility, and transport mechanisms. Although complementary high-resolution analyses (e.g., electron microscopy, synchrotron-based XAS) help provide important insights into the partitioning of Cr, such methods are often not accessible or practical for routine analysis by researchers and stakeholders. For that, SEPs are far more useful. Sequential extractions are widely used to study metal partitioning, but they are often not specific and are confronted with problems, including poor selectivity of reagents, redistribution of metals, and incomplete dissolution of minerals (e.g., Fe (oxyhydr)oxides). Many of these drawbacks have been observed in earlier sequential extractions of Cr (Becquer et al., 2006; Delina et al., 2020). More importantly, prior to my doctoral research there was no SEP that was optimized for laterites or for Cr. Most SEPs were developed for cationic species (Gleyzes et al., 2002), and thus, when applied to Cr, they often underestimate the distribution of adsorbed Cr(VI) oxyanions.

By robust calibration with a wide range of synthetic and natural Cr-, Al-, and Fe-bearing mineral standards and certified laterite reference materials, I documented and validated an optimized SEP tailored to Cr in iron-rich laterites (Figure 3.3, Section 3.3.3) (**Chapter 3**). Major advantages over existing SEPs include: (1) quantification of strongly adsorbed Cr; (2) efficient dissolution of more resistant metal-substituted Fe phases; and the (3) prevention of overestimating organic Cr. When critically evaluated with non-Cr and non-laterite specific methods, my new SEP demonstrated up to seven times higher Cr recovery in Philippine laterite samples. The new SEP also efficiently partitioned Cr from the studied mine tailings in **Chapter 5,** as evidenced by XRD characterization at each step (Figure 5.6, Section 5.3.3) of the SEP linking the nominal target phase to the actual phases mobilized.

The sequential extraction procedure that I optimized offers a valuable characterization tool for monitoring and predicting pathways for the environmental release and transport of Cr. Perhaps one of the most important applications of the new SEP was the quantification of easily mobilizable Cr fractions (water-soluble, exchangeable, adsorbed) from the laterites and mine tailings since these can be released under normal environmental conditions, thus, representing a higher risk of affecting the environment or being bioavailable for organisms. For example, exchangeable Cr, targeted by $Ca(NO_3)_2$ or $MgCl_2$, represents weakly-bound Cr that is readily released upon changes in ionic strength (e.g., during interaction with saline waters). Meanwhile, adsorbed Cr is likely to be mobilized in the presence of competing ions (e.g., phosphate in agricultural drainage). My SEP data from representative Philippine Ni laterite samples (**Chapter 3**) showed that while the majority (>90%) of Cr was hosted in more recalcitrant Cr fractions, up to a thousand mg kg^{-1} of Cr occurred as easily mobilizable Cr(VI), comparable with Cr(VI) concentrations found in other Ni laterite deposits worldwide (Gunkel-Grillon et al., 2014; Economou-Eliopoulos et al., 2016). On the other hand, easily mobilizable Cr fractions were not detected in all mine tailings, corroborating the negligible total Cr and Cr(VI) concentrations observed in the interacting waters (**Chapter 5**). More importantly, by comparing the partitioning of Cr between the active and rehabilitated tailings, I was able to gain insights into the long-term behavior of Cr.

Knowledge of the potential mobility and long-term behavior of Cr is crucial in the context of the metal-reliant global energy transition where the demand for Ni and Co is expected to continue to rise in the coming decades. With the consequent increase in mining and processing operations in the next decades, we can now better pinpoint areas where we would expect Cr(VI) and based on these, identify better strategies for water quality management and sustainable mining and processing operations.

6.4. Future Directions

My results provide fundamental new insights into the geochemical controls and mechanisms that dictate the fate and mobility of Cr species in Ni laterite areas. Although I closed many previously open knowledge gaps, my findings also raised many new questions that need to be addressed to further improve our knowledge of the (bio)geochemical pathways of Cr in ultramafic and lateritic environments across multiple fronts. These present extensive opportunities for future research.

With my findings in **Chapter 4**, I demonstrated the transformation pathways of Cr from primary ultramafic to secondary laterite minerals. Although the Ni laterite profiles studied in this work present mineral compositions commonly found in most worldwide Ni laterite deposits (Fu et al., 2014; Aiglsperger et al., 2016; Ulrich et al., 2019), there is still an open question about the speciation and binding mechanisms of Cr in other mineral phases that could be present and be more dominant in other deposits. For instance, in clay-rich deposits like in Murrin Murrin, Western Australia, the smectite zone can be as thick as 25 m. Gaudin et al. (2005) detected Cr in all types of smectites in this layer but did not provide enough analysis to ascertain the redox and binding of Cr. Although I have shown an example of Cr(III) adsorption in smectite (i.e., nontronite) in my work, there are many other types of smectite clays (e.g., dioctahedral – montmorillonite, beidelite; trioctahedral – saponite) that have been found in Murrin Murrin and other clay type deposits (Tauler et al., 2023) where different species of Cr could bind differently (e.g., substitution, interlayer cation exchange, adsorption, surface precipitation). The association and binding mechanism of Cr with smectites and the quantification of Cr species developing under such clay-forming conditions could be valuable for evaluating the potential mobility and toxicity of Cr in areas mining and processing clay-rich Ni laterite deposits.

I documented in **Chapter 5** the fate of Cr in tailings that were generated, stored, and rehabilitated after HPAL processing of laterites. While I unraveled that Cr has been so far stable in the solid phase after >10 years of rehabilitation, it is important to assess the effect of the vegetative cover on the mobility of Cr in rehabilitated tailings since organic acids from root exudates and siderophores can induce proton- and ligand-promoted dissolution of Cr-bearing minerals like hematite (Lin et al., 2018). It would be relevant to experimentally test the effect of rhizosphere organic acids (e.g., citric, oxalic, formic acid) on the leaching of Cr from the mine tailings. Similar studies have been documented for heavy metal leaching from Fe mine tailings (Geng et al., 2020), As from Pb-Zn mine tailings (Wang & Mulligan, 2013), and Pb, Cd, Zn, and Cu from alkaline and acid mine soils (Ding et al., 2013). What is also crucial to understand is the uptake and bioaccumulation of Cr in crops grown on the mine tailings as certain plant species can accumulate high levels of Cr (Ullah et al., 2023) occasionally exceeding the safe limits for human intake (Ahmed, 2016).

The detailed characterization of mine tailings presented in this study also raises questions about circular economy strategies for these mine wastes. For example, there is a growing interest in the recovery of critical metals like Sc from wastes and various resources (Salman et al., 2022). Scandium has been found in Ni laterite deposits worldwide (Aiglsperger et al., 2016; Ulrich et al., 2019), and according to Gibaga et al. (2022), Philippine Ni laterite deposits also have significant Sc concentrations. However, it was not until recently that Sc was recovered through HPAL from Philippine Ni laterite ores. Thus, I would expect to detect previously non-targeted Sc in the studied mine tailings. It would, therefore, be of great relevance to explore the speciation of critical metals like Sc for their potential recovery. Alternatively, waste valorization or reprocessing these mine wastes into raw materials presents a promising area for research. In fact, there have already been initial efforts to refine hematite from HPAL residues for steel production (Ang et al., 2017). Nonetheless, in every case, it is crucial to follow the behavior of Cr and ensure its environmental mobility is effectively controlled. Furthermore, while this study represents a significant step towards understanding the fate of Cr in mine tailings generated from HPAL, it also emphasizes the need for research evaluating the occurrence of Cr in the different mine wastes resulting from other types of metallurgical treatments.

Finally, future research is also warranted to compare Cr speciation obtained from the optimized Cr SEP (**Chapter 3**) and from synchrotron-based XAS techniques. Although in this research, XANES and EXAFS analysis have been used to complement our SEP data, it could also be aimed to validate each sequential extraction step and assess each method's (SEP versus XAS) uncertainties and limitations, similar to the study on P speciation by Gu et al. (2020). It would also be beneficial to test the effectiveness of the optimized Cr SEP to the other types Ni laterite ores (e.g., clay type) and mine wastes mentioned above.

Appendix A

Visualizing chromium binding to iron (oxyhydr)oxides

Ruth Esther G. Delina[1,2], Jeffrey Paulo H. Perez[1], Vladimir V. Roddatis[1], Anja Schreiber[1], Liane G. Benning[1,2]

[1] GFZ German Research Centre for Geosciences, Telegrafenberg, 14473 Potsdam, Germany

[2] Department of Earth Sciences, Freie Universität Berlin, 12249 Berlin, Germany

The data presented in this Appendix are preliminary results from experiments and atomic-scale investigations on how Cr is bound to synthetic iron (oxyhydr)oxides, and this story will be further expanded and concluded after the viva.

A1. Introduction

Iron(III) (oxyhydr)oxides such as ferrihydrite, goethite (FeOOH), and hematite (Fe_2O_3) are known for their widespread occurrence in soils and sediments, where they can serve as sinks for nutrients, critical metals, and contaminants (Brown et al., 1999; Cornell & Schwertmann, 2003). Owing to their usual small particle size and thus high surface areas, as well as high density of reactive sites, these minerals act as effective sorbents (Cornell et al., 2003). They also have crystal structures (Cornell & Schwertmann, 2003) that allow them to structurally accommodate divalent (e.g., Ni^{2+}, Cu^{2+}, Zn^{2+}), trivalent (e.g., Cr^{3+}, Co^{3+}, Mn^{3+}) and some tetravalent (e.g., Pb^{4+}, Tc^{4+}, Si^{4+}) cations by partial substitution for Fe(III) (Kaur et al., 2009; Liu et al., 2018; Scullett-Dean et al., 2023). Because of their ubiquity, low solubility, and high stability in nature (Cornell & Schwertmann, 2003), the geochemical uptake of trace elements onto and into the structures of Fe (oxyhydr)oxides play a crucial role in controlling the mobility and availability of metals in the environment.

Various soils contain <0.1 to >50% Fe (oxyhydr)oxides (Schwertmann, 1991). Specifically relevant to this study are soils derived from the weathering of ultramafic rocks that ultimately form iron-rich laterites which consist mainly of Fe phases, contributing up to 90% of the bulk mass of the soils (Ulrich et al., 2019; Delina et al., 2020). Such laterites also contain elevated amounts of potentially toxic elements, including chromium. Chromium is characterized by the different toxicities of its two most stable oxidation states (III and VI). In contrast to Cr(III), a vital micronutrient (Anderson, 1997), exposure to Cr(VI) causes skin damage and organ

complications and promotes stomach, bronchogenic, and nasal cancers (Katz & Salem, 1994). Concentrations of Cr(VI) in natural waterbodies associated with ultramafic rocks can be as high as 73 µg L^{-1} (Fantoni et al., 2002; McClain & Maher, 2016), while in mining-impacted lateritic environments, they can reach up to 1620 µg L^{-1} (Gunkel-Grillon et al., 2014; Delina et al., 2020), far exceeding international drinking water standards (50–100 µg L^{-1}) (USEPA, 2006; WHO, 2017).

Fe (oxyhydr)oxides have been identified as significant hosts for Cr in laterites, as well as in the resulting mine tailings after processing. In **Chapters 3 and 4**, I have already shown that both Cr species occur in laterites, with Cr(III) substituting for Fe(III) and stabilizing the crystal structure of Fe (oxyhydr)oxides or it being present as the oxidized Cr(VI) primarily adsorbed onto Fe mineral surfaces. I have also documented through XAS how the formation of Fe (oxyhydr)oxides, from ferrihydrite to hematite, efficiently sequesters Cr during the weathering of ultramafic rocks into laterites (see **Chapter 4**). However, the nanosized occurrence of Fe (oxyhydr)oxides in highly weathered laterites and tailings prevents a direct visualization of the binding mechanisms of Cr on these Fe (oxyhydr)oxides. Therefore, my goal with this study was to synthesize Cr-bearing Fe (oxyhydr)oxides, and use them as synthetic analogs to derive nanoscale mechanistic evidence for the uptake of Cr(III) during their formation and oxidation to Cr(VI).

A2. Methods

A2.1. Mineral synthesis

Fe (oxyhydr)oxides (i.e., goethite, hematite, ferrihydrite) were co-precipitated with Cr using standard procedures adapted from Schwertmann and Cornell (2000) and further detailed in **Chapter 3**. In brief, Cr-goethite was synthesized by adding 45 mL of 0.2 M $Fe(NO_3)_3 \cdot 9H_2O$ to a mixed solution of 135 mL of an alkaline Cr solution (0.1 M $Cr(NO_3)_3 \cdot 9H_2O$ and 1 M NaOH) and 64 mL of 1 M NaOH. The resulting slurry was aged for 120 d at 70°C and shaken occasionally. Adsorbed ions and amorphous phases were removed from the precipitates by a 2 h treatment with 3 M H_2SO_4 at 50°C and at a solid to liquid ratio of 1:100, followed by washing with Milli-Q water (~18.2 MΩ·cm) and oven-drying at 50°C for 24 h (Bousserrhine et al., 1999). Cr-hematite was prepared by vigorously mixing $Fe(NO_3)_3 \cdot 9H_2O$ and 0.6 g of $Cr(NO_3)_3 \cdot 9H_2O$ into a 0.01 M HNO_3 at 98°C (Liu et al., 2019). After 25 d of aging at 98°C, the precipitates were washed with 0.25 M HCl (1:100) for 2 h and then Milli-Q water until a pH >5. The washed precipitate was oven-dried at 70°C. Cr-ferrihydrite was made by dropwise addition of 1 M NaOH to 150 mL of mixed solution of 0.17 M $Fe(NO_3)_3 \cdot 9H_2O$ and $Cr(NO_3)_3 \cdot 9H_2O$ until pH 7 was reached (Schwertmann & Cornell, 2000). The slurry was

washed with Milli-Q water through eight cycles of centrifugation and dried in a vacuum desiccator to prevent possible transformation to crystalline Fe (oxyhydr)oxides.

A2.2. Sodium hypochlorite (NaOCl) treatment

To investigate the binding mechanism of Cr after oxidative reactions, the Cr-bearing Fe (oxyhydr)oxides were treated with an oxidizing 5% NaOCl solution (pH 8.5) at boiling temperature for 30 min following NaOCl extractions applied in soils (Shuman, 1983; La Force & Fendorf, 2000). The supernatant was separated by centrifugation at 10,052*g* for 10 min and analyzed for Cr and Fe concentrations by inductively coupled plasma optical emission spectrometry (ICP-OES) using a Varian 720-ES spectrometer (detailed in **Chapter 3**).

A2.3. Characterization and atomic-scale investigation

Mineralogical characterization of the Cr-bearing Fe (oxyhydr)oxides was performed through X-ray diffraction (XRD) and infrared (IR) spectroscopy. Powdered samples for XRD analyses were loaded into 0.5-mm glass capillaries and analyzed using a STOE STADI P diffractometer with two DECTRIS MYTHEN2 R detectors and operating at 40 kV and 40 mA. The measurements were done in transmission mode applying Ag Kα radiation (λ = 0.55941 Å) over a Q scan range of 0 to 13.42 $Å^{-1}$. Using a ThermoFisher Nicolet iS5 FTIR spectrometer with an iD7 diamond attenuated total reflectance (ATR) accessory, the IR spectra of the samples were collected in the 4000-400 cm^{-1} range after coadding 64 scans obtained at a resolution of 4 cm^{-1}. The minerals were also observed under a FEI Quanta 3D FEG scanning electron microscope (SEM) coupled with an energy dispersive spectroscopy (EDS) system to determine their morphology. SEM images of the carbon-coated samples were collected at high vacuum mode, 20 kV, and 60 pA, using an Everhart Thornley secondary electron detector. Chromium and Fe concentrations of the minerals were determined using ICP-OES (Varian 720-ES) after aqua regia digestion (full details of these methods can be found in **Chapter 3**).

In addition, high-resolution imaging and analyses of the synthesized phases by transmission electron microscopy (TEM) were acquired. For this, dry powder or focused ion beam (FIB) sections of the Cr-bearing Fe (oxyhydr)oxides before and after treatment with NaOCl were examined under a Thermo Fisher Scientific Themis Z (3.1) operated at 300 kV and equipped with an FEI Super-X 4-detector EDX system, a Gatan Quantum 1065 ER imaging filter continuum (EELS/EFTEM) and a Gatan One-View CCD.

A3. Preliminary results

Our initial results indicate that the NaOCl treatment did not change the Fe bulk structure of the Cr-bearing Fe (oxyhydr)oxides, and no secondary Fe phases were detected in the XRD patterns. However, we could document the release of a significant amount of Cr, ranging from 16 to 61% of the total Cr concentration in the samples. The NaOCl extracts showed faint to intense yellow colors, implying the oxidation of Cr(III) to Cr(VI) since chromate anions give off a yellow tinge. In particular, the Cr-goethite leachate yielded the highest proportion of extracted Cr and showed the strongest yellow tinge. Below, we discuss the results of the work carried out so far to assess the binding mechanisms of Cr during the formation and oxidation of Cr-goethite. The Cr-ferrihydrite and Cr-hematite work is still pending.

Elemental mapping of the Cr-goethite sample prior to NaOCl treatment shows that Cr was seemingly distributed throughout the Fe (oxyhydr)oxides (**Figure A1 a-b**). Only by examining the Cr distribution in the FIB cross-sections could we confirm that there was an apparent high Cr signal intensities on the edges of the goethite crystals (**Figure A1 c-d**), suggesting surface enrichment of Cr during the formation of Cr-goethite crystals. Previous studies on synthetic Cr-goethite have suggested heterogeneous distribution and/or accumulation of Cr on the goethite surface but have not provided conclusive proof (Bousserrhine et al., 1999; Singh et al., 2002b; Choppala & Burton, 2018).

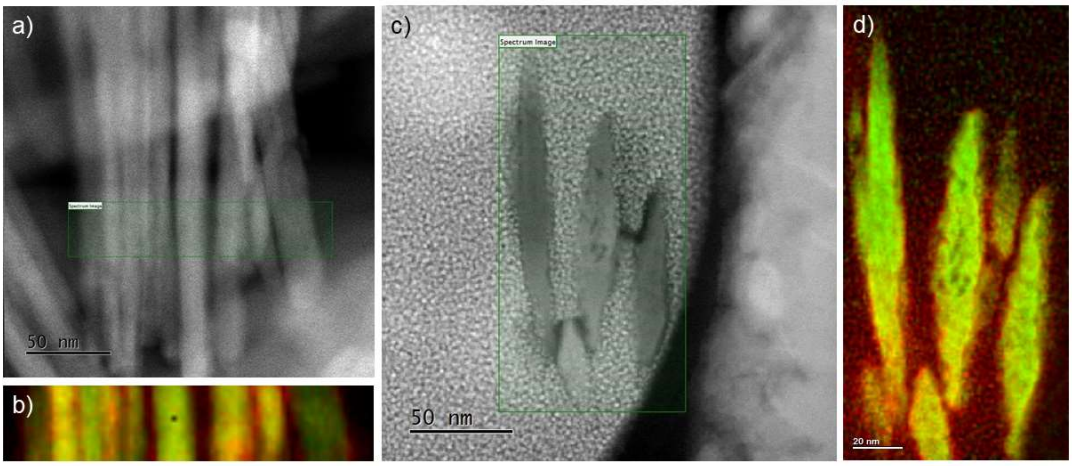

Figure A1. (a) TEM image of Cr-goethite deposited on a TEM grid (not FIB sectioned) before NaOCl treatment and the (b) corresponding EDX elemental map of the inset showing the distribution of Cr (red) and Fe (green). (c-d) A FIB cross-section of the Cr-goethite further looks into the distribution of these metals and, documenting the distribution of Cr within the goethite crystals at the edges.

This surface enrichment of Cr became even more evident after the NaOCl treatment (**Figure A2**). High resolution TEM (HRTEM) imaging coupled with EDX mapping (**Figure A3 a-b**) showed an irregular distribution of Cr along the edges of the treated Cr-goethite. Moreover, fast

Fourier transform (FFT) patterns of the HRTEM images revealed the presence of two different phases (**Figure A3c**): an inner phase with a goethite-like structure, and an exterior "shell" with a structure that is not yet clear what it is and needs to be further studied. EDX mapping combined with electron energy loss spectra (EELS) showed the occurrence of Cr mainly in the outer shell of the leached goethite. Based on these results, we hypothesize that the oxidation of Cr-goethite leaches Cr from the goethite crystal structure, and reprecipitates it on the surface of the goethite crystals, forming a secondary phase with a structure and identity of which still needs to be elucidated. This is supported by a previous study (Lee & Hering, 2005) where they followed the oxidative dissolution of $Cr(OH)_3$ with NaOCl. Their results suggested that Cr(VI) was adsorbed on the surface and that the NaOCl treatment led to the formation of Cr(VI)-Cr(III) solid precipitates on the surface of the Cr(III) hydroxide. Our FFT and EELS data indicate that our new precipitate is not Cr(III) hydroxide, but further analysis will follow to confirm the identity of the formed phase and the speciation of the outer Cr-rich shell. Nevertheless, these preliminary results provide a first direct visualization of the fate of Cr(III) in Cr-substituted Fe (oxyhydr)oxides – as exemplified above for goethite – and its fate upon oxidation to Cr(VI) by strong oxidants. These results support my findings in **Chapter 4,** highlighting the structural incorporation and adsorption of Cr onto Fe (oxyhydr)oxides as the main sequestration mechanisms for Cr during laterite formation. They also provide important insights on the potential release of Cr in environments where natural oxidants exist (e.g., Mn phases, ROS).

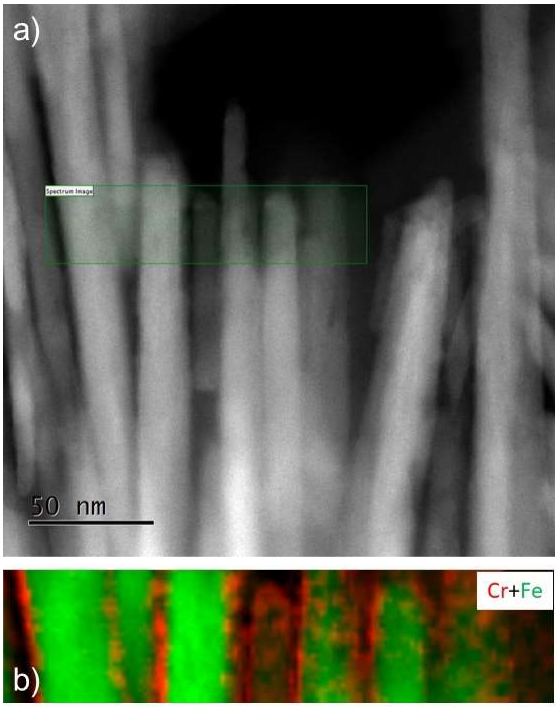

Figure A2. (a) TEM image of Cr-goethite after NaOCl extraction and the (b) corresponding EDX elemental map of the boxed area.

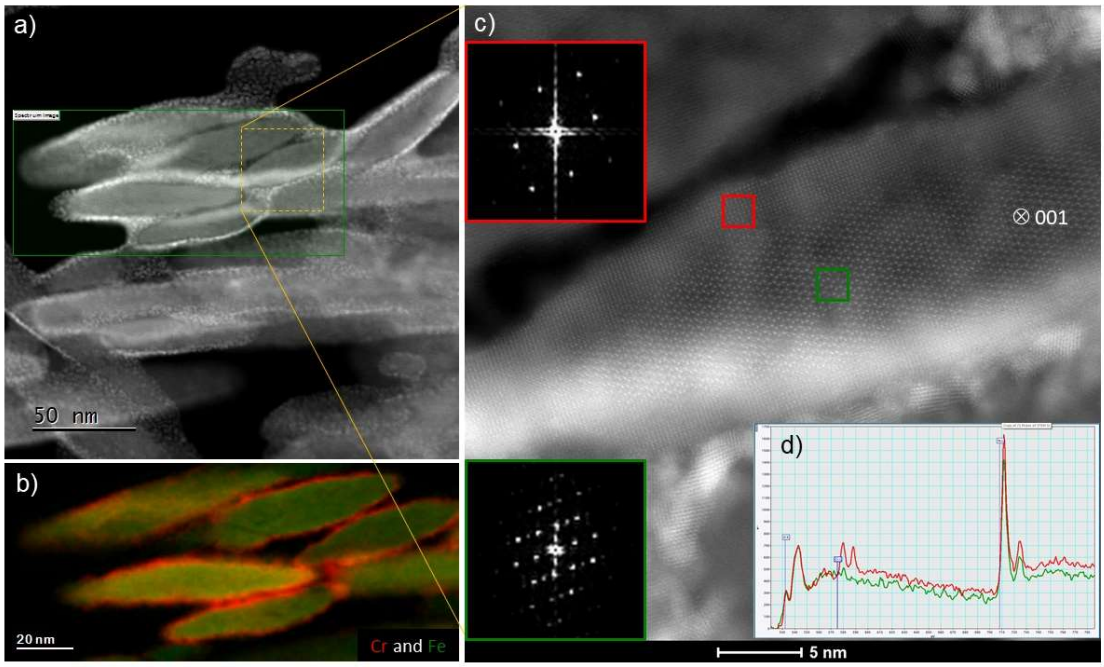

Figure A3. (a) High resolution TEM image of a FIB section of NaOCl treated Cr-goethites, (b) the EDX elemental map of the green boxed inset in (a), and (c) an enlarged figure of the yellow boxed area in (a). The fast Fourier transform (FFT) patterns and (d) electron energy loss spectroscopy (EELS) spectrum correspond to the red and green boxes in (c) highlighting the two different phases: goethite on the center (green box) and the unidentified phase along the edge (red box).

Appendix B

Investigating chromium evolution during high pressure acid leaching of nickel laterite ores

Ruth Esther G. Delina[1,2], Keith Batemann[3], Alicja Lacinska[3], Finlay Banks[3,†], Matthew Vosper[3], Jeffrey Paulo H. Perez[1], Liane G. Benning[1,2]

[1] GFZ German Research Centre for Geosciences, Telegrafenberg, 14473 Potsdam, Germany

[2] Department of Earth Sciences, Freie Universität Berlin, 12249 Berlin, Germany

[3] British Geological Survey, Natural Environment Research Council, Environmental Science Centre, Keyworth, Nottingham NG12 5GG, United Kingdom

[†] Present address: Sevenoaks Environmental Consultancy Ltd, Pembury, Tunbridge Wells TN2 4JU, United Kingdom

The data presented in this Appendix are preliminary results from experiments and laboratory analyses performed during and after a 2-week exchange visit at the British Geological Survey.

The results will be further evaluated and the manuscript expanded after the viva.

B1. Introduction

Nickel (Ni) and cobalt (Co) are technology-enabling metals that play a significant role in the global transition to cleaner energy sources. The energy transition has driven a significant increase in the demand for Ni and Co, leading to greater mining and new processing efforts in the coming decades (Bahini et al., 2024; Dilshara et al., 2024). With the decline in high-grade Ni and Co resources (e.g., sulfide ores), the mining industry has shifted to utilizing and advancing processing technologies in particular for lower-grade bulk tonnage Ni (±Co) laterite deposits (Mudd, 2010) that generate vast quantities of liquid and solid wastes containing potentially toxic metals (e.g., chromium) (Marsh et al., 2013; Aitken & Maluly Kemeid, 2016).

Chromium (Cr) is naturally enriched in Ni laterite deposits, mainly occurring as Cr(III). However, significant concentrations of the more toxic, mobile, and carcinogenic Cr(VI) species has been detected in Ni laterite deposits and surrounding waters at levels above the global regulatory limits for drinking water (50-100 µg L^{-1}) (Gunkel-Grillon et al., 2014; Economou-

Eliopoulos et al., 2016; Delina et al., 2020). Previous studies in the Philippines, one of the world's largest producers of Ni laterite ore (USGS, 2023), have shown significant Cr(VI) concentrations in Ni laterite ores (see **Chapter 3 and 4**). However, no traces of Cr(VI) were detected in mine tailings generated after high pressure acid leaching and extraction of Ni and Co from these ores (see **Chapter 5**), raising questions on the possible detoxification of Cr. The main goal of this study was to trace the fate of Cr during hydrometallurgical processing of laterites and to elucidate the underlying processes that control its speciation and mobility in the resulting mine tailings.

High pressure acid leaching (HPAL) is a hydrometallurgical extraction technique mainly used for processing Ni and Co from the limonite or Fe (oxyhydr)oxide-rich layer of Ni laterites (Whittington & Muir, 2000). In this process, laterite ores are reacted with sulfuric acid under high temperature (230-270 °C) and pressure (33 to 55 bar). Under these conditions, Ni and Co are leached from the ore because the HPAL solubilizes host (oxyhydr)oxides (e.g., goethite (FeOOH)) (Eq. 1-3) in the ores and transforms the Fe via a dissolution-precipitation pathway into Fe oxide and sulfate minerals (Whittington & Muir, 2000; Ucyildiz & Girgin, 2017).

$$2FeOOH_{(s)} + 3H_2SO_4 \rightarrow Fe_2(SO_4)_{3(aq)} + 4H_2O \quad (1)$$

$$NiO_{(s)} + H_2SO_4 \rightarrow NiSO_{4(aq)} + H_2O \quad (2)$$

$$CoO_{(s)} + H_2SO4 \rightarrow CoSO_{4(aq)} + H_2O \quad (3)$$

$$Fe_2(SO_4)_{3(aq)} + 3H_2O \rightarrow Fe_2O_{3(s)} + 3H_2SO_4 \quad (4)$$

Hematite (Fe_2O_3) is the main Fe oxide precipitated (Eq. 4) during the HPAL process and in **Chapter 5**, we documented its immobilization of Cr in HPAL tailings. In this study, we aimed to test and validate the observations we documented on the natural Ni laterite ores and therefore conducted HPAL experiments on limonite samples from the Philippines to follow and to derive mechanistic information about the transformation pathways of Cr from the laterite ores to the mine tailings.

B2. Methods

B2.1. Experimental set-up

High pressure acid leaching batch experiments were carried out at 250 °C and 40 bar in 150-mL Valtech Ltd digestion vessels. Ore slurries with 30 wt.% solids were prepared with deionized (DI) water, followed by the addition of technical grade sulfuric acid (96–98%) at an acid-to-ore ratio of 0.30. The start of the reaction, hereafter referred to as t = 0 min, was defined when the target temperature was reached. Individual batch experiments were quenched after 30, 60, 90 and 120 min of reaction, and after allowing the respective autoclave to cool to room temperature for approximately 20 min using tap water circulation, the autoclave contents,

together with the initial slurry were prepared for analyses. The metal-rich, or as typical in the field termed 'pregnant leach solution' (PLS), were separated using stacked 0.45-μm and 0.2-μm Nuclepore™ syringe filters, while the solid leach residues were washed with DI water adjusted to pH 2 to prevent precipitation of ions and then filtered under vacuum through a Buchner funnel with a Whatman grade-40 filter paper. The resultant leach residue was dried overnight at 50 °C. Control experiments with DI water instead of the sulfuric acid were conducted at the same conditions for a selected time interval.

B2.2. Material characterization

The specific surface area (SSA) of the starting limonite ore and the leach residues were measured by N_2 adsorption/desorption at 77 K with a Micromeritics Gemini VII 2390 Surface Area Analyzer and calculated using the Brunauer–Emmett–Teller (BET) equation (Brunauer et al., 1938). Prior to measurements, the solid samples were degassed at room temperature for ≥16 h and then at 80 °C for at least 4 h using a VacPrep™ 061 Sample Degas System (Micromeritics, Norcross, GA, USA). Powder X-ray diffraction (XRD) was performed to determine the mineralogical composition of the starting limonite ore and each of the leach residues using a PANalytical X'Pert Pro in Bragg-Brentano geometry, equipped with a Co source, X'Celerator detector and operated at 45 kV and 40 mA. Measurements were done over a scanning range of 4.5-85 °2θ and at 2.76 °2θ/minute. In addition, samples were analyzed using a ThermoFisher Nicolet iS5 Fourier transform infrared (FTIR) spectrometer with an iD7 diamond attenuated total reflectance (ATR) accessory by scanning in the 4000–400 cm^{-1} range at a resolution of 4 cm^{-1} and coadding 64 scans. Scanning electron microscopy analyses were carried out using a field emission gun (FEG) Zeiss Sigma 300 VP-FEG equipped with a Bruker Quantax XFlash 6|30 energy dispersive X-ray (EDX) detector system and operating at accelerating voltages from 2–15 kV. Prior to analyses, powder samples were dispersed on carbon pad covered aluminum stubs and carbon coated (≈25 nm thick). In addition, bulk chemical analysis of all solids was performed on fused beads with an X-ray fluorescence (XRF) spectrometer (AXIOS, Malvern Panalytical, UK). Loss on ignition (LOI) was measured by calculating the weight difference after fusion. Reproducibility was assessed using three certified reference materials (CRM), OREAS 182, 185, and 190. The results showed reproducibility within the analytical precision, with an accuracy better than 2% for major elements and better than 10% for trace elements.

The pH and oxidation–reduction potential (ORP) of the pregnant leach solutions was determined at room temperature after the cooling of each autoclave using a Thermo Scientific™ Orion™ Versa Star Pro™ benchtop electrochemistry meter. The major, minor, and trace cation concentrations of these solutions were analyzed using inductively coupled plasma mass spectrometry (ICP-MS). We used an Agilent 8900 series triple quadrupole ICP-MS-QQQ with

an octopole reaction system (ORS), in combination with an autosampler. Multi-element quality control (QC) check standards, containing the trace elements of interest (ca. 1 µg L^{-1}) and separate major elements standards at varying element concentration were analyzed at the start and end of each run and after no more than every 30 samples. Quality control data are assessed using Shewhart Charts and each analytical run is independently verified by a different analyst, including post processing of the data for drift, dilution and collation.

B3. Preliminary results

Preliminary analysis of the pregnant leach solutions from a representative experimental series revealed a consistent increase in Ni and Co in the leached solution with time (**Figure B1a**). In contrast, the dissolved concentrations of Fe and Cr (**Figure B1b**) deviated from this trend, exhibiting an initial fast increase between 0 and 30 min, followed by a decline from 30 to 120 min. Specific surface area measurements of the solid leach residues (**Figure B1c**) displayed an analogous trend, suggesting a concomitant change in the liquid and solid phases affecting Cr and Fe concentrations during the experimental HPAL treatment. Analyzing the mineralogy of the initial laterite ore sample with IR spectroscopy (**Figure B1d**) confirmed the presence of goethite (790–890 cm^{-1}) and serpentine (953–984 cm^{-1}) and with increasing

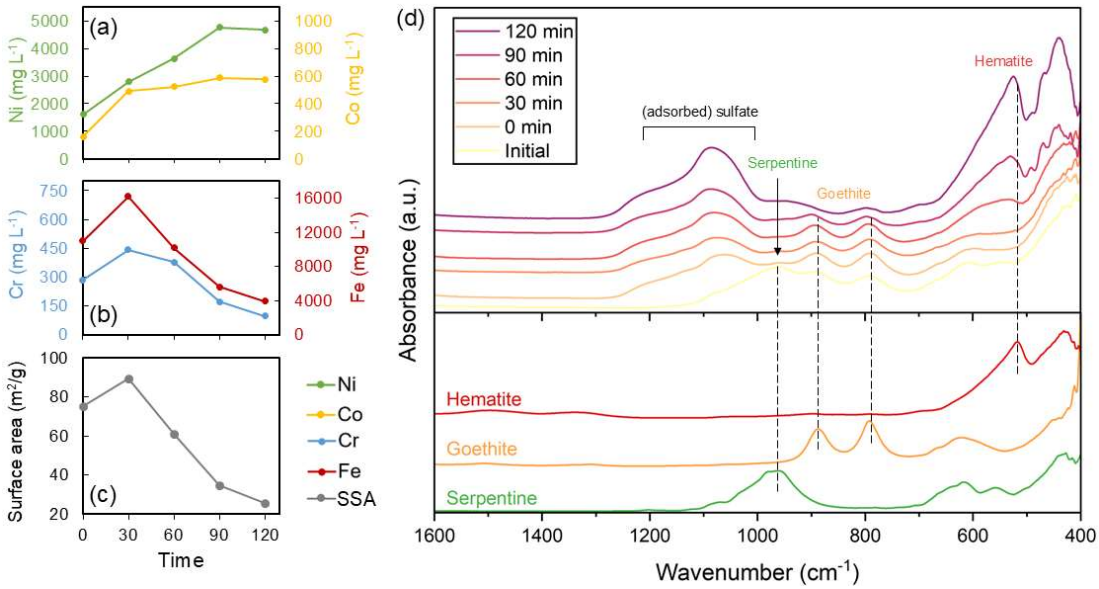

Figure B1. (a) Dissolved Ni and Co and (b) Cr and Fe concentrations in the pregnant leach solutions and the (c) specific surface area (SSA) of the solid leach residues from the HPAL experiments as a function of leaching duration. (d) Comparisons of the FTIR spectra of the solid leach residues with pure reference minerals (hematite, goethite, serpentine) show the dominant mineralogy of the residues. More information about the reference minerals was presented in Chapter 3.

experimental HPAL time, these signals slowly disappeared, while IR bands for hematite (e.g., increasingly sharper band between 425–520 cm^{-1}) and broad bands for sulfate (1080–1200 cm^{-1}) (Peak et al., 1999) appeared and became dominant. Hematite bands became prominent in the sample collected after 60 min, coinciding with the initial decline in Cr and Fe concentrations in the pregnant leach solution and the reduction in the surface area of the leach residue. The broadness of the sulfate band suggests that the sulfate is mostly adsorbed and crystalline phases, if present, are of minor quantity. SEM-EDX analysis of the solid leach residue collected after 120 minutes confirmed the presence of Fe oxide phase (pale red) associated with Cr and/or Al (**Figure B2a**). It also shows the occurrence of amorphous silica (dark green) and chromite (bright green). Higher resolution imaging of the Fe-rich particles (**Figure B2b**) revealed an individual nano-sized rhombohedral morphology consistent with previous studies on hematite (Min et al., 2007; Supattarasakda et al., 2013).

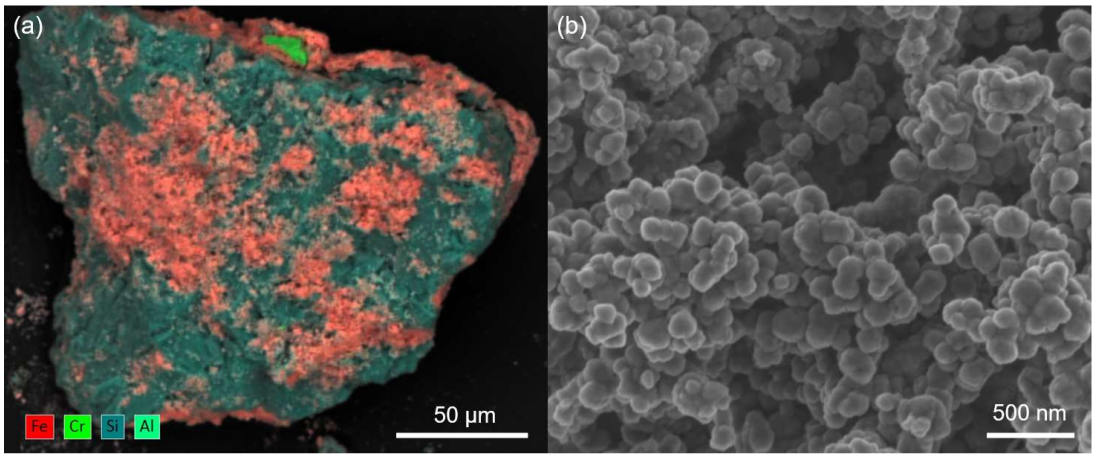

Figure B2. (a) SEM-EDX map (false color) of a large particle in the solid leach residue obtained after 120 minutes showing the distribution of Fe (red), Cr (bright green), Si (dark green), and Al (pale green) and an (b) SEM image of the smaller hematite particles.

Based on these preliminary results, we hypothesize that before 60 min, dissolution of goethite-rich laterite ore material (see Eq.1) releases Cr and Fe into solution, and that this is the dominant process controlling their mobility. Between 30 and 60 min, the aqueous ions become oversaturated leading to the precipitation of hematite according to Eq. 4. In this process, Cr becomes sequestered with the hematite. Although, more analyses and geochemical modelling is still needed to fully confirm these assertions, these preliminary experimental data support our findings from natural tailings samples collected from an HPAL plant in the Philippines (see **Chapter 5**) where we have documented the structural incorporation of Cr into hematite that formed during HPAL was the main sequestration mechanism limiting the environmental mobility of Cr.

Appendix C

List of Publications, Presentations, and Synchrotron Work

A. Scientific publications

Manuscripts under review, submitted or in preparation

Delina, R.E.G.; Perez, J.P.H.; Bazarkina, E.F.; Prieur, D.; Kvashnina, K.O.; Scheinost, A.C.; Mathon, O.; Stammeier, J.A.; Rabang, D.C.V.; Arcilla, C.A.; Benning, L.G. Coupling of iron and manganese controls chromium speciation in laterites developed from ultramafic rocks. In advanced stages of preparation for submission to *Geochimica et Cosmochimica Acta.*

Delina, R.E.G.; Perez, J.P.H.; Roddatis, V.V.; Stammeier, J.A.; Prieur, D.; Scheinost, A.C.; Tan, M.M.; Garcia, J.J.L.; Arcilla, C.A.; Benning, L.G. Immobilization of chromium by iron oxides in nickel-cobalt laterite mine tailings. In revision with *Environmental Science & Technology.*

Corkett, A.J.; Okhrymenko, M.; Roddatis, V.; Lebedev, O.; Leusen, J.V.; **Delina, R.E.G.**; Perez, J.P.H.; Benning, L.G.; Dronskowskia, R. The mixed transition-metal cyanamide $MnCr_2(NCN)_4$. *Under review in Inorganic Chemistry.*

Perez, J.P.H.; Tobler, D.J.; **Delina, R.E.G.**; Mathon, O.; Guilbaud, R.; Chi Fru, E.; Benning, L.G. Simulating iron mineral formation in Early Earth oceans and its impact on phosphorus bioavailability. *In the final stages of preparation for submission.*

Publications in peer-reviewed journals

Delina, R.E.G.; Perez, J.P.H.; Stammeier, J.A.; Bazarkina, E.F.; Benning, L.G. (2024). Partitioning and Mobility of Chromium in Iron-Rich Laterites from an Optimized Sequential Extraction Procedure. *Environmental Science & Technology,* 58, 6391-6401.

Delina, R.E.G.; Arcilla, C.; Otake, T.; Garcia, J. J.; Tan, M.; Ito, A. (2020). Chromium occurrence in a nickel laterite profile and its implications to surrounding surface waters. *Chemical Geology*, 558, 119863

B. Invited talks and conference contributions

Delina, R.E.G.; Perez, J.P.H.; Bazarkina, E.F.; Kvashnina K.O.; Scheinost, A.C.; Benning L.G. *From rocks to wastes: Tracing the fate of chromium in nickel mining areas.* European Mineralogical Conference 2024, Dublin (Ireland), August 18-23, 2024, oral presentation.

Delina, R.E.G.; Perez, J.P.H.; Roddatis, V.V.; Stammeier, J.A.; Bazarkina, E.F.; Prieur, D.; Scheinost, A.C.; Tan, M.M.; Garcia, J.J.L.; Arcilla, C.A.; Benning, L.G. *From rocks to wastes: Tracing the fate of chromium in nickel laterite mining areas.* GFZ Doctoral Days 2024, Potsdam (Germany), June 17-18, 2024, poster presentation, *Poster Prize Runner-up*.

Delina, R.E.G. *Chromium speciation and mobility in nickel laterite areas: from ores to mine wastes.* British Geological Survey, Nottingham (United Kingdom), November 15, 2023, oral presentation (invited talk).

Delina, R.E.G.; Perez, J.P.H.; Stammeier, J. A.; Syczewski, M.; Rabang, D.C.V.; Tan, M.M.; Garcia, J.J.L.; Arcilla, C.A.; Benning, L.G. *Distribution and speciation of chromium in active and legacy nickel laterite tailings.* Goldschmidt 2023, Lyon (France), July 9-14, 2023, oral presentation.

Delina, R.E.G.; Perez, J.P.H.; Stammeier, J.; Benning, L.B. *Optimizing a sequential extraction for iron-rich laterites: A case study on chromium.* GFZ Doctoral Days 2023, Potsdam (Germany), June 12-13, 2023, poster presentation, *Best Poster Prize*.

Delina, R.E.G.; Perez, J.P.H.; Stammeier, J. A.; Syczewski, M.; Rabang, D.C.V.; Tan, M.M.; Garcia, J.J.L.; Arcilla, C.A.; Benning, L.G. *Immobilization of Chromium by Iron Minerals: Ores to Tailings.* European Synchrotron Radiation Facility (ESRF) User Meeting 2023, Grenoble (France), February 6-8, 2023, poster presentation.

Delina, R.E.G.; Perez, J.P.H.; Stammeier, J. A.; Syczewski, M.; Rabang, D.C.V.; Tan, M.M.; Garcia, J.J.L.; Arcilla, C.A.; Benning, L.G. *Chromium speciation and mobility from nickel laterite ore profiles to mine tailings.* Helmholtz-Zentrum Dresden-Rossendorf (HZDR) ROBL Workshop 2023, Dresden (Germany), January 25, 2023, oral presentation (invited talk).

Delina, R.E.G.; Perez, J.P.H.; Stammeier, J.; Benning, L.B. *Optimization and validation of a new technique for estimating Cr partitioning in Ni laterites.* GeoCon 2022, December 5-7, 2022*,* Manila (Philippines), oral presentation (online).

Delina, R.E.G.; Perez, J.P.H.; Stammeier, J.; Blukis, R.; Benning, L.B. *Optimized sequential extraction for chromium from laterite deposits.* GeoMinKöln 2022, September 11-15, 2022*,* Cologne (Germany), oral presentation.

C. Synchrotron work

Funded synchrotron beamtime, including travel expenses, awarded for:

HERFD Cr and Mn K-edge X-ray absorption spectroscopy at the BM20 beamline of the European Synchrotron Radiation Facility (ESRF), Grenoble, France, September 20-25, 2023.
Principal investigators: **Delina, R.E.G.** and Perez, J.P.H.

Micro-X-ray absorption spectroscopy and micro-X-ray fluorescence at the ID21 beamline of the ESRF, Grenoble, France, May 20-24, 2022.
Co-investigator: **Delina, R.E.G.**; Principal investigator: Perez, J.P.H.

Cr and Fe K-edge X-ray absorption spectroscopy at the BM20 beamline of the ESRF, Grenoble, France, September 27-October 03, 2022.
Principal investigators: **Delina, R.E.G.** and Perez, J.P.H.

Fe K-edge X-ray absorption spectroscopy at the BM23 beamline of the ESRF, Grenoble, France, November 23-28, 2021.
Co-investigator: **Delina, R.E.G.**; Principal investigator: Perez, J.P.H.

Appendix D

List of Awards and Grants

The following awards and grants were received in association with this doctoral thesis:

2020 – 2024

Doctoral Research Grant, a 4-year funding (October 2020-December 2024) awarded by the Deutscher Akademischer Austauschdienst (DAAD) to support the completion of this doctoral project

2024

Poster Presentation Runner-up (150 EUR) awarded during the Helmholtz-Zentrum Potsdam – Deutsches GeoForschungZentrum GFZ Doctoral Days 2024 in Potsdam, Germany

2023

Best Poster Presentation Prize (800 EUR) awarded during the GFZ Doctoral Days 2023 in Potsdam, Germany

Student Travel Grant (300 EUR) awarded by the European Mineralogical Union (EMU) to present in the Goldschmidt 2023 Conference in Lyon, France.

Travel Grant given by the Deutsche Mineralogische Gesellschaft (DMG) to attend the YoungMineralogists Kickoff Meeting 2023 in Hannover, Germany

2022

Hackathon Winner ("GeoBox" Group) awarded during the Topic 8 ECR Workshop "Shaping the Future of Georesources" at GFZ in Potsdam, Germany

Travel Grant (50 EUR) given by the DMG to present in the GeoMinKöln 2022 Conference in Cologne, Germany

PhD Student Research Grant (2,300 USD) awarded by the International Association of GeoChemistry (IAGC) to support geochemical analyses conducted during this doctoral study

Field scholarship (800 CAD) awarded by the TravelingGeologist and **Travel Grant (1,550 EUR)** given by DAAD for the fieldwork conducted in Palawan, Philippines

References

Adamo, P., Agrelli, D., & Zampella, M. (2018). Chapter 9 - Chemical Speciation to Assess Bioavailability, Bioaccessibility and Geochemical Forms of Potentially Toxic Metals (PTMs) in Polluted Soils. In B. De Vivo, H. E. Belkin, & A. Lima (Eds.), *Environmental Geochemistry (Second Edition)* (pp. 153-194). Elsevier.

Ahmed, F., Hossain, M., Abdullah, A.T., Akbor, M., Ahsan, M.,. (2016). Public health risk assessment of chromium intake from vegetable grown in the wastewater irrigated site in Bangladesh. *Pollution*, *2*(4), 425-432.

Aiglsperger, T., Proenza, J. A., Lewis, J. F., Labrador, M., Svojtka, M., Rojas-Purón, A., Longo, F., & Ďurišová, J. (2016). Critical metals (REE, Sc, PGE) in Ni laterites from Cuba and the Dominican Republic. *Ore Geology Reviews*, *73*, 127-147.

Aitken, S. E., & Maluly Kemeid, F. (2016). Evolution to Dry Stack Tailings for the Vale Nouvelle Caledonie Nickel Project. Tailings and Mine Waste 2016 Conference, Colorado, USA.

Al-Khirbash, S. (2015). Genesis and mineralogical classification of Ni-laterites, Oman Mountains. *Ore Geology Reviews*, *65*, 199-212.

Al Khirbash, S., & Semhi, K. (2015). Mobilization and Redistribution of Elements in Laterites of Semail Ophiolite, Oman: A Mass Balance Study. *Sultan Qaboos University Journal for Science*, *20*(1), 39-54.

Alloway, B. J., & Ayres, D. C. (1997). *Chemical Principles of Environmental Pollution*. Blackie Academic & Professional.

Alvarez, M., Rueda, E. H., & Sileo, E. E. (2007). Simultaneous incorporation of Mn and Al in the goethite structure. *Geochimica et Cosmochimica Acta*, *71*(4), 1009-1020.

Andal, E. S., Arai, S., & Yumul Jr, G. P. (2005). Complete mantle section of a slow-spreading ridge-derived ophiolite: An example from the Isabela ophiolite in the Philippines. *Island Arc*, *14*(3), 272-294.

Anderson, R. A. (1997). Chromium as an essential nutrient for humans. *Regulatory Toxicology and Pharmacology*, *26*(1), S35-S41.

Ang, C. A., Zhang, F., & Azimi, G. (2017). Waste Valorization Process: Sulfur Removal and Hematite Recovery from High Pressure Acid Leach Residue for Steelmaking. *ACS Sustainable Chemistry & Engineering*, *5*(9), 8416-8423.

Apodaca, D. C., Domingo, J. P. T., David, C. P. C., & David, S. D. (2018). Siltation load contribution of nickel laterite mining on the coastal water quality of Hinadkaban Bay, Surigao Provinces, Philippines. *IOP Conference Series: Earth and Environmental Science*, *191*(012048), 1-10.

Aquino, K. A., Arcilla, C. A., Schardt, C., & Tupaz, C. A. J. (2022). Mineralogical and Geochemical Characterization of the Sta. Cruz Nickel Laterite Deposit, Zambales, Philippines. *Minerals*, *12*(3), 305.

Arcilla, C., Reyes, R., Aguda, N., Panlaqui, A., Ruelo, R., Vargas, J., & Palattao, B. (2019). *Exploratory Characterization of Scandium and Rare Earth Elements on Zambales, Palawan and Surigao Del Norte Nickeliferous Laterite Deposits* [Report]. E. Department of Science and Technology Philippine Council for Industry, and Emerging Technology Research and Development (DOST-PCIEERD)

Azimi, G., & Papangelakis, V. G. (2010). The solubility of gypsum and anhydrite in simulated laterite pressure acid leach solutions up to 250°C. *Hydrometallurgy*, *102*(1), 1-13.

Bacon, J. R., & Davidson, C. M. (2008). Is there a future for sequential chemical extraction? *Analyst*, *133*(1), 25-46.

Bahini, Y., Mushtaq, R., & Bahoo, S. (2024). Global energy transition: The vital role of cobalt in renewable energy. *Journal of Cleaner Production*, *470*, 143306.

Bang, J., & Hesterberg, D. (2004). Dissolution of trace element contaminants from two coastal plain soils as affected by pH. *Journal of Environmental Quality*, *33*(3), 891-901.

Barlett, R. J., & James, B. R. (1996). Chromium. In A. L. P. D.L. Sparks, P.A. Helmke, R.H. Loeppert, P. N. Soltanpour, M. A. Tabatabai, C. T. Johnston, M. E. Sumner (Ed.),

Methods of Soil Analysis: Part 3 Chemical Methods (pp. 683–701). Soil Science Society of America, Inc., American Society of Agronomy, Inc.

Bartlett, R. J. (1991). Chromium cycling in soils and water: links, gaps, and methods. *Environmental Health Perspectives*, *92*, 17-24.

Bartlett, R. J., & Kimble, J. M. (1976). Behavior of Chromium in Soils: II. Hexavalent Forms. *Journal of Environmental Quality*, *5*(4), 383-386.

Beaumont, J. J., Sedman, R. M., Reynolds, S. D., Sherman, C. D., Li, L. H., Howd, R. A., Sandy, M. S., Zeise, L., & Alexeeff, G. V. (2008). Cancer mortality in a Chinese population exposed to hexavalent chromium in drinking water. *Epidemiology*, *19*(1), 12-23.

Becquer, T., Pétard, J., Duwig, C., Bourdon, E., Moreau, R., & Herbillon, A. J. (2001). Mineralogical, chemical and charge properties of Geric Ferralsols from New Caledonia. *Geoderma*, *103*(3), 291-306.

Becquer, T., Quantin, C., Rotte-Capet, S., Ghanbaja, J., Mustin, C., & Herbillon, A. J. (2006). Sources of trace metals in Ferralsols in New Caledonia. *European Journal of Soil Science*, *57*(2), 200-213.

Becquer, T., Quantin, C., Sicot, M., & Boudot, J. P. (2003). Chromium availability in ultramafic soils from New Caledonia. *Science of The Total Environment*, *301*(1-3), 251-261.

Benitez, L. N., & Dubois, J.-P. (1999). Evaluation of the Selectivity of Sequential Extraction Procedures Applied to the Speciation of Cadmium in Soils. *International Journal of Environmental Analytical Chemistry*, *74*(1-4), 289-303.

Berger, A., & Frei, R. (2014). The fate of chromium during tropical weathering: A laterite profile from Central Madagascar. *Geoderma*, *213*, 521-532.

Bethke, C. M. (2022). *Geochemical and Biogeochemical Reaction Modeling* (3rd ed.). Cambridge University Press.

Biber, M. V., dos Santos Afonso, M., & Stumm, W. (1994). The coordination chemistry of weathering: IV. Inhibition of the dissolution of oxide minerals. *Geochimica et Cosmochimica Acta*, *58*(9), 1999-2010.

Bokhari, S. N. H., & Meisel, T. C. (2017). Method Development and Optimisation of Sodium Peroxide Sintering for Geological Samples. *Geostandards and Geoanalytical Research*, *41*(2), 181-195.

Bolaños-Benítez, V., van Hullebusch, E. D., Birck, J.-L., Garnier, J., Lens, P. N. L., Tharaud, M., Quantin, C., & Sivry, Y. (2021). Chromium mobility in ultramafic areas affected by mining activities in Barro Alto massif, Brazil: An isotopic study. *Chemical Geology*, *561*, 120000.

Borra, C. R. (2024). Iron extracted from hazardous waste *Nature*, *625*, 665-667.

Börsig, N., Scheinost, A. C., Shaw, S., Schild, D., & Neumann, T. A. (2017). Uptake mechanisms of selenium oxyanions during the ferrihydrite-hematite recrystallization. *Geochimica et Cosmochimica Acta*, *206*, 236-253.

Bots, P., Shaw, S., Law, G. T., Marshall, T. A., Mosselmans, J. F., & Morris, K. (2016). Controls on the Fate and Speciation of Np(V) During Iron (Oxyhydr)oxide Crystallization. *Environmental Science & Technology*, *50*(7), 3382-3390.

Bousserrhine, N., Gasser, U. G., Jeanroy, E., & Berthelin, J. (1999). Bacterial and Chemical Reductive Dissolution of Mn-, Co-, Cr-, and Al-Substituted Goethites. *Geomicrobiology Journal*, *16*(3), 245-258.

Brand, N. W., Butt, C., & Elías, M. (1998). Nickel laterites: classification and features.

Brown, G. E., Henrich, V. E., Casey, W. H., Clark, D. L., Eggleston, C., Felmy, A., Goodman, D. W., Grätzel, M., Maciel, G., McCarthy, M. I., Nealson, K. H., Sverjensky, D. A., Toney, M. F., & Zachara, J. M. (1999). Metal Oxide Surfaces and Their Interactions with Aqueous Solutions and Microbial Organisms. *Chemical Reviews*, *99*(1), 77-174.

Brunauer, S., Emmett, P. H., & Teller, E. (1938). Adsorption of Gases in Multimolecular Layers. *Journal of the American Chemical Society*, *60*(2), 309-319.

Buarzaiga, M., Marshall, D., Boissoneault, M., Hoffman, M., & Potter, C. A. (2003). *Chromium removal from leach liquors produced during high pressure acid leaching of lateritic ores* (Canada Patent No. CA 2366095).

Burgess, J. (1988). *Ions in Solution: Basic Principles of Chemical Interactions*. Halsted Press.
Burke, I. T., Mayes, W. M., Peacock, C. L., Brown, A. P., Jarvis, A. P., & Gruiz, K. (2012). Speciation of arsenic, chromium, and vanadium in red mud samples from the Ajka spill site, Hungary. *Environmental Science & Technology*, *46*(6), 3085-3092.
Butt, C. R. M., & Cluzel, D. (2013). Nickel Laterite Ore Deposits: Weathered Serpentinites. *Elements*, *9*(2), 123-128.
Caraballo, M. A., Asta, M. P., Perez, J. P. H., & Hochella, M. F. (2022). Past, present and future global influence and technological applications of iron-bearing metastable nanominerals. *Gondwana Research*, *110*, 283-304.
Charlet, L., & Manceau, A. A. (1992). X-ray absorption spectroscopic study of the sorption of Cr(III) at the oxide-water interface: II. Adsorption, coprecipitation, and surface precipitation on hydrous ferric oxide. *Journal of Colloid and Interface Science*, *148*(2), 443-458.
Chen, K., Bocknek, L., & Manning, B. (2021). Oxidation of Cr(III) to Cr(VI) and Production of Mn(II) by Synthetic Manganese(IV) Oxide. *Crystals*, *11*(4), 443.
Chen, Z., Perez, J. P. H., Smales, G. J., Blukis, R., Pauw, B. R., Stammeier, J. A., Radnik, J., Smith, A. J., & Benning, L. G. (2024). Impact of organic phosphates on the structure and composition of short-range ordered iron nanophases. *Nanoscale Advances*, *6*(10), 2656-2668.
Choppala, G., & Burton, E. D. (2018). Chromium(III) substitution inhibits the Fe(II)-accelerated transformation of schwertmannite. *PLoS One*, *13*(12), e0208355.
Chrysochoou, M., Theologou, E., Bompoti, N., Dermatas, D., & Panagiotakis, I. (2016). Occurrence, Origin and Transformation Processes of Geogenic Chromium in Soils and Sediments. *Current Pollution Reports*, *2*(4), 224-235.
Claff, S. R., Sullivan, L. A., Burton, E. D., & Bush, R. T. (2010). A sequential extraction procedure for acid sulfate soils: Partitioning of iron. *Geoderma*, *155*(3-4), 224-230.
Corker, J. M., Evans, J., & Rummey, J. M. (1991). EXAFS studies of pillared clay catalysts. *Materials Chemistry and Physics*, *29*(1), 201-209.
Cornell, R. M., Giovanoli, R., & Schindler, P. W. (1987). Effect of Silicate Species on the Transformation of Ferrihydrite into Goethite and Hematite in Alkaline Media. *Clays and Clay Minerals*, *35*(1), 21-28.
Cornell, R. M., & Schwertmann, U. (2003). *The Iron Oxides: Structure, Properties, Reactions, Occurrences and Uses*. Wiley.
Cudennec, Y., & Lecerf, A. (2006). The transformation of ferrihydrite into goethite or hematite, revisited. *Journal of Solid State Chemistry*, *179*(3), 716-722.
D'Amore, J. J., Al-Abed, S. R., Scheckel, K. G., & Ryan, J. A. (2005). Methods for speciation of metals in soils: a review. *Journal of Environmental Quality*, *34*(5), 1707-1745.
Dalvi, A., Bacon, W., & Osborne, R. (2004). The Past and the Future of Nickel Laterites.
De los Santos, V. (1959). Preliminary report on the geology and mineral resources of central Palawan. *Philippine Geologist*, *13*, 104-141.
Delina, R. E., Arcilla, C., Otake, T., Garcia, J. J., Tan, M., & Ito, A. (2020). Chromium occurrence in a nickel laterite profile and its implications to surrounding surface waters. *Chemical Geology*, *558*, 119863.
Delina, R. E. G., Perez, J. P. H., Roddatis, V. V., Stammeier, J. A., Prieur, D., Scheinost, A. C., Tan, M. M., Garcia, J. J. L., Arcilla, C. A., & Benning, L. G. (under review). Immobilization of chromium by iron oxides in nickel-cobalt laterite mine tailings. *Environmental Science & Technology*.
Delina, R. E. G., Perez, J. P. H., Stammeier, J. A., Bazarkina, E. F., & Benning, L. G. (2024). Partitioning and Mobility of Chromium in Iron-Rich Laterites from an Optimized Sequential Extraction Procedure. *Environmental Science & Technology*, *58*(14), 6391-6401.
Denys, A., Janots, E., Auzende, A.-L., Lanson, M., Findling, N., & Trcera, N. (2021). Evaluation of selectivity of sequential extraction procedure applied to REE speciation in laterite. *Chemical Geology*, *559*, 119954.

Dilshara, P., Abeysinghe, B., Premasiri, R., Dushyantha, N., Ratnayake, N., Senarath, S., Sandaruwan Ratnayake, A., & Batapola, N. (2024). The role of nickel (Ni) as a critical metal in clean energy transition: applications, global distribution and occurrences, production-demand and phytomining. *Journal of Asian Earth Sciences*, *259*, 105912.

Ding, Y. Z., Song, Z. G., Feng, R. W., & Guo, J. K. (2013). Interaction of organic acids and pH on multi-heavy metal extraction from alkaline and acid mine soils. *International Journal of Environmental Science and Technology*, *11*(1), 33-42.

Dódony, I. n., Pósfai, M. l., & Buseck, P. R. (2002). Revised structure models for antigorite: An HRTEM study. *American Mineralogist*, *87*(10), 1443-1457.

Doelsch, E., Moussard, G., & Macary, H. S. (2008). Fractionation of tropical soilborne heavy metals—Comparison of two sequential extraction procedures. *Geoderma*, *143*(1-2), 168-179.

Dold, B. (2003). Speciation of the most soluble phases in a sequential extraction procedure adapted for geochemical studies of copper sulfide mine waste. *Journal of Geochemical Exploration*, *80*(1), 55-68.

Domènech, C., Villanova-de-Benavent, C., Proenza, J. A., Tauler, E., Lara, L., Galí, S., Soler, J. M., Campeny, M., & Ibañez-Insa, J. (2022). Co–Mn Mineralisations in the Ni Laterite Deposits of Loma Caribe (Dominican Republic) and Loma de Hierro (Venezuela). *Minerals*, *12*(8), 927.

Drahota, P., Grosslova, Z., & Kindlova, H. (2014). Selectivity assessment of an arsenic sequential extraction procedure for evaluating mobility in mine wastes. *Analytica Chimica Acta*, *839*, 34-43.

Dublet, G., Juillot, F., Brest, J., Noël, V., Fritsch, E., Proux, O., Olivi, L., Ploquin, F., & Morin, G. (2017). Vertical changes of the Co and Mn speciation along a lateritic regolith developed on peridotites (New Caledonia). *Geochimica et Cosmochimica Acta*, *217*, 1-15.

Dublet, G., Juillot, F., Morin, G., Fritsch, E., Fandeur, D., & Brown, G. E. (2015). Goethite aging explains Ni depletion in upper units of ultramafic lateritic ores from New Caledonia. *Geochimica et Cosmochimica Acta*, *160*, 1-15.

Dublet, G., Juillot, F., Morin, G., Fritsch, E., Fandeur, D., Ona-Nguema, G., & Brown, G. E. (2012). Ni speciation in a New Caledonian lateritic regolith: A quantitative X-ray absorption spectroscopy investigation. *Geochimica et Cosmochimica Acta*, *95*, 119-133.

Eary, L. E., & Rai, D. (1987). Kinetics of chromium(III) oxidation to chromium(VI) by reaction with manganese dioxide. *Environmental Science & Technology*, *21*(12), 1187-1193.

Economou-Eliopoulos, M., Frei, R., & Megremi, I. (2016). Potential leaching of Cr(VI) from laterite mines and residues of metallurgical products (red mud and slag): An integrated approach. *Journal of Geochemical Exploration*, *162*, 40-49.

Economou-Eliopoulos, M., Megremi, I., Vasilatos, C., Frei, R., & Mpourodimos, I. (2017). Geochemical constraints on the sources of Cr(VI) contamination in waters of Messapia (Central Evia) Basin. *Applied Geochemistry*, *84*, 13-25.

EFSA. (2014). Scientific Opinion on the risks to public health related to the presence of chromium in food and drinking water. *European Food and Safety Authority (EFSA) Journal*, *12*(3), 3595.

Eiche, E., Kramar, U., Berg, M., Berner, Z., Norra, S., & Neumann, T. (2010). Geochemical changes in individual sediment grains during sequential arsenic extractions. *Water Research*, *44*(19), 5545-5555.

Ekstrom, E. B., Learman, D. R., Madden, A. S., & Hansel, C. M. (2010). Contrasting effects of Al substitution on microbial reduction of Fe(III) (hydr)oxides. *Geochimica et Cosmochimica Acta*, *74*(24), 7086-7099.

Elias, M. (2002). Nickel laterite deposits – geological overview, resources and exploitation. *CODES Special Publication*, *4*, 205-220.

Elias, M., Donaldson, M. J., & Giorgetta, N. E. (1981). Geology, mineralogy, and chemistry of lateritic nickel-cobalt deposits near Kalgoorlie, Western Australia. *Economic Geology*, *76*(6), 1775-1783.

Eliopoulos, D. G., Economou-Eliopoulos, M., Apostolikas, A., & Golightly, J. P. (2012). Geochemical features of nickel-laterite deposits from the Balkan Peninsula and Gordes, Turkey: The genetic and environmental significance of arsenic. *Ore Geology Reviews*, *48*, 413-427.

EU. (2011). Regulation (EU) No 1169/2011 of the European Parliament and of the council of 25 October 2011. *Official Journal of the European Union (EU)*, *304*, 18-63.

European Commission. (2023). *Study on the critical raw materials for the EU 2023 – Final report*.

Fandeur, D., Juillot, F., Morin, G., Olivi, L., Cognigni, A., Ambrosi, J. P., Guyot, F., & Fritsch, E. (2009a). Synchrotron-based speciation of chromium in an Oxisol from New Caledonia: Importance of secondary Fe-oxyhydroxides. *American Mineralogist*, *94*(5-6), 710-719.

Fandeur, D., Juillot, F., Morin, G., Olivi, L., Cognigni, A., Webb, S. M., Ambrosi, J.-P., Fritsch, E., Guyot, F., & Brown, J. G. E. (2009b). XANES Evidence for Oxidation of Cr(III) to Cr(VI) by Mn-Oxides in a Lateritic Regolith Developed on Serpentinized Ultramafic Rocks of New Caledonia. *Environmental Science & Technology*, *43*(19), 7384-7390.

Fantoni, D., Brozzo, G., Canepa, M., Cipolli, F., Marini, L., Ottonello, G., & Zuccolini, M. (2002). Natural hexavalent chromium in groundwaters interacting with ophiolitic rocks. *Environmental Geology*, *42*(8), 871-882.

Fendorf, S., Eick, M. J., Grossl, P., & Sparks, D. L. (1997). Arsenate and Chromate Retention Mechanisms on Goethite 1. Surface Structure. *Environmental Science & Technology*, *31*(2), 315–320.

Fendorf, S. E., Lamble, G. M., Stapleton, M. G., Kelley, M. J., & Sparks, D. L. (1994). Mechanisms of chromium(III) sorption on silica. 1. Chromium(III) surface structure derived by extended x-ray absorption fine structure spectroscopy. *Environmental Science & Technology*, *28*(2), 284-289.

Filgueiras, A. V., Lavilla, I., & Bendicho, C. (2002). Chemical sequential extraction for metal partitioning in environmental solid samples. *Journal of Environmental Monitoring*, *4*(6), 823-857.

Foster, A. L., Brown, G. E., Tingle, T. N., & Parks, G. A. (1998). Quantitative arsenic speciation in mine tailings using X-ray absorption spectroscopy. *American Mineralogist*, *83*(5-6), 553-568.

Frierdich, A. J., Luo, Y., & Catalano, J. G. (2011). Trace element cycling through iron oxide minerals during redox-driven dynamic recrystallization. *Geology*, *39*(11), 1083-1086.

Fu, W., Feng, Y., Luo, P., Zhang, Y., Huang, X., Zeng, X., Cai, Q., & Zhou, Y. (2019). Weathering of Ophiolite Remnant and Formation of Ni Laterite in a Strong Uplifted Tectonic Region (Yuanjiang, Southwest China). *Minerals*, *9*(1), 51.

Fu, W., Yang, J., Yang, M., Pang, B., Liu, X., Niu, H., & Huang, X. (2014). Mineralogical and geochemical characteristics of a serpentinite-derived laterite profile from East Sulawesi, Indonesia: Implications for the lateritization process and Ni supergene enrichment in the tropical rainforest. *Journal of Asian Earth Sciences*, *93*, 74-88.

Galivarapu, J. K., Kumar, D., Banerjee, A., Sathe, V., Aquilanti, G., & Rath, C. (2016). Effect of size reduction on cation distribution and magnetic transitions in CoCr2O4 multiferroic: EXAFS, magnetic and diffused neutron scattering measurements. *RSC Advances*, *6*(68), 63809-63819.

Garnier, J., Quantin, C., Guimarães, E., & Becquer, T. (2008). Can chromite weathering be a source of Cr in soils? *Mineralogical Magazine*, *72*(1), 49-53.

Garnier, J., Quantin, C., Guimarães, E., Garg, V. K., Martins, E. S., & Becquer, T. (2009). Understanding the genesis of ultramafic soils and catena dynamics in Niquelândia, Brazil. *Geoderma*, *151*(3-4), 204-214.

Garnier, J., Quantin, C., Guimarães, E. M., Vantelon, D., Montargès-Pelletier, E., & Becquer, T. (2013). Cr(VI) genesis and dynamics in Ferralsols developed from ultramafic rocks: The case of Niquelândia, Brazil. *Geoderma*, *193-194*, 256-264.

Garnier, J., Quantin, C., Martins, E., & Becquer, T. (2006). Solid speciation and availability of chromium in ultramafic soils from Niquelândia (Brazil) : chemical and spectroscopic approaches. *Journal of Geochemical Exploration*, *88*(1), 206-209.

Gaudin, A., Decarreau, A., Noack, Y., & Grauby, O. (2005). Clay mineralogy of the nickel laterite ore developed from serpentinised peridotites at Murrin Murrin, Western Australia. *Australian Journal of Earth Sciences*, *52*(2), 231-241.

Geng, H., Wang, F., Yan, C., Tian, Z., Chen, H., Zhou, B., Yuan, R., & Yao, J. (2020). Leaching behavior of metals from iron tailings under varying pH and low-molecular-weight organic acids. *Journal of Hazardous Materials*, *383*, 121136.

Gibaga, C. R. L., Samaniego, J. O., Tanciongco, A. M., Quierrez, R. N. M., Montano, M. O., Gervasio, J. H. C., Reyes, R. C. G., & Peralta, M. J. V. (2022). The rare earth element (REE) potential of the Philippines. *Journal of Geochemical Exploration*, *242*, 107082.

Giovanoli, R., & Cornell, R. M. (1992). Crystallization of Metal Substituted Ferrihydrites. *Journal of Plant Nutrition and Soil Science*, *155*(5), 455-460.

Gleeson, S. A., Butt, C. R. M., & Elias, M. (2003). Nickel Laterites: A Review. *Society for Economic Geologists Newsletter*, *54*, 1-18.

Gleeson, S. A., Herrington, R., Durango, J., Velasquez, C., & Koll, G. (2004). The Mineralogy and Geochemistry of the Cerro Matoso S.A. Ni Laterite Deposit, Montelibano, Colombia. *Economic Geology*, *99*, 1197-1213.

Gleyzes, C., Tellier, S., & Astruc, M. (2002). Fractionation studies of trace elements in contaminated soils and sediments: a review of sequential extraction procedures. *TrAC Trends in Analytical Chemistry*, *21*(6), 451-467.

Golightly, J. P., Goldfarb, R. J., Marsh, E. E., & Monecke, T. (2010). Progress in Understanding the Evolution of Nickel Laterites. In *The Challenge of Finding New Mineral Resources: Global Metallogeny, Innovative Exploration, and New Discoveries* (Vol. 15, pp. 451–485). Society of Economic Geologists.

Gruebel, K. A., Davis, J. A., & Leckie, J. O. (1988). The Feasibility of Using Sequential Extraction Techniques for Arsenic and Selenium in Soils and Sediments. *Soil Science Society of America Journal*, *52*(2), 390-397.

Gu, C., Dam, T., Hart, S. C., Turner, B. L., Chadwick, O. A., Berhe, A. A., Hu, Y., & Zhu, M. (2020). Quantifying Uncertainties in Sequential Chemical Extraction of Soil Phosphorus Using XANES Spectroscopy. *Environmental Science & Technology*, *54*(4), 2257-2267.

Guertin, J., Jacobs, J., & Avakian, C. P. (2016). *Chromium(VI) Handbook*. CRC Press.

Gultom, T., & Sianipar, A. (2020). High pressure acid leaching: a newly introduced technology in Indonesia. *IOP Conference Series: Earth and Environmental Science*, *413*, 012015.

Gunkel-Grillon, P., Laporte-Magoni, C., Lemestre, M., & Bazire, N. (2014). Toxic chromium release from nickel mining sediments in surface waters, New Caledonia. *Environmental Chemistry Letters*, *12*(4), 511-516.

Hans Wedepohl, K. (1995). The composition of the continental crust. *Geochimica et Cosmochimica Acta*, *59*(7), 1217-1232.

Hansel, C. M., Wielinga, B. W., & Fendorf, S. (2003). Structural and compositional evolution of Cr/Fe solids after indirect chromate reduction by dissimilatory iron-reducing bacteria. *Geochimica et Cosmochimica Acta*, *67*(3), 401-402.

Hao, W., Chen, N., Sun, W., Mänd, K., Kirsimäe, K., Teitler, Y., Somelar, P., Robbins, L. J., Babechuk, M. G., Planavsky, N. J., Alessi, D. S., & Konhauser, K. O. (2022). Binding and transport of Cr(III) by clay minerals during the Great Oxidation Event. *Earth and Planetary Science Letters*, *584*, 117503.

Hass, A., & Fine, P. (2010). Sequential Selective Extraction Procedures for the Study of Heavy Metals in Soils, Sediments, and Waste Materials—a Critical Review. *Critical Reviews in Environmental Science and Technology*, *40*(5), 365-399.

Hausladen, D. M., & Fendorf, S. (2017). Hexavalent Chromium Generation within Naturally Structured Soils and Sediments. *Environmental Science & Technology*, *51*(4), 2058-2067.

Helvacı, C., Oyman, T., Gündoğan, İ., Sözbilir, H., Parlak, O., Kadir, S., & Güven, N. (2018). Mineralogy and genesis of the Ni–Co lateritic regolith deposit of the Çaldağ area (Manisa, western Anatolia), Turkey. *Canadian Journal of Earth Sciences*, *55*(3), 252-271.

Houben, G., & Kaufhold, S. (2011). Multi-method characterization of the ferrihydrite to goethite transformation. *Clay Minerals*, *46*, 387-395.

Hua, J., Chen, M., Liu, C., Li, F., Long, J., Gao, T., Wu, F., Lei, J., & Gu, M. (2018). Cr Release from Cr-Substituted Goethite during Aqueous Fe(II)-Induced Recrystallization. *Minerals*, *8*(9), 1-16.

Hudson-Edwards, K., & Dold, B. (2015). Mine Waste Characterization, Management and Remediation. *Minerals*, *5*(1), 82-85.

IEA. (2021). *The Role of Critical Minerals in Clean Energy Transitions*. International Energy Agency (IEA).

Isaure, M.-P., Laboudigue, A., Manceau, A., Sarret, G., Tiffreau, C., Trocellier, P., Lamble, G., Hazemann, J.-L., & Chateigner, D. (2002). Quantitative Zn speciation in a contaminated dredged sediment by μ-PIXE, μ-SXRF, EXAFS spectroscopy and principal component analysis. *Geochimica et Cosmochimica Acta*, *66*(9), 1549-1567.

Islam, M. A., Angove, M. J., Morton, D. W., Pramanik, B. K., & Awual, M. R. (2020). A mechanistic approach of chromium (VI) adsorption onto manganese oxides and boehmite. *Journal of Environmental Chemical Engineering*, *8*(2), 103515.

Jackson, M. L. R. (1969). *Soil Chemical Analysis: Advanced Course*. Parallel Press University of Wisconsin-Madison Libraries.

Jang, J.-H., Dempsey, B. A., & Burgos, W. D. (2007). Solubility of Hematite Revisited: Effects of Hydration. *Environmental Science & Technology*, *41*(21), 7303-7308.

Johnson, D. B., Smith, S. L., & Santos, A. L. (2021). Bioleaching of Transition Metals From Limonitic Laterite Deposits and Reassessment of the Multiple Roles of Sulfur-Oxidizing Acidophiles in the Process. *Frontiers in Microbiology*, *12*, 1-10.

Johnston, C. P., & Chrysochoou, M. (2014). Mechanisms of chromate adsorption on hematite. *Geochimica et Cosmochimica Acta*, *138*, 146-157.

Kadır, S., Aydoğan, M. S., Elıtok, Ö., & Helvaci, C. (2015). Composition and Genesis of the Nickel-Chrome-Bearing Nontronite and Montmorillonite in Lateritized Ultramafic Rocks in the Muratdği Region (Uşak, Western Anatolia), Turkey. *Clays and Clay Minerals*, *63*(3), 163-184.

Kaiser, K., & Zech, W. (1996). Defects in Estimation of Aluminum in Humus Complexes of Podzolic Soils by Pyrophosphate Extraction. *Soil Science*, *161*(7), 452-458.

Kaiser, M., Ellerbrock, R. H., Wulf, M., Dultz, S., Hierath, C., & Sommer, M. (2012). The influence of mineral characteristics on organic matter content, composition, and stability of topsoils under long-term arable and forest land use. *Journal of Geophysical Research: Biogeosciences*, *117*(G2), 1-16.

Katz, S., & Salem, H. (1994). *The Biological and Environmental Chemistry of Chromium*. VCH Publishers.

Kaur, N., Gräfe, M., Singh, B., & Kennedy, B. (2009). Simultaneous incorporation of Cr, Zn, Cd, and Pb in the goethite structure. *Clays and Clay Minerals*, *57*(2), 234-250.

Kaya, Ş., & Topkaya, Y. A. (2011). High pressure acid leaching of a refractory lateritic nickel ore. *Minerals Engineering*, *24*(11), 1188-1197.

Kazakis, N., Kantiranis, N., Kalaitzidou, K., Kaprara, E., Mitrakas, M., Frei, R., Vargemezis, G., Tsourlos, P., Zouboulis, A., & Filippidis, A. (2017). Origin of hexavalent chromium in groundwater: The example of Sarigkiol Basin, Northern Greece. *Science of The Total Environment*, *593-594*, 552-566.

Kazakis, N., Kantiranis, N., Voudouris, K. S., Mitrakas, M., Kaprara, E., & Pavlou, A. (2015). Geogenic Cr oxidation on the surface of mafic minerals and the hydrogeological conditions influencing hexavalent chromium concentrations in groundwater. *Science of The Total Environment*, *514*, 224-238.

Keller, P., & Anderson, C. (2018). The Production of Critical Materials as By Products. *Aspects in Mining & Mineral Science.*, *2*(2), 208-221.

Kelly, S. D., Hesterberg, D., & Ravel, B. (2008). Analysis of Soils and Minerals Using X-ray Absorption Spectroscopy. In L. R. D. A. L. Ulery (Ed.), *Methods of Soil Analysis Part 5—Mineralogical Methods* (pp. 387-463). Soil Science Society of America, Inc.

Keon, N. E., Swartz, C. H., Brabander, D. J., Harvey, C., & Hemond, H. F. (2001). Validation of an Arsenic Sequential Extraction Method for Evaluating Mobility in Sediments. *Environmental Science & Technology*, *35*(13), 2778-2784.

Kim, C.-J., Chung, C.-S., Jung, J.-M., Kim, Y.-R., Kang, D.-W., Kim, H.-E., Shin, K.-H., & Choi, K.-Y. (2023). Long-term effects of chromium from red mud (bauxite residue) ocean dumping on the benthic environment in South Korea. *Marine Pollution Bulletin*, *196*, 115584.

Kim, J. G., Dixon, J. B., Chusuei, C. C., & Deng, Y. (2002). Oxidation of Chromium(III) to (VI) by Manganese Oxides. *Soil Science Society of America Journal*, *66*(1), 306-315.

Klementiev, K., & Chernikov, R. (2016). XAFSmass: a program for calculating the optimal mass of XAFS samples. *Journal of Physics: Conference Series*, *712*(1), 012008.

Klementiev, K. V. (2006). *XANES dactyloscope for Windows, freeware: www.desy.de/~klmn/xanda.html*.

Kotaś, J., & Stasicka, Z. (2000). Chromium occurrence in the environment and methods of its speciation. *Environmental Pollution*, *107*(3), 263-283.

Kraal, P., van Genuchten, C. M., & Behrends, T. (2022). Phosphate coprecipitation affects reactivity of iron (oxyhydr)oxides towards dissolved iron and sulfide. *Geochimica et Cosmochimica Acta*, *321*, 311-328.

Kraal, P., van Genuchten, C. M., Behrends, T., & Rose, A. L. (2019). Sorption of phosphate and silicate alters dissolution kinetics of poorly crystalline iron (oxyhydr)oxide. *Chemosphere*, *234*, 690-701.

Kuo, H. W., Lai, J. S., & Lin, T. I. (1997). Nasal septum lesions and lung function in workers exposed to chromic acid in electroplating factories. *International Archives of Occupational and Environmental Health*, *70*(4), 272-276.

Kvashnina, K. O., & Scheinost, A. C. (2016). A Johann-type X-ray emission spectrometer at the Rossendorf beamline. *Journal of Synchrotron Radiation*, *23*(Pt 3), 836-841.

La Force, M. J., & Fendorf, S. (2000). Solid-Phase Iron Characterization During Common Selective Sequential Extractions. *Soil Science Society of America Journal*, *64*(5), 1608-1615.

Landers, M. (2010). *The crystal chemistry, dissolution kinetics and dehydroxylation of oxide-type lateritic Ni ore* [Doctoral Thesis, Unversity of Western Australia].

Langmuir, D. (1997). *Aqueous Environmental Geochemistry*. Prentice-Hall, Inc.

Larios, R., Fernandez-Martinez, R., & Rucandio, I. (2012). Comparison of three sequential extraction procedures for fractionation of arsenic from highly polluted mining sediments. *Analytical and Bioanalytical Chemistry*, *402*(9), 2909-2921.

Lee, G., & Hering, J. G. (2005). Oxidative Dissolution of Chromium(III) Hydroxide at pH 9, 3, and 2 with Product Inhibition at pH 2. *Environmental Science & Technology*, *39*(13), 4921-4928.

Leleyter, L., & Probst, J.-L. (1999). A New Sequential Extraction Procedure for the Speciation of Particulate Trace Elements in River Sediments. *International Journal of Environmental Analytical Chemistry*, *73*(2), 109-128.

Lenaz, D., Logvinova, A. M., Princivalle, F., & Sobolev, N. V. (2009). Structural parameters of chromite included in diamond and kimberlites from Siberia: A new tool for discriminating ultramafic source. *American Mineralogist*, *94*(7), 1067-1070.

Li, M., Liu, H., Chen, T., Wei, L., Wang, C., Hu, W., & Wang, H. (2019). The transformation of α-(Al, Fe)OOH in natural fire: Effect of Al substitution amount on fixation of phosphate. *Chemical Geology*, *524*, 368-382.

Li, W., Liang, X., An, P., Feng, X., Tan, W., Qiu, G., Yin, H., & Liu, F. (2016). Mechanisms on the morphology variation of hematite crystals by Al substitution: The modification of Fe and O reticular densities. *Scientific Reports*, *6*(1), 35960.

Li, X., Guo, C., Jin, X., Yao, Q., Liu, Q., Zhang, L., Lu, G., Reinfelder, J. R., Huang, W., & Dang, Z. (2022). Molecular-scale study of Cr(VI) adsorption onto lepidocrocite facets

by EXAFS, in situ ATR-FTIR, theoretical frequency calculations and DFT+U techniques. *Environmental Science: Nano*, *9*(2), 568-581.
Li, Y., Lv, G., Wu, L., Li, Z., & Liao, L. (2023). Facile Adjustment of Exposed Crystal Facet of Hematite Derived-From Goethite to Enhance Cr (VI) Sorption. *Crystals*, *13*(1), 79.
Lim-Nunez, R., & Gilkes, R. (1985). Acid dissolution of synthetic metal-containing goethites and hematites. International Clay Conference, Denver.
Lin, Q., Wang, Y., Yang, X., Ruan, D., Wang, S., Wei, X., & Qiu, R. (2018). Effect of low-molecular-weight organic acids on hematite dissolution promoted by desferrioxamine B. *Environmental Science and Pollution Research*, *25*(1), 163-173.
Lindsay, D. R., Farley, K. J., & Carbonaro, R. F. (2012). Oxidation of CrIII to CrVI during chlorination of drinking water. *Journal of Environmental Monitoring*, *14*(7), 1789-1797.
Liu, F., Li, X., Sheng, A., Shang, J., Wang, Z., & Liu, J. (2019). Kinetics and Mechanisms of Protein Adsorption and Conformational Change on Hematite Particles. *Environmental Science & Technology*, *53*(17), 10157-10165.
Liu, H., Lu, X., Li, M., Zhang, L., Pan, C., Zhang, R., Li, J., & Xiang, W. (2018). Structural Incorporation of Manganese into Goethite and Its Enhancement of Pb(II) Adsorption. *Environmental Science & Technology*, *52*(8), 4719-4727.
Ma, Y. B., & Uren, N. C. (1998). Transformations of heavy metals added to soil — application of a new sequential extraction procedure. *Geoderma*, *84*(1), 157-168.
Majzlan, J. (2011). Thermodynamic Stabilization of Hydrous Ferric Oxide by Adsorption of Phosphate and Arsenate. *Environmental Science & Technology*, *45*(11), 4726-4732.
Manceau, A., & Charlet, L. (1992). X-ray absorption spectroscopic study of the sorption of Cr(III) at the oxide-water interface: I. Molecular mechanism of Cr(III) oxidation on Mn oxides. *Journal of Colloid and Interface Science*, *148*(2), 425-442.
Manceau, A., & Drits, V. A. (1993). Local Structure of Ferrihydrite and Feroxyhite by Exafs Spectroscopy. *Clay Minerals*, *28*(2), 165–184.
Manceau, A., Lanson, B., Schlegel, M., Musso, M., Hazemann, J. L., Chateigner, D., & Lamble, G. M. (2000a). Quantitative Zn speciation in smelter-contaminated soils by EXAFS spectroscopy. *American Journal of Science*, *300*, 289-343.
Manceau, A., Marcus, M. A., & Grangeon, S. (2012). Determination of Mn valence states in mixed-valent manganates by XANES spectroscopy. *American Mineralogist*, *97*(5-6), 816-827.
Manceau, A., Marcus, M. A., Tamura, N., Proux, O., Geoffroy, N., & Lanson, B. (2004). Natural speciation of Zn at the micrometer scale in a clayey soil using X-ray fluorescence, absorption, and diffraction. *Geochimica et Cosmochimica Acta*, *68*(11), 2467-2483.
Manceau, A., Schlegel, M. L., Musso, M., Sole, V. A., Gauthier, C., Petit, P. E., & Trolard, F. (2000b). Crystal chemistry of trace elements in natural and synthetic goethite. *Geochimica et Cosmochimica Acta*, *64*(21), 3643-3661.
Margiotta, S., Mongelli, G., Summa, V., Paternoster, M., & Fiore, S. (2012). Trace element distribution and Cr(VI) speciation in Ca-HCO3 and Mg-HCO3 spring waters from the northern sector of the Pollino massif, southern Italy. *Journal of Geochemical Exploration*, *115*, 1-12.
Marker, A., Friedrich, G., Carvalho, A., & Melfi, A. (1991). Control of the distribution of Mn, Co, Zn, Zr, Ti and REEs during the evolution of lateritic covers above ultramafic complexes. *Journal of Geochemical Exploration*, *40*(1), 361-383.
Marsh, E. E., Anderson, E. D., & Gray, F. (2013). *Nickel-cobalt laterites: a deposit model: Chapter H in Mineral deposit models for resource assessment* [Scientific Investigations Report](2010-5070H). United States Geological Survey.
Marshall, T. A., Morris, K., Law, G. T., Livens, F. R., Mosselmans, J. F., Bots, P., & Shaw, S. (2014). Incorporation of Uranium into Hematite during crystallization from ferrihydrite. *Environmental Science & Technology*, *48*(7), 3724-3731.
Mathon, O., Beteva, A., Borrel, J., Bugnazet, D., Gatla, S., Hino, R., Kantor, I., Mairs, T., Munoz, M., Pasternak, S., Perrin, F., & Pascarelli, S. (2015). The time-resolved and extreme conditions XAS (TEXAS) facility at the European Synchrotron Radiation

Facility: the general-purpose EXAFS bending-magnet beamline BM23. *Journal of Synchrotron Radiation*, *22*(6), 1548-1554.
Maurizot, P., Sevin, B., Iseppi, M., & Giband, T. (2019). Nickel-Bearing Laterite Deposits in Accretionary Context and the Case of New Caledonia: From the Large-Scale Structure of Earth to Our Everyday Appliances. *GSA Today*, *29*(5), 4-10.
Mayes, W. M., Jarvis, A. P., Burke, I. T., Walton, M., Feigl, V., Klebercz, O., & Gruiz, K. (2011). Dispersal and attenuation of trace contaminants downstream of the Ajka bauxite residue (red mud) depository failure, Hungary. *Environmental Science & Technology*, *45*(12), 5147-5155.
McClain, C. N., Fendorf, S., Webb, S. M., & Maher, K. (2017). Quantifying Cr(VI) Production and Export from Serpentine Soil of the California Coast Range. *Environmental Science & Technology*, *51*(1), 141-149.
McClain, C. N., & Maher, K. (2016). Chromium fluxes and speciation in ultramafic catchments and global rivers. *Chemical Geology*, *426*, 135-157.
MGB. (2010). *Geology of the Philippines* (Second ed.). Mines and Geosciences Bureau (MGB).
Mikutta, R., Kleber, M., Kaiser, K., & Jahn, R. (2005). Review. *Soil Science Society of America Journal*, *69*(1), 120-135.
Min, C.-y., Huang, Y.-d., & Liu, L. (2007). High-yield synthesis and magnetic property of hematite nanorhombohedras through a facile solution route. *Materials Letters*, *61*(25), 4756-4758.
Min, S., & Kim, Y. (2020). Physicochemical Characteristics of the Birnessite and Todorokite Synthesized Using Various Methods. *Minerals*, *10*(10), 884.
Mongelli, G., Taghipour, B., Sinisi, R., & Khadivar, S. (2019). Mineralization and element redistribution in the Chah-Gheib Ni-laterite ore zone, Bavanat, Zagros Belt, Iran. *Ore Geology Reviews*, *111*, 102990.
Morrison, J. M., Goldhaber, M. B., Mills, C. T., Breit, G. N., Hooper, R. L., Holloway, J. M., Diehl, S. F., & Ranville, J. F. (2015). Weathering and transport of chromium and nickel from serpentinite in the Coast Range ophiolite to the Sacramento Valley, California, USA. *Applied Geochemistry*, *61*, 72-86.
Mudd, G. M. (2010). Global trends and environmental issues in nickel mining: Sulfides versus laterites. *Ore Geology Reviews*, *38*(1-2), 9-26.
Muehe, E. M., Adaktylou, I. J., Obst, M., Zeitvogel, F., Behrens, S., Planer-Friedrich, B., Kraemer, U., & Kappler, A. (2013). Organic Carbon and Reducing Conditions Lead to Cadmium Immobilization by Secondary Fe Mineral Formation in a pH-Neutral Soil. *Environmental Science & Technology*, *47*(23), 13430-13439.
Myagkiy, A., Truche, L., Cathelineau, M., & Golfier, F. (2017). Revealing the conditions of Ni mineralization in the laterite profiles of New Caledonia: Insights from reactive geochemical transport modelling. *Chemical Geology*, *466*, 274-284.
Newville, M. (2001). IFEFFIT : interactive XAFS analysis and FEFF fitting. *Journal of Synchrotron Radiation*, *8*(2), 322-324.
Noël, V., Marchand, C., Juillot, F., Ona-Nguema, G., Viollier, E., Marakovic, G., Olivi, L., Delbes, L., Gelebart, F., & Morin, G. (2014). EXAFS analysis of iron cycling in mangrove sediments downstream a lateritized ultramafic watershed (Vavouto Bay, New Caledonia). *Geochimica et Cosmochimica Acta*, *136*, 211-228.
Noël, V., Morin, G., Juillot, F., Marchand, C., Brest, J., Bargar, J. R., Muñoz, M., Marakovic, G., Ardo, S., & Brown, G. E. (2015). Ni cycling in mangrove sediments from New Caledonia. *Geochimica et Cosmochimica Acta*, *169*, 82-98.
Önal, M. A. R., & Topkaya, Y. A. (2014). Pressure acid leaching of Çaldağ lateritic nickel ore: An alternative to heap leaching. *Hydrometallurgy*, *142*, 98-107.
Oze, C., Fendorf, S., Bird, D. K., & Coleman, R. G. (2004a). Chromium geochemistry in serpentinized ultramafic rocks and serpentine soils from the Franciscan complex of California. *American Journal of Science*, *304*(1), 67-101.
Oze, C., Fendorf, S., Bird, D. K., & Coleman, R. G. (2004b). Chromium Geochemistry of Serpentine Soils. *International Geology Review*, *46*(2), 97-126.

Oze, C., Sleep, N. H., Coleman, R. G., & Fendorf, S. (2016). Anoxic oxidation of chromium. *Geology*, *44*(7), 543-546.

PAGASA. (2011). *Climate Change in the Philippines*. Philippine Atmospheric Geophysical and Astronomical Services Administration (PAGASA).

PAGASA. (2024). *Climatological Normals*. Philippine Atmospheric, Geophysical and Astronomical Services Administration. Retrieved 09/2024 from https://www.pagasa.dost.gov.ph/climate/climatological-normals

Pan, C., Liu, H., Catalano, J. G., Qian, A., Wang, Z., & Giammar, D. E. (2017). Rates of Cr(VI) Generation from Cr(x)Fe(1-x)(OH)(3) Solids upon Reaction with Manganese Oxide. *Environmental Science & Technology*, *51*(21), 12416-12423.

Papassiopi, N., Pinakidou, F., Katsikini, M., Antipas, G. S., Christou, C., Xenidis, A., & Paloura, E. C. (2014). A XAFS study of plain and composite iron(III) and chromium(III) hydroxides. *Chemosphere*, *111*, 169-176.

Pasquet, C., Le Monier, P., Monna, F., Durlet, C., Brigaud, B., Losno, R., Chateau, C., Laporte-Magoni, C., & Gunkel-Grillon, P. (2016). Impact of nickel mining in New Caledonia assessed by compositional data analysis of lichens. *Springerplus*, *5*(1), 2022.

Patzner, M. S., Mueller, C. W., Malusova, M., Baur, M., Nikeleit, V., Scholten, T., Hoeschen, C., Byrne, J. M., Borch, T., Kappler, A., & Bryce, C. (2020). Iron mineral dissolution releases iron and associated organic carbon during permafrost thaw. *Nature Communications*, *11*(1), 1-11.

Peak, D., Ford, R. G., & Sparks, D. L. (1999). An in Situ ATR-FTIR Investigation of Sulfate Bonding Mechanisms on Goethite. *Journal of Colloid and Interface Science*, *218*(1), 289-299.

Penner-Hahn, J. E. (2005). Characterization of "spectroscopically quiet" metals in biology. *Coordination Chemistry Reviews*, *249*(1), 161-177.

Perez, J. P. H., Tobler, D. J., Thomas, A. N., Freeman, H. M., Dideriksen, K., Radnik, J., & Benning, L. G. (2019). Adsorption and Reduction of Arsenate during the Fe2+-Induced Transformation of Ferrihydrite. *ACS Earth and Space Chemistry*, *3*(6), 884-894.

Peterson, M. L., Brown, G. E., Parks, G. A., & Stein, C. L. (1997). Differential redox and sorption of Cr (III/VI) on natural silicate and oxide minerals: EXAFS and XANES results. *Geochimica et Cosmochimica Acta*, *61*(16), 3399-3412.

Pickering, W. F. (1986). Metal ion speciation — soils and sediments (a review). *Ore Geology Reviews*, *1*(1), 83-146.

Porsch, K., & Kappler, A. (2011). FeII oxidation by molecular O2 during HCl extraction. *Environmental Chemistry*, *8*(2), 190-197.

Poulton, S. W., & Canfield, D. E. (2005). Development of a sequential extraction procedure for iron: implications for iron partitioning in continentally derived particulates. *Chemical Geology*, *214*(3), 209-221.

Proux, O., Lahera, E., Del Net, W., Kieffer, I., Rovezzi, M., Testemale, D., Irar, M., Thomas, S., Aguilar-Tapia, A., Bazarkina, E. F., Prat, A., Tella, M., Auffan, M., Rose, J., & Hazemann, J.-L. (2017). High-Energy Resolution Fluorescence Detected X-Ray Absorption Spectroscopy: A Powerful New Structural Tool in Environmental Biogeochemistry Sciences. *Journal of Environmental Quality*, *46*(6), 1146-1157.

Putzolu, F., Boni, M., Mondillo, N., Maczurad, M., & Pirajno, F. (2019). Ni-Co enrichment and High-Tech metals geochemistry in the Wingellina Ni-Co oxide-type laterite deposit (Western Australia). *Journal of Geochemical Exploration*, *196*, 282-296.

Quantin, C., Becquer, T., Rouiller, J., & Berthelin, J. (2002). Redistribution of Metals in a New Caledonia Ferralsol After Microbial Weathering. *Soil Science Society of America Journal*, *66*(6), 1797-1804.

Quareni, S., & De Pieri, R. (1965). A three-dimensional refinement of structure of crocoite, $PbCrO_4$. *Acta Crystallographica*, *19*, 287-289.

Rai, D., Eary, L. E., & Zachara, J. M. (1989). Environmental chemistry of chromium. *Science of The Total Environment*, *86*(1-2), 15-23.

Rai, D., Sass, B. M., & Moore, D. A. (1987). Chromium(III) hydrolysis constants and solubility of chromium(III) hydroxide. *Inorganic Chemistry*, *26*(3), 345-349.

Raiswell, R., Canfield, D. E., & Berner, R. A. (1994). A comparison of iron extraction methods for the determination of degree of pyritisation and the recognition of iron-limited pyrite formation. *Chemical Geology*, *111*(1), 101-110.

Raous, S., Echevarria, G., Sterckeman, T., Hanna, K., Thomas, F., Martins, E., & Becquer, T. (2013). Potentially toxic metals in ultramafic mining materials: Identification of the main bearing and reactive phases. *Geoderma*, *192*, 111-119.

Ratié, G., Garnier, J., Calmels, D., Vantelon, D., Guimarães, E., Monvoisin, G., Nouet, J., Ponzevera, E., & Quantin, C. (2018). Nickel distribution and isotopic fractionation in a Brazilian lateritic regolith: Coupling Ni isotopes and Ni K-edge XANES. *Geochimica et Cosmochimica Acta*, *230*, 137-154.

Ravel, B., & Newville, M. (2005). ATHENA, ARTEMIS, HEPHAESTUS: data analysis for X-ray absorption spectroscopy using IFEFFIT. *Journal of Synchrotron Radiation*, *12*, 537-541.

Rehr, J. J., Albers, R. C., & Zabinsky, S. I. (1992). High-order multiple-scattering calculations of x-ray-absorption fine structure. *Physical Review Letters*, *69*(23), 3397-3400.

Richard, F. C., & Bourg, A. C. M. (1991). Aqueous geochemistry of chromium: A review. *Water Research*, *25*(7), 807-816.

Robles-Camacho, J., & Armienta, M. A. (2000). Natural chromium contamination of groundwater at León Valley, México. *Journal of Geochemical Exploration*, *68*(3), 167-181.

Rodgers, K. J., Hursthouse, A., & Cuthbert, S. (2015). The Potential of Sequential Extraction in the Characterisation and Management of Wastes from Steel Processing: A Prospective Review. *Int J Environ Res Public Health*, *12*(9), 11724-11755.

Ruttenberg, K. C. (1992). Development of a sequential extraction method for different forms of phosphorus in marine sediments. *Limnology and Oceanography*, *37*(7), 1460-1482.

Salman, A. D., Juzsakova, T., Mohsen, S., Abdullah, T. A., Le, P. C., Sebestyen, V., Sluser, B., & Cretescu, I. (2022). Scandium Recovery Methods from Mining, Metallurgical Extractive Industries, and Industrial Wastes. *Materials*, *15*(7), 2376.

Santoro, L., Putzolu, F., Mondillo, N., Boni, M., & Herrington, R. (2022). Trace element geochemistry of iron-(oxy)-hydroxides in Ni(Co)-laterites: Review, new data and implications for ore forming processes. *Ore Geology Reviews*, *140*, 104501.

Scheinost, A. C., Claussner, J., Exner, J., Feig, M., Findeisen, S., Hennig, C., Kvashnina, K. O., Naudet, D., Prieur, D., Rossberg, A., Schmidt, M., Qiu, C. R., Colomp, P., Cohen, C., Dettona, E., Dyadkin, V., & Stumpf, T. (2021). ROBL-II at ESRF: a synchrotron toolbox for actinide research. *Journal of Synchrotron Radiation*, *28*, 333-349.

Scheinost, A. C., Stanjek, H., Schulze, D. G., Gasser, U., & Sparks, D. L. (2001). Structural environment and oxidation state of Mn in goethite-groutite solid-solutions. *American Mineralogist*, *86*(1-2), 139–146.

Schroeder, D. C., & Lee, G. F. (1975). Potential transformations of chromium in natural waters. *Water, Air, and Soil Pollution*, *4*(3), 355-365.

Schwertmann, U. (1991). Solubility and dissolution of iron oxides. *Plant and Soil*, *130*(1), 1-25.

Schwertmann, U., & Cornell, R. M. (2000). *Iron Oxides in the Laboratory: Preparation and Characterization*. Wiley.

Schwertmann, U., & Latham, M. (1986). Properties of iron oxides in some new caledonian oxisols. *Geoderma*, *39*(2), 105-123.

Scicchitano, M. R., Rubatto, D., Hermann, J., Shen, T., Padrón-Navarta, J. A., Williams, I. S., & Zheng, Y. F. (2018). In Situ Oxygen Isotope Determination in Serpentine Minerals by Ion Microprobe: Reference Materials and Applications to Ultrahigh-Pressure Serpentinites. *Geostandards and Geoanalytical Research*, *42*(4), 459-479.

Scullett-Dean, G., Hamilton, J. L., Repina, O., Brand, H. E. A., Burton, E. D., Saunders, M., & Santini, T. C. (2023). Uptake and incorporation of Al, Cr, V, Zn and Mo in hematite: Competition, synergies and influence on structural properties. *Journal of Hazardous Materials*, *445*, 130630.

Shanker, A., & Venkateswarlu, B. (2011). Chromium: Environmental Pollution, Health Effects and Mode of Action. *in-Chief: Jerome ON (ed) Encyclopedia of environmental health. Elsevier, Burlington*, *65*, 650-659.

Shibayama, K., Yokogawa, T., Sato, H., Enomoto, M., Nakai, O., Ito, T., Mizuno, F., & Hattori, Y. (2016). Taganito HPAL Plant Project. *Minerals Engineering*, *88*, 61-65.

Shuman, L. M. (1982). Separating Soil Iron- and Manganese-Oxide Fractions for Microelement Analysis. *Soil Science Society of America Journal*, *46*(5), 1099-1102.

Shuman, L. M. (1983). Sodium Hypochlorite Methods for Extracting Microelements Associated with Soil Organic Matter. *Soil Science Society of America Journal*, *47*(4), 656-660.

Shuman, L. M. (1985). Fractionation method for soil microelements. *Soil Science*, *140*(1), 11-22.

Siebecker, M. G., Chaney, R. L., & Sparks, D. L. (2017). Nickel speciation in several serpentine (ultramafic) topsoils via bulk synchrotron-based techniques. *Geoderma*, *298*, 35-45.

Silveira, M. L., Alleoni, L. R., O'Connor, G. A., & Chang, A. C. (2006). Heavy metal sequential extraction methods--a modification for tropical soils. *Chemosphere*, *64*(11), 1929-1938.

Singh, B., Sherman, D. M., Gilkes, R. J., Wells, M., & Mosselmans, J. F. W. (2000). Structural Chemistry of Fe, Mn, and Ni in Synthetic Hematites as Determined by Extended X-Ray Absorption Fine Structure Spectroscopy. *Clays and Clay Minerals*, *48*(5), 521-527.

Singh, B., Sherman, D. M., Gilkes, R. J., Wells, M. A., & Mosselmans, J. F. W. (2002a). Incorporation of Cr, Mn and Ni into goethite (a-FeOOH): mechanism from extended X-ray absorption fine structure spectroscopy. *Clay Minerals 37*, 639–649.

Singh, B., Sherman, D. M., Gilkes, R. J., Wells, M. A., & Mosselmans, J. F. W. (2002b). Incorporation of Cr, Mn and Ni into goethite (α-FeOOH): mechanism from extended X-ray absorption fine structure spectroscopy. *Clay Minerals*, *37*(4), 639-649.

Sobol, S. I. (1969). Physico-chemical studies of the composition and conditions of formation of the crust (scale) in the reactors of Moa Bay leaching plant. *Revisita Technologica*, *7*(1), 1-43.

Stoops, G., & Marcelino, V. (2018). Chapter 24 - Lateritic and Bauxitic Materials. In G. Stoops, V. Marcelino, & F. Mees (Eds.), *Interpretation of Micromorphological Features of Soils and Regoliths (Second Edition)* (pp. 691-720). Elsevier.

Sulzberger, B., Suter, D., Siffert, C., Banwart, S., & Stumm, W. (1989). Dissolution of fe(iii)(hydr)oxides in natural waters; laboratory assessment on the kinetics controlled by surface coordination. *Marine Chemistry*, *28*(1), 127-144.

Sun, J., Mailloux, B. J., Chillrud, S. N., van Geen, A., Thompson, A., & Bostick, B. C. (2018). Simultaneously Quantifying Ferrihydrite and Goethite in Natural Sediments Using the Method of Standard Additions with X-ray Absorption Spectroscopy. *Chemical Geology*, *476*, 248-259.

Sun, S., Deng, T., Ao, M., Mo, Y., Li, J., Liu, T., Yang, W., Jin, C., Qiu, R., & Tang, Y. (2023). Release of chromium from Cr(III)- and Ni(II)-substituted goethite in presence of organic acids: Role of pH in the formation of colloids and complexes. *Science of The Total Environment*, *904*, 166979.

Supattarasakda, K., Petcharoen, K., Permpool, T., Sirivat, A., & Lerdwijitjarud, W. (2013). Control of hematite nanoparticle size and shape by the chemical precipitation method. *Powder Technology*, *249*, 353-359.

Tabios, G. Q. I. (2018). Impacts of laterite mining of nickel and iron ores on watersheds. *National Academy of Science and Technology Bulletin*(12), 1-4.

Tang, B., Xiang, Q., Fang, Z., Zhang, X., Xiong, Z., Li, H., Yuan, C., & Zhang, S. (2019). Influence of Cr3+ substitution for Mg2+ on the crystal structure and microwave dielectric properties of CaMg1-xCr2x/3Si2O6 ceramics. *Ceramics International*, *45*(9), 11484-11490.

Tardy, Y. (1992). Chapter 15 - Diversity and terminology of lateritic profiles. In I. P. Martini & W. Chesworth (Eds.), *Developments in Earth Surface Processes* (Vol. 2, pp. 379-405). Elsevier.

Tardy, Y. (1997). *Petrology of laterites and tropical soils*. Oxford and IBH publishing.

Tashakor, M., Zuhairi Wan Yaacob, W., Mohamad, H., Abdul Ghani, A., & Saadati, N. (2014). Assessment of selected sequential extraction and the toxicity characteristic leaching test as indices of metal mobility in serpentinite soils. *Chemical Speciation & Bioavailability*, *26*(3), 139-147.

Tauler, E., Galí, S., Villanova-de-Benavent, C., Chang-Rodríguez, A., Núñez-Cambra, K., Khazaradze, G., & Proenza, J. A. (2023). Geochemistry and Mineralogy of the Clay-Type Ni-Laterite Deposit of San Felipe (Camagüey, Cuba). *Minerals*, *13*(10), 1281.

Tchounwou, P. B., Yedjou, C. G., Patlolla, A. K., & Sutton, D. J. (2012). Heavy Metal Toxicity and the Environment. In A. Luch (Ed.), *Molecular, Clinical and Environmental Toxicology: Volume 3: Environmental Toxicology* (pp. 133-164). Springer Basel.

Teitler, Y., Cathelineau, M., Ulrich, M., Ambrosi, J. P., Munoz, M., & Sevin, B. (2019). Petrology and geochemistry of scandium in New Caledonian Ni-Co laterites. *Journal of Geochemical Exploration*, *196*, 131-155.

Tessier, A., Campbell, P. G. C., & Bisson, M. (1979). Sequential extraction procedure for the speciation of particulate trace metals. *Analytical Chemistry*, *51*(7), 844-851.

Thomas, A. N., Eiche, E., Göttlicher, J., Steininger, R., G. Benning, L., M. Freeman, H., Dideriksen, K., & Neumann, T. (2018). Products of Hexavalent Chromium Reduction by Green Rust Sodium Sulfate and Associated Reaction Mechanisms. *Soil Systems*, *2*(4), 58.

Toby, B. H., & Von Dreele, R. B. (2013). GSAS-II: the genesis of a modern open-source all purpose crystallography software package. *Journal of Applied Crystallography*, *46*(2), 544-549.

Tokunaga, T. K., Lipton, D. S., Benson, S. M., Yee, A. W., Oldfather, J. M., Duckart, E. C., Johannis, P. W., & Halvorsen, K. E. (1991). Soil selenium fractionation, depth profiles and time trends in a vegetated site at Kesterson Reservoir. *Water, Air, and Soil Pollution*, *57*(1), 31-41.

Toner, B. M., Santelli, C. M., Marcus, M. A., Wirth, R., Chan, C. S., McCollom, T., Bach, W., & Edwards, K. J. (2009). Biogenic iron oxyhydroxide formation at mid-ocean ridge hydrothermal vents: Juan de Fuca Ridge. *Geochimica et Cosmochimica Acta*, *73*(2), 388-403.

Trolard, F., Bourrie, G., Jeanroy, E., Herbillon, A. J., & Martin, H. (1995). Trace metals in natural iron oxides from laterites: A study using selective kinetic extraction. *Geochimica et Cosmochimica Acta*, *59*(7), 1285-1297.

Tupaz, C. A. J., Watanabe, Y., Sanematsu, K., & Echigo, T. (2020). Mineralogy and geochemistry of the Berong Ni-Co laterite deposit, Palawan, Philippines. *Ore Geology Reviews*, *125*, 103686.

Ucyildiz, A., & Girgin, I. (2017). High pressure sulphuric acid leaching of lateritic nickel ore. *Physicochemical Problems of Mineral Processing*, *53*(1), 475-488.

Ugwu, I. M., & Sherman, D. M. (2019). The solubility of goethite with structurally incorporated nickel and cobalt: Implication for laterites. *Chemical Geology*, *518*, 1-8.

Ullah, S., Liu, Q., Wang, S., Jan, A. U., Sharif, H. M. A., Ditta, A., Wang, G., & Cheng, H. (2023). Sources, impacts, factors affecting Cr uptake in plants, and mechanisms behind phytoremediation of Cr-contaminated soils. *Science of The Total Environment*, *899*, 165726.

Ulrich, M., Cathelineau, M., Muñoz, M., Boiron, M.-C., Teitler, Y., & Karpoff, A. M. (2019). The relative distribution of critical (Sc, REE) and transition metals (Ni, Co, Cr, Mn, V) in some Ni-laterite deposits of New Caledonia. *Journal of Geochemical Exploration*, *197*, 93-113.

USEPA. (1978). *Method 310.1: Alkalinity (Titrimetric, pH 4.5)*. United States Environmental Protection Agency (USEPA).

USEPA. (1992). *Method 7196A: Chromium, Hexavalent (Colorimetric, 1,5-Diphenylcarbazide)*. United States Environmental Protection Agency (USEPA).
USEPA. (2006). *2006 Edition of the drinking water standards and health advisories*. United States Environmental Protection Agency (USEPA) Office of Water.
USGS. (2023). *Mineral commodity summaries 2023*. United States Geological Survey (USGS).
Villanova-de-Benavent, C., Domènech, C., Tauler, E., Galí, S., Tassara, S., & Proenza, J. A. (2017). Fe–Ni-bearing serpentines from the saprolite horizon of Caribbean Ni-laterite deposits: new insights from thermodynamic calculations. *Mineralium Deposita*, *52*(7), 979-992.
Villanova-de-Benavent, C., Proenza, J. A., Galí, S., García-Casco, A., Tauler, E., Lewis, J. F., & Longo, F. (2014). Garnierites and garnierites: Textures, mineralogy and geochemistry of garnierites in the Falcondo Ni-laterite deposit, Dominican Republic. *Ore Geology Reviews*, *58*, 91-109.
Voelz, J. L., Johnson, N. W., Chun, C. L., Arnold, W. A., & Penn, R. L. (2019). Quantitative Dissolution of Environmentally Accessible Iron Residing in Iron-Rich Minerals: A Review. *ACS Earth and Space Chemistry*, *3*(8), 1371-1392.
Vu, H. P., Shaw, S., Brinza, L., & Benning, L. G. (2013). Partitioning of Pb(II) during goethite and hematite crystallization: Implications for Pb transport in natural systems. *Applied Geochemistry*, *39*, 119-128.
Wang, S., & Mulligan, C. N. (2013). Effects of three low-molecular-weight organic acids (LMWOAs) and pH on the mobilization of arsenic and heavy metals (Cu, Pb, and Zn) from mine tailings. *Environ Geochem Health*, *35*(1), 111-118.
Weast, R. C. (1988). *CRC Handbook of chemistry and physics* (1st student ed ed.). CRC Press.
Webb, S. M. (2005). SIXpack: a graphical user interface for XAS analysis using IFEFFIT. *Physica Scripta*, *2005*(T115), 1011.
Wells, M. A., Ramanaidou, E. R., Verrall, M., & Tessarolo, C. (2009). Mineralogy and crystal chemistry of "garnierites" in the Goro lateritic nickel deposit, New Caledonia. *European Journal of Mineralogy*, *21*(2), 467-483.
Wells, M. A., Ramanaidou, E. R., Zakaria Quadir, M., Roberts, M., Bourdet, J., & Verrall, M. (2022). Morphology, composition and dissolution of chromite in the Goro lateritic nickel deposit, New Caledonia: Insight into ophiolite and laterite genesis. *Ore Geology Reviews*, *143*, 104752.
Whittington, B. I., Johnson, J. A., Quan, L. P., McDonald, R. G., & Muir, D. M. (2003). Pressure acid leaching of arid-region nickel laterite ore: Part II. Effect of ore type. *Hydrometallurgy*, *70*(1-3), 47-62.
Whittington, B. I., & Muir, D. (2000). Pressure Acid Leaching of Nickel Laterites: A Review. *Mineral Processing and Extractive Metallurgy Review*, *21*(6), 527-599.
Whittleston, R. A., Stewart, D. I., Mortimer, R. J. G., Tilt, Z. C., Brown, A. P., Geraki, K., & Burke, I. T. (2011). Chromate reduction in Fe(II)-containing soil affected by hyperalkaline leachate from chromite ore processing residue. *Journal of Hazardous Materials*, *194*, 15-23.
WHO. (2003). *Chromium in Drinking-water: Background document for development of WHO Guidelines for Drinking-water Quality*. World Health Organization (WHO).
WHO. (2017). *Guidelines for drinking-water quality: fourth edition incorporating the first addendum*. World Health Organization (WHO).
Wilbur, S., Abadin, H., Fay, M., Yu, D., Tencza, B., Ingerman, L., Klotzbach, J., & James, S. (2012). Agency for Toxic Substances and Disease Registry (ATSDR) Toxicological Profiles. In *Toxicological Profile for Chromium*. Agency for Toxic Substances and Disease Registry (US).
Wilburn, D. R. (2011). *Cobalt mineral exploration and supply from 1995 through 2013* [Scientific Investigations Report](2011-5084). United States Geological Survey.
Wilke, M., Farges, F., Petit, P.-E., Brown, G. E., & Martin, F. (2001). Oxidation state and coordination of Fe in minerals: An Fe K-XANES spectroscopic study. *American Mineralogist*, *86*, 714–730.

Wright, M. T., Parker, D. R., & Amrhein, C. (2003). Critical Evaluation of the Ability of Sequential Extraction Procedures To Quantify Discrete Forms of Selenium in Sediments and Soils. *Environmental Science & Technology*, *37*(20), 4709-4716.

Wu, W.-C., Wang, S.-L., Tzou, Y.-M., Chen, J.-H., & Wang, M.-K. (2007). The adsorption and catalytic transformations of chromium on Mn substituted goethite. *Applied Catalysis B: Environmental*, *75*(3-4), 272-280.

Xu, Y. H., Huang, J. H., & Brandl, H. (2017). An optimised sequential extraction scheme for the evaluation of vanadium mobility in soils. *Journal of Environmental Sciences*, *53*, 173-183.

Zahoransky, T., Wegorzewski, A. V., Huong, W., & Mikutta, C. (2023). X-ray absorption spectroscopy study of Mn reference compounds for Mn speciation in terrestrial surface environments. *American Mineralogist: Journal of Earth and Planetary Materials*, *108*(5), 847-864.

Zhou, M. F., Yumul, G. P., Malpas, J., & Sun, M. (2000). Comparative study of platinum-group elements in the Coto and Acoje blocks of the Zambales Ophiolite Complex, Philippines. *Island Arc*, *9*(4), 556-564.